Graphene Nanoribbon Growth and Substrate Transfer for Device Applications

Inaugural dissertation of the Faculty of Science, University of Bern

presented by

Rimah, Darawish

from Palestine

Supervisor of the doctoral thesis:
Prof. Dr. Roman Fasel
University of Bern (Department of Chemistry, Biochemistry and Pharmaceutical Sciences)
Swiss Federal Laboratories for Material Science and Technology (Empa)

Graphene Nanoribbon Growth and Substrate Transfer for Device Applications

Inaugural dissertation
of the Faculty of Science,
University of Bern

presented by

Rimah, Darawish

from Palestine

Supervisor of the doctoral thesis:
Prof. Dr. Roman Fasel
University of Bern (Department of Chemistry, Biochemistry and Pharmaceutical Sciences)
Swiss Federal Laboratories for Material Science and Technology (Empa)

Accepted by the Faculty of Science.

Bern, 03/11/2023

The Dean
Prof. Dr. Marco Herwegh

Table of Contents

Abstract

Graphene nanoribbons (GNRs) – quasi-one-dimensional stripes of graphene – have emerged as promising materials for next-generation nano-electronic devices. This interest stems from their tunable physicochemical properties, which can be achieved through precise control of ribbon width and edge structure. Atomic precision is achieved by on-surface synthesis, which relies on the metal surface-assisted covalent coupling of specifically designed molecular precursors in ultra-high vacuum. Metallic single-crystal surfaces serve both as a template and a catalyst. However, GNRs located on a metallic substrate are not suitable for many types of characterization and, more importantly, for most applications and device integration. Therefore, the development of efficient substrate transfer procedures for bringing the synthesized GNR materials onto technologically relevant substrates is a necessity. Additionally, it is crucial to optimize growth conditions to maximize GNR length and alignment for high device yield. Finally, GNR quality needs to be maintained and monitored throughout the entire path from GNR growth to device integration.

This thesis focuses on the growth, substrate transfer, and characterization of aligned 9-atom-wide armchair GNRs (9-AGNRs) grown on the surface of the regularly stepped Au(788) single crystal. The (788) surface has 3 nm wide (111) terraces separated by monoatomic steps that are running in parallel across the entire single-crystal surface. The GNRs grow along the step edges, leading to an uniaxial GNR alignment across the single crystal surface. Using scanning tunneling microscopy (STM) and Raman and polarized Raman spectroscopy, the quality and the alignment of the GNRs pre- and post-substrate transfer are characterized and the transfer efficiency is quantified.

Chapters 1 and 2 introduce the main topics of this thesis and the methods and materials used. The scientific results obtained are presented in Chapters 3 to 7. Chapter 8 gives a short review, discusses the implications of the main findings, and outlines an outlook on the further development of the research topic.

Chapter 3 is motivated by previous works that demonstrated a significant increase in device yield, from 10-15% to 85%, by employing uniaxially aligned GNRs. It describes a new model to quantify GNR alignment based on Polarized Raman spectroscopy measurements, which led to a thorough understanding of GNR alignment before and after substrate transfer. In particular, it is shown that low-coverage samples grown on Au(788) exhibit superior uniaxial alignment compared to high-coverage samples, which is attributed to preferential growth along step edges. However, upon transferring the GNRs to a device substrate, the degree of alignment decreases in the low-coverage samples, while it is maintained for high-coverage ones. The loss of alignment can be attributed to the strictly in-plane lateral diffusion of the GNRs that is sterically prevented at high coverages.

Chapter 4 investigates in detail the growth dynamics of uniaxial aligned 9-AGNRs using both STM and Raman measurements. It particularly explores the role of the precursor dose –

essentially the density of the molecular precursors sublimated onto the substrate – in determining GNR length and quality of alignment. It is found that the GNR growth location on the Au(788) substrate and their degree of alignment are coverage-dependent. The GNR length evolution clearly correlates with the precursor dose and the GNR growth location on the substrate. Also, it is found that GNR alignment after substrate transfer is coverage-dependent.

In Chapter 5, a mathematical model is introduced to determine the coverage of GNRs on various substrates using Raman spectroscopy. This allows the quantification of the GNR transfer efficiency by comparing GNR coverages before and after substrate transfer. It is found that the transfer efficiency strongly correlates with the initial coverage of the GNRs on the Au vicinal substrate (Au(788)): It increases from 35 % for low-coverage samples to 52-70 % for high-coverage samples. It is thus concluded that the adsorption of the GNRs next to step edges significantly hinders their transfer compared to a full monolayer.

In addition to the exploration of GNR growth and transfer conditions, this thesis also attempts to develop techniques to improve the quality of the transferred samples, which are reported in Chapter 6. The applied GNR substrate transfer process relies on the use of poly-methyl methacrylate (PMMA) to support the GNRs as they are detached from the Au(788) surface. PMMA is notorious for leaving behind residues, and even at low concentrations, it can prevent electrical contact with the GNRs. An optimized cleaning procedure was thus developed that yielded clean enough samples to obtain the first STM images of transferred 9-AGNRs.

Finally, Chapter 7 addresses the strong adsorption of GNRs next to the step edges that adversely impact their transfer efficiency. It shows that the step edges can be passivated using the one-dimensional polymer poly-*para*-phenyelene (PPP). Given PPP's wide band gap, it is expected to act as an insulator without hindering device performance and instead supports aligned GNR growth on terraces and during substrate transfer. Additionally, the intercalation of GNRs with self-assembled monolayers (SAMs) has been investigated as a strategy for decreasing GNR-Au interactions.

The work presented in this thesis is foundational for innovations in nano-electronic devices employing GNRs. Notable progress was achieved, particularly in establishing Raman spectroscopy as a quantitative tool to monitor GNR quality, degree of alignment, and quantity. However, the experiments summarized in this thesis also highlight the intrinsic variability of the GNR substrate transfer process that must be addressed to achieve consistent reproducibility. Overall, this thesis offers a deep understanding of GNR growth, alignment, and transfer efficiency, which are key parameters for the prospective use of GNRs in functional devices.

Zusammenfassung

Graphen-Nanobänder (GNRs) – quasi-eindimensionale Streifen aus Graphen – haben sich als vielversprechende Materialien für die nächste Generation von nanoelektronischen Bauteilen wie Feldeffekt-Transistoren herauskristallisiert. Das Interesse an GNRs liegt in ihren anpassbaren physikalisch-chemischen Eigenschaften begründet, die durch Steuerung der Breite und der Kantenstruktur der Nanobänder präzise eingestellt werden können. Atomare Präzision in der GNR Herstellung wird durch Oberflächensynthese erreicht, welche auf der Metalloberflächen-gestützten kovalenten Kopplung von molekularen Vorläuferverbindungen basiert. Metallische Einkristall-Oberflächen dienen dabei sowohl als Templat als auch als Katalysator. Allerdings sind GNRs auf einem metallischen Substrat für viele Charakterisierungsmethoden, und wichtiger noch, für Anwendungen und Bauteilintegration, nicht geeignet. Daher ist die Entwicklung effizienter Substratübertragungsverfahren essenziell, um die synthetisierten GNR-Materialien auf technologisch relevante Substrate zu transferieren. Darüber hinaus ist es von entscheidender Bedeutung, die Wachstumsbedingungen zu optimieren, um die GNR-Länge und -Ausrichtung für eine hohe Bauelementausbeute zu maximieren. Schließlich muss die GNR-Qualität während des gesamten Weges vom GNR-Wachstum bis zur Bauelementintegration erhalten und überwacht werden.

Diese Arbeit konzentriert sich auf das Wachstum, den Substrattransfer und die Charakterisierung von 9-Atom-breiten sogenannten "armchair" (Sesselrand) GNRs (9-AGNRs), die auf der Oberfläche von regelmässig gestuften Au(788)-Einkristallen gewachsen sind. Die (788) Oberfläche weist 3 nm breite (111)-Terrassen auf, die durch monoatomare Stufen getrennt sind und parallel über die gesamte Einkristall-Oberfläche verlaufen. Die GNRs wachsen entlang der Stufenkanten, was zu einer uniaxialen GNR-Ausrichtung über die gesamte Einkristall-Oberfläche führt. Mit Hilfe von Rastertunnelmikroskopie (STM) und Raman-Spektroskopie wird eine detaillierte Charakterisierung der Qualität und der Ausrichtung der GNRs vor und nach dem Substrattransfer durchgeführt sowie eine Quantifizierung der Transfereffizienz.

In Kapitel 1 und 2 werden die Hauptthemen dieser Arbeit sowie die verwendeten Methoden und Materialien eingeführt. Die erzielten wissenschaftlichen Resultate werden in den Kapiteln 3 bis 7 dargelegt. Kapitel 8 gibt einen kurzen Rückblick, diskutiert Implikationen der wichtigsten Erkenntnisse, und skizziert einen Ausblick auf die weitere Entwicklung des Forschungsthemas.

Kapitel 3 ist motiviert durch frühere Arbeiten, die eine signifikante Steigerung der Bauelementausbeute von 10-15% auf 85% durch den Einsatz von uniaxial ausgerichteten GNRs zeigten. Es wird ein Modell zur Quantifizierung der GNR-Ausrichtung auf Basis von polarisierten Raman-Spektroskopiemessungen präsentiert. Dieses Modell vertieft das Verständnis der GNR-Ausrichtung vor und nach dem Substrattransfer, und es zeigt, dass die Ausrichtung der GNRs abdeckungsabhängig ist. Auf Au(788) gewachsene Proben mit geringer GNR-Bedeckung weisen eine bessere uniaxiale Ausrichtung auf als Proben mit hoher Bedeckung, was auf ein bevorzugtes Wachstum entlang der Stufenkanten zurückzuführen ist. Bei einem Transfer der GNRs auf ein Bauelement-Substrat nimmt der Grad der Ausrichtung jedoch in den Proben mit

niedriger Bedeckung ab, während er bei denen mit hoher Bedeeckung erhalten bleibt. Der Verlust der Ausrichtung kann der strikt in der Ebene liegenden lateralen Diffusion der GNRs zugeschrieben werden, die bei hoher Abdeckung sterisch verhindert ist.

Kapitel 4 untersucht die Wachstumsdynamik der uniaxial ausgerichteten 9-AGNRs im Detail mit Hilfe von STM und Raman-Spektrokopie. Es werden insbesondere die Rolle der Dosis bzw. Dichte der Vorläuferverbindungen untersucht, und wie sich diese auf die GNR-Länge und die Qualität der Ausrichtung auswirken. Die Wachstumsposition und -ausrichtung der GNRs auf dem Au(788)-Substrat ist abhängig von der Abdeckung, wobei eine starke Korrelation zwischen der Entwicklung der GNR-Länge und sowohl der Vorläuferverbindungsdosis als auch der Wachstumsposition der GNRs auf dem Substrat besteht. Darüber hinaus erweist sich auch die Qualität der GNR-Ausrichtung nach dem Substrattransfer als abhängig von der Bedeckung.

In Kapitel 5 wird ein mathematisches Modell für die Bestimmung der GNR Bedeckung auf verschiedenen Substraten aufgrund von Raman-Spektroskopie eingeführt. Dies ermöglicht die Quantifizierung der GNR-Substrattransfereffizienz durch den Vergleich der GNR-Bedeckungen vor und nach dem Substrattransfer. Die Resultate deuten darauf hin, dass die Übertragungseffizienz stark mit der anfänglichen Bedeckung der GNRs auf dem Au(788) Substrat korreliert: Sie steigt von 35 % für Proben mit niedriger GNR Bedeckung auf 52-70 % für Proben mit hoher Bedeckung. Diese Beobachtung impliziert, dass die GNR-Adsorption in Stufenkantennähe den Substrattransfer, vor allem im Vergleich zu einer vollen Monoschicht, erheblich behindert.

Neben der Erforschung der Wachstums- und Transferbedingungen für GNRs wird die Entwicklung neuer Techniken zur Verbesserung der Qualität der übertragenen Proben in Kapitel 6 beleuchtet. Das angewendete GNR-Substrattransferverfahren stützt sich auf die Verwendung von Poly-Methyl-Methacrylat (PMMA), um die GNRs zu stützen, während sie von der Au(788)-Oberfläche abgelöst werden. PMMA ist dafür bekannt, Rückstände zurückzulassen, und selbst bei niedrigen Konzentrationen kann es den elektrischen Kontakt der GNRs kompromittieren. Daher wurde ein optimiertes Reinigungsverfahren entwickelt, welches es ermöglichte, erstmals STM-Bilder von Substrat-übertragenen 9-AGNRs zu erhalten.

Schließlich befasst sich Kapitel 7 mit der starken Adsorption von GNRs an den Stufenkanten, die ihre Übertragungseffizienz negativ beeinflusst. Es zeigt, dass die Stufenkanten durch Verwendung des eindimensionalen Polymers Poly-*Para*-Phenylene (PPP) passiviert werden können. Angesichts der weiten energetischen Bandlücke von PPP wird erwartet, dass es als Isolator fungiert ohne die Charakteristika eines GNR Bauteils zu beeinträchtigen, und stattdessen das ausgerichtete Wachstum von GNRs auf Terrassen unterstützt. Darüber hinaus wird die Interkalation von GNRs mit selbstorganisierten Monoschichten (self-assembled monolayers, SAMs) als Strategie zur Verringerung der GNR-Au-Wechselwirkung untersucht.

Die in dieser Dissertation vorgestellte Arbeit ist grundlegend für Innovationen in nanoelektronischen Bauteilen unter Verwendung von GNRs. Sie hat bemerkenswerte Fortschritte erzielt, insbesondere bei der Etablierung der Raman-Spektroskopie als quantitatives Instrument zur Überwachung der GNR-Qualität und -Ausrichtung. Die hier zusammengefassten

Experimente heben aber auch die intrinsische Variabilität des GNR-Substrattransferprozesses hervor, die adressiert werden muss um eine konsistente Reproduzierbarkeit zu erreichen. Insgesamt bietet diese Dissertation ein vertieftes Verständnis für das Wachstum, die Ausrichtung und die Transfereffizienz von GNRs, welche Schlüsselparameter für die zukünftige Verwendung von GNRs in funktionalen nanoelektronischen Bauteilen darstellen.

Chapter 1
Introduction

Graphene

Carbon, an essential element for life on Earth, plays a crucial role in numerous aspects of our daily lives due to its remarkable versatility and abundance. Being the fourth most abundant element in the universe[1], carbon is ubiquitous, found in everything from the air we breathe to the food we consume. Its unique ability to form stable covalent bonds, especially with hydrogen, oxygen, and nitrogen, makes it the foundational element of living matter[2]. This bonding capability positions carbon as the primary component of vital macromolecules, including proteins, nucleic acids, carbohydrates, and lipids[3]. The intricate nature of organic compounds essential for life, from DNA structures to cellular reactions, is deeply rooted in carbon's versatile bonding properties. In essence, the distinct characteristics of carbon are at the heart of the diversity and functionality of living organisms. From a materials perspective, the electron configuration of carbon ($1s^2\ 2s^2\ 2p^2$) and the different hybridizations of the 2p orbitals (sp, sp^2, sp^3) give rise to diverse allotropes, each possessing unique properties and applications[4]. The sp^2-hybridized allotrope graphite, for instance, includes a wide range of substructures where graphene, fullerenes, carbon nanotubes (CNTs), and graphene nanoribbons (GNRs) are the most important ones (Fig. 1).

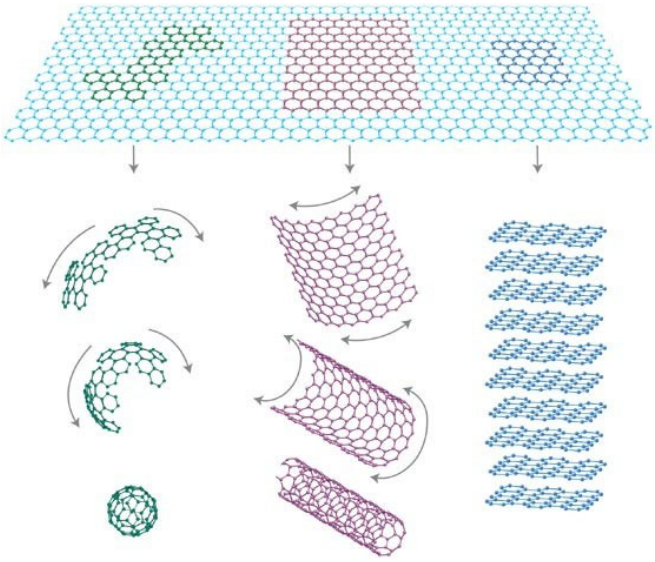

Figure 1: Carbon allotropes with sp^2 hybridization vary in dimensions and shapes, all derived from graphene. Graphene is the parent material of several carbon allotropes, including CNTs, buckyballs, and GNRs. These structures can be conceptually formed by cutting specific shapes out of graphene. The scheme is Reprinted with permission from [Geim, A. K. & Novoselov, K. S. et al., Nature materials 6, 183–191 (2007)][5] Copyright © 2007, Springer Nature.

Graphene is a single layer of graphite with a two-dimensional (2D) hexagonal lattice[5,6]. Fullerenes, CNTs, and GNRs are nanostructures that can be conceptually formed by cutting specific shapes out of graphene. Fullerenes (e.g. C_{60}) are spherical zero-dimensional (0D) sp^2 molecules known as buckyballs[7], formed by introducing five-membered carbon rings to the graphene lattice. CNTs are rolled-up graphene cylinders with a one-dimensional (1D) shape[8], while graphite is a stack of graphene layers with a 3.35 Å distance between them and weakly coupled van der Waals forces, arranged in three dimensions (3D). Lastly, GNRs are narrow strips of graphene with a width of a few nanometers or less[9].

Basic material properties of graphene

In 2004, Geim and Novoselov isolated graphene from graphite using the mechanical exfoliation method, which is also known as the scotch tape method[6]. Since then, graphene has been the subject of significant interest among researchers due to its outstanding properties, such as high electron mobility (200 000 $cm^2\ V^{-1}\ s^{-1}$)[6], high thermal conductivity (5000W $m^{-1}\ K^{-1}$)[10], and impressive mechanical strength[11].

Graphene has a single layer of sp^2-hybridized carbon atoms arranged in a 2D hexagonal structure, forming a triangular lattice with two carbon atoms, A and B, per unit cell, as shown in Fig. 2. The unit vectors $a_{1,2}$ form an angle of 60° and have a length of $a = |a_{1,2}| = \sqrt{3}\ a = 2.46$ Å, which results in a C-C bond length of a = 1.42 Å (Fig. 2a)[5,12]. The first Brillouin zone has three points with high symmetry: Γ at the center, M at the edges, and K at the corners (Fig. 2b).

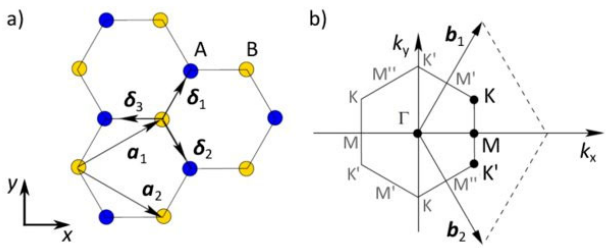

Figure 2: The structure of graphene. a) Graphene lattice structure representation in real space consisting of two triangular lattices with a basis of two carbon atoms A and B and unit vectors a_1 and a_2 (δ_i= 1, 2, 3 are the nearest-neighbor vectors). b) The associated Brillouin zone has three high-symmetry points labeled Γ, M, and K. Dirac cones are located at the K and K' points. The scheme is Reprinted with permission from [Castro Neto, A. H. et al., Rev. Mod. Phys. 81, 109–162 (2009)][12] Copyright © 2009 by American Physical Society.

The crystal structure of graphene results from the sp^2 hybridization, where the three sp^2-hybridized orbitals (2s and $2p_x$, $2p_y$ orbital) form a trigonal planar structure with strong planar σ bonds between C-C atoms. These bonds are responsible for the planar structure of graphene and its mechanical and thermal properties. The remaining non-hybridized $2p_z$ orbital is perpendicular to the plane and forms a weak π bond based on overlap with p_z orbitals of neighboring carbon atoms. The resulting half-filled π bands are responsible for the electronic and optical properties of graphene[5,12].

To determine the electronic band structure of graphene, a tight-binding technique is utilized, which takes into account the hopping of electrons to the nearest neighbor, as described by Eq. (1):[12,13]

$$E\left(k_x, k_y\right) = \pm\gamma_0\left[1 + 4\cos\left(\frac{\sqrt{3}k_x a}{2}\right).\ \cos\left(\frac{k_y a}{2}\right) + 4\cos^2\left(\frac{k_y a}{2}\right)\right]^{1/2} \qquad (1)$$

Here, k_x, k_y are the wave vectors in reciprocal space indicated in Fig. 2b, $a_{1,2}$ is the graphene lattice constant (2.46 Å), E is the electron energy, and γ_0 the nearest-neighbor (π-orbital) hopping parameter (2.8 eV). Figure 3a represents the linear dispersion of electrons around the K and K′ points (also known as the Dirac points), where the valence π and conduction π* band meet at K, K′ point[6,14]. Accordingly, graphene is a gapless semiconductor or semimetal. In contrast to conventional semimetals, the linear dispersion in graphene at low energy suggests that charge carriers (electrons and holes) act as massless Dirac fermions. For pristine graphene (undoped), the Fermi level is located at the intersection of the Dirac cones with the same carrier density of both holes and electrons. However, the Fermi level in graphene can be smoothly tuned (shifted) by using an external 'gate', allowing for the tuning of the charge carrier density[6]. By applying a negative (positive) gate voltage, the Fermi level of graphene will shift below (above) the Dirac point due to the field-effect transistors (FETs)-induced hole (electron) doping, as shown in Fig. 3b. This tuning capability has led to the development of graphene-based FETs with ambipolar characteristics. These FETs allow for the continuous switching of Dirac fermions from holes to electrons and vice versa by simply adjusting the gate voltage[6].

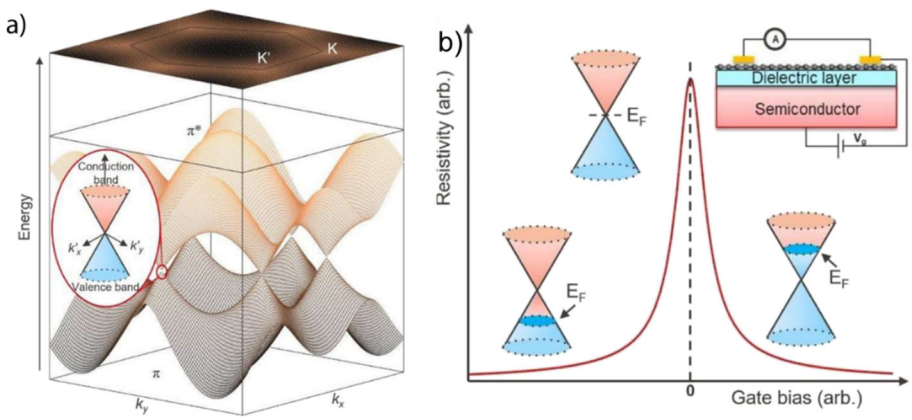

Figure 3: Linear dispersion relation of graphene. a) Band structure of monolayer graphene. b) Ambipolar electric field effect in single-layer graphene. The scheme is Reprinted with permission from [Tang, H. et al. Nanophotonics 11, 917–940 (2022)][15], used under Creative Commons CC-BY license (CC BY 4.0).

Synthesis of graphene

Graphene can be synthesized through two main approaches: top-down and bottom-up[16–18]. The top-down approach involves exfoliating bulk graphite into individual sheets of graphene, typically via micromechanical exfoliation (also known as the Scotch tape or peel-off method)[5,6] or chemical exfoliation[19–21]. However, these approaches often generate structural defects that lower electrical conductivity. In contrast, the bottom-up approach involves a transformation of

carbon-containing precursor molecules into high-quality graphene with good electrical properties, but typically with limited production yield. Chemical vapor deposition (CVD) is one example of a bottom-up approach that enables the large-scale synthesis of high-quality graphene by dissociating methane molecules on a catalytic metal substrate[22,23]. Another bottom-up method is epitaxial graphene growth based on selective Si sublimation from silicon carbide (SiC)[24]. This method produces high-quality graphene but is relatively expensive due to the high cost of SiC substrates and the high temperature required.

Applications of graphene

Graphene's remarkable properties have made it a promising material for a wide range of applications, such as sensors, biosensors, water purification, energy storage, drug delivery, and electronics[16–18,25,26]. Its high electrical conductivity can change with the adsorption of molecules on the surface, making it useful for gas and biosensors[11,27]. The large surface area of graphene allows its use in catalysis, electrochemical applications such as supercapacitors and batteries[28], and as a sorbent for water purification[29]. Additionally, its stability, large surface area, and low toxicity make it suitable as a carrier for gene and drug delivery[30].

Graphene's high carrier mobility and current carrying capacity make it suitable for electronic devices, particularly in the field of FETs. However, due to the zero bandgap in 2D large-area graphene, graphene-based FETs exhibit low I_{on}/I_{off} current ratios, making it challenging to turn off devices at room temperature. To address this issue, various approaches have been proposed to open a bandgap through different ways, such as forming GNRs [31,32], fabricating bilayer graphene[33,34], and applying chemical modifications to graphene[35]. Developing graphene-based devices with enhanced I_{on}/I_{off} ratios remains a significant challenge for practical applications.

As researchers continue to explore graphene's properties and overcome its limitations, this remarkable material holds immense promise for revolutionizing numerous industries and driving technological advancements.

Graphene nanoribbons (GNRs)

Graphene is a material with extraordinary properties that make it a promising candidate for high-frequency FETs. However, its lack of a bandgap poses a significant obstacle to room temperature switching devices. To overcome this challenge, researchers have developed a promising approach through synthesizing GNRs of narrow width to confine charge carriers laterally and hence induce an electronic bandgap. The magnitude of the bandgap depends on their width and edge structure, which thus opens ways to widely tune the electronic properties and achieve optimized on/off switching properties in FET applications. In this part, we discuss various approaches to synthesizing GNRs, which could potentially be used as the main active material in future electronic applications. There are two main strategies for synthesizing GNRs: top-down and bottom-up approaches.

The top-down approaches

The top-down approach involves cutting large carbon-based structures such as graphite, graphene, and carbon nanotubes laterally to achieve the desired size and shape of GNRs[36,37](Fig. 4). This approach produces a large quantity of GNRs with micrometer-scale length but with uncontrollable edges and width.

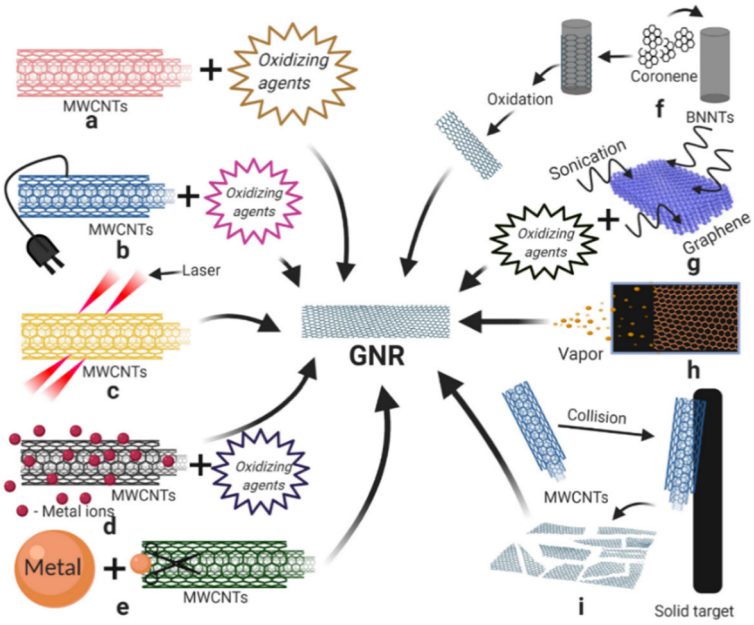

Figure 4: Various top-down approaches to synthesize GNRs. Top-down approaches include a) oxidation cutting, b) electrochemical unzipping, c) laser irradiation, d) intercalation and exfoliation, e) metal-catalyzed cutting, f) GNR synthesis in boron nitride nanotubes (BNNTs), g) sonochemical method, h) chemical vapor deposition, i) high impact collision method. The scheme is Reprinted with permission from [Johnson, A. P. et al., Journal of Controlled Release 325, 141–162 (2020)][38] Copyright © 2020 Elsevier B.V.

One such approach is electron-beam lithography[39], which selectively removes weakly bonded carbon atoms located at edge-sites of multilayer graphene. This approach is based on using an electron beam with an energy of 80 keV, which is just below the threshold to displace a carbon atom. However, this approach can also result in damage, dangling bonds, and chemical functional groups on the edges of GNRs, which, in turn, can lead to a low I_{ON}/I_{OFF} ratio in integrated FET devices[40]. Another approach involves cutting graphene with catalytic reactions using metal nanoparticles such as Ni to break the C-C bonds[41,42]. However, it lacks control over the width, placement, and alignment of GNRs due to the difficulty in controlling the trajectory of nanoparticles as they etch graphene. The sonochemical unzipping of graphite is an alternative approach that involves chemically exfoliating graphite to obtain graphene sheets. Subsequently, the graphene sheets are sonicated in an organic solvent, such as flavin mononucleotide (FMN), which serves both as a surfactant and 1D template, facilitating the unzipping of graphene into GNRs with diverse shapes[43]. Although this approach offers significant GNR quantities, it lacks width selectivity. Additionally, the GNRs synthesized using this approach suffer from the presence of vacancies, edge defects, and fractionalized edges. Finally, the most common top-down approach is unzipping CNTs or multi-walled CNTs (MWCNTs) through longitudinal unzipping utilizing plasma treatment[44], chemical unzipping (chemical oxidation or reduction)[45],

or electrochemistry. However, the width of the GNR is restricted by the diameter of the CNTs, limiting GNRs to be wider than 10 nm, and the random chirality of the initial CNT structure makes it difficult to control the edge structure affecting their electronic properties[46]. Although the top-down approach is capable of producing large quantities of GNRs, it cannot precisely control the edges and width at an atomic level, which is crucial for electronic device applications.

Bottom-up approaches

The bottom-up approach involves assembling molecular building blocks and has emerged as a promising approach to fabricating atomically precise GNRs for electronic device applications. Several approaches have been developed for the bottom-up fabrication of GNRs, and here, we will discuss some of them[9,47–52].

On-surface synthesis

On-surface synthesis is a process that involves the sublimation of dihalogenated precursor monomers onto metal surfaces under ultra-vacuum (UHV) conditions, leading to the formation of biradical intermediates through surface-assisted carbon-halogen bond cleavage (Fig. 5). The intermediates then undergo radical polymerization through Ullmann coupling upon the first thermal activation, followed by surface-assisted cyclodehydrogenation upon the second thermal activation, resulting in the planarization of the polymers and the formation of atomically precise GNRs [9,52–54].

In 2010, Cai et al. reported the first synthesis of atomically precise GNRs using the on-surface synthesis approach. They showed that 7-atom wide armchair GNRs (7-AGNRs) can be synthesized by using 10,10'-dibromo-9,9'-bianthryl (DBBA) as precursor monomers. Using this approach, it is possible to modify the precursor design to tailor the width and the edge structure and hence control the physical properties of GNRs. Furthermore, this approach allows for achieving more complex GNR architectures, such as armchair[52], chiral-type[55], topological-type[56], and zigzag[57]-type GNRs. However, there are challenges associated with on-surface synthesis, such as the scalability of the process, the requirement for expensive equipment and UHV conditions, and the controlled transfer of the ribbons onto device substrates since on-surface synthesis requires the catalytic role of metal substrates.

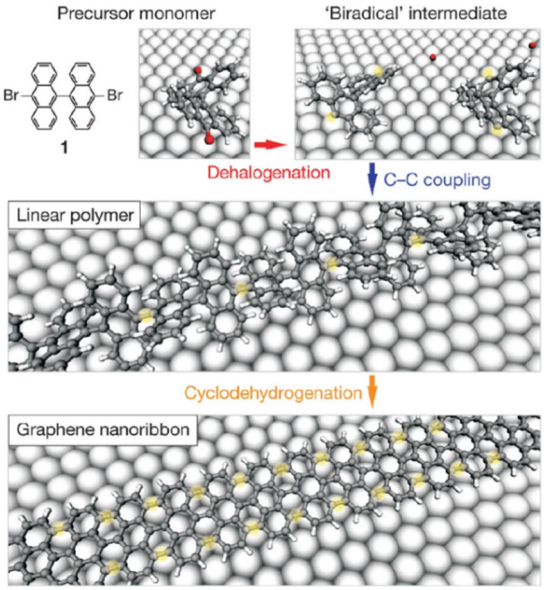

Figure 5: Schematic overview of on-surface GNR fabrication for the case of 7-AGNR, starting from the (DBBA) precursor monomers. Dehalogenation occurs during monomer adsorption, followed by the formation of linear polymers, and finally, the formation of fully aromatic GNRs by cyclodehydrogenation. The scheme is Reprinted with permission from [Cai, J. et al., Nature 466, 470–473 (2010)][9] Copyright © 2010, Springer Nature.

Solution-phase approaches

This approach involves solution-mediated cyclodehydrogenation and planarization of 3D polyphenylene precursors[58–60,48] (Fig. 6a). To form GNRs, suitable polyphenylene precursors that can form C-C bonds between the benzene rings are required. Various polymerization methods, such as Diels-Alder[59], Yamamoto[61], and Suzuki polymerization[62], can be used to fabricate the polymer. The resulting polymer is subsequently planarized using oxidative cyclodehydrogenation typically with $FeCl_3$, a reaction known as the Scholl reaction. The choice of polymerization method plays a crucial role in determining the molecular weight of the polyphenylene precursors and, hence, the longitudinal dimension of the resulting GNRs. Despite successfully scaling up the solution syntheses of GNRs to the gram scale and producing GNRs longer than 100 nm on average[58,59], perfect shape definition remains challenging due to defects resulting from incomplete cyclodehydrogenation and side reactions. Furthermore, the low solubility of the precursors, due to strong π-π interactions, makes it challenging to extend the length of GNRs[58,59,62,48].

Radical-polymerized chemical vapor deposition (RP-CVD)

In 2014, Sakaguchi and Nakae reported an approach for fabricating GNR films using radical-polymerized chemical vapor deposition (RP-CVD) at a pressure of 1 Torr with a flow of argon gas[63] (Fig. 6b). This approach involves the sublimation of dihalogenated monomer precursors on a catalytic gold surface inside a tube furnace, followed by thermal annealing to promote surface-assisted polymerization and cyclodehydrogenation, similar to the on-surface synthesis approach in UHV[63–66]. This approach allowed for the synthesis of diverse AGNRs and chevron-type GNRs across large areas at atmospheric pressure under argon/hydrogen[65].

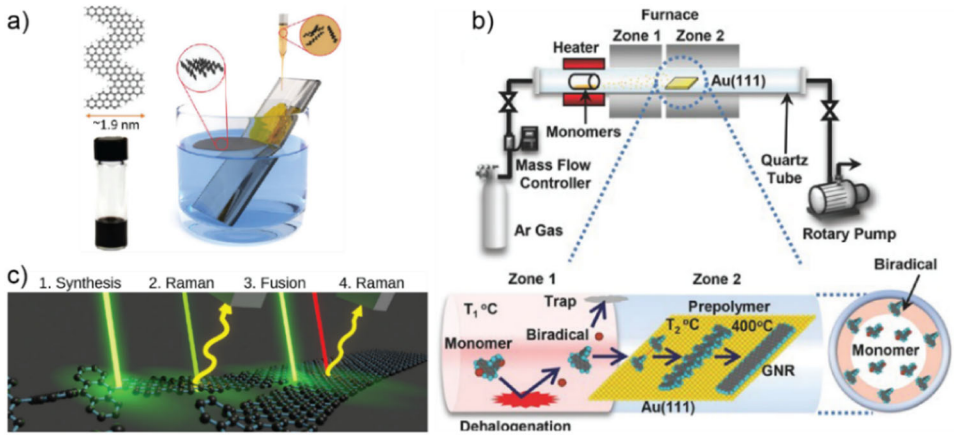

Figure 6: Bottom-up approaches for GNR synthesis. a) Solution-based polymerization produces GNRs and interfacial self-assembly forms uniform thin films of GNRs. The scheme is Reprinted with permission from [Shekhirev, M. et al., ACS Applied Materials & Interfaces 9, 693–700 (2017)][60], Copyright © 2017, American Chemical Society. b) Experimental setup of RP-CVD and the GNR growth mechanism illustrated using (DBBA) as a monomer precursor. The scheme is Reprinted with permission from [Sakaguchi, H. et al., Adv. Mater. 26, 4134–4138 (2014)][63], Copyright © 2014 WILEY-VCH Verlag GmbH & Co. KGaA, Weinheim. c) Laser-induced photothermal approach is used to synthesize GNRs. The scheme is Reprinted with permission from [Falke, Y. et al., Nano Lett. 20, 4761–4767 (2020)][67], Copyright © 2020, American Chemical Society.

Photothermal bottom-up synthesis

In this approach, a high laser power (λ = 532 nm, P = 130 mW, spot-size ~4 µm) is used to locally irradiate and heat precursor monomer of (DBBA) on a thin gold film, leading to the synthesis of atomically precise 7-AGNRs[67]. Additionally, exposing the fabricated 7-AGNRs to the same laser beam fuses them laterally, forming 14-GNRs (Fig. 6c). Ultrahigh vacuum Raman spectroscopy in the same system is used to study the reaction intermediates in real time and investigate the growth kinetics of different types of GNRs, leading to determining the rate constants for various reaction steps. This approach is useful for the fabrication of atomically precise GNRs and the investigation of on-surface reactions.

Electronic structure of GNRs

GNRs are narrow strips of graphene with unique electronic and optical properties that depend on their crystallographic edge structure, width, and orientation[48,50]. Based on their edge structure, GNRs can be classified into three main categories: zigzag, armchair, and chiral (Fig. 7). Cutting graphene along $[10\bar{1}0]$ and $[11\bar{2}0]$ crystallographic orientations lead to the formation of armchair and zigzag edges, respectively, while cuts along intermediate orientations result in chiral edges with a combination of both zigzag and armchair edges[68].

Zigzag-edged GNRs (ZGNRs) exhibit unique electronic properties due to the presence of spin-polarized and localized edge states, which make them suitable for spintronic applications[69–71]. The presence of edge states in ZGNRs results in magnetic structures characterized by ferromagnetism ordering along the ribbons and antiferromagnetism across them[69–71]. ZGNRs are identified by the number of zigzag lines, and their electronic properties can be fine-tuned

by structural or chemical modifications, doping, or external perturbations. However, ZGNRs are chemically more reactive than AGNRs due to the edge state-related open-shell character[72].

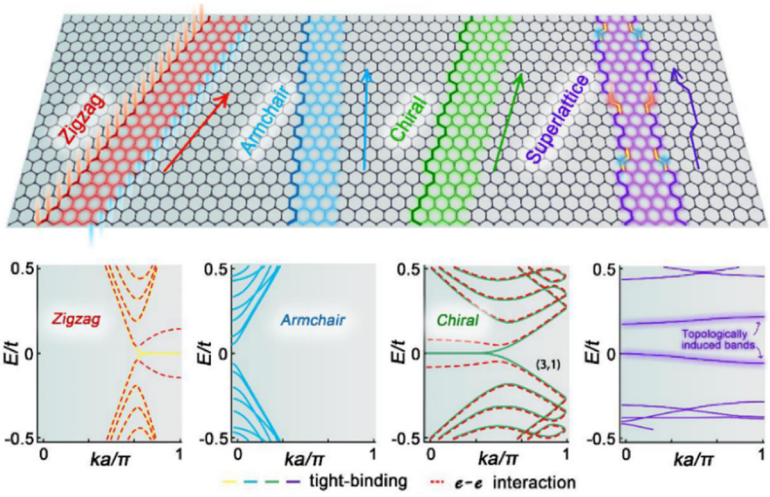

Figure 7: Electronic properties of GNRs. a) Scheme illustrating different types of GNR edges including armchair, zigzag, chiral, and superlattice GNRs with the representative electronic band structures for various widths derived from tight-binding calculations. The scheme is Reprinted with permission from [Wang, H. et al., Nat Rev Phys 3, 791–802 (2021)][68]. Copyright © 2021, Springer Nature.

Armchair-edged GNRs (AGNRs) exhibit semiconducting properties, with the bandgap size determined by the ribbon width[73–75]. AGNRs can be expressed as *N*-AGNRs, with *N* representing the number of carbon dimer lines across the ribbon width. The *N*-AGNRs are divided into three families: $N = 3p$, $N = 3p+1$, and $N = 3p+2$. The bandgap of each *N*-AGNR family is inversely proportional to the ribbon width (Fig. 8), as suggested by both theoretical calculations[73,75] and experimental data[76,77]. The $N = 3p$ and $N = 3p+1$ families exhibit large bandgaps that are inversely proportional to the ribbon width[74,78,79], indicating their potential as promising candidates for scaled logic transistors[80]. Conversely, the $N = 3p+2$ family is predicted to have a very small bandgap[75,81,73].

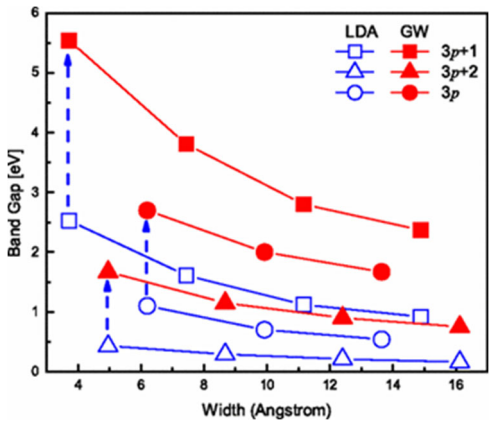

Figure 8: The bandgap variation of AGNRs. The three families of AGNRs as a function of width were obtained using LDA (local (spin) density approximation) and GW calculations. The scheme is Reprinted with permission from [Yang, L.et al., Phys. Rev. Lett. 99, 186801 (2007)][73], Copyright ©2007 American Physical Society.

Finally, chiral GNRs (chGNRs) have a unique structure with a combination of zigzag and armchair edges, where the orientation of the edges is determined by the number of graphene unit cells along the edge of the chGNR unit cell[55]. The electronic properties of chGNRs can be adjusted by changing the ribbon's width and chirality angle.

As our work specifically focuses on 9-atom wide AGNR, we present the fabricated 9-AGNRs from previous work as depicted in Fig. 9[52]. The figure illustrates the synthetic route toward 3′,6′-dibromo-1,1′:2′,1″-terphenyl and the on-surface synthesis of 9-AGNRs, along with representative characterizations using scanning tunneling microscopy (STM) and noncontact atomic force microscopy (nc-AFM).

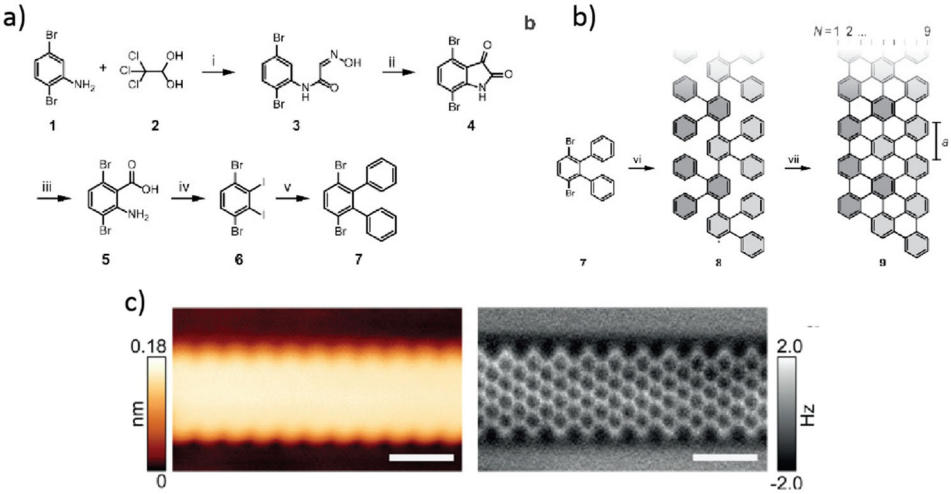

Figure 9: The fabrication of 9-AGNRs. a) Synthetic route toward 3′,6′-dibromo-1,1′:2′,1″-terphenyl, monomer 7. b) On-surface synthesis of 9-AGNR (9) via surface-assisted dehalogenation and polymerization of monomer 7, followed by cyclodehydrogenation of polymer 8. The synthetic steps involve (i) hydroxylamine hydrochloride, H_2O, EtOH, 80 °C, 12 h; (ii) H_2SO_4, 100 °C, 30 min; (iii) NaOH, H_2O_2, 50 °C, 30 min, then HCl, rt; (iv) isoamylnitrite, I2, 1,2-dichloroethane, dioxane, 1 h, reflux; (v) phenylboronic acid, Na_2CO_3, $Pd(PPh_3)_4$, H_2O, dioxane, 80 °C, 2 d; (vi) sublimation onto Au(111) held at 250 °C, then annealing at 250 °C, 10 min; (vii) annealing at 350 °C, 10 min. c)and d) represent the characteristic characterization of 9-AGNRs. Left panel c) High-resolution STM topography image of a single 9-AGNR (V = 0.1 V, I = 0.5 nA, scale bar: 1 nm). Right panel c) High-resolution nc-AFM frequency shift image of 9-AGNR using a CO-functionalized tip with an oscillation amplitude of 70 pm (scale bar: 1 nm). The scheme is Reprinted with permission from [Talirz, L. et al. ACS Nano 11, 1380–1388 (2017)][52], Copyright © 2017, American Chemical Society.

Vibrational properties of GNRs

GNRs are subject to theoretical modeling to explore their vibrational properties in a manner analogous to graphene. Gillen et al.[82] employed Density Functional Theory (DFT) to calculate the vibrations of armchair GNRs and the resulting data were mapped onto the phonon dispersion of graphene (Fig. 10a). This figure highlights the relationship between GNR and graphene vibrations, presenting the atomic displacement patterns for six representative normal modes of an infinitely long GNR (Fig. 10b). Notably, GNRs exhibit vibrational modes that bear resemblance to those found in graphene, including the Longitudinal Optical (LO) and Transverse Optical (TO) vibrations, indicated in Figs. 10a and b as 1 and 2, respectively. Consequently, GNRs also display a Raman G-peak at frequencies similar to graphene's G-peak. Additionally, specific vibrational modes in GNRs become Raman-allowed, as mentioned in Figs. 10b and c modes 3-

6, and appear at frequencies similar to the D-peak observed in graphene. Compared to graphene and CNTs, the presence of additional phonon modes CH-D in the 1100-1500 cm^{-1} spectral range doesn't indicate defects. Instead, it's due to the hydrogen-passivated edges, which break the periodicity of the honeycomb lattice (Fig.10c). This comprehensive understanding of GNRs' vibrational properties in relation to graphene provides crucial insights into their Raman spectra and overall behavior.

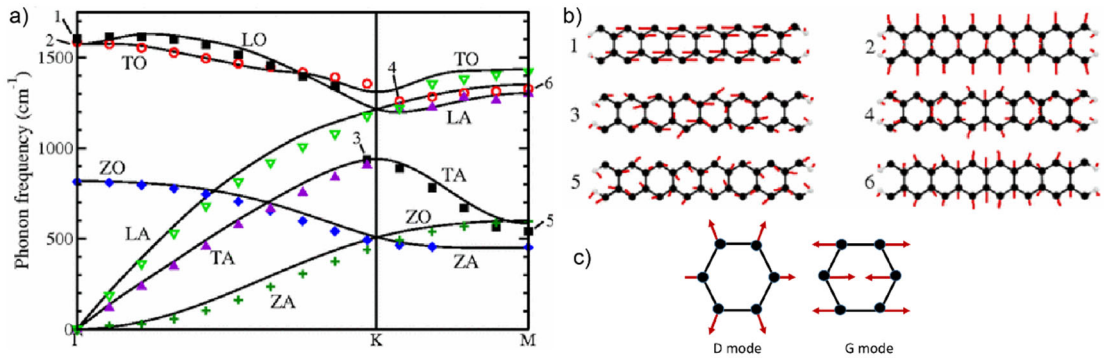

Figure 10: The phonon dispersion of graphene (solid lines) is used to map the fundamental and overtone frequencies of a 15-AGNR. a) The longitudinal ribbon modes correspond to transverse graphene modes, represented by TO (Transverse Optical, filled squares), LO (Longitudinal Optical, circles), ZO (Zone-Center Optical, filled diamonds), TA (Transverse Acoustic, open triangles), LA (Longitudinal Acoustic, filled triangles), and ZA (Zone-Center Acoustic, pluses). b) The eigenvectors of selected ribbon TO and LO frequencies are shown with the corresponding modes indicated. The scheme is Reprinted with permission from [Gillen, R. . et al., Phys. Rev. B 80, 155418 (2009)][82], Copyright ©2009 American Physical Society. c) Vibrational modes of carbon atoms encompass both the D-band, indicative of breathing modes, and the G-band, associated with stretching modes.

GNRs characterization

Extensive research has been conducted on GNRs to investigate their dynamic, structural, and chemical properties. To gain valuable insights, a combination of in-situ and ex-situ (meaning in UHV and outside UHV environments) characterization techniques has been employed. These techniques include scanning tunneling microscopy (STM), X-ray photoelectron spectroscopy (XPS), transmission electron microscopy (TEM) for in situ analysis, as well as, atomic force microscopy (AFM), and Raman spectroscopy for ex situ analysis. This section aims to provide a comprehensive overview of the commonly used characterization techniques for GNRs, graphene, and 2D material.

STM is a versatile and powerful technique that allows for the investigation of the atomic structure, morphology, and electronic properties of various low-dimensional materials. It enables the determination of GNR width, edge topology, and the presence of defects at the atomic level, which significantly influence their electronic properties and energy band formation due to quantum confinement (Fig. 11a). Additionally, STM provides access to local electronic properties, such as density of states, band structure, and charge distribution, offering essential information about the bandgap and carrier mobility[9,54,83].

Raman spectroscopy is a powerful technique that utilizes laser-induced inelastic scattering of light to provide information on the vibrational modes of carbon-based materials. Each material has a unique Raman spectrum that can be used to identify the material and provide information on its quality, orientation, defects, and changes induced by different treatments or environments. For GNRs, Raman spectroscopy is particularly useful in determining the width, edge structure (AGNRs or ZGNRs), defect density, strain, and level of doping by examining the Raman fingerprint of GNRs (Fig. 11b)[9,54,83–88].

XPS is a representative surface analysis method used to determine the chemical composition, bonding, and states of carbon materials. It is particularly useful in examining defects such as sp^3-hybridized C atoms, edge C–H bonds, functional groups, vacancy defects, and pentagonal and heptagonal rings in graphene. In the case of GNRs, XPS provides insights into their edge structure (AGNRs or ZGNRs), electronic structure, work function, presence of impurities and functional groups, and the effects of edge functionalization on their electronic properties (Fig. 11b)[54,87,89].

AFM is employed to investigate the surface morphology and topography of 2D materials by scanning a sharp tip over the sample and detecting the forces between the tip and the sample. AFM generates a 3D map of the surface, providing information on thickness, defects, and morphology, as well as mechanical properties like elasticity, adhesion, stiffness, and bending behavior. For GNRs, AFM particularly in UHV conditions is utilized to determine their width, thickness, morphology, and edge structure, which greatly impact their electronic properties (Fig. 11c)[43,52,54,83].

TEM is a powerful characterization technique that provides high-resolution images of the internal structure of 2D materials by passing an electron beam through a thin sample. This technique allows for the investigation of GNR width, thickness, and crystal structure, as well as the examination of strain, defects, and the effects of edge functionalization on electronic properties (Fig. 11d)[45,90].

Additionally, other techniques such as high-resolution electron energy-loss spectroscopy (HREELS)[91], angle-resolved photoelectron spectroscopy (ARPES)[77], low-energy electron diffraction (LEED)[92], and scanning electron microscopy (SEM)[93] are also used to characterize GNRs. All these characterization techniques collectively contribute to a comprehensive understanding of GNR properties and pave the way for their applications in various fields.

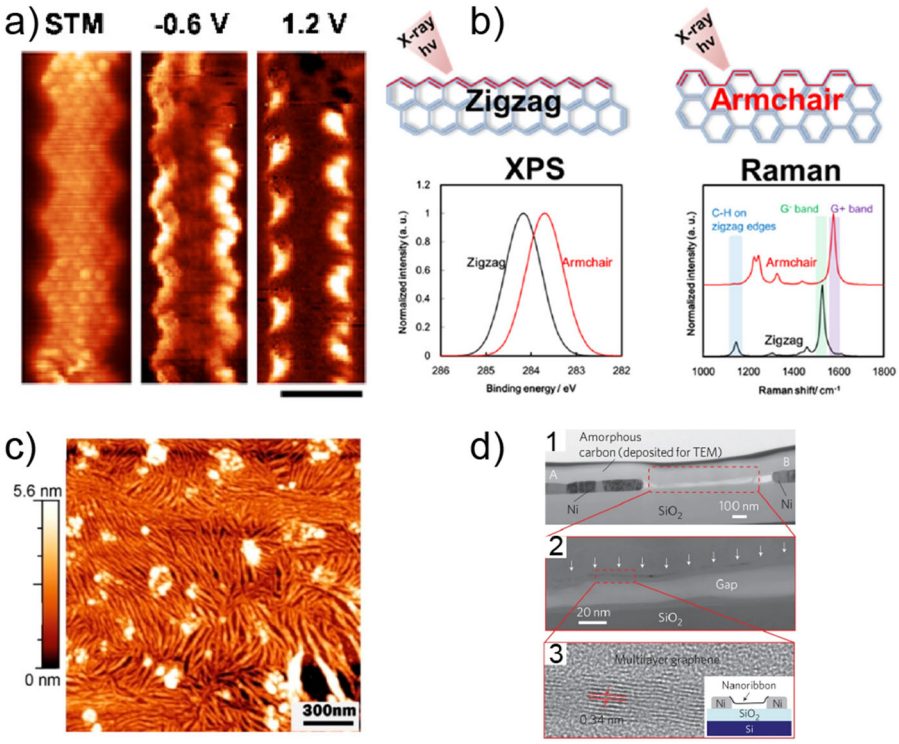

Figure 11: GNRs characterization techniques. a) STM constant-height current image and constant-current dI/dV mapping of zigzag edge-extended GNRs (zeeGNRs). The scheme is Reprinted with permission from [Beyer, D. et al., J. Am. Chem. Soc. 141, 2843–2846 (2019)][94], Copyright © 2019 American Chemical Society. b) XPS C 1s and Raman spectra comparing 8-atom wide armchair GNRs (8-AGNRs) and 8-atom wide zigzag GNRs (8-ZGNRs), alongside the simulated Raman spectra of Z8-A2 (zigzag/armchair = 4:1) and A8-Z2 (zigzag/armchair = 1:4) GNRs. The scheme is Reprinted with permission from [Kim, J. et al., ACS Omega 3, 17789–17796 (2018)][87], Copyright © 2022 American Chemical Society, used under Creative Commons license. c) AFM topography images of 9-AGNRs transferred onto an Al_2O_3 substrate. The scheme is Reprinted with permission from [Borin Barin, G. et al., ACS Appl. Nano Mater 2, 2184–2192 (2019)][83], used under Creative Commons license. d) Presents cross-sectional TEM images of multilayer (5–10) GNRs suspended between Ni islands, displayed at different magnifications: low (1), middle (2), and high (3). The arrows in the image (d2 and d3) indicate the locations of the GNRs and the schematic structure of the suspended GNR, respectively. The scheme is Reprinted with permission from [Kato, T. et al., Nature Nanotechnology 7, 651–656 (2012)][90], Copyright © 2012, Springer Nature.

Substrate transfer of GNRs

In the fabrication of GNR-based electronic devices, the transfer of GNRs from their metallic growth surfaces onto insulator substrates, such as SiO_2/Si, is a crucial step. Various transfer methods developed for 2D materials like graphene have been later adapted for GNRs. In this section, we give a detailed description of transfer methods that are specifically tailored for bottom-up synthesized GNRs.

One widely utilized method for transferring GNRs from thin Au(111) films on mica or glass is the polymer-free wet transfer method (Fig. 12a)[63,83]. The process involves floating the GNR/Au/mica substrate on an aqueous HCl solution (38%, room temperature), which separates the GNR/Au film from the mica substrate. Subsequently, the GNRs/Au film is placed onto a SiO_2/Si substrate with the GNRs facing the dielectric surface. To increase adhesion between the Au film and the clean target substrate, a drop of ethanol is applied to the Au film and annealed

at 100°C for 10 minutes. To remove the Au film, an etchant solution of potassium iodide (KI/I_2) is employed, leaving behind only the GNRs on the clean target substrate. Finally, The resulting GNR/substrate sample is cleaned by soaking in ultrapure water for 5 minutes, rinsed with acetone/ethanol, and dried with nitrogen. This method enables the transfer of relatively large GNR samples without the need for additional support layers that may influence the GNR properties. We used this transfer process in Chapter 5.

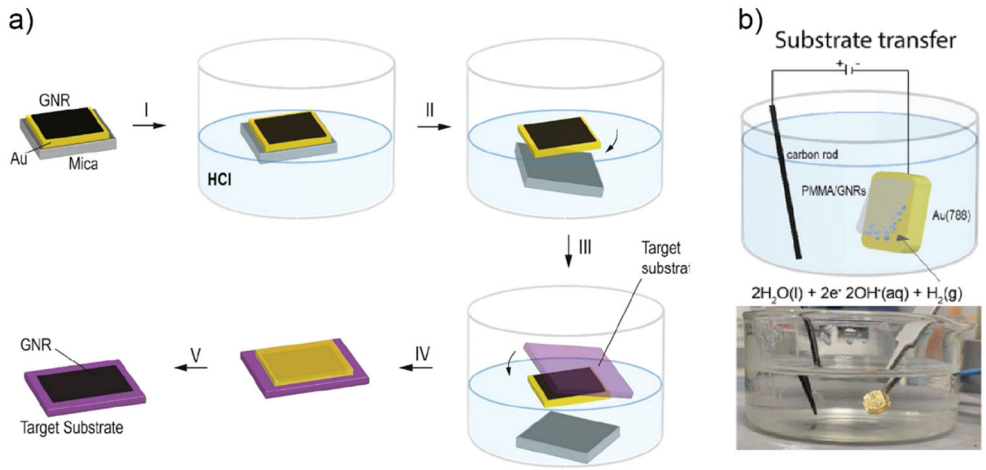

Figure 12: Schematic representation of different substrate transfer methods for GNRs. a) Illustration of the fundamental steps involved in the polymer-free transfer method of GNRs. The scheme is Reprinted with permission from [Borin Barin, G. et al., ACS Appl. Nano Mater 2, 2184–2192 (2019)] [83], used under Creative Commons license. b) Schematic diagram of the electrochemical delamination transfer process (top) with an accompanying image depicting the ongoing transfer (bottom). The scheme is Reprinted with permission from [Overbeck, J. et al. Phys. Status Solidi B 256, 1900343 (2019)][95], used under Creative Commons CC-BY license (CC BY 4.0).

To address the issue of the costly etching of single-crystal surfaces, a modified transfer method called electrochemical delamination transfer has been developed. This method enables the transfer of GNRs without the need for etching the crystal surfaces, thus allowing for the reuse of expensive substrates and reducing overall costs. The electrochemical delamination transfer, also known as bubble transfer, is a commonly used method for transferring aligned GNRs from bulk single crystals, such as the Au(788) substrate (Fig. 12b)[84,95]. This method was initially developed for delaminating graphene from Cu[96] and Pt foil[97] and has been adapted for GNR transfer.

The process involves spin-coating a supporting layer of poly-methyl methacrylate (PMMA) onto the GNR/Au(788) sample, which is then placed in an electrochemical cell containing NaOH solution. In this setup, the PMMA/GNR/Au(788) serves as the cathode, while a carbon rod acts as the anode. When a negative bias is applied to the gold, hydrogen bubbles form at the PMMA/GNRs and Au interface, leading to the delamination of the PMMA/GNR stack. The delaminated PMMA/GNR structure is then transferred onto the target substrate, such as SiO_2/Si. To enhance adhesion to the substrate and remove water residue, the PMMA/GNR/target substrate is baked, followed by immersion in warm acetone to dissolve the PMMA layer. While the electrochemical delamination transfer method offers advantages such as cost-effectiveness, scalability, and substrate reuse, it does have certain limitations. These limitations include the requirement for precise control of parameters such as bubbling time, electrolyte concentration,

and applied voltage, which may potentially cause damage to the transferred GNRs[95]. Additionally, the transfer process may lead to randomly distributed and oriented GNRs[98]. The influence of this substrate transfer on GNR orientation will be discussed in detail in Chapters 3 and 4. Most of our work in this thesis is based on using this transfer process, which will be used in Chapters 3-6.

Another transfer method for GNRs is the mechanical delamination method based on the intercalation process using octanethiol self-assembled monolayers (SAMs), which strongly bind to noble metal surfaces such as Au (Fig. 13)[99,100]. In this method, GNRs are initially synthesized on the Au(788) substrate and then spin-coated with a hydrogen silsesquioxane (HSQ) layer, which acts as a nano-porous support layer. The GNR-coated substrate is then immersed in an octanethiol SAMs solution (1M) to intercalate the GNRs from the Au(788) substrate. The intercalated GNRs are subsequently removed from the gold surface using a thermal release tape and placed onto the SiO_2/Si substrate. The tape is then removed through annealing, and the HSQ layer is dissolved using a tetramethylammonium (TMAH) developer. While this method offers the advantage of reusable metal catalysts, it also has some drawbacks, such as orientation disorder of GNRs and potential HSQ residue contamination[99]. This transfer method is adapted in our study in Chapter 7 which will be studied in detail.

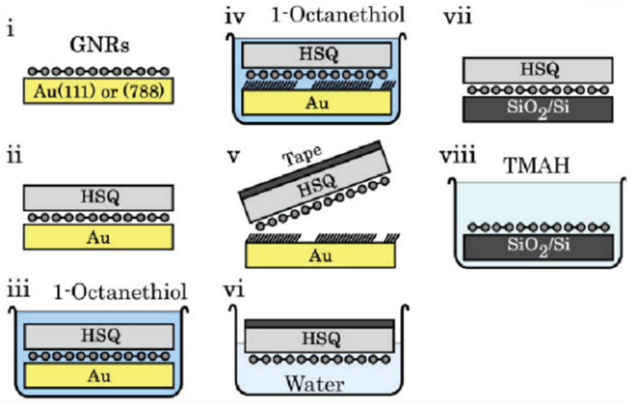

Figure 13: Schematic diagram illustrating the etchant-free transfer procedure. It is based on the mechanical delamination of GNRs through the intercalation of octanethiol SAMs. The scheme is Reprinted with permission from [Ohtomo, M. et al., Appl. Phys. Lett.112, 021602 (2018)][99] with the permission of AIP Publishing.

In the end, direct synthesis of GNRs on insulating or semiconducting surfaces would eliminate the need for a substrate transfer step. However, this is challenging due to the requirement of a catalytic surface, typically Au, for the on-surface synthesis of GNRs. To address this challenge, a transfer-free placement method has been developed[101]. This method involves growing GNRs on a thin layer of gold deposited onto an insulating substrate (SiO_2/Si) and subsequently etching away the gold layer (using KI/I_2), leaving the GNRs directly on the SiO_2/Si substrate without the need for a transfer step. However, this method requires careful control of parameters, as intense annealing can lead to the formation of blisters on the gold-thin films on SiO_2/Si substrates, resulting in non-uniform coverage and thickness of GNRs.

GNR-based electronic devices

GNRs have gained significant attention due to their exceptional electronic properties, making them highly promising materials for a wide range of applications. In particular, GNRs have been integrated into room temperature switching devices, revealing high on/off ratios (I_{on}/I_{off}) for FET devices. Recent advancements in GNR research have led to the realization of high-performance FET based on wide-bandgap 9- and 13-atom AGNRs[102]. In this research, metallic contacts were achieved through electron beam lithography (EBL) (~20 nm), and HfO_2 was used as gate dielectric (1.5 nm thick) to enhance gate efficiency and on-current (I_{on}) (Fig. 14a). The resulting transistors exhibit excellent switching behavior, with high I_{on} (I_{on} > 1 µA at V_d = −1 V) and high I_{on}/I_{off} ~ 10^5 at room temperature. Despite the remarkable performance of these GNR-based FETs, a significant challenge lies in the low device yield, attributed to the random orientation of 9- and 13-AGNRs during growth on the Au(111)/mica substrate. This random orientation leads to a low yield below 10% [102], as not all transferred GNRs successfully bridge between the source and drain contacts. To overcome the low device yield challenge, researchers have explored a novel approach involving the growth of GNRs on a vicinal surface, such as Au(788), which promotes alignment, followed by a transfer method that preserves their alignment during the transfer process. This enables efficient bridging between the source and drain contacts, resulting in a significant improvement in device yield. In particular, GNR-FETs based on dense aligned 7- and 5-AGNRs have demonstrated higher device yield compared to non-aligned GNR devices (Figs. 14b and c)[103,89]. Notably, the aligned 5-AGNR devices exhibited a substantially higher device yield of 82% compared to 12% for non-aligned GNR devices combined with higher device performance for aligned GNR devices, as shown in Fig. 14b[89].

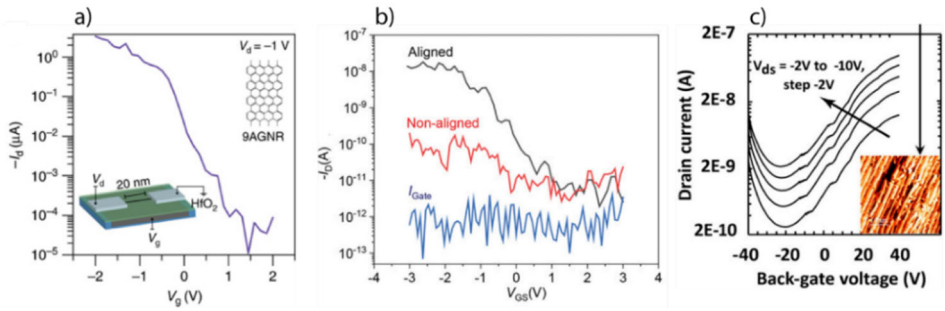

Figure 14: Electrical characteristics of the device. a) I_D-V_G characteristics of the device with a channel length of L = 20 nm, a thin HfO_2 gate dielectric, and GNRs oriented perpendicular to the channel. The scheme is Reprinted with permission from [Llinas, J. P. et al., Nat Commun 8, 633 (2017)][102], used under Creative Commons CC-BY license. b) I_D – V_{GS} characteristics of an aligned and non-aligned 5-AGNR FET at V_{DS} = −1 V at room temperature. The scheme is Reprinted with permission from [Borin Barin, G. et al., Small 2202301 (2022)][89], used under a Creative Commons CC-BY license. c) Transfer characteristics at varying drain-source bias of an aligned 7-AGNR. The scheme is Reprinted with permission from [Passi, V. et al. ACS Appl. Mater. Interfaces 10, 9900–9903 (2018)] [103], used under Creative Commons license.

The influence of GNR coverage (spatial distributions) and device geometries on device performance has been systematically investigated in several studies. In a recent study, 9-AGNRs were synthesized on Au(111)/mica substrates under different coverage levels: 0.3 monolayer (low-coverage), 0.5 monolayer (medium-coverage), and 1 monolayer (high-coverage)[104]. These coverage levels represented varying densities of GNRs on the substrate. Both simulated and

experimental results revealed a significant impact of GNR coverage on device yield, I_{on}, and I_{on}/I_{off}, as shown in Fig. 15.

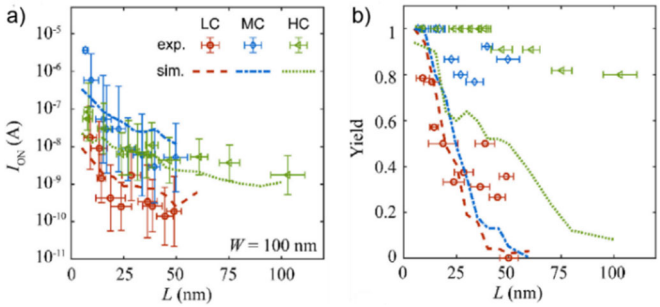

Figure 15: Dependence of I_{on}, device yield, and I_{on}/I_{off} on the GNRs surface coverage and FET channel length (*L*). a), and b) I_{on}, and yield plotted against *L* for devices with different surface coverages of GNRs and V_{DS} = -1 V. The scheme is Reprinted with permission from [Lin, Y. C. et al. Carbon 205, 519–526 (2023)][104], Copyright © 2023 Elsevier Ltd.

Higher device yields were observed for samples with higher GNR coverage, even when considering devices with larger channel lengths (e.g., 100 nm) and smaller widths. This indicates that a higher coverage of GNRs in the device improves the likelihood of successful GNR bridging between the source and drain contacts. Experimental results further demonstrated that the I_{on} was affected by the coverage of GNRs in the device (Fig. 15a). The low-coverage sample exhibited lower I_{on} values, attributed to both the smaller number of connected GNRs and lower GNR quality compared to the medium- and high-coverage samples. Interestingly, the experimental data showed higher device yields than the simulated results for the medium- and high-coverage samples (Fig. 15b). This discrepancy can be attributed to the presence of hopping transport (inter-GNR conduction), resulting from GNR-GNR bundling, and GNR relocation during the wet-transfer process of medium- and high-coverage, which was not considered in the simulated results. Similar observations of inter-ribbon conductance were reported in the work by Ohtomo, M et. al[99]. They measured source-drain currents in two situations: first, they measured FETs with longer channels (channel length of 60 nm and width of 50 µm), and second, they measured FET devices with ribbons aligned perpendicular to the channel channels (channel length of 20 nm and width of 500 nm) (Fig. 16). In both cases, low source-drain currents were observed, indicating the presence of inter-ribbon conductance.

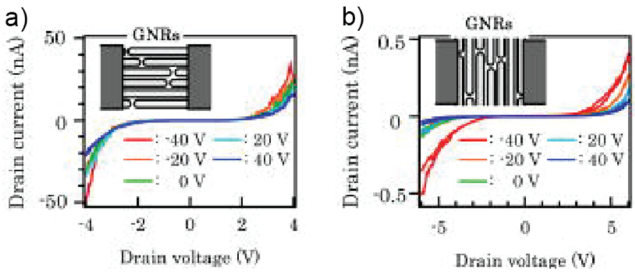

Figure 16: Electrical characterization of a 7-AGNR FET. a) I_D-V_D characteristics of the device with a channel length of *L* = 60 nm, channel width *W*= 50 µm, and electrode metal Au/Ti (15-nm-thick film of Au), with GNRs oriented parallel to the channel. b) I_D-V_D characteristics of the device with *L* = 20 nm, *W*= 500 nm, and GNRs oriented perpendicular to the channel. The scheme is Reprinted with permission from [Ohtomo, M. et al., Appl. Phys. Lett.112, 021602 (2018)][99], with the permission of AIP Publishing.

Previously mentioned studies have utilized metal electrodes in GNR-FET devices, which suffer from limitations such as Schottky barriers and the screening effects[102]. Additionally, metal electrodes are typically p-type conductors but can become unstable in the air and switch to n-type conduction after undergoing UHV annealing[105]. Furthermore, the preparation process for metal electrodes can introduce contaminants at the contact-GNR interface and may cause GNR damage. To address these issues, graphene electrodes have been proposed as an alternative. Graphene electrodes exhibit lower contact barriers, resulting in nearly charge-neutral conducting devices regardless of the environment[65,106]. The process of preparing graphene electrodes involves transferring a graphene flake onto a SiO_2 substrate and creating a gap through electro-burning (10-50 nm) (Fig. 17a)[107,108]. The resulting graphene FETs demonstrate p-type conduction, high I_{on}/I_{off} ratios, and robust performance that is not significantly affected by temperature variations[107,108].

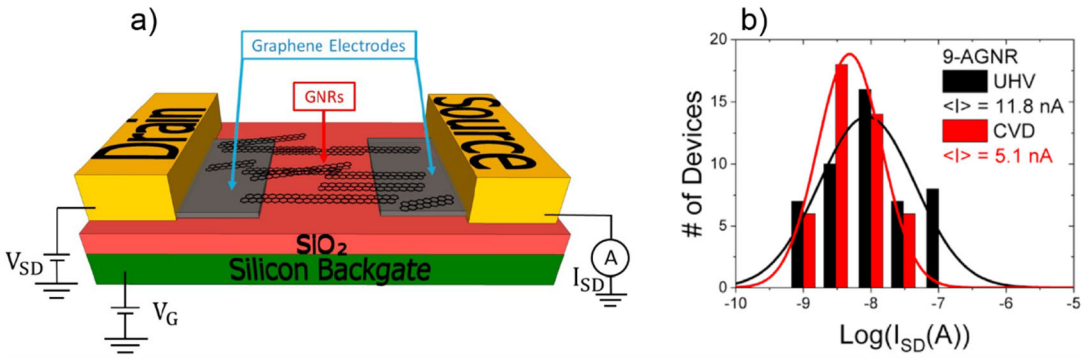

Figure 17: Schematic representation of the devices used in several studies. a) Devices with metal electrodes (Cr/Au) contacting graphene electrodes, bridged by GNRs. Situated on a Si substrate covered by a 300 nm SiO_2 layer as a global back-gate. b) Output current distributions for devices based on 9-AGNRs grown using ultra-high vacuum (UHV, black) and chemical vapor deposition (CVD, red) methods. The corresponding current values are approximately 5 nA and 12 nA, respectively. The scheme a and c is Reprinted with permission from [Martini, L. et al., Carbon 146, 36–43 (2019)][108], Copyright © 2019 Elsevier Ltd.

Moreover, the performance of FETs has been extensively studied in relation to the widths and lengths of GNRs. FETs utilizing graphene electrodes based on 9-AGNRs grown through an on-surface approach under UHV conditions have shown significantly higher device performance compared to those grown using the CVD approach (Fig. 17b)[65,108]. This UHV synthesis process results in longer GNRs compared to the CVD approach, which in turn leads to a larger contact area, lower contact barrier, and fewer inter-ribbon junctions, resulting in higher source-drain current and improved device performance. Furthermore, the width of AGNRs has been found to have a significant impact on the performance of FETs, since the GNRs' electronic bandgap is width and edge structure-dependent, affecting the GNRs' electronic properties. In the present study, it was observed that the output current values exhibited a width-dependent behavior for both 5-AGNRs and 9-AGNRs FETs. Specifically, FETs based on 5-AGNRs demonstrated substantially higher output currents, with a two-order-of-magnitude increase compared to 9-AGNRs[108]. This difference in output currents indicates electronic bandgaps consistent with theoretical predictions, highlighting the importance of AGNR width in determining device performance.

References

1. Palmer, B. S. A review on the spontaneous formation of the building blocks of life and the generation of a set of hypotheses governing universal abiogenesis. *International Journal of Astrobiology* **12**, 39–44 (2013).

2. Clayden, Jonathan., Greeves, Nick. & Warren, Stuart. *Organic chemistry*. (Oxford University Press, 2012).

3. Smith, A. D. Oxford dictionary of biochemistry and molecular biology. (Oxford University Press, 2003).

4. Banhart, F. Elemental carbon in the sp1 hybridization. *ChemTexts* **6**, 3 (2020).

5. Geim, A. K. & Novoselov, K. S. The rise of graphene. *Nature materials* **6**, 183–191 (2007).

6. Novoselov, K. S. Electric Field Effect in Atomically Thin Carbon Films. *Science* **306**, 666–669 (2004).

7. Kroto, H. W., Heath, J. R., O'Brien, S. C., Curl, R. F. & Smalley, R. E. C60: Buckminsterfullerene. *Nature* **318**, 162–163 (1985).

8. Iijima, S. Carbon nanotubes: past, present, and future. *Physica B* 5 (2002).

9. Cai, J. *et al.* Atomically precise bottom-up fabrication of graphene nanoribbons. *Nature* **466**, 470–473 (2010).

10. Balandin, A. A. *et al.* Superior Thermal Conductivity of Single-Layer Graphene. *Nano Lett.* **8**, 902–907 (2008).

11. Lee, C., Wei, X., Kysar, J. W. & Hone, J. Measurement of the Elastic Properties and Intrinsic Strength of Monolayer Graphene. *Science* **321**, 385–388 (2008).

12. Castro Neto, A. H., Guinea, F., Peres, N. M. R., Novoselov, K. S. & Geim, A. K. The electronic properties of graphene. *Rev. Mod. Phys.* **81**, 109–162 (2009).

13. Wallace, P. R. Erratum: The Band Theory of Graphite [Phys. Rev. 71, 622 (1947)]. *Phys. Rev.* **72**, 258–258 (1947).

14. Novoselov, K. S. *et al.* Two-dimensional gas of massless Dirac fermions in graphene. *Nature* **438**, 197–200 (2005).

15. Tang, H. *et al.* Photo-modulated optical and electrical properties of graphene. *Nanophotonics* **11**, 917–940 (2022).

16. Santhiran, A., Iyngaran, P., Abiman, P. & Kuganathan, N. Graphene Synthesis and Its Recent Advances in Applications—A Review. *C* **7**, 76 (2021).

17. Madurani, K. A. *et al.* Progress in Graphene Synthesis and its Application: History, Challenge and the Future Outlook for Research and Industry. *ECS J. Solid State Sci. Technol.* **9**, 093013 (2020).

18. Mbayachi, V. B. *et al.* Graphene synthesis, characterization and its applications: A review. *Results in Chemistry* **3**, 100163 (2021).

19. Hernandez, Y. *et al.* High-yield production of graphene by liquid-phase exfoliation of graphite. *Nature Nanotech* **3**, 563–568 (2008).

20. Parvez, K., Yang, S., Feng, X. & Müllen, K. Exfoliation of graphene via wet chemical routes. *Synthetic Metals* **210**, 123–132 (2015).

21. Viculis, L. M., Mack, J. J., Mayer, O. M., Hahn, H. T. & Kaner, R. B. Intercalation and exfoliation routes to graphite nanoplatelets. *J. Mater. Chem.* **15**, 974 (2005).

22. Reina, A. *et al.* Large Area, Few-Layer Graphene Films on Arbitrary Substrates by Chemical Vapor Deposition. *Nano Letters* **9**, 30–35 (2009).

23. Zhang, Y., Zhang, L. & Zhou, C. Review of Chemical Vapor Deposition of Graphene and Related Applications. *Acc. Chem. Res.* **46**, 2329–2339 (2013).

24. Emtsev, K. V. *et al.* Towards Wafer-Size Graphene Layers by Atmospheric Pressure Graphitization of Silicon Carbide. *Nat. Mater.* **8**, 203 (2009).

25. Olabi, A. G., Abdelkareem, M. A., Wilberforce, T. & Sayed, E. T. Application of graphene in energy storage device – A review. *Renewable and Sustainable Energy Reviews* **135**, 110026 (2021).

26. Yusuf, M., Kumar, M., Khan, M. A., Sillanpää, M. & Arafat, H. A review on exfoliation, characterization, environmental and energy applications of graphene and graphene-based composites. *Advances in Colloid and Interface Science* **273**, 102036 (2019).

27. Schedin, F. *et al.* Detection of individual gas molecules adsorbed on graphene. *Nature Mater* **6**, 652–655 (2007).

28. El-Kady, M. F., Shao, Y. & Kaner, R. B. Graphene for batteries, supercapacitors and beyond. *Nat Rev Mater* **1**, 16033 (2016).

29. Perreault, F., Fonseca de Faria, A. & Elimelech, M. Environmental applications of graphene-based nanomaterials. *Chem. Soc. Rev.* **44**, 5861–5896 (2015).

30. Wang, Y., Li, Z., Wang, J., Li, J. & Lin, Y. Graphene and graphene oxide: biofunctionalization and applications in biotechnology. *Trends in Biotechnology* **29**, 205–212 (2011).

31. Weiss, N. O. *et al.* Graphene: An Emerging Electronic Material. *Adv. Mater.* **24**, 5782–5825 (2012).

32. Shi, Z. *et al.* Patterning Graphene with Zigzag Edges by Self-Aligned Anisotropic Etching. *Adv. Mater.* **23**, 3061–3065 (2011).

33. Ohta, T., Bostwick, A., Seyller, T., Horn, K. & Rotenberg, E. Controlling the Electronic Structure of Bilayer Graphene. *Science* **313**, 951–954 (2006).

34. Zhang, Y. *et al.* Direct observation of a widely tunable bandgap in bilayer graphene. *Nature* **459**, 820–823 (2009).

35. Zhang, S. J. *et al.* Opening the band gap of graphene through silicon doping for the improved performance of graphene/GaAs heterojunction solar cells. *Nanoscale* **8**, 226–232 (2015).

36. Xu, W. & Lee, T.-W. Recent progress in fabrication techniques of graphene nanoribbons. *Mater. Horiz.* **3**, 186–207 (2016).

37. Saraswat, V., Jacobberger, R. M. & Arnold, M. S. Materials Science Challenges to Graphene Nanoribbon Electronics. 35.

38. Johnson, A. P., Gangadharappa, H. V. & Pramod, K. Graphene nanoribbons: A promising nanomaterial for biomedical applications. *Journal of Controlled Release* **325**, 141–162 (2020).

39. Han, M. Y., Özyilmaz, B., Zhang, Y. & Kim, P. Energy Band-Gap Engineering of Graphene Nanoribbons. *Phys. Rev. Lett.* **98**, 206805 (2007).

40. Hwang, W. S. *et al.* Transport Properties of Graphene Nanoribbon Transistors on Transport Properties of Graphene Nanoribbon Transistors on Chemical-Vapor-Deposition Grown Wafer-Scale Graphene. *Applied Physics Letters* **100**, 203107 (2012).

41. Campos, L. C., Manfrinato, V. R., Sanchez-Yamagishi, J. D., Kong, J. & Jarillo-Herrero, P. Anisotropic Etching and Nanoribbon Formation in Single-Layer Graphene. *Nano Lett.* **9**, 2600–2604 (2009).

42. Ci, L. *et al.* Controlled nanocutting of graphene. *Nano Res.* **1**, 116–122 (2008).

43. Li, X., Wang, X., Zhang, L., Lee, S. & Dai, H. Chemically Derived, Ultrasmooth Graphene Nanoribbon Semiconductors. *Science* **319**, 1229–1232 (2008).

44. Jiao, L., Zhang, L., Wang, X., Diankov, G. & Dai, H. Narrow graphene nanoribbons from carbon nanotubes. *Nature* **458**, 877–880 (2009).

45. Kosynkin, D. V. *et al.* Longitudinal unzipping of carbon nanotubes to form graphene nanoribbons. *Nature* **458**, 872–876 (2009).

46. Wang, X. *et al.* Room-Temperature All-Semiconducting Sub-10-nm Graphene Nanoribbon Field-Effect Transistors. *Physical Review Letters* **100**, (2008).

47. Chen, Z., Narita, A. & Müllen, K. Graphene Nanoribbons: On-Surface Synthesis and Integration into Electronic Devices. *Advanced Materials* **n/a**, 2001893.

48. Narita, A., Wang, X.-Y., Feng, X. & Müllen, K. New advances in nanographene chemistry. *Chem. Soc. Rev.* **44**, 6616–6643 (2015).

49. Yano, Y., Mitoma, N., Ito, H. & Itami, K. A Quest for Structurally Uniform Graphene Nanoribbons: Synthesis, Properties, and Applications. *J. Org. Chem.* **85**, 4–33 (2020).

50. Narita, A., Chen, Z., Chen, Q. & Müllen, K. Solution and on-surface synthesis of structurally defined graphene nanoribbons as a new family of semiconductors. *Chemical Science* **10**, 964–975 (2019).

51. Houtsma, R. S. K., Rie, J. de la & Stöhr, M. Atomically precise graphene nanoribbons: interplay of structural and electronic properties. *Chem. Soc. Rev.* **50**, 6541–6568 (2021).

52. Talirz, L. *et al.* On-Surface Synthesis and Characterization of 9-Atom Wide Armchair Graphene Nanoribbons. *ACS Nano* **11**, 1380–1388 (2017).

53. Talirz, L., Ruffieux, P. & Fasel, R. On-Surface Synthesis of Atomically Precise Graphene Nanoribbons. *Adv. Mater.* **28**, 6222–6231 (2016).

54. Di Giovannantonio, M. *et al.* On-Surface Growth Dynamics of Graphene Nanoribbons: The Role of Halogen Functionalization. *ACS Nano* **12**, 74–81 (2018).

55. Han, P. *et al.* Bottom-Up Graphene-Nanoribbon Fabrication Reveals Chiral Edges and Enantioselectivity. *ACS Nano* **8**, 9181–9187 (2014).

56. Gröning, O. *et al.* Engineering of robust topological quantum phases in graphene nanoribbons. *Nature* **560**, 209–213 (2018).

57. Ruffieux, P. *et al.* On-surface synthesis of graphene nanoribbons with zigzag edge topology. *Nature* **531**, 489–492 (2016).

58. Vo, T. H. *et al.* Large-scale solution synthesis of narrow graphene nanoribbons. *Nat Commun* **5**, 3189 (2014).

59. Narita, A. *et al.* Synthesis of structurally well-defined and liquid-phase-processable graphene nanoribbons. *Nat Chem* **6**, 126–132 (2014).

60. Shekhirev, M. *et al.* Interfacial Self-Assembly of Atomically Precise Graphene Nanoribbons into Uniform Thin Films for Electronics Applications. *ACS Applied Materials & Interfaces* **9**, 693–700 (2017).

61. Siyushev, P. *et al.* Coherent properties of single rare-earth spin qubits. *Nat. Commun.* **5**, 3895 (2014).

62. Schwab, M. G. *et al.* Structurally Defined Graphene Nanoribbons with High Lateral Extension. *J. Am. Chem. Soc.* **134**, 18169–18172 (2012).

63. Sakaguchi, H. *et al.* Width-Controlled Sub-Nanometer Graphene Nanoribbon Films Synthesized by Radical-Polymerized Chemical Vapor Deposition. *Advanced Materials* **26**, 4134–4138 (2014).

64. Chen, Z. *et al.* Chemical Vapor Deposition Synthesis and Terahertz Photoconductivity of Low-Band-Gap N = 9 Armchair Graphene Nanoribbons. *J. Am. Chem. Soc.* **139**, 3635–3638 (2017).

65. Chen, Z. *et al.* Synthesis of Graphene Nanoribbons by Ambient-Pressure Chemical Vapor Deposition and Device Integration. *J. Am. Chem. Soc.* **138**, 15488–15496 (2016).

66. Sakaguchi, H., Song, S., Kojima, T. & Nakae, T. Homochiral polymerization-driven selective growth of graphene nanoribbons. *Nature Chem* **9**, 57–63 (2017).

67. Falke, Y. *et al.* Photothermal Bottom-up Graphene Nanoribbon Growth Kinetics. *Nano Lett.* **20**, 4761–4767 (2020).

68. Wang, H. *et al.* Graphene nanoribbons for quantum electronics. *Nat Rev Phys* **3**, 791–802 (2021).

69. Wolf, S. A. Spintronics: A Spin-Based Electronics Vision for the Future. *Science* **294**, 1488–1495 (2001).

70. Son, Y.-W., Cohen, M. L. & Louie, S. G. Half-metallic graphene nanoribbons. *Nature* **444**, 347–349 (2006).

71. Li, Y., Zhang, W., Morgenstern, M. & Mazzarello, R. Electronic and Magnetic Properties of Zigzag Graphene Nanoribbons on the (111) Surface of Cu, Ag, and Au. *Phys. Rev. Lett.* **110**, 216804 (2013).

72. Ma, C. *et al.* Oxidization stability of atomically precise graphene nanoribbons. *Physical Review Materials* **2**, (2018).

73. Yang, L., Park, C.-H., Son, Y.-W., Cohen, M. L. & Louie, S. G. Quasiparticle Energies and Band Gaps in Graphene Nanoribbons. *Phys. Rev. Lett.* **99**, 186801 (2007).

74. Nakada, K., Fujita, M., Dresselhaus, G. & Dresselhaus, M. S. Edge state in graphene ribbons: Nanometer size effect and edge shape dependence. *Phys. Rev. B* **54**, 17954–17961 (1996).

75. Son, Y.-W., Cohen, M. L. & Louie, S. G. Energy Gaps in Graphene Nanoribbons. *Phys. Rev. Lett.* **97**, 216803 (2006).

76. Merino-Díez, N. *et al.* Width-Dependent Band Gap in Armchair Graphene Nanoribbons Reveals Fermi Level Pinning on Au(111). *ACS Nano* **11**, 11661–11668 (2017).

77. Ruffieux, P. *et al.* Electronic Structure of Atomically Precise Graphene Nanoribbons. *ACS Nano* **6**, 6930–6935 (2012).

78. Fujita, M., Wakabayashi, K., Nakada, K. & Kusakabe, K. Peculiar Localized State at Zigzag Graphite Edge. *J. Phys. Soc. Jpn.* **65**, 1920–1923 (1996).

79. Radocea, A. *et al.* Solution-Synthesized Chevron Graphene Nanoribbons Exfoliated onto H:Si(100). *Nano Lett.* **17**, 170–178 (2017).

80. Trauzettel, B., Bulaev, D. V., Loss, D. & Burkard, G. Spin qubits in graphene quantum dots. *Nature Physics* **3**, 192–196 (2007).

81. Brey, L. & Fertig, H. A. Electronic states of graphene nanoribbons studied with the Dirac equation. *Physical Review B* **73**, (2006).

82. Gillen, R., Mohr, M., Thomsen, C. & Maultzsch, J. Vibrational properties of graphene nanoribbons by first-principles calculations. *Physical Review B* **80**, 155418 (2009).

83. Borin Barin, G. *et al.* Surface-Synthesized Graphene Nanoribbons for Room Temperature Switching Devices: Substrate Transfer and ex Situ Characterization. *ACS Applied Nano Materials* **2**, 2184–2192 (2019).

84. Senkovskiy, B. V. *et al.* Making Graphene Nanoribbons Photoluminescent. *Nano Lett.* **17**, 4029–4037 (2017).

85. Verzhbitskiy, I. A. *et al.* Raman Fingerprints of Atomically Precise Graphene Nanoribbons. *Nano Lett.* **16**, 3442–3447 (2016).

86. Overbeck, J. *et al.* A Universal Length-Dependent Vibrational Mode in Graphene Nanoribbons. *ACS Nano* **13**, 13083–13091 (2019).

87. Kim, J. *et al.* Distinguishing Zigzag and Armchair Edges on Graphene Nanoribbons by X-ray Photoelectron and Raman Spectroscopies. *ACS Omega* **3**, 17789–17796 (2018).

88. Senkovskiy, B. V. *et al.* Boron-Doped Graphene Nanoribbons: Electronic Structure and Raman Fingerprint. *ACS Nano* **12**, 7571–7582 (2018).

89. Borin Barin, G. *et al.* Growth Optimization and Device Integration of Narrow-Bandgap Graphene Nanoribbons. *Small* 2202301 (2022) doi:10.1002/smll.202202301.

90. Kato, T. & Hatakeyama, R. Site- and alignment-controlled growth of graphene nanoribbons from nickel nanobars. *Nature Nanotechnology* **7**, 651–656 (2012).

91. Cavani, N. *et al.* Vibrational signature of the graphene nanoribbon edge structure from high-resolution electron energy-loss spectroscopy. *Nanoscale* **12**, 19681–19688 (2020).

92. Basagni, A. *et al.* Molecules–Oligomers–Nanowires–Graphene Nanoribbons: A Bottom-Up Stepwise On-Surface Covalent Synthesis Preserving Long-Range Order. *Journal of the American Chemical Society* **137**, 1802–1808 (2015).

93. Wu, Z.-S. *et al.* Efficient synthesis of graphene nanoribbons sonochemically cut from graphene sheets. *Nano Research* **3**, 16–22 (2010).

94. Beyer, D. *et al.* Graphene Nanoribbons Derived from Zigzag Edge-Encased Poly(para-2,9-dibenzo[bc,kl]coronenylene) Polymer Chains. *J. Am. Chem. Soc.* **141**, 2843–2846 (2019).

95. Overbeck, J. *et al.* Optimized Substrates and Measurement Approaches for Raman Spectroscopy of Graphene Nanoribbons. *Phys. Status Solidi B* **256**, 1900343 (2019).

96. Wang, Y. *et al.* Electrochemical Delamination of CVD-Grown Graphene Film: Toward the Recyclable Use of Copper Catalyst. *ACS Nano* **5**, 9927–9933 (2011).

97. Gao, L. *et al.* Repeated growth and bubbling transfer of graphene with millimetre-size single-crystal grains using platinum. *Nat Commun* **3**, 699 (2012).

98. Darawish, R. *et al.* Quantitative Characterization of Graphene Nanoribbons Orientation and Quality by Polarized Raman Spectroscopy. *submitted* (2023).

99. Ohtomo, M., Sekine, Y., Hibino, H. & Yamamoto, H. Graphene nanoribbon field-effect transistors fabricated by etchant-free transfer from Au(788). *Applied Physics Letters* **112**, 021602 (2018).

100. Vericat, C., Vela, M. E., Benitez, G., Carro, P. & Salvarezza, R. C. Self-assembled monolayers of thiols and dithiols on gold: new challenges for a well-known system. *Chemical Society Reviews* **39**, 1805 (2010).

101. Mutlu, Z. *et al.* Transfer-Free Synthesis of Atomically Precise Graphene Nanoribbons on Insulating Substrates. *ACS Nano* **15**, 2635–2642 (2021).

102. Llinas, J. P. *et al.* Short-channel field-effect transistors with 9-atom and 13-atom wide graphene nanoribbons. *Nat Commun* **8**, 633 (2017).

103. Passi, V. *et al.* Field-Effect Transistors Based on Networks of Highly Aligned, Chemically Synthesized N = 7 Armchair Graphene Nanoribbons. *ACS Applied Materials & Interfaces* **10**, 9900–9903 (2018).

104. Lin, Y. C. *et al.* Scaling and statistics of bottom-up synthesized armchair graphene nanoribbon transistors. *Carbon* **205**, 519–526 (2023).

105. Bennett, P. B. *et al.* Bottom-up graphene nanoribbon field-effect transistors. *Applied Physics Letters* **103**, 253114 (2013).

106. Candini, A. *et al.* High Photoresponsivity in Graphene Nanoribbon Field-Effect Transistor Devices Contacted with Graphene Electrodes. *J. Phys. Chem. C* **121**, 10620–10625 (2017).

107. Braun, O. *et al.* Optimized graphene electrodes for contacting graphene nanoribbons. *Carbon* **184**, 331–339 (2021).

108. Martini, L. *et al.* Structure-dependent electrical properties of graphene nanoribbon devices with graphene electrodes. *Carbon* **146**, 36–43 (2019).

Chapter 2
Experimental techniques and materials

This chapter serves as an introduction to the techniques used in the studies discussed in Chapters 3-7. It provides a brief overview of Scanning Tunneling Microscopy (STM), Raman spectroscopy, and Polarized Raman spectroscopy, highlighting the key theoretical concepts that are relevant to the subsequent chapters. Additionally, the chapter includes detailed information on the measurement setup, measurement conditions, and general aspects of sample preparation and characterization. Its purpose is to lay the foundation for a comprehensive understanding of the experimental methods employed throughout the study.

Scanning tunneling microscopy

STM is a powerful imaging technique used in nanotechnology and surface science to obtain ultra-high-resolution images of surface structures at the atomic scale. STM was invented in 1981 by Gerd Binnig and Heinrich Rohrer at IBM, which earned them the Nobel Prize in physics in 1986[1,2]. This groundbreaking technique has significantly contributed to the exploration and understanding of various important phenomena in the field of surface science[3,4].

In classical mechanics, a particle cannot pass through a potential energy barrier if its kinetic energy is less than the potential energy. However, in quantum mechanics, particles are described by their wavefunction. When the wavefunction of a particle encounters a finite potential energy barrier that is greater than the kinetic energy of the particle, the wavefunction does not immediately go to zero. Instead, the wavefunction exponentially decays into the barrier. Thus if the barrier is sufficiently small, there is a substantial probability that the particle can pass through it. This phenomenon, referred to as quantum tunneling, is utilized by an STM to image conducting surfaces with atomic spatial resolution. In an STM, a sharp metal tip is brought close enough to a metal surface so that the electrons can tunnel through the vacuum barrier separating the tip from the surface (Fig. 1). In this situation, when a bias voltage (V_{bias}) is applied between the tip and the sample, a net tunneling current (I_t) is generated. Crucially, It varies exponentially with the tip-sample separation (d) according to:

$$I_t\,(z) \propto e^{-2\,\kappa d} \quad with\ \kappa = \frac{\sqrt{2\,m\,\Phi}}{\hbar} \tag{1}$$

Here, m is the electron mass, $\hbar$ is the reduced Planck's constant, and Φ is the effective work function given by $\Phi = \frac{\Phi_T + \Phi_S}{2}$, representing the average work function combining the tip's work function Φ_T and the sample's work function Φ_S [5]. Typically, for a metal surfaces $\Phi \sim 5$ eV leading to $\kappa = 1.15\ \text{Å}^{-1}$ which implies that the length scale of the tip-sample distance over which the

tunnelling current decays by one order of magnitude is 1 Å [6]. Thus, to achieve atomic resolution, the tunneling distance must be typically within a few Ångströms.

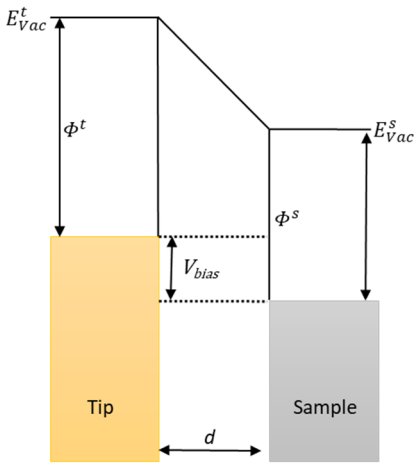

Figure 1: Schematic energy diagram and wave function in one dimension illustrating the tunneling process between the tip and sample in an STM junction. It shows the Fermi energies ($\boldsymbol{E_{Fermi}^{t/s}}$), vacuum levels ($\boldsymbol{E_{Vac}^{t/s}}$), and work functions ($\boldsymbol{\Phi^{t/s}}$) of the tip (*t*) and sample (*s*), as well as the applied bias voltage (V_{bias}). Quantum tunneling of electrons between the tip and the sample across a vacuum barrier of width *d* upon applying V_{bias} between the two. If a positive V_{bias} is applied to the sample, the Fermi level of the sample ($\boldsymbol{E_{Fermi}^{s}}$) shifts down with respect to the Fermi level of the tip($\boldsymbol{E_{Fermi}^{t}}$), and electrons tunnel from the occupied states of the tip into the empty states of the sample.

The tunneling current also crucially depends upon the local density of states (LDOS) of the tip and the surface[7,8]. A framework to understand STM measurements was provided by Tersoff and Hamann[9], who developed a theoretical model describing the tunneling process in STM based on Bardeen's mathematical approach[10] for quantum tunneling. The model simplifies the system by assuming a locally spherical tip geometry, employing an s-type wave function for the tip, applying a small bias voltage across the tip-sample junction, and considering low-temperature conditions. The tunneling current derived within this model, given by Eqs. (2) and (3), is proportional to the LDOS of the sample at its Fermi level and the center position of the tip.

$$I_t \propto \int_0^{V_{bias}} \rho_s(E)\rho_t(E+V_{bias})\, T(E,V_{bias})dE \tag{2}$$

$$T(E,V_{bias}) = exp\left(\frac{-2d\sqrt{2\,m}}{\hbar}\sqrt{\frac{\Phi_s+\Phi_t}{2}+\frac{V_{bias}}{2}-E}\right) \tag{3}$$

Here, $\rho_t(E)$ and $\rho_s(E)$ represent the LDOS for the tip and sample, respectively, measured with respect to their individual Fermi levels, and $T(E,V_{bias})$ is the transmission probability for electrons at energy *E* and applied potential V_{bias}. The equation can be simplified substantially by assuming that ρ_t is constant over the energy interval probed, depending only on the LDOS of the surface:

$$I_t\,(V_{bais}) \propto e^{-2\,\kappa d}\int_0^{V_{bias}} \rho_s(E)dE \tag{4}$$

Raman spectroscopy

Raman spectroscopy is an analytical technique based on the interaction of light with the chemical bonds within a material to probe vibrational modes and generate unique molecular fingerprints[11,12]. Light can interact with materials through various processes such as absorption, reflection, photoluminescence, and scattering, both inelastically and elastically. The Raman effect, a fascinating inelastic scattering phenomenon, was first predicted theoretically by L. Brillouin and A. Smekal in 1923[13] and later observed by C.V. Raman in 1928[14], for which he was awarded the Physics Nobel Prize. Subsequently, L. Mandelstam and G. Landsberg proved the effect in solids[15]. Today, Raman spectroscopy has become a powerful and widely used tool in optical spectroscopy, enabling the study of crystals and chemical compounds, and aiding in the identification of constituents in complex materials. Moreover, Raman spectroscopy provides invaluable information regarding the structural quality and chemical functionalizations of sp^2 hybridized carbon nanomaterials including graphene, carbon nanotubes, and GNRs.

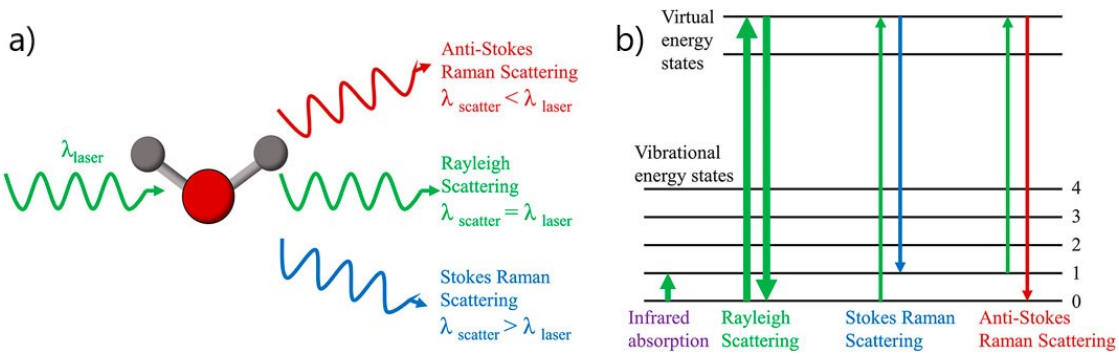

Figure *2*: Principle of Raman scattering. a) Basic concept of elastic and inelastic Raman scattering of light by molecules. b) Energy level diagram of Raman scattering, Rayleigh scattering, and infrared absorption. The scheme is Reprinted with permission from [Liu, K, Front. et al., Bioeng. Biotechnol. 10, 856591 (2022)][16], used under Creative Commons Attribution License (CC BY).

When exposed to a specific light wavelength (λ_{laser}), most photons primarily undergo an elastic scattering known as Rayleigh scattering, emitting photons with wavelengths identical to the incident ones ($\lambda_{laser} = \lambda_{scatter}$), as shown in Fig. 2[16]. A smaller fraction (approximately 1 in 10^7) undergo inelastic scattering, referred to as the Raman effect[17]. This inelastic effect arises when light influences the electron density of a molecule's chemical bonds, generating an electromagnetic field within the molecule and inducing shifts in its vibrational frequencies. This interaction can briefly elevate an electron to a virtual state, a state that doesn't represent an actual molecular energy level. Spontaneous Raman scattering occurs when molecules transition from their ground state to this virtual state and subsequently relax into a different vibrational state, emitting a photon whose energy is different from the incident photon. The difference in the energy of the incident and the emitted photon is called the Raman shift and is equal to the difference between the ground state and the final vibrational state of the electron. Thus a careful spectroscopic measurement characterizing the Raman shifts allows for the identification of a molecule's vibrational modes. When the emitted photon has less energy compared to the incident photon, the process is termed as Stokes scattering. However, under certain conditions, the incident photon can excite an electron from a molecule in a thermally excited state and the

electron finally relaxes to the ground state thus, emitting a photon with higher energy. This process is termed anti-Stokes scattering[16,17], as illustrated in Fig. 2. Notably, anti-Stokes scattering is far less probable than Stokes scattering as relatively more molecules are in the ground state than an excited state and therefore, only Stokes scattering Raman measurements were performed in this thesis.

Enhancement of Raman signal

Raman scattering is a process where incident light interacts with the vibrational modes of a material, resulting in scattered light with different frequencies. Non-resonant Raman scattering occurs when the energy of the exciting laser does not match any electronic transition of the insulators and wide band gap semiconductors. The excitation thus relies on the existence of virtual states. However, when the photon can excite an electron to an intrinsic electronic state in the material the scattering cross-section is greatly increased. This is called resonant scattering. In this study, we utilized 9-AGNRs characterized by an optical bandgap of 1.0−1.1 eV[18,19]. We performed Raman spectroscopy with three excitation wavelengths, 457 nm (2.7 eV), 532 nm (2.3 eV) and 785 nm (1.6 eV). Crucially, the 785 nm wavelength laser is sufficiently close to the optical band gap of 9-AGNRs leading to greatly enhanced scattering[18,19].

Aside from utilizing the resonance condition, there are alternative methods to enhance the intensity of the Raman signal. In particular, the scattering cross section can be increased by increasing the local electric field strength (E_0) that is generated by the photon on the scattering surface. These techniques include Surface-Enhanced Raman Scattering (SERS), utilizing plasmonic resonance on metallic surfaces or nanoparticles, and Tip-Enhanced Raman Scattering (TERS), employing sharp scanning probe tips to enhance the local electric field. TERS in particular enables nanoscale Raman imaging to approach the atomic limit[20–22]. Lastly, Interference-Enhanced Raman Scattering (IERS) harnesses interference effects in thin films to enhance Raman signal sensitivity. In our Raman-optimized substrate (ROS) device, IERS is utilized to amplify the Raman signal.

Polarization-dependent Raman

Polarized Raman spectroscopy is a powerful tool that offers insights into molecular orientation and bond vibration symmetry[23]. This is particularly valuable when investigating 1D anisotropies found in materials such as nanowires, CNTs, and GNRs[23,24]. This analysis is crucial not only for practical device applications but also for enhancing our comprehension of the vibrational symmetry of distinct Raman modes. By adjusting the polarization directions of both the incident and scattered light, we can access and distinguish specific vibrational modes, linked directly to the lattice structure. Moreover, the polarization-dependent nature of the Raman modes gives a direct view of the underlying symmetry, making this technique particularly powerful in identifying in-plane anisotropy and deducing the crystallographic orientation of two-dimensional crystals[23].

Porto notation is used to describe the experimental configuration for polarization conditions[25]. It provides information about the orientations of the incident laser beam, scattered light detection, and their respective polarizations relative to the sample orientation (Fig. 3)[26]. For example, $\bar{Z}(XY)Z$ represents the sequence of the direction of the incident light ($\bar{Z}$), the polarization direction of the incident light (*X*), the selected polarization state in the detection path (*Y*), and the direction of scattered light toward the detector (*Z*), the bar indicating the negative direction.

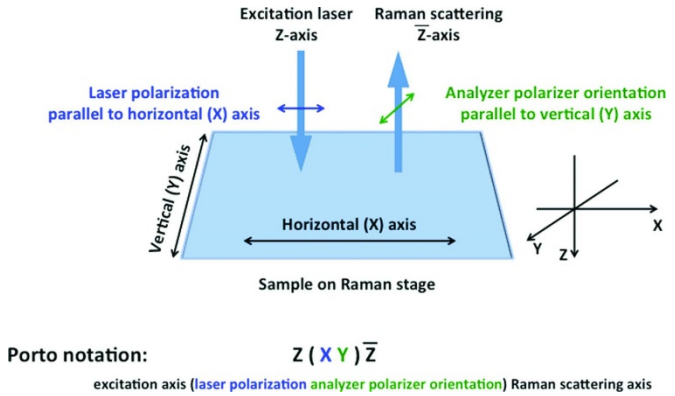

Figure 3: Schematic illustrates the orientation of polarization axes in a Raman microscope at the sample, along with the corresponding Porto notation for non-oriented samples. The scheme is Reprinted with permission from [El Mendili, Y. et al., J Appl Crystallogr 52, 618–625 (2019)][26], used under Creative Commons Attribution License (CC BY).

Experimental setups

Variable-temperature scanning tunneling microscope (VT-STM)

The experiments and sample preparations described in this thesis were conducted using a Scienta-Omicron VT-STM system. The STM operates at room temperature and under ultra-high vacuum (UHV) conditions, with a base pressure of approximately 10^{-10} mbar. The experimental setup consists of two main chambers: an analysis chamber (AC) housing the STM and a preparation chamber (PC). A small fast-entry load-lock chamber is attached to the PC, facilitating rapid sample transfer into and out of the system (Fig. 4).

The PC is specifically designed for sample fabrication, allowing for the in-situ characterization of the samples using the VT-STM. The PC is equipped with an argon ion sputter gun to obtain clean surfaces in UHV. A manipulator is used for positioning the sample within the chamber as well as transferring samples between the PC and the AC. The manipulator also hosts an e-beam heating stage allowing for controlled annealing of the samples. The temperature of the surface is measured by an externally mounted optical pyrometer, in addition to a thermocouple on the heating stage. A custom-built UHV evaporator is used for the thermal evaporation of molecules and is mounted on the PC. Thus permitting the in-situ deposition of molecular precursors onto cleaned gold surfaces. The sublimation rate of the molecules is calibrated using a quartz crystal

microbalance (QCM). Lastly, pressure gauges monitor the pressure levels in all three systems. The three chambers are separated by gate valves allowing for their independent operation.

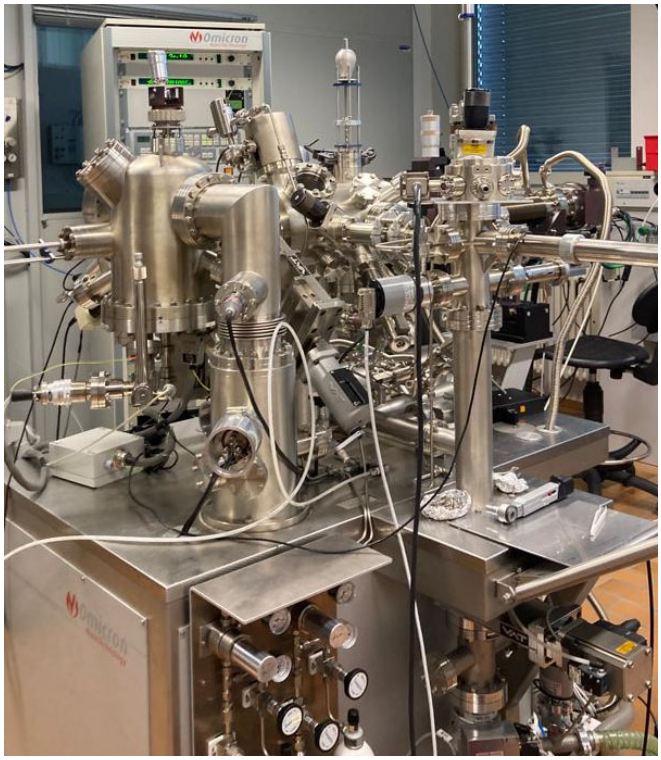

Figure 4: The Scienta Omicron VT-STM system used for the experiments presented in this thesis.

In our study, the VT-STM in the AC was used to operate at room temperature. Mechanically cleaved or electrochemically etched Pt/Ir wires were used as the STM tips. The STM was operated in constant current mode under the control of the Omicron Nanotechnology GmbH MATRIX system. Data processing and analysis utilized the matrixfilereader package[27], along with custom procedures in Wavemetrics IGOR Pro.

GNR reactor

A novel vacuum system called the GNR reactor, has been developed to optimize the production process of GNRs under UHV conditions of approximately 10^{-10} mbar (Fig. 5)[19]. This innovative system enables efficient and consistent fabrication of high-quality GNRs on various growth surfaces such as Au(111)/mica, Au(111), Au(11,12,12), or Au(788) crystals, which are crucial for comprehensive studies on transfer and device processing. It consists of a UHV-preparation chamber, to which a fast-entry load lock chamber is attached. The preparation chamber contains a retractable sample stage equipped with an integrated heater and thermocouples, an argon ion sputtering gun, a QCM for measuring molecule deposition rates, and a custom-built six-fold evaporator for deposition of the precursors.

Most importantly, all the instruments pertinent to sample fabrication are computer-controlled using custom LabView software. This allows for very controlled conditions for GNR growth and

leads to highly reproducible samples (Fig. 5). The automation also enables the creation of up to 3-4 samples on Au(788) and 12-16 samples on Au(111)/mica per day. This represents a significant reduction in processing time compared to traditional STM systems that require continuous manual operation. For GNRs that are chemically stable (this applies to all the GNRs studied in this thesis) the GNR reactor is an invaluable tool for the efficient and reproducible synthesis of samples.

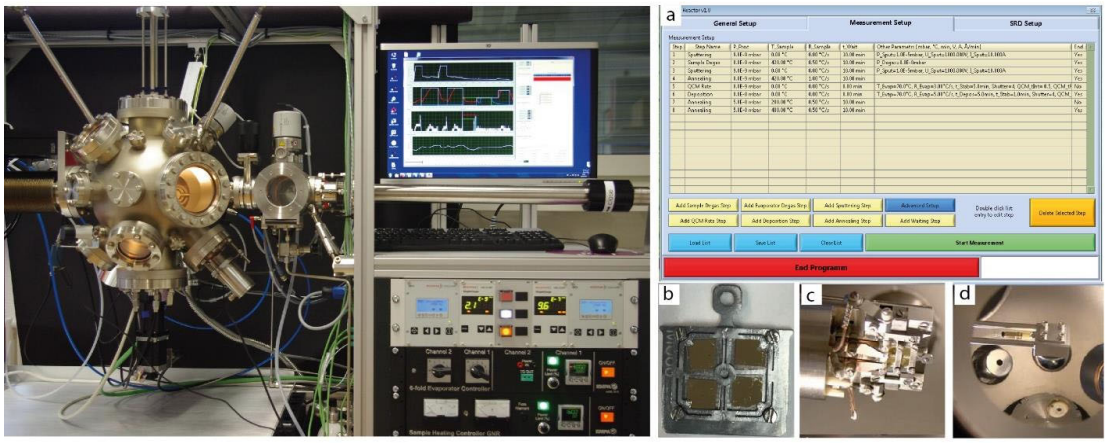

Figure 5: Schematic representation of the GNR reactor and its components. Left panel: An overview of the GNR reactor and the electronic rack. The right panel illustrates the following: a) User-friendly software interface for defining the growth steps. b) Loading up to 4 Au/mica substrates onto the sample holder. c) Transfer of the sample onto the sample stage. d) View of the quartz crystal microbalance (QCM), the shutter of the six-fold evaporator, and the sputter gun. The scheme is Reprinted with permission from [Borin Barin, G. et al., ACS Appl. Nano Mater 2, 2184–2192 (2019)][19], used under Creative Commons license.

Raman spectroscopy

In this thesis, Raman measurements were performed using a WITec Alpha 300R system (Fig. 6a), with three excitation sources at visible and near-infrared wavelengths (λ_{laser} = 488, 532, 785 nm). The system is modularly designed, connecting lasers and spectrometers to a coupling tower atop an optical microscope via optical fibers, allowing for conventional bright-field imaging. The sample is mounted on *XY*-stage for spatial scanning. Laser light is directed through a single-mode optical fiber, with power adjusted using a motorized attenuator, and then focused onto the sample using an objective lens. A shutter blocks the laser when it's not in use, and a half-wave plate is used to control the polarization of the light. The scattered light from the sample is collected through the same objective lens and travels upward as a parallel beam.

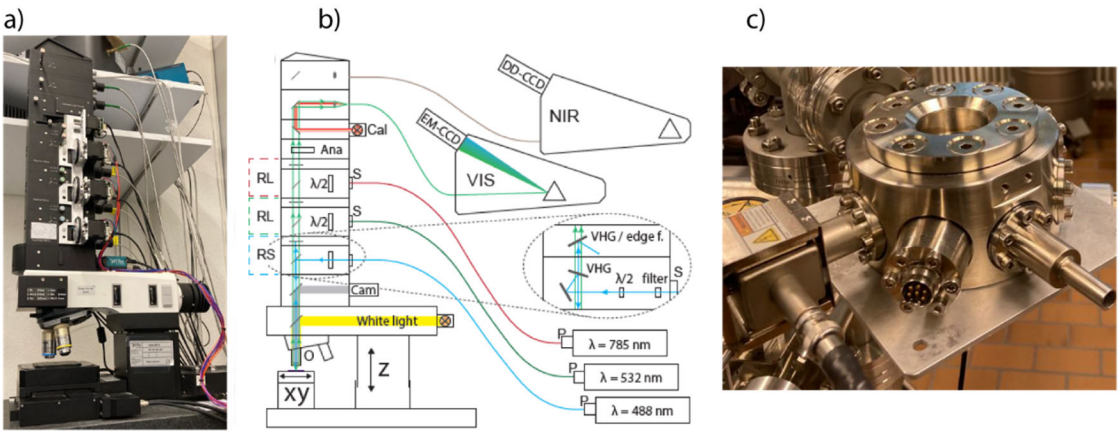

Figure 6: Raman Spectroscopy Instrumentation. a) Picture of the WITec Alpha 300R modular coupling tower. b) Diagram illustrating the system and its light pathway. Starting from the bottom, the microscope tower features a white light source, followed by a camera unit (Cam), three coupling segments for excitation wavelengths of 488 nm, 532 nm, and 785 nm, an analyzing polarizer (Ana), a calibration light source (Cal), and two coupling units to both spectrometers[28]. The depicted light path is for the 488nm excitation scenario. Also, the system has adjustable *λ/2* plates for the three wavelengths and software-controlled stepper motors for precise manipulation of the analyzing polarizer. c)Home-built vacuum chamber.

Microscope objectives are critical in obtaining better Raman signals. A higher magnification lens leads to greater spatial resolution and smaller laser spot sizes. However, the Numerical Aperture (NA) determines the amount of scattered light that is captured and focused on the analyzer. A higher NA therefore leads to more of the scattered light being captured, leading to higher intensity of the signal. Most measurements presented in this thesis were performed with a 50x long working distance (9mm) objective with NA = 0.55 (corresponding to a 1.5 µm diameter laser spot).

To eliminate unwanted scattered light, notch filters (for 488 nm excitation) or edge filters (for 532 nm/785 nm excitation) are used. Filtered light is focused onto a photonic-crystal fiber at the top of the tower, acting as the second focal point for the confocal Raman setup. An analyzing polarizer can be inserted into the beam path. Raman spectra in the visible range are recorded using a 300 mm visible (VIS) spectrometer with optimized optics and a thermoelectrically cooled, electron-multiplying CCD (EMCCD). Near-infrared excitation spectra are dispersed using a 400 mm NIR-spectrometer with specific gratings and a deep-depletion CCD (DD-CCD). We determine polarized Raman intensities using a setup featuring polarizers and an analyzer inserted in the beam path. The incident laser light is linearly polarized, and specific scattered signals are captured by an analyzer before the detector. We used an automated polarization control system for polarization-dependent measurements. The polarization is controlled by *λ/2* plates whose orientation can be changed using stepper motors. The system is controlled by a custom LabView software that is linked with the WITec Control software of the microscope. This automated system allows for precise and consistent polarization adjustments. (Fig. 6b)[28].

We calibrated the Raman shift by recording the silicon TO phonon F_{1g} mode's spectrum and applying an offset correction to precisely align the F_{1g} band position at 520.70 cm^{-1}. While many samples are measurable in ambient conditions, GNRs risk photochemical reactions at certain photon energies[29]. We mitigated this by using a home-built vacuum chamber with a 0.2mm

fused silica window for our measurements (See Fig. 6c). Higher laser power leads to greater Raman peak intensity, however, it can also lead to sample heating or cause light-induced damage therefore necessitating a fine-tuning of laser intensity. By analyzing the degradation of the signal versus laser power and time, we could establish the optimal laser power and integration time[19,29]. Additionally, as the samples are prepared uniformly over mm scale surfaces, we integrated the Raman signal over 10s to 100s and micrometers (µm) scale regions to improve the signal quality. Lastly, laser-induced damage was also minimized by performing the measurements in a custom-built vacuum chamber with a base pressure of 10^{-5} mbar.

In this thesis, apart from obtaining Raman signals on the growth substrate, we additionally used Raman-optimized substrates (ROS) for post-substrate transfer, as introduced by Overbeck, J. et al[29]. This ROS features an aluminum oxide layer, fabricated by atomic layer deposition (ALD) on top of a thick gold film on SiO_2 (See Fig. 7)[29]. The gold layer of the ROS eliminates the SiO_2 signal leading to a flat background. The right choice of the aluminum oxide layer leads to interference enhancement of the Raman signal, amplifying signals by 11.5, 19.5, and 43.0 times for excitation wavelengths of 488, 532, and 785 nm, respectively compared to the signal directly on the Au pad.

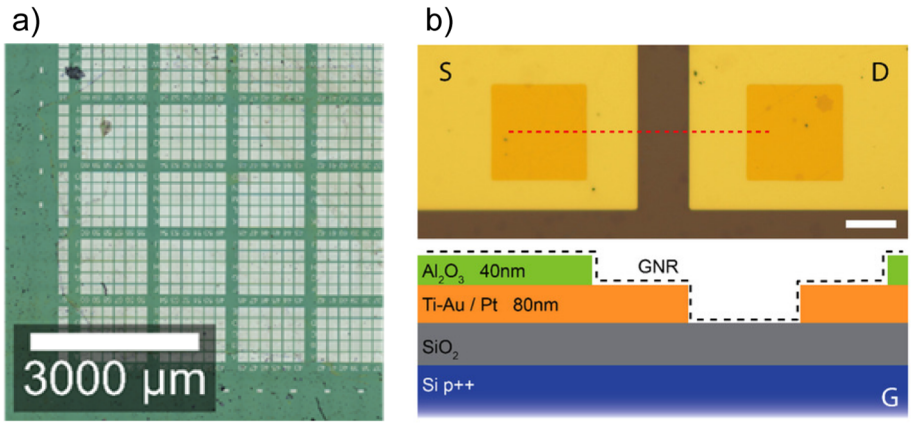

Figure 7: Raman-optimized substrate (ROS) device. a) Image of a ROS device. b) Optical micrograph of the ROS device with sketched representations of the individual layers. The scheme is Reprinted with permission from [Overbeck, J. et al. Phys. Status Solidi B 256, 1900343 (2019)][29], used under Creative Commons CC-BY license (CC BY 4.0).

References

1. Binnig, G., Rohrer, H., Gerber, Ch. & Weibel, E. Surface Studies by Scanning Tunneling Microscopy. *Phys. Rev. Lett.* **49**, 57–61 (1982).
2. Binnig, G. & Rohrer, H. Scanning tunneling microscopy. *Surface Science* **126**, 236–244 (1983).
3. Tierney, H. L. & Sykes, E. C. H. Scanning Tunneling Microscopy in Surface Science, Nanoscience and Catalysis. *J. Am. Chem. Soc.* **132**, 11387–11387 (2010).
4. *Springer Handbook of Microscopy*. (Springer International Publishing, 2019). doi:10.1007/978-3-030-00069-1.
5. Simmons, J. G. Electric Tunnel Effect between Dissimilar Electrodes Separated by a Thin Insulating Film. *Journal of Applied Physics* **34**, 2581–2590 (1963).
6. Wiesendanger, R. Scanning Probe Microscopy and Spectroscopy: Methods and Applications. (Cambridge University Press, 1994).
7. Hofer, W. A., Foster, A. S. & Shluger, A. L. Theories of scanning probe microscopes at the atomic scale. *Rev. Mod. Phys.* **75**, 1287–1331 (2003).
8. Sautet, P. Images of Adsorbates with the Scanning Tunneling Microscope: Theoretical Approaches to the Contrast Mechanism. *Chem. Rev.* **97**, 1097–1116 (1997).
9. Tersoff, J. D. & Hamann, D. R. Theory of the scanning tunneling microscope. *Phys. Rev. B* **31**, 805–813 (1985).
10. Bardeen, J. Tunnelling from a Many-Particle Point of View. *Physical Review Letters* **6**, 57–59 (1961).
11. Jorio, A., Saito, R., Dresselhaus, G. & Dresselhaus, M. S. *Raman Spectroscopy in Graphene Related Systems: JORIO:RAMAN O-BK*. (Wiley-VCH Verlag GmbH & Co. KGaA, 2011). doi:10.1002/9783527632695.
12. Casiraghi, C. & Prezzi, D. Raman Spectroscopy of Graphene Nanoribbons: A Review. in GraphITA: Selected papers from the Workshop on Synthesis, Characterization and Technological Exploitation of Graphene and 2D Materials Beyond Graphene (eds. Morandi, V. & Ottaviano, L.) 19–30 (Springer International Publishing, 2017). doi:10.1007/978-3-319-58134-7_2.
13. Smekal, A. Zur Quantentheorie der Dispersion. *Naturwissenschaften* **11**, 873–875 (1923).
14. Raman, C. V. A new radiation. *Indian Journal of Physics* **2**, 387–398 (1928).
15. Landsberg, G. Über die lichtzerstreuung in kristallen. *Zeitschrift für Physik* **50**, 769–780 (1928).
16. Liu, K., Zhao, Q., Li, B. & Zhao, X. Raman Spectroscopy: A Novel Technology for Gastric Cancer Diagnosis. *Front. Bioeng. Biotechnol.* **10**, 856591 (2022).
17. Ferraro, J. R., Nakamoto, K. & Brown, C. W. *Introductory Raman spectroscopy*. (Academic Press, 2003).
18. Talirz, L. *et al.* On-Surface Synthesis and Characterization of 9-Atom Wide Armchair Graphene Nanoribbons. *ACS Nano* **11**, 1380–1388 (2017).
19. Borin Barin, G. *et al.* Surface-Synthesized Graphene Nanoribbons for Room Temperature Switching Devices: Substrate Transfer and ex Situ Characterization. *ACS Applied Nano Materials* **2**, 2184–2192 (2019).

20. Lee, J., Crampton, K. T., Tallarida, N. & Apkarian, V. A. Visualizing vibrational normal modes of a single molecule with atomically confined light. *Nature* **568**, 78–82 (2019).

21. Zhang, Y. *et al.* Visually constructing the chemical structure of a single molecule by scanning Raman picoscopy. *National Science Review* **6**, 1169–1175 (2019).

22. Gutzler, R., Garg, M., Ast, C. R., Kuhnke, K. & Kern, K. Light–matter interaction at atomic scales. *Nat Rev Phys* **3**, 441–453 (2021).

23. *Confocal Raman Microscopy*. vol. 158 (Springer Berlin Heidelberg, 2011).

24. Overbeck, J. *et al.* A Universal Length-Dependent Vibrational Mode in Graphene Nanoribbons. *ACS Nano* **13**, 13083–13091 (2019).

25. Damen, T. C., Porto, S. P. S. & Tell, B. Raman Effect in Zinc Oxide. *Phys. Rev.* **142**, 570–574 (1966).

26. El Mendili, Y. *et al.* Raman Open Database: first interconnected Raman–X-ray diffraction open-access resource for material identification. *J Appl Crystallogr* **52**, 618–625 (2019).

27. Braun, T. MatrixFileReader. (2021).

28. Overbeck, J. Nanojunctions from Molecules to Graphene Nanoribbons: Optical Characterization and Transport Properties. (2019).

29. Overbeck, J. *et al.* Optimized Substrates and Measurement Approaches for Raman Spectroscopy of Graphene Nanoribbons. *Phys. Status Solidi B* **256**, 1900343 (2019).

Chapter 3

Quantifying alignment and quality of graphene nanoribbons: A polarized Raman spectroscopy approach

Introduction

Graphene nanoribbons (GNRs) are quasi-one-dimensional stripes of graphene with an intriguing set of physicochemical properties deriving from quantum confinement and related bandgap tunability[1]. The ability to tune the properties of GNRs at the atomic scale by changing their width[2–5] and edge topology[6–10] has opened up a promising avenue for their application in electronics[11–23], spintronics[24–26], and photonic devices[27–31]. The required atomic precision in GNR synthesis could only be met by a bottom-up approach based on the covalent coupling of specifically designed precursor molecules followed by cyclodehydrogenation on metallic surfaces. Since the pioneering work of Cai *et al.* in 2010[5], GNRs with various widths[2,3,30,32,33], edge topologies (armchair[34], zigzag[10], cove[35], etc.), as well as specific edge extensions giving rise to exotic topological quantum phases, have been reported[7,6].

To explore the exciting properties of GNRs in functional devices, a substrate transfer step is necessary to transfer the GNRs from their metallic growth substrate (usually Au(111)) to semiconducting or insulating substrates suitable for digital logic applications, such as SiO_2/Si[11–13]. Most of the substrate transfer strategies developed so far involve aqueous solutions or the presence of polymers as a support layer, which can lead to residues or defects in the GNRs[36]. To successfully integrate GNRs into devices, GNR properties must be preserved and monitored, also upon substrate transfer, which remains one of the main bottlenecks in the development of GNR-based electronics.

Due to its speed, sensitivity, and non-destructive nature, Raman spectroscopy has emerged as one of the main techniques for probing the width, structural integrity[37–39], and even the length[38,40] of GNRs. Because it probes vibrational modes via inelastic scattering of photons, Raman spectroscopy is extremely sensitive to geometric structure within molecules[41]. This makes it a powerful technique to characterize GNRs from their growth conditions under ultrahigh vacuum (UHV) to their device integration[11–15]. Owing to the largely anisotropic properties of GNRs, polarization-dependent Raman spectroscopy is key to characterizing the overall alignment of such quasi-1D structures[29,38]. From a device perspective, the degree of GNR alignment is an extremely important feature[12,13,15,16]. For FETs, for example, the device yield is significantly improved when transferring GNRs in the same orientation as the pre-patterned

source and drain contacts[13,40]. Similar to optoelectronic devices, where absorption and emission of light are most efficient for polarization along the GNR axis[30,27].

To characterize the degree of GNR alignment, previous studies used the Raman polarization anisotropy (*P*) which is defined as $P = (I_{\parallel} - I_{\perp})/ (I_{\parallel} + I_{\perp})$, where $I_{\parallel}$ and $I_{\perp}$ are the Raman intensities measured with polarization along and perpendicular to the GNR axis, respectively. Polarization anisotropy $P = 1$ thus corresponds to perfect uniaxial alignment of GNRs, whereas $P = 0$ indicates random GNR orientation with no preferential direction of alignment[29,38,27]. These studies demonstrated preservation of the GNRs' overall degree of alignment upon substrate transfer for the case of a complete monolayer of 7- and 9-atom-wide armchair GNRs (7-AGNR and 9-AGNR, respectively), with $P > 0.7$-0.8[29,38,27]. Despite the fact that GNR alignment within a full monolayer was successfully preserved, GNR transport properties were heavily deteriorated by GNR-GNR bundling, which resulted in hopping transport (inter-GNR conduction) perpendicular to the source and drain contacts in FETs with channel lengths of 60 nm[15]. Theoretical studies on semiconducting carbon nanotubes (SCNTs) also showed that, as the separation between CNTs decreases, the CNT-FET characteristics are degraded. This degradation was associated with charge screening between neighboring CNTs in the channel and to Schottky barriers at the CNT/metal contact interface[42]. It is thus clear that the alignment and distribution of GNRs are important characteristics that impact device performance. The Raman polarization anisotropy (*P*) approach used in previous studies provides the overall alignment by only taking into account two data points: the intensity parallel and perpendicular to the assumed GNR alignment distribution, which, however, is generally not precisely known. Therefore, this method is limited in its ability to provide a complete characterization of the angular distribution of the GNRs' long axis relative to an arbitrary in-plane axis, and it does not consider any other contributions that may arise from polarization-independent Raman intensities.

In this work, we investigate the influence of 9-AGNR surface coverage on GNR quality and orientation on the growth substrate and after substrate transfer. We characterize the overall GNR quality and the alignment of high- and low-coverage samples by scanning tunneling microscopy (STM) and polarized Raman spectroscopy. We extend a Gaussian distribution model to extract the GNRs' angle distribution (quality of alignment) and to quantify the polarization-independent Raman signal (isotropic contribution) upon growth on vicinal template surfaces and after substrate transfer. By applying this model to different coverages of GNRs and substrates, we unveil the main parameters that influence the GNRs' quality of alignment and give rise to the isotropic contribution to the Raman signal.

Results and discussion

To synthesize aligned 9-AGNRs the precursor monomer 3′,6′-di-iodine-1,1′:2′,1′′-terphenyl (DITP)[34] is deposited on a vicinal catalytic surface (Au(788)) followed by two annealing steps to activate the polymerization and cyclodehydrogenation reactions[5,2,4]. Samples are prepared with two different coverages (~ 0.4 of a monolayer and ~1 full monolayer, ML, herein referred to as low- and high-coverage samples, respectively) as shown in Fig. 1. The vicinal surface enables

the growth of GNRs along the low-coordination sites of the Au(788) step edges, which act as favorable nucleation sites[43,44]. This allows GNRs to grow gradually with deposition time, and after 8 minutes with a fixed deposition rate of 1 Å /min, a full monolayer of aligned 9-AGNRs (high-coverage sample) is formed. A representative STM image of a high-coverage sample with 9-AGNRs of an average length of 34 nm is shown in Fig. 1a, the corresponding GNR length histogram is given in Fig. S1a. For the low-coverage 9-AGNR samples, a deposition time of 3 minutes is used (with a fixed deposition rate of 1 Å /min), which provides just enough precursor molecules for individual 9-AGNRs to grow along all Au(788) step edges, resulting in an average GNR length of 37 nm (Fig. 1c, see Fig. S1b for the length histogram).

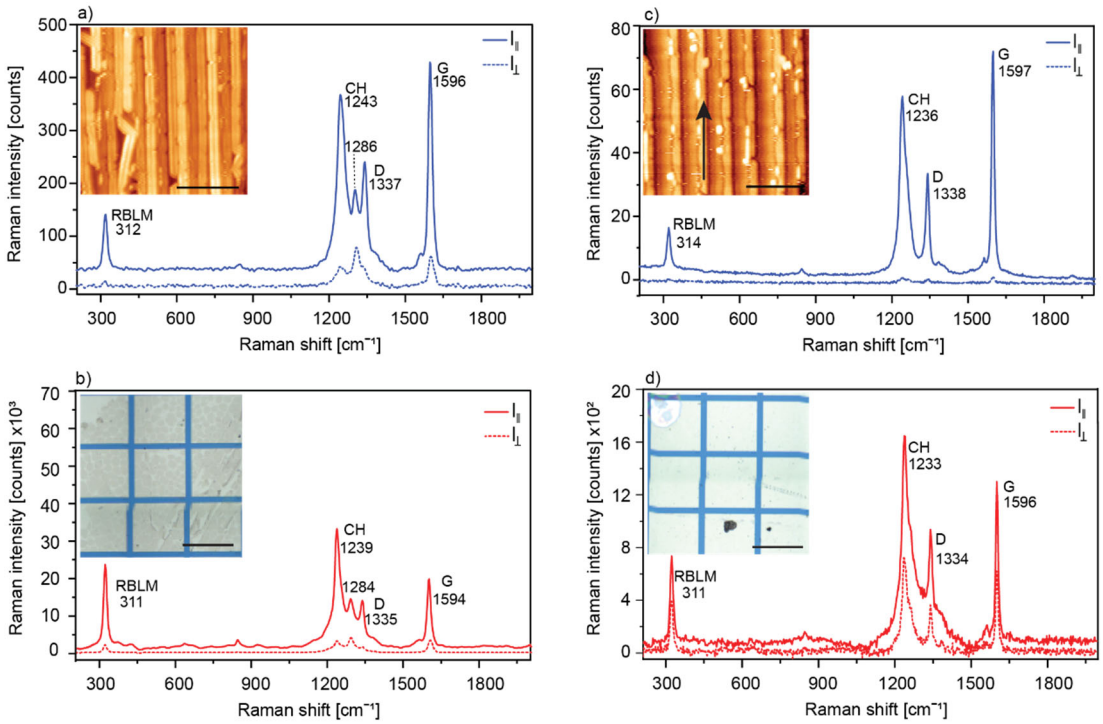

Figure 1: Characterization of aligned 9-AGNRs samples at high (a,b) and low (c,d) coverage before (a,c) and after (b,d) substrate transfer. Raman spectra of the high-coverage sample on Au(788) (a) and after substrate transfer onto a Raman-optimized substrate (ROS)(b)[36]. The spectra are acquired with an excitation wavelength of 785 nm under vacuum conditions with polarization parallel ($I_{\parallel}$) to the GNR alignment direction (along the Au(788) step edges) in red, and perpendicular ($I_{\perp}$) to the GNR alignment direction in blue. The inset in panel (a) shows a STM topography image for the high-coverage sample on Au(788) (black arrow highlighting the GNR growth direction and position) with a scale bar of 10 nm (V_b =-1.5 V, I_t =0.3 nA). The inset in panel (b) shows an optical micrograph of ribbons transferred onto a ROS, with a scale bar of 180 µm. Raman spectra of the low-coverage sample (c) on Au(788), and (d) after substrate transfer onto a ROS, with polarizations/colors as indicated above. The inset in panel (c) shows an STM image for the low-coverage sample on Au(788), with a black arrow highlighting the GNR growth direction and position along the Au(788) step edges of (V_b =-1.5 V, I_t =0.3 nA, scale bar: 10 nm). The inset in panel (d) shows an optical micrograph of GNRs transferred onto a ROS, with a scale bar of 180 µm. All Raman spectra show four main modes: RBLM (width-dependent mode), CH (C-H bend-ing mode at the edges), D (breathing mode of the sp^2 lattice) and G (stretching of C-C bonds within the sp^2 lattice)

While STM is a powerful technique to characterize the atomic structure of GNRs, to determine their surface coverage and local alignment on metallic growth substrates, it cannot be applied after transfer to insulating device substrates, which are normally based on SiO_2/Si. To follow the structural quality and alignment of GNRs on the growth substrate and upon substrate transfer,

we thus carry out a detailed Raman spectroscopy investigation. Raman spectroscopy is a powerful technique for characterizing sp^2-hybridized carbon materials by identifying their Raman-active phonons[45–47]. The vibrational fingerprints of GNRs are named in analogy to the terminology of Raman-active phonons in other sp^2-hybridized carbon nanomaterials such as graphite[45], graphene[48], and CNTs[46]. The most prominent active mode in the high-frequency range of GNRs is the G mode at ~1600 cm^{-1}, which corresponds to the stretching of carbon-carbon bonds within the sp^2 lattice of the ribbon[37,49,50]. Besides the G mode, in the high-frequency region, the D and CH modes are observed[37,49,51] between 1100 and 1400 cm^{-1}, which are fingerprints of the GNRs' confinement-derived vibration modes and their hydrogen-passivated edges, respectively. At low frequency, the radial-breathing-like mode (RBLM) is observed, which is related to the ribbon width[37,38,50,51].

Here, Raman characterization of the high- and low-coverage samples is carried out in a home-built vacuum chamber (~10^{-2} mbar) to prevent photochemical reactions during the measurements[29,36]. Additionally, an optimal mapping approach (maps of 10 µm x 10 µm) is adopted to obtain the average characteristics of 9-AGNRs with a high signal-to-noise ratio[36]. Figures. 1a and 1c show the Raman profiles for both high- and low-coverage 9-AGNR samples acquired with a 785 nm wavelength (1.58 eV) laser on Au(788), with the red spectrum taken with light polarized parallel to the nominal GNR alignment direction (along the Au(788) step edges) and blue for perpendicular to it, respectively. The spectra reveal the main 9-AGNR Raman active modes, namely the RBLM, CH, D, and G modes with frequencies of 312, ~1235, 1337, and 1596 cm^{-1}, respectively. Interestingly, the CH mode frequency for the high-coverage samples (shown in Figs. 1a and 1c) is observed to be slightly higher than that for the low-coverage samples (1240 vs 1235 cm^{-1}). Another difference is the mode at ~1285 cm^{-1} only resolved for the high-coverage case. These differences could indicate that at higher coverage, the nearby GNRs are more likely to be in closer proximity, possibly forming contacts or bundles, leading to higher inter-ribbon interactions and the emergence of new modes due to such interactions. Further studies will be conducted to examine this phenomenon in more detail.

To explore and exploit GNRs' electronic properties in a device configuration, a substrate transfer step is required to transfer the GNRs from the catalytic growth surface to the target device substrate. For transferring aligned GNRs, an electrochemical delamination method is used[29,36], which was primarily developed to transfer graphene layers grown by chemical vapor deposition[52,53], (see methods for a detailed description). This transfer method is based on the formation of hydrogen bubbles from water electrolysis at the GNR/Au(788) interface and the use of a poly(methyl methacrylate) (PMMA) layer as polymer support upon GNR delamination. As previously demonstrated, GNRs are extremely sensitive to the electrochemical delamination transfer parameters, such as delamination time, applied current, and PMMA thickness[36]. Raman spectroscopy has previously been proven to be the method of choice to assess the quality of GNRs and monitor changes upon transfer by detecting the Raman shift, relative intensities, and peak widths of the vibrational fingerprints [37,36].

Here, we transfer both high- and low-coverage 9-AGNR samples onto Raman-optimized substrates (ROS), consisting of a Si/SiO_2 (285nm) substrate with 80 nm Au layer and a 40 nm

Al_2O_3 top layer. ROS allows for signal enhancement factors of up to 120 times in comparison with standard SiO_2/Si[36]. Figures. 1b and 1d show the Raman profiles for both high- and low-coverage 9-AGNR samples transferred to ROS, respectively. While both samples show the presence of all Raman active modes as measured on the Au(788) growth substrate, significant differences between the high- and low-coverage samples are observed after substrate transfer. To follow the GNRs' structural quality, we first extract the full width at half maximum (FWHM) of the RBLM, D, CH, and G peaks. The average Raman profile of the high-coverage sample shows similar FWHMs before and after the substrate transfer (~14 cm^{-1} for RBLM, ~24 cm^{-1} for CH, ~18 cm^{-1} for D, and ~12 cm^{-1} for G mode). On the other hand, the low-coverage sample shows significant broadening upon transfer for RBLM (from ~12 to 19 cm^{-1}), CH (from ~20 to 40 cm^{-1}), D (from ~11 to 25 cm^{-1}), and G modes (from ~10 to 18 cm^{-1}), accompanied by an overall decrease in the signal-to-noise ratio, indicating that the GNRs' overall quality and quantity are not entirely preserved. This behavior suggests that 9-AGNRs growing along the Au(788) step edges have a stronger physical interaction with the gold substrate, and are less likely to transfer efficiently and without defects. As for the Raman shifts, both samples show similar frequencies before and after transfer for the RBLM, D and G modes. For the high coverage sample, we observe a more significant shift of the CH mode, from 1243 cm^{-1} to 1239 cm^{-1}, before and after transfer, respectively. This could be related to inter-ribbon interactions and/or the interaction of GNR "bundles" with the substrate.

Besides monitoring the GNRs' structural quality, Raman spectroscopy is also a powerful technique to characterize their orientation due to GNR's anisotropy. Raman polarization anisotropy (P) is the most used parameter for assessing GNR's average orientation. We extract P for all Raman active modes as a function of coverage before and after substrate transfer. Figure 1 shows $I_{\parallel}$ (red spectra) and $I_{\perp}$ (blue spectra), which represent Raman spectra for incoming and scattered light polarized parallel and perpendicular to the GNRs' nominal alignment direction (the Au(788) step direction), respectively, for both high- and low-coverage 9-AGNR samples on the growth surface (Figs. 1a and 1c, respectively) and on the ROS (Figs. 1b and 1d, respectively). The high-coverage sample shows an anisotropy of P = 0.86 on the Au(788) substrate, which only slightly decreases to P = 0.85 after substrate transfer, indicating that the degree of GNR alignment is largely preserved. Similar preservation of GNR alignment upon substrate transfer was reported previously for high-coverage 7-AGNRs and 9-AGNRs[29,27]. On the other hand, the low-coverage sample shows very different behavior, with polarization anisotropy decreasing significantly from P = 0.95 on Au (788) to P = 0.58 upon substrate transfer.

The preservation of the overall degree of alignment is thus clearly coverage-dependent. In a high-coverage sample, the 9-AGNR layer seems to behave very much like a film, with very low GNR mobility during substrate transfer, which preserves the overall degree of GNR alignment. This film-like behavior is absent in the low-coverage 9-AGNR samples, where only individual GNRs grow along the Au(788) step edges. In addition, GNRs growing solely along the step edge appear to show a stronger interaction with the substrate (due to a higher site reactivity caused by the enhanced negative charge density of the Au atoms at the lower step edges compared to the terraces), contributing to a less efficient transfer. Although the polarization anisotropy

provides clear information on the overall degree of GNR alignment, it does not include detailed information on the angular distribution nor the isotropic contributions of small polyaromatic hydrocarbons (PAHs), short GNRs, or PMMA residues to the overall Raman intensity. To address that, we model the GNRs' angular distribution as a Gaussian distribution and quantify the isotropic contribution to the Raman intensity by taking into account a polarization angle-independent intensity in addition to the usual polarization-dependent intensity distribution resulting from the aligned GNRs.

Raman profiles are obtained by polarizing the incoming and scattered light in parallel ("VV configuration") with different angles between the nominal GNR alignment direction and the polarization of the incident light. Using the VV configuration implies that for the Raman resonant modes, the intensity of the GNR modes is projected to be $cos^4(\vartheta)$ polarization-dependent, which results from a product of two $cos^2(\vartheta)$ factors, one for photon absorption and the other for photon emission, Eq. (1)[54–59]. This means that the Raman signal is maximum with the incident polarization parallel to the ribbon axis (0°, 180°) and zero when perpendicular to it (90°, 270°) (Fig. 2). In Eq. (1), ϑ_0 is the orientation of the long axis of the GNR with respect to an arbitrary in-plane axis, and ϑ is the direction of the light polarization. Due to the significant absorption anisotropy of the quasi-1D GNRs, all Raman modes exhibit roughly the same polarization dependency.

$$I_{Raman}^{pol}(\vartheta) \approx cos^4(\vartheta - \vartheta_0) \tag{1}$$

To model the polarized Raman intensity as a function of polarization direction for samples with many GNRs that are not perfectly aligned, we assume that the GNRs are on average aligned along the direction ϑ_0, with a normalized Gaussian distribution of angles ϑ [29,57], $G(\vartheta)$ as in Eq. (2), where σ is the standard deviation that is related to the FWHM=$2\sigma\sqrt{2\ln 2}$.

$$G(\vartheta) = \frac{1}{\sigma\sqrt{2\pi}} e^{-\frac{(\vartheta-\vartheta_0)^2}{2\sigma^2}} \tag{2}$$

In addition to the GNRs aligned according to $G(\vartheta)$, we assume that small PAHs, short GNRs, or polymer residues from the substrate transfer step give rise to an isotropic Raman intensity contribution that does not depend on the polarization direction. Such polarization-independent Raman intensity contributions have been observed in the case of CNTs, owing to the presence of amorphous carbon and/or carbon nanocomposites[54,57,59,60]. To account for such contributions in the Raman and optical absorption intensities in the single-walled carbon nanotubes (SWCNTs) samples, an angle-independent component was introduced to the fit function[57]. Here, we use a similar strategy to account for the isotropic contribution of such Raman polarization-independent intensity (i.e. intensity that does not depend on ϑ) by adding a constant H (Eq. (3)).

$$H(\vartheta) = H \tag{3}$$

The total angular distribution function $D(\vartheta)$ of species contributing to the Raman intensity (GNRs, PAHs, PMMA residues.) is then defined in Eq. (4) as the sum of $G(\vartheta)$ weighted with the

fraction of the surface area *A* exhibiting aligned GNRs and of *H(ϑ)* weighted with the fraction of the surface area *B* producing the isotropic contribution.

$$D(\vartheta) = A \cdot G(\vartheta) + B \cdot H \tag{4}$$

For *A* and *B* to be meaningful fit parameters, it is necessary to properly normalize the constant *H* and the Gaussian distribution *G(ϑ)*. The Gaussian distribution *G(ϑ)* is normalized to 1 (integral from 0° to 360° is 1), thus we normalize *H(ϑ)* correspondingly to an integral from 0° to 360° of 1, implying *H= 1/360*. Eq. (5) gives the resulting normalized angular distribution function *D(ϑ)*, including the homogeneous background.

$$D(\vartheta) = \frac{A}{\sigma\sqrt{2\pi}} e^{-\frac{(\vartheta-\vartheta_0)^2}{2\sigma^2}} + \frac{B}{360} \tag{5}$$

The expected Raman signal $I_{exp}(\vartheta)$ is obtained from the convolution of $I_{Raman}^{pol}(\vartheta)$ and *D(ϑ):*

$$I_{exp}(\vartheta) = \int_{0°}^{360°} I_{Raman}^{pol}(\varphi) \cdot D(\vartheta - \varphi) d\varphi \tag{6}$$

$$= \int_{0°}^{360°} cos^4(\varphi) \cdot \left(\frac{A}{\sigma\sqrt{2\pi}} e^{-\frac{(\vartheta-\varphi-\vartheta_0)^2}{2\sigma^2}} + \frac{B}{360} \right) d\varphi \tag{7}$$

$$= A \cdot \int_{0°}^{360°} cos^4(\varphi) \cdot \frac{1}{\sigma\sqrt{2\pi}} e^{-\frac{(\vartheta-\varphi-\vartheta_0)^2}{2\sigma^2}} d\varphi + \frac{B}{360} \cdot \int_{0°}^{360°} cos^4(\varphi)\ d\varphi \tag{8}$$

The first integral in Eq. (8) is simply the convolution of $cos^4(\vartheta)$with a normalized Gaussian distribution, whereas the second integral is a constant that equals $3 \cdot 180°/4$, in degrees.

From that, we obtain:

$$\begin{aligned} I_{exp}(\vartheta) &= A \cdot \int_{0°}^{360°} cos^4(\varphi) \cdot \frac{1}{\sigma\sqrt{2\pi}} e^{-\frac{(\vartheta-\varphi-\vartheta_0)^2}{2\sigma^2}} d\varphi + \frac{B}{360} \cdot \frac{3 \cdot 180}{4} \\ &= A \cdot \int_{0°}^{360°} cos^4(\varphi) \cdot \frac{1}{\sigma\sqrt{2\pi}} e^{-\frac{(\vartheta-\varphi-\vartheta_0)^2}{2\sigma^2}} d\varphi + B \cdot \frac{3}{8} \end{aligned} \tag{9}$$

In Fig. 2, we illustrate the main contributions to the expected Raman intensity: The $cos^4(\vartheta)$ polarization-dependent Raman intensity (in red) and the angular distribution function *D(ϑ)* (in blue) which includes aligned GNRs with an angle distribution *G(ϑ)* and the isotropic contribution (polarization-independent component) to account for the homogeneous background.

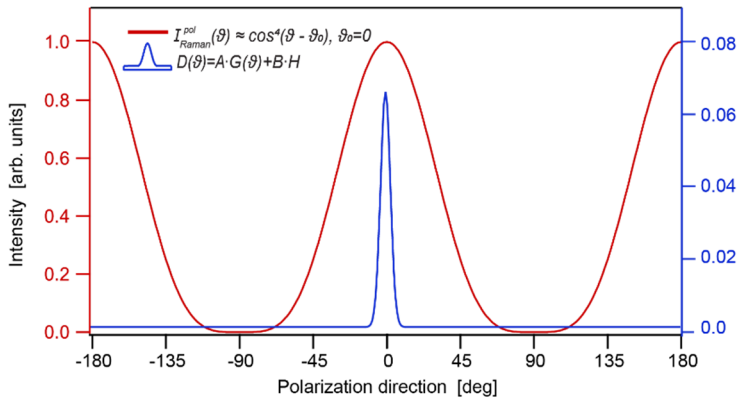

Figure 2: Illustration of the major contributions to the expected polarized Raman intensity as described in Eq. (9). The Raman intensity of a single GNR follows $cos^4(\vartheta)$ dependence (red). In blue, the angular distribution function $D(\vartheta)$ is shown, which includes the normalized Gaussian distribution of angle and the normalized isotropic contribution. For this particular plot, σ=3°, A= 0.5, and B=0.5 have been used.

By using Eq. (9) for the fitting of angle-dependent polarized Raman intensity data, it is possible to extract the following relevant information: ϑ_0, the azimuthal angle along which GNRs are preferentially aligned (the center of the Gaussian distribution); the fraction A of surface area exhibiting aligned GNRs; σ, the width of the Gaussian distribution characterizing the angular distribution around ϑ_0 (here defined as the quality of alignment); and the fraction B of the surface area contributing to the isotropic, polarization-independent Raman signal. From A and B, we can define the "overall disorder" present on the surface (*OD*) as follows (Eq. (10)):

$$OD = \frac{B}{(B + A)} \cdot 100\% \tag{10}$$

To illustrate the effect of increasing *OD* for specific values of σ (and vice versa) on the Raman intensity, we plot the Raman intensity versus polarization angle for varying σ from 1° to 30° and *OD* from 0% up to 30%, as shown in Fig. S2. When keeping σ constant and increasing *OD* from 0% to 30%, we observe an increase in baseline with a higher vertical offset of Raman intensity for larger values of *OD*. The increase in the baseline is a direct indication of the increased disorder present on the surface. On the other hand, when we increase the width of σ from 1° to 30° while keeping *OD* constant, we observe a significant decrease in Raman intensity along with significant broadening – a direct measure of how well the GNRs are aligned and their angle distribution within the sample. Furthermore, we discuss the impact of both σ and *OD* on the *P* in the supplementary information (Fig. S3). We observe that *P* is significantly affected by *OD*, with an almost linear decrease as *OD* increases, whereas for σ, *P* is only significantly affected for σ > 15°. This indicates that *P* is a reasonably good indicator of the combined impact of σ and *OD* for larger values of σ, but rather insensitive to width differences for narrow (σ < 15°) angle distributions.

To investigate the influence of GNR coverage and substrate transfer on σ and *OD*, we fit all Raman active modes of high- and low-coverage 9-AGNR samples on both the growth and ROS using Eq. (9). Figure. 3 shows the G mode peak intensity as a function of the polarization angle ϑ for the VV configuration and the related polar diagrams for both high- (Figs. 3a and 3b) and

low-coverage samples (Figs. 3c and 3d) on Au(788) (in blue) and after substrate transfer (in red), respectively (see Figs. S4 and S5 for similar plots for CH, D, and RBLM modes). The intensity of the G mode as a function of polarization angle (-90° to +90°) is determined from Raman maps of 10 x 10 pixels in vacuum conditions using a 785 nm laser energy. We fit the polar dependence of the Raman intensity using Eq. (9).

It is important to note that the G peak of GNRs is composed of two in-plane optical modes: a transverse-optical (TO) and a longitudinal-optical (LO) mode[2,37,49]. The longitudinal optical (LO) (G1 peak, phonon mode with A_g symmetry) generates an atomic displacement parallel to the GNR axis and has a maximum intensity along the GNR, whereas the transverse optical (TO) (G2 peak, phonon mode with B_{1g} symmetry) has a maximum intensity perpendicular to the GNR axis. Here, all the measurements are done using a 785 nm laser energy, and in our spectra, we only resolve the LO (G1) mode, which for simplicity we call G mode.

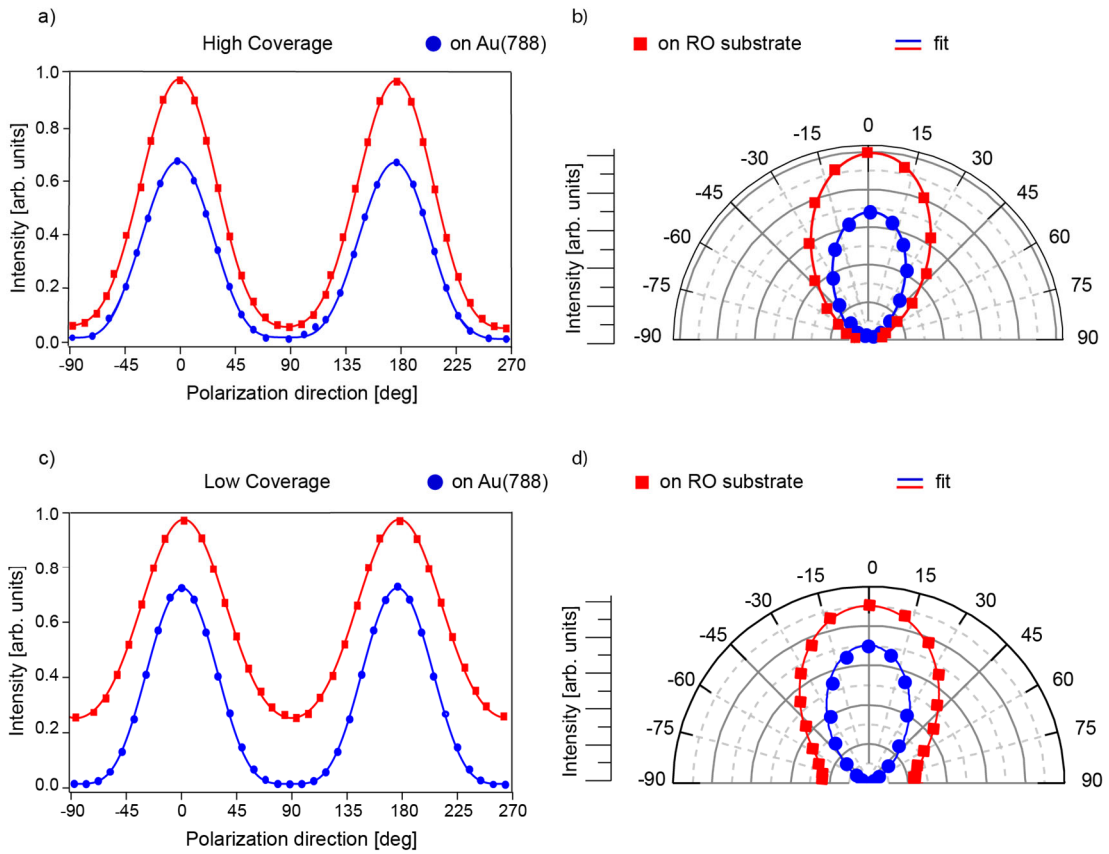

Figure 3: Polarized Raman intensity of G mode (785 nm, VV configuration). (a, c) G mode intensity as a function of polarization angle ϑ for high- and low-coverage samples on Au(788) (blue circles) and after substrate transfer onto ROS (red squares). Blue and red solid lines represent data fits using Eq. (9). (b, d) Polar diagrams showing G mode intensities for high- and low-coverage samples on Au(788) (blue circles) and after transfer to ROS (red squares). Blue and red solid lines represent fits to the measured data using Eq. (9).

Table shows the relevant fitting results for the G mode data: the quality of alignment (σ), and the overall disorder on the surface (*OD*) for both high- and low-coverage samples on Au(788) and on the ROS extracted from Fig. 3. For comparison, we also show the values of Raman

polarization anisotropy for all cases; see Table S1 and Table S2 for *P*, *σ*, and *OD* values for RBLM, CH, and D modes for both high- and low-coverage samples on Au(788) and the ROS.

	High-coverage sample		Low-coverage sample	
	Au(788)	ROS	Au(788)	ROS
Quality of alignment (*σ*) [°]	3 ± 1	13±1	1.0± 0.1	22± 3
Overall disorder on the surface (*OD*) [%]	8± 1	13±1	8± 3	39± 3
Raman polarization anisotropy *(P)*	0.86	0.85	0.95	0.58

Table 1: Comparison of high- and low-coverage samples (*σ*, *OD*, and *P*) on Au(788) and after substrate transfer onto ROS.

A small value of *σ* means a narrow-angle distribution and, thus, a high degree/ quality of uniaxial alignment. We observe that *σ* increases upon substrate transfer from 3° to 13° for the high-coverage sample and from 1° to 22° for the low-coverage one, indicating poorer quality of alignment after the transfer, especially for the low-coverage sample. This behavior can be attributed to two main factors: the strong interaction of GNRs with the Au(788) step edges, making it less likely for the GNRs to transfer efficiently, and the increased GNR mobility (especially for the low surface coverage), which increases the angle distribution within GNRs upon transfer. In addition, when comparing *σ* for both coverages of 9-AGNRs on Au(788), we observe slightly lower *σ* values for the low-coverage sample, indicating a better quality of alignment for 9-AGNRs grown only on the step edges of the Au(788). This is also reflected in the polarization anisotropy measurements, with *P* = 0.95 for the low-coverage 9-AGNR sample and *P* = 0.85 for the high-coverage one on Au(788), indicating the higher degree of alignment of 9-AGNRs grown along the step-edge compared to the complete monolayer (see Fig. S6 for a STM image of a 9-AGNR high-coverage sample highlighting the presence of smaller GNRs growing perpendicular to the terraces in some areas).

From Table 1, it can also be seen that substrate transfer increases the *OD* fraction from 8 to 13% and from 8 to 39% for high- and low-coverage samples, respectively. The significant increase for the low-coverage samples is explained by GNRs' strong interaction with the Au(788) step edges which makes the low-coverage samples much higher susceptibility to inefficient transfer, leading to a higher prevalence of partially broken GNRs. In addition, the low-coverage sample leaves considerably more exposed gold substrate to PMMA and other impurities that might react with the Au surface and transfer along with the GNRs, increasing the *OD* on the transferred surface.

On the Au(788) growth substrate we observe a similar *OD* for both high- and low-coverage samples (8%). The disorder observed on the growth substrate may originate from short (and thus non-aligned) GNRs, irregularly fused precursor monomers, or also the presence of impurities from the precursor monomer.

Conclusions

In this study, we employed polarized Raman spectroscopy and scanning tunneling microscopy to characterize and quantify the structural quality and degree of alignment 9-AGNRs in samples

with different surface coverages on both their growth substrate and after substrate transfer. using an extended data angular model, which describes GNR alignment by a Gaussian distribution of angles, allowed us to extract both the quality of alignment (σ) and the overall surface disorder (*OD*).

Our results show that low-coverage samples exhibit better uniaxial alignment than high-coverage samples on the growth substrate. This behavior results from GNRs in low-coverage samples growing preferentially along the step-edges of Au(788), as observed in our STM investigations. However, upon transfer, the quality of alignment of low-coverage samples is significantly reduced, which we attribute mostly to the strong interaction of GNRs with the Au(788) step edges as well as increased GNR mobility, whereas high-coverage samples show better alignment preservation upon substrate transfer, owing to the densely packed GNR film facilitating the transfer process. With the extended model developed in this study, we also quantified the *OD*, which results in an isotropic (polarization-independent) contribution to the Raman intensity. After substrate transfer, low-coverage samples show systematically higher *OD* values than high-coverage samples (39% vs 13% respectively). The significantly higher *OD* for low-coverage samples is associated with the strong interaction of GNRs to the Au(788) step edges, making it less likely for the GNRs to transfer efficiently, as well as to the fact that more gold surface area is exposed to PMMA and other impurities that may react with the metal and transfer along with the GNRs to the target substrate. Based on these findings, strategies to improve GNR alignment and quality are needed. One approach could be the passivation of Au(788) step edges with other materials, such as wide bandgap polymers. The presence of a polymer at the step edges could simultaneously decrease the strong interaction between GNR-Au and act as a scaffold, mitigating GNR's lateral diffusion and preserving GNR alignment throughout the substrate transfer process.

Overall, our results shed light on the crucial role of surface coverage in determining the degree of alignment and the *OD* present on the surface on both the Au(788) growth surface and, in particular, after substrate transfer. Our extended model provided a quantitative description of GNR alignment and quality, which is a pivotal step toward the development of integrated GNR-based nanoelectronic devices and establishes polarized Raman as the method of choice for tracking GNR quality and degree of alignment during transfer and device fabrication steps.

Methods

On-surface synthesis and STM characterization of 9-AGNRs

The Au(788) single crystal growth substrate (MaTecK GmbH, Germany) was cleaned in ultra-high vacuum (UHV) with two cycles of sputtering at1 kV Ar^+ for 10 minutes and annealing at 420 °C for 10 minutes. The 9-AGNR precursor monomer 3′,6′-di-iodine-1,1′:2′,1′′-terphenyl (DITP) was then sublimated onto the clean Au surface from a quartz crucible heated to 70 °C while the substrate remained at room temperature[34]. A quartz microbalance was used to control the deposition rate of the precursor molecules at 1 Å /min. The deposition rate is not calibrated to

accurately correspond to the true surface coverage. Instead, it is calibrated relative to a standard measurement obtained through STM. High- and low-coverage samples were obtained by DITP deposition for 8 and 3 minutes, respectively. Following deposition, the substrate was heated to 200 °C (0.5 K/s) for 10 minutes to initiate DITIP polymerization, followed by annealing at 400 °C (0.5 K/s) for 10 minutes to form the GNRs by cyclodehydrogenation [5,2,4,34].

Scanning tunneling microscopy images of 9-AGNRs grown on Au(788) were acquired at room temperature using a Scienta Omicron VT-STM. Topographic images were acquired in constant current mode using a sample bias of -1.5 V and a setpoint current of 0.03 nA.

Substrate transfer of GNRs

Transfer of 9-AGNRs from their Au(788) growth substrate to the Raman-optimized substrates (ROS) was done by electrochemical delamination transfer[29,36]. First, a support layer of poly(methyl methacrylate) (PMMA) was spin-coated (4 PMMA layers, 2500 rpm for 90 s) on the 9-AGNR/Au(788) samples, followed by a 10-minute curing process at 80 °C. To shorten the time required for PMMA delamination, PMMA was removed from the Au(788) crystal's edges using a two-step process: a 80-minute UV exposure (leading to the breakdown of the chemical bonds in the PMMA), followed by a 3-minute development in water/isopropanol (to remove the PMMA from the surface's edges). Electrochemical delamination was performed in an aqueous solution of NaOH (1 M) as the electrolyte. A DC voltage of 5V (current ~0.2 A) was applied between the PMMA/9-AGNR/Au(788) cathode and a glassy carbon electrode used as the anode. At the interface between PMMA/GNRs and Au, hydrogen bubbles form, resulting from the water reduction: $2H_2O(l) + 2e^- \rightarrow H_2(g) + 2OH^-(aq)$. The H_2 bubbles mechanically delaminate the PMMA/GNR layer from the Au(788) surface. The delaminated PMMA/GNR layer was left in ultra-pure water for 5 minutes before being transferred to the target substrate. To increase the adhesion between the target substrate and the PMMA/GNR layer, the sample was annealed for 10 minutes at 80°C and then 20 minutes at 110°C. Finally, the PMMA was dissolved in acetone for 15 minutes, and the resulting GNR/ROS was washed with ethanol and ultrapure water.

Raman spectroscopy

Raman spectroscopy measurements were obtained using a WITec confocal Raman microscope (WITec Alpha 300R) with a laser line of 785 nm (1.5 eV) and a power of 40 mW. A 50× microscope objective (0.55 numerical aperture) with a working distance of 9.1 mm (resulting laser spot size of 600 nm) was used to focus the laser beam onto the sample and collect the scattered light. Calibration of Raman spectra was performed using the Si peak at 520.5 cm^{-1}. Also, the laser wavelength, power, and integration time factors were optimized for each substrate to maximize signal while minimizing sample damage. Furthermore, to avoid sample damage, a Raman mapping approach with 10× 10 pixels (10× 10 µm) was used and samples were measured in a home-built vacuum suitcase with pressure ~10^{-2} mbar. The vacuum chamber was mounted on a piezo stage for scanning.

The "VV" configuration was used for polarized Raman measurements, with the polarizer oriented parallel to the polarization of the incident light. A motorized half-wave plate was used to change the polarization direction of the incident laser beam from -90° to +90° in steps of 10°. To control the scattered light direction and keep it parallel in the detection path a manual analyzing polarizer and a λ/2 plate were inserted before the detector. For measurements with 785 nm excitation wavelength, the scattered signal was detected with an analyzing polarizer coupled with a 300 mm lens-based spectrometer with a grating of 300 g mm^{-1} (grooves/mm) and equipped with a cooled deep-depletion CCD.

Raman data processing

Using the WITec software, a cosmic ray filter was applied to all raw maps for removing signatures of photoluminescence. Afterward, the Raman maps were averaged and polynomial background subtraction was applied, followed by batched fitting with a Lorentzian function for all polarization angles between -90° to 90° for each Raman mode. The fitting using Eq. (9) was done in IGOR Pro software (Wavemetrics Inc.), and the fitting parameters were obtained through the lowest stable Chi-square values.

References

1. Yang, L., Park, C.-H., Son, Y.-W., Cohen, M. L. & Louie, S. G. Quasiparticle Energies and Band Gaps in Graphene Nanoribbons. *Phys. Rev. Lett.* **99**, (2007).
2. Talirz, L. *et al.* On-Surface Synthesis and Characterization of 9-Atom Wide Armchair Graphene Nanoribbons. *ACS Nano* **11**, 1380–1388 (2017).
3. Kimouche, A. *et al.* Ultra-narrow metallic armchair graphene nanoribbons. *Nat. Commun.* **6**, 10177 (2015).
4. Talirz, L., Ruffieux, P. & Fasel, R. On-Surface Synthesis of Atomically Precise Graphene Nanoribbons. *Adv Mater* **28**, 6222–6231 (2016).
5. Cai, J. *et al.* Atomically precise bottom-up fabrication of graphene nanoribbons. *Nature* **466**, 470–473 (2010).
6. Gröning, O. *et al.* Engineering of robust topological quantum phases in graphene nanoribbons. *Nature* **560**, 209–213 (2018).
7. Rizzo, D. J. *et al.* Topological band engineering of graphene nanoribbons. *Nature* **560**, 204–208 (2018).
8. Sun, Q. *et al.* Massive Dirac Fermion Behavior in a Low Bandgap Graphene Nanoribbon Near a Topological Phase Boundary. *Adv. Mater.* **32**, 1906054 (2020).
9. Cao, T., Zhao, F. & Louie, S. G. Topological Phases in Graphene Nanoribbons: Junction States, Spin Centers, and Quantum Spin Chains. *Phys. Rev. Lett.* **119**, 076401 (2017).
10. Ruffieux, P. *et al.* On-surface synthesis of graphene nanoribbons with zigzag edge topology. *Nature* **531**, 489–492 (2016).

11. Llinas, J. P. *et al.* Short-channel field-effect transistors with 9-atom and 13-atom wide graphene nanoribbons. *Nat. Commun.* **8**, 633 (2017).

12. El Abbassi, M. *et al.* Controlled Quantum Dot Formation in Atomically Engineered Graphene Nanoribbon Field-Effect Transistors. *ACS Nano* **14**, 5754–5762 (2020).

13. Braun, O. *et al.* Optimized graphene electrodes for contacting graphene nanoribbons. *Carbon* **184**, 331–339 (2021).

14. Bennett, P. B. *et al.* Bottom-up graphene nanoribbon field-effect transistors. *Appl. Phys. Lett.* **103**, 253114 (2013).

15. Ohtomo, M., Sekine, Y., Hibino, H. & Yamamoto, H. Graphene nanoribbon field-effect transistors fabricated by etchant-free transfer from Au(788). *Appl. Phys. Lett.* **112**, 021602 (2018).

16. Passi, V. *et al.* Field-Effect Transistors Based on Networks of Highly Aligned, Chemically Synthesized *N* = 7 Armchair Graphene Nanoribbons. *ACS Appl. Mater. Interfaces* **10**, 9900–9903 (2018).

17. Chen, Z., Narita, A. & Müllen, K. Graphene Nanoribbons: On-Surface Synthesis and Integration into Electronic Devices. *Adv. Mater.* **32**, 2001893 (2020).

18. Mutlu, Z. *et al.* Short-Channel Double-Gate FETs with Atomically Precise Graphene Nanoribbons. in *2021 IEEE International Electron Devices Meeting (IEDM)* 37.4.1-37.4.4 (2021). doi:10.1109/IEDM19574.2021.9720620.

19. Wang, H. *et al.* Graphene nanoribbons for quantum electronics. *Nat. Rev. Phys.* **3**, 791–802 (2021).

20. Lin, Y. C. *et al.* Scaling and statistics of bottom-up synthesized armchair graphene nanoribbon transistors. *Carbon* **205**, 519–526 (2023).

21. Zhang, J. *et al.* Tunable Quantum Dots from Atomically Precise Graphene Nanoribbons Using a Multi-Gate Architecture. *Adv. Electron. Mater.* **9**, 2201204 (2023).

22. Zhang, J. *et al.* Ultimately-scaled electrodes for contacting individual atomically-precise graphene nanoribbons. Preprint at https://doi.org/10.48550/arXiv.2209.04353 (2022).

23. Niu, W. *et al.* Exceptionally clean single-electron transistors from solutions of molecular graphene nanoribbons. *Nat. Mater.* **22**, 180–185 (2023).

24. Slota, M. *et al.* Magnetic edge states and coherent manipulation of graphene nanoribbons. *Nature* **557**, 691–695 (2018).

25. Blackwell, R. E. *et al.* Spin splitting of dopant edge state in magnetic zigzag graphene nanoribbons. *Nature* **600**, 647–652 (2021).

26. Kan, E., Li, Z., Yang, J. & Hou, J. G. Half-Metallicity in Edge-Modified Zigzag Graphene Nanoribbons. *J. Am. Chem. Soc.* **130**, 4224–4225 (2008).

27. Zhao, S. *et al.* Optical Imaging and Spectroscopy of Atomically Precise Armchair Graphene Nanoribbons. *Nano Lett.* **20**, 1124–1130 (2020).

28. Zhao, S. *et al.* Optical Investigation of On-Surface Synthesized Armchair Graphene Nanoribbons. *Phys. Status Solidi B* **254**, 1700223 (2017).

29. Senkovskiy, B. V. *et al.* Making Graphene Nanoribbons Photoluminescent. *Nano Lett.* **17**, 4029–4037 (2017).

30. Denk, R. *et al.* Exciton-dominated optical response of ultra-narrow graphene nanoribbons. *Nat. Commun.* **5**, 4253 (2014).

31. Cocchi, C. *et al.* Optical Excitations and Field Enhancement in Short Graphene Nanoribbons. *J. Phys. Chem. Lett.* **3**, 924–929 (2012).

32. Chen, Y.-C. *et al.* Tuning the Band Gap of Graphene Nanoribbons Synthesized from Molecular Precursors. *ACS Nano* **7**, 6123–6128 (2013).

33. Linden, S. *et al.* Electronic Structure of Spatially Aligned Graphene Nanoribbons on Au(788). *Phys. Rev. Lett.* **108**, 216801 (2012).

34. Di Giovannantonio, M. *et al.* On-Surface Growth Dynamics of Graphene Nanoribbons: The Role of Halogen Functionalization. *ACS Nano* **12**, 74–81 (2018).

35. Shinde, P. P. *et al.* Graphene nanoribbons with mixed cove-cape-zigzag edge structure. *Carbon* **175**, 50–59 (2021).

36. Overbeck, J. *et al.* Optimized Substrates and Measurement Approaches for Raman Spectroscopy of Graphene Nanoribbons. *Phys. Status Solidi B* **256**, 1900343 (2019).

37. Borin Barin, G. *et al.* Surface-Synthesized Graphene Nanoribbons for Room Temperature Switching Devices: Substrate Transfer and ex Situ Characterization. *ACS Appl. Nano Mater.* **2**, 2184–2192 (2019).

38. Overbeck, J. *et al.* A Universal Length-Dependent Vibrational Mode in Graphene Nanoribbons. *ACS Nano* **13**, 13083–13091 (2019).

39. Verzhbitskiy, I. A. *et al.* Raman Fingerprints of Atomically Precise Graphene Nanoribbons. *Nano Lett.* **16**, 3442–3447 (2016).

40. Borin Barin, G. *et al.* Growth Optimization and Device Integration of Narrow-Bandgap Graphene Nanoribbons. *Small* 2202301 (2022) doi:10.1002/smll.202202301.

41. Jorio, A., Saito, R., Dresselhaus, G. & Dresselhaus, M. S. *Raman Spectroscopy in Graphene Related Systems*. (Wiley-VCH Verlag GmbH & Co. KGaA, 2011).

42. Léonard, F. Crosstalk between nanotube devices: contact and channel effects. *Nanotechnology* **17**, 2381 (2006).

43. Classen, T. *et al.* Templated Growth of Metal-Organic Coordination Chains at Surfaces. *Angew. Chem. Int. Ed.* **44**, 6142–6145 (2005).

44. Cañas-Ventura, M. E. *et al.* Self-Assembly of Periodic Bicomponent Wires and Ribbons. *Angew. Chem. Int. Ed.* **46**, 1814–1818 (2007).

45. Tuinstra, F. Raman Spectrum of Graphite. *J. Chem. Phys.* **53**, 1126 (1970).

46. Dresselhaus, M. S., Jorio, A., Hofmann, M., Dresselhaus, G. & Saito, R. Perspectives on Carbon Nanotubes and Graphene Raman Spectroscopy. *Nano Lett.* **10**, 751–758 (2010).

47. Maghsoumi, A., Brambilla, L., Castiglioni, C., Müllen, K. & Tommasini, M. Overtone and combination features of G and D peaks in resonance Raman spectroscopy of the C78H26 polycyclic aromatic hydrocarbon. *J. Raman Spectrosc.* **46**, 757–764 (2015).

48. Tommasini, M., Castiglioni, C. & Zerbi, G. Raman scattering of molecular graphenes. *Phys. Chem. Chem. Phys.* **11**, 10185 (2009).

49. Gillen, R., Mohr, M., Thomsen, C. & Maultzsch, J. Vibrational properties of graphene nanoribbons by first-principles calculations. *Phys. Rev. B* **80**, (2009).

50. Gillen, R., Mohr, M. & Maultzsch, J. Symmetry properties of vibrational modes in graphene nanoribbons. *Phys. Rev. B* **81**, (2010).

51. Liu, D., Daniels, C., Meunier, V., Every, A. G. & Tománek, D. In-plane breathing and shear modes in low-dimensional nanostructures. *Carbon* **157**, 364–370 (2020).

52. Wang, Y. *et al.* Electrochemical Delamination of CVD-Grown Graphene Film: Toward the Recyclable Use of Copper Catalyst. *ACS Nano* **5**, 9927–9933 (2011).

53. Gao, L. *et al.* Repeated growth and bubbling transfer of graphene with millimetre-size single-crystal grains using platinum. *Nat. Commun.* **3**, 699 (2012).

54. Gommans, H. H. *et al.* Fibers of aligned single-walled carbon nanotubes: Polarized Raman spectroscopy. *J. Appl. Phys.* **88**, 2509–2514 (2000).

55. Kramberger, C., Thurakitseree, T., Chiashi, S., Einarsson, E. & Maruyama, S. On the polarization-dependent Raman spectra of aligned carbon nanotubes. *Appl. Phys. A* **109**, 509–513 (2012).

56. Hwang, J. *et al.* Polarized spectroscopy of aligned single-wall carbon nanotubes. *Phys. Rev. B* **62**, R13310–R13313 (2000).

57. Ichida, M., Mizuno, S., Kataura, H., Achiba, Y. & Nakamura, A. Anisotropic optical properties of mechanically aligned single-walled carbon nanotubes in polymer. *Appl. Phys. A* **78**, 1117–1120 (2004).

58. Gupta, A. K., Russin, T. J., Gutiérrez, H. R. & Eklund, P. C. Probing Graphene Edges *via* Raman Scattering. *ACS Nano* **3**, 45–52 (2009).

59. Li, Z. *et al.* Quantitative determination of the spatial orientation of graphene by polarized Raman spectroscopy. *Carbon* **88**, 215–224 (2015).

60. Kannan, P., Eichhorn, S. J. & Young, R. J. Deformation of isolated single-wall carbon nanotubes in electrospun polymer nanofibres. *Nanotechnology* **18**, 235707 (2007).

Supporting information

STM characterization of 9-AGNRs

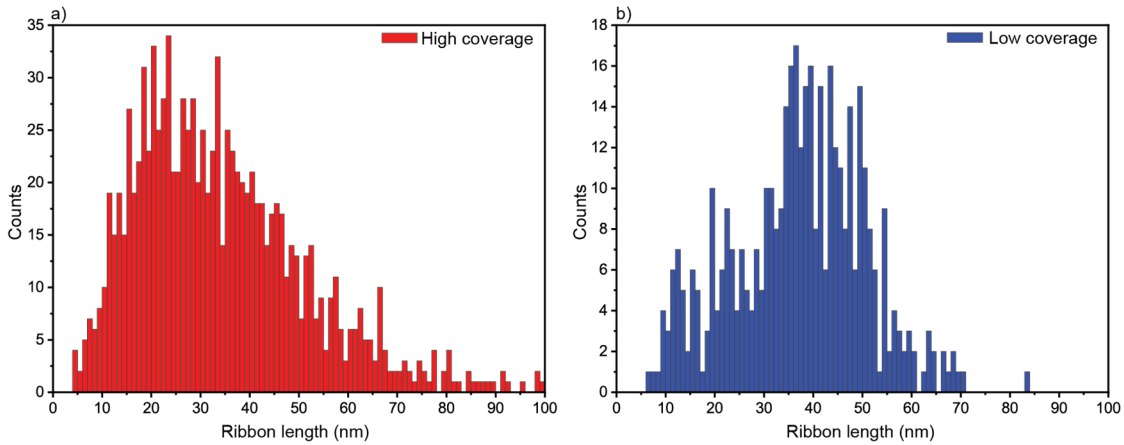

Figure S1: Length Distribution of 9-AGNRs for High- and Low-Coverage Samples on Au(788). a) Histogram of GNR lengths for the high-coverage sample, with an average length of 34 nm. The histogram is generated by analyzing 5 representative STM images, encompassing a total of 1051 GNRs. b) Histogram of GNR lengths for the low-coverage sample, with an average length of 37 nm. The histogram is generated by analyzing 15 representative STM images, totaling 416 GNRs. GNRs shorter than 4 nm and ill-defined structures are excluded from the analysis.

The influence of quality of alignment (*σ*) and overall disorder on the surface (*OD*) on polarized Raman intensity and Raman polarization anisotropy (*P*)

To understand the effect of σ (represented by the width of the GNR angle distribution) and *OD* on the Raman intensity, let's have a closer look at the meaning and impact of these parameters. Precisely speaking, σ is the standard deviation of the Gaussian angle distribution centered around the mean azimuthal direction ϑ_0 and is directly related to the $\mathrm{FWHM} = 2\sigma \times \sqrt{2 \times \mathrm{In}(2)} = 2.35\sigma$. We thus assume the GNRs to be aligned "on average" along an azimuthal direction ϑ_0, with the distribution of GNR angles described by a Gaussian distribution $G(\vartheta) = \frac{1}{\sigma\sqrt{2\pi}} e^{-\frac{(\vartheta-\vartheta_0)^2}{2\sigma^2}}$ as defined in Eq. (2). The *OD* parameter defines the ratio of the isotropic (polarization-independent) contribution (*B*) to the total Raman intensity (*A*+*B*), where *A* is the polarization-dependent Raman intensity resulting from the aligned GNRs. More precisely, if *A* and *B* are the fractional (*A*+*B*=1) surface areas giving rise to polarization-dependent and polarization-independent Raman intensities, respectively, then *OD* = *B/(A+B)* = *B*.

The degree of alignment is frequently characterized by the value of the polarization anisotropy $P = (I_{max} - I_{min})/(I_{max} + I_{min})$ determined from the Raman intensity Imax measured along the preferred angle direction ϑ_0 and Imin measured orthogonal to it, but this implies that ϑ_0 is known, which is not generally the case. Also, the determination of *P* in this way does not allow to distinguish between low polarization anisotropy due to a broad distribution of GNR angles (low degree of uniaxial alignment) or due to an important contribution of polarization-independent Raman intensity stemming from contributions other than preferentially aligned GNRs (such as polymer residues, contaminants, randomly oriented unreacted precursor molecules, etc.). Therefore, measuring the polarization dependence of the Raman intensity $I_{exp}(\vartheta)$ over a 180° range of azimuthal angles ϑ provides much more detailed information, with which both contributions discussed above can be disentangled.

Practically, the experimental data of $I_{exp}(\vartheta)$ is fitted with Eq. (9),

$$I_{exp}(\vartheta) = A \cdot \int_{0°}^{360°} cos^4(\varphi) \cdot \frac{1}{\sigma\sqrt{2\pi}} e^{-\frac{(\vartheta-\varphi-\vartheta_0)^2}{2\sigma^2}} d\varphi + B \cdot \frac{3}{8}$$

and the resulting fit parameters ϑ_0, σ and *B* (*A*=1-*B*) determine the direction of preferential GNR alignment (ϑ_0), the degree of GNR alignment (σ), and the overall degree of disorder *OD* = *B*.

To understand the impact of σ and *OD* on the polarized Raman intensity $I_{pol}(\vartheta)$, we plot in Fig. S2 the dependence of $I_{pol}(\vartheta)$ on both parameters individually. It can be seen that an increasing contribution of polarization-independent Raman intensity (as specified by *OD*) leads to a vertical offset of the $I_{pol}(\vartheta)$ curves, i.e. the minimum Raman intensity I_{min} no longer drops to zero even for polarization directions perpendicular to the GNR axis. Increasing the width of the Gaussian distribution of GNR angles, on the other hand, leads to a broadening of $I_{pol}(\vartheta)$ and a quick decrease of the maximum Raman intensity I_{max} measured along the preferential direction of

alignment, whereas the minimum intensity I_{min} measured in the perpendicular direction is significantly less affected.

The corresponding P values as a function of both σ and OD are depicted in Fig S3. Increasing OD ($OD > 0$) immediately decreases P strongly, in an almost linear fashion. P is, however, much less sensitive to the width of the Gaussian distribution (as specified by σ), at least for values smaller than 10-15° where P depends only weakly on σ. Larger σ (15-60°) then strongly decreases P. In other words, P is a reasonably good indicator of the combined impact of σ and OD, but rather insensitive to width differences of narrow ($\sigma < 15°$) angle distributions.

It is thus clear that measuring the full polarization dependence of the Raman intensity $I_{exp}(\vartheta)$ over a 180° range of azimuthal angles ϑ provides much more complete information than simply determining the polarization anisotropy $P = (I_{Max} - I_{min})/(I_{max} + I_{min})$ determined from the Raman intensities I_{Max} measured along the (generally unknown) preferred angles direction ϑ_0 and I_{min} measured orthogonal to it. In particular, fitting $I_{exp}(\vartheta)$ with Eq. (9) allows for characterizing both the angular distribution of GNRs and the disordered surface area contributions.

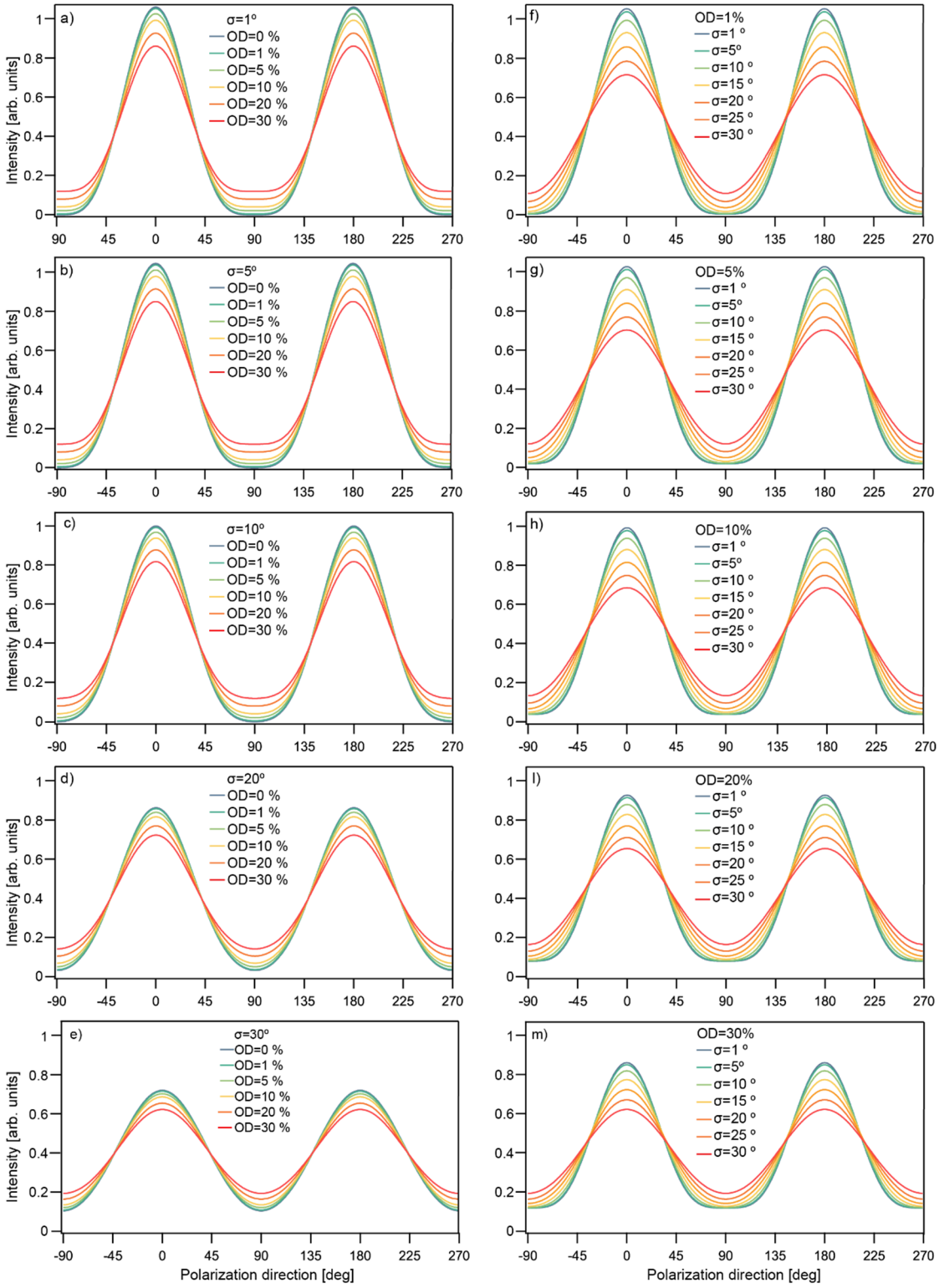

Figure S2: Polarized Raman intensity behavior with varying *σ* and *OD*.

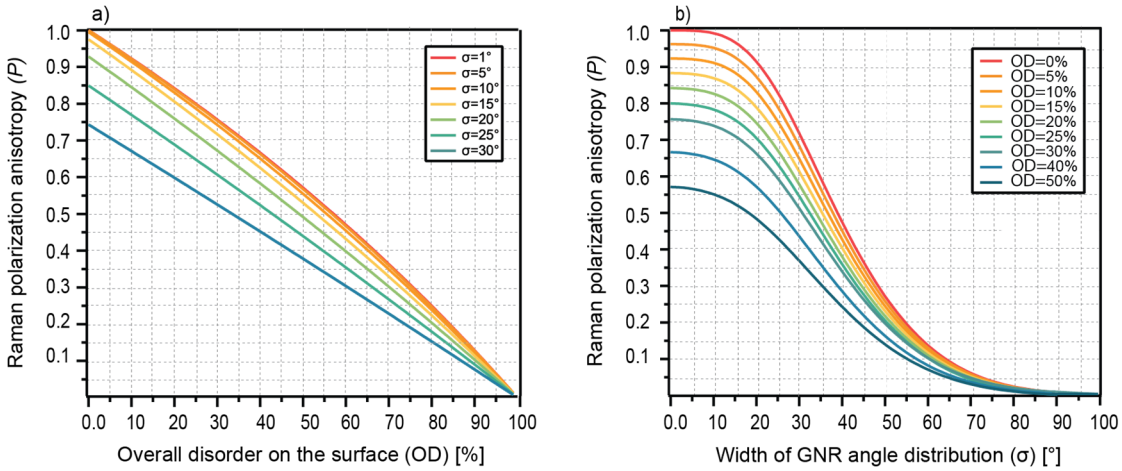

Figure S3: Impact of *OD* and *σ* on *P*. a) Relationship between *P* and *OD* for different values of *σ*. b) Relationship between *P* and *σ* for different values of *OD*.

Polarization dependence of 9-AGNRs Raman active modes with VV configuration

To explore the polarization dependence of the other Raman active modes of 9-AGNRs, we have also acquired polarized Raman intensity data as a function of polarization direction for the RBLM, CH, and D modes, both from the same high- and low-coverage 9-AGNR samples in the main text on the Au(788) growth substrate and after transfer to a ROS. The resulting data sets are shown in Figs S4 and S5 for the high- and low-coverage samples, respectively. We observed that CH, D, and RBLM modes exhibit roughly the same polarization dependence (VV configuration) as the G mode, with a maximum intensity when the incident polarization is parallel to the ribbon axis (0°, 180°) and minimum when perpendicular.

As discussed and shown in the main text for the G mode data, the extended polarization fitting model has also been applied to the RBLM, CH, and D peak Raman data. Tables S1 and S2 summarize the resulting *σ*, *OD*, and *P*-values for the high- and low-coverage samples on Au(788) and after substrate transfer onto the ROS, respectively. The *σ*, *OD*, and *P*-values of RBLM, CH, and D in Tables S1 and S2 exhibit comparable values to the G mode (presented in the main manuscript Tables 1) for both high- and low-coverage samples on Au(788) and ROS, with a larger error range for low-coverage samples, which is due to the low Raman intensities for these samples.

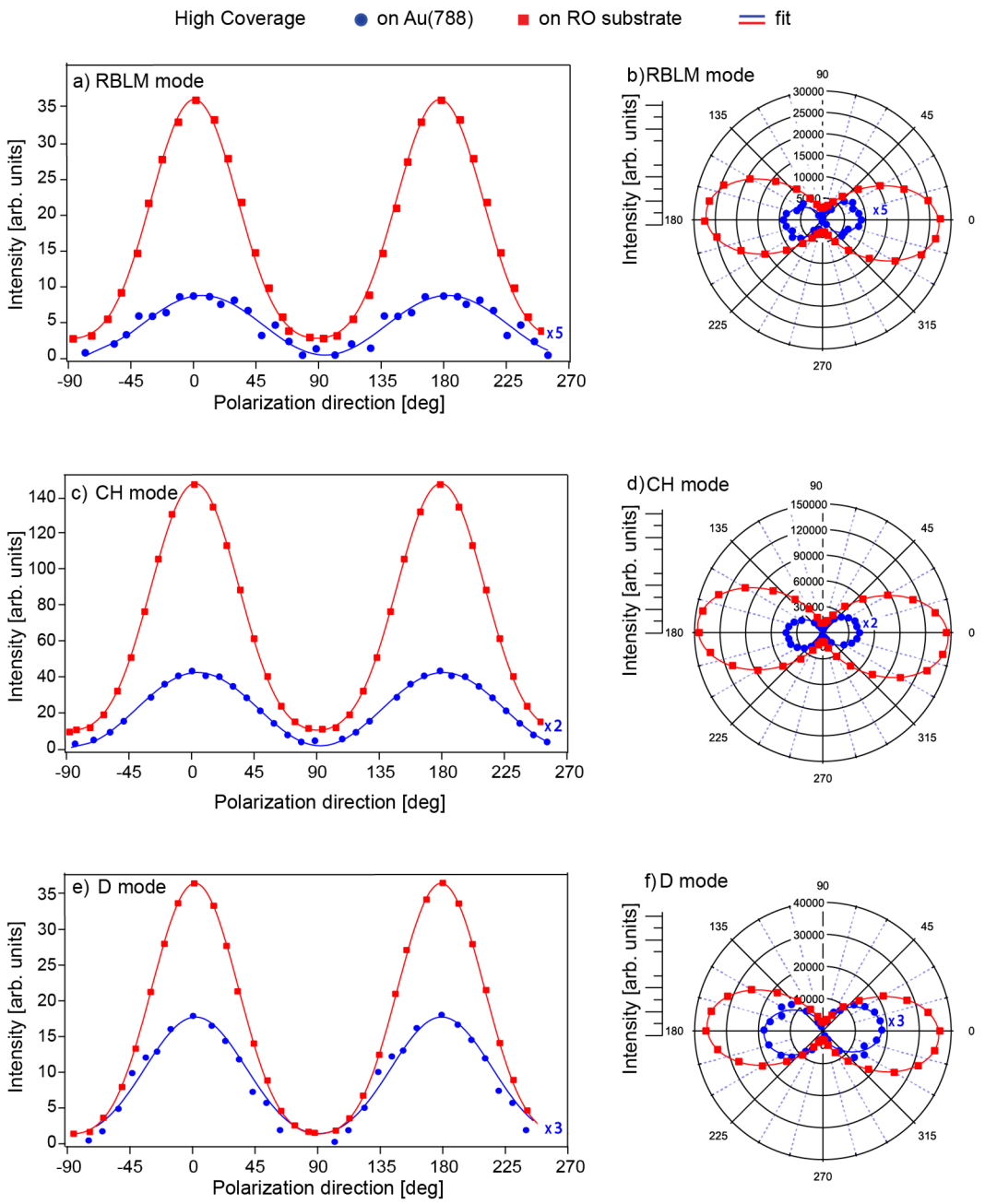

Figure S4: Polarized Raman intensity of RBLM, CH, and D modes for high-coverage sample. a), c), and e) Measured RBLM, CH, and D mode intensities as a function of polarization angle ϑ on Au(788) (blue circles) and after substrate transfer onto ROS (red squares). Data fits using Eq. (9) are represented by blue and red solid lines. b), d), and f) Representative polar diagrams illustrating the RBLM, CH, and D mode intensities on Au(788) (blue circles) and ROS (red squares), corresponding to a), c), and e). Blue and red solid lines represent the fits to the measured data using Eq. (9).

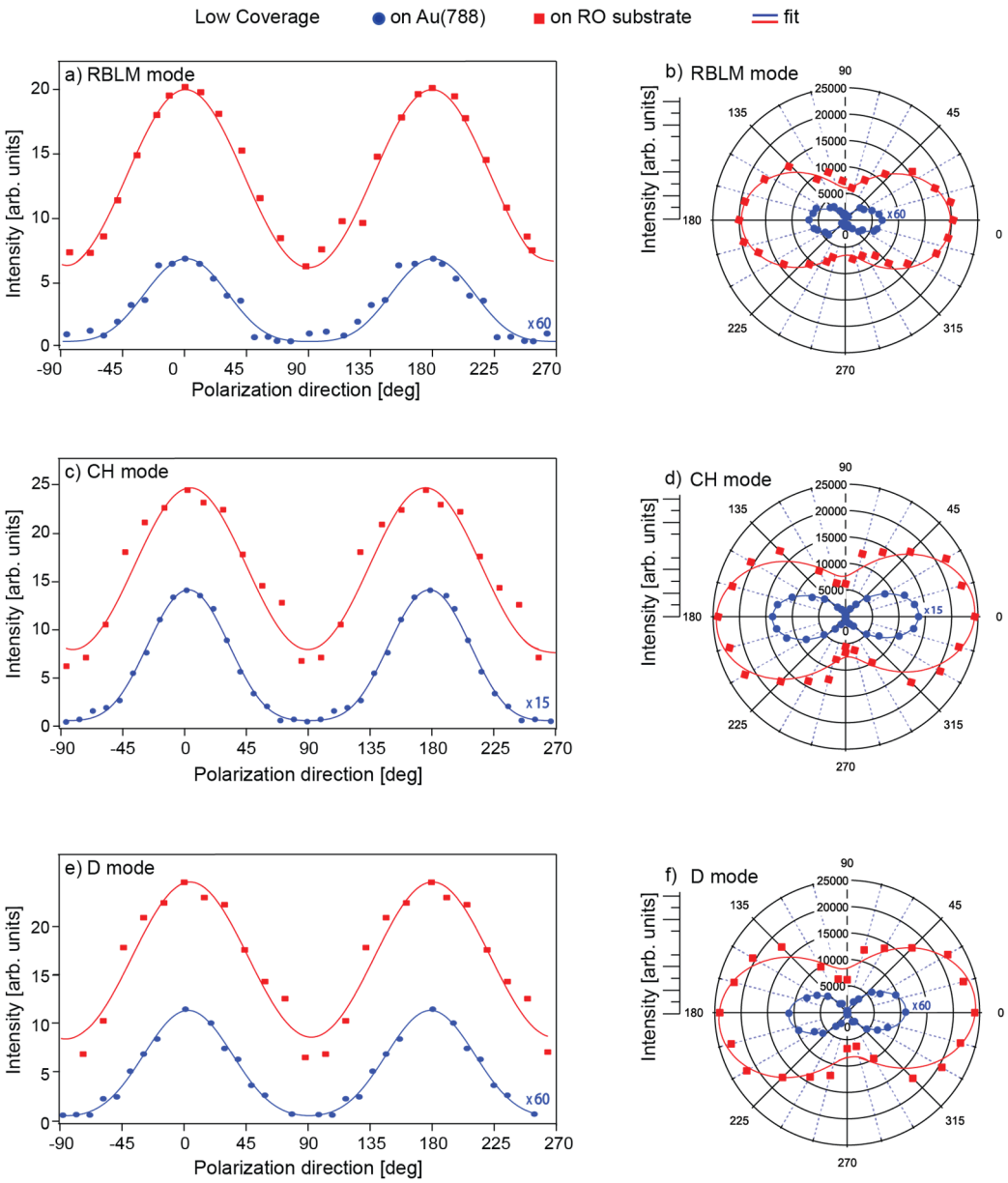

Figure S5: Polarized Raman intensity of RBLM, CH, and D modes for low-coverage sample. a), c), and e) Measured RBLM, CH, and D mode intensities as a function of polarization angle ϑ on Au(788) (blue circles) and after substrate transfer onto ROS (red squares). Data fits using Eq. (9) are represented by blue and red solid lines. b), d), and f) Representative polar diagrams illustrating the RBLM, CH, and D mode intensities on Au(788) (blue circles) and ROS (red squares), corresponding to a), c), and e). Blue and red solid lines represent the fits to the measured data using Eq. (9).

High-coverage sample	RBLM peak		CH peak		D peak	
	Au(788)	ROS	Au(788)	ROS	Au(788)	ROS
Quality of alignment (σ) [°]	3± 1	13± 1	3± 1	15± 2	2± 1	14± 1
Overall disorder on the surface (*OD*) [%]	8± 1	14± 1	7± 1	13± 1	8± 2	14± 1
Raman polarization anisotropy (*P*)	0.86	0.81	0.86	0.84	0.86	0.85

Table S1: High-coverage 9-AGNR sample *σ*, *OD*, and *P*-values resulting from the fitting of the RBLM, CH, and D mode data with the 9-AGNRs on Au(788) and after transfer onto a ROS.

Low-coverage sample	RBLM peak		CH peak		D peak	
	Au(788)	ROS	Au(788)	ROS	Au(788)	ROS
Quality of alignment (*σ*) [°]	1.0± 0.3	22± 4	1.1± 0.2	26± 4	1.5± 0.4	26± 1
Overall disorder on the surface (*OD*) [%]	8± 4	48± 6	8± 2	39± 3	6± 4	43± 5
Raman polarization anisotropy *(P)*	0.91	0.54	0.90	0.50	0.90	0.55

Table S2: Low-coverage 9-AGNR sample *σ*, *OD*, and *P*-values resulting from the fitting of the RBLM, CH, and D mode data with the 9-AGNRs on Au(788) and after transfer onto a ROS.

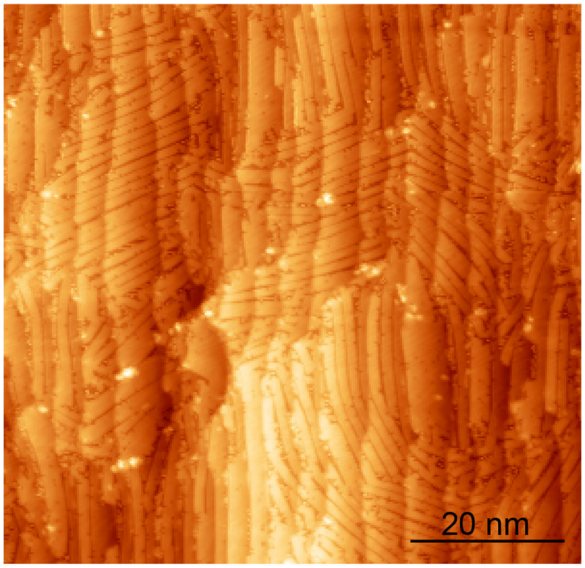

Figure S6: Constant current STM image of the high-coverage sample of 9-AGNRs on Au(788). Taken at a location showing GNRs growing across the terraces (V_b = -1.5 V, I_t = 0.3nA, scale bar of 20 nm).

Chapter 4

Unraveling the role of precursor coverage in the synthesis and substrate transfer of graphene nanoribbons

Introduction

Quasi-one-dimensional atomically precise graphene nanoribbons (GNRs) have gathered significant interest in recent years due to their tunable physicochemical properties[1–3], achieved through precise control over their width[4–7] and edge structure[8–13]. This makes GNRs appealing candidates for various electronic [14–25], spintronic [26–28], and optical applications [2,3,29,30].

Among the different types of GNRs, armchair-edged graphene nanoribbons (AGNRs) have particularly attracted attention due to their width-dependent electronic band gap, which can be adjusted from quasi-metallic to wide band gap semiconductors[31]. AGNRs are classified into three families based on their width: $N=3p$ (medium gap), $N=3p+1$ (wide gap), and $N=3p+2$ (quasi-metallic / narrow gap), where p is an integer and N indicates the number of carbon-dimers across the ribbon width[31,32]. However, achieving a well-defined band gap requires precise control over the ribbons' width and edge structure.

To synthesize atomically precise GNRs, on-surface synthesis is a versatile approach that involves assembling molecular building blocks on a catalyst substrate (usually Au(111)) under ultrahigh vacuum conditions [7,11]. This process is based on depositing suitably designed molecular precursors on the metal surface, followed by their surface-assisted covalent coupling. By carefully designing the precursor monomer, atomic precision over GNR width and edge topology is achieved, enabling the synthesis of ultra-narrow GNRs with atomically precise widths (5-[5], 7-[24], 9-[4], and 13-[14]AGNRs) and defined edge topology (armchair-[4], zigzag-[11], chiral-[33], and GNRs with topological phases[13]).

To fully exploit GNR properties in device architectures, GNRs need to be transferred from their metallic growth substrate to semiconducting or insulating substrates, such as SiO_2/Si[34,35]. Various methods have been developed to transfer GNRs, depending on whether the growth substrate is a gold film or a single crystal. A polymer-free transfer is typically used for GNRs grown on Au(111) films on mica, using the gold film itself to support the GNRs throughout the transfer [35]. In the case of GNRs growing uniaxially aligned on a regularly stepped gold single crystal surface such as Au(788), the method of choice is an electrochemical delamination transfer, primarily developed for graphene transfer from copper foils[36], and later optimized for GNRs[30,34]. This approach

uses a polymer layer, usually poly(methyl methacrylate) (PMMA), to support the GNRs, and relies on water electrolysis to generate hydrogen bubbles at the interface between the PMMA/GNRs layer and the metal substrate. The hydrogen bubbles mechanically delaminate the PMMA/GNRs layer from the metal substrate, resulting in the transfer of uniaxially aligned GNRs [30,34,37].

Among AGNRs, 9-atom-wide armchair GNRs (9-AGNRs) have been most extensively integrated into devices due to their suitable electronic gap (1.4 eV measured on Au)[4] enabling switching behavior at room temperature, suitable length to bridge source and drain contacts [38] and robustness and stability under ambient conditions[35,39]. Another important aspect of the integration of AGNRs into devices is the device yield, which typically ranges between 10-15% when using AGNRs grown on Au (111) surfaces, due to their non-preferential growth direction[14]. By growing uniaxially aligned AGNRs, device yields can reach ~85%, as the GNRs can be deposited aligned with the source to drain direction of the device[22].

In this work, we investigate the growth of aligned 9-AGNRs on Au(788) and characterize their length as a function of precursor dose (PD) in 30 different samples using scanning tunneling microscopy (STM). We also characterize the quality of alignment and surface disorder as a function of PD and length on both the growth substrate (40 samples) and after substrate transfer (27 samples) utilizing polarized Raman spectroscopy and discuss the impact of PD on the substrate transfer success rate.

Results and discussion

9-AGNR growth and length evolution on Au (788)

To investigate the growth of 9-AGNRs on a vicinal surface, we deposit the precursor molecule 3′,6′-di-iodine-1,1′:2′,1′′-terphenyl (DITP)[38] onto Au(788) at a fixed deposition rate of 1 Å/min (as measured with a quartz microbalance), with deposition times varying from 1 to 9 minutes. Subsequently, thermal annealing steps at 200°C and 400°C activate polymerization and induce cyclodehydrogenation, respectively. By maintaining a constant deposition rate of 1 Å/min and increasing the deposition time by 1-minute steps, we achieve PDs ranging from 1 to 9 Å on the surface. Figs. 1a-h shows representative STM images of 9-AGNRs samples with PDs of 1 to 9 Å, respectively.

We observe that, as PD increases, the growth of 9-AGNRs on Au(788) occurs at three different positions. Initially, GNRs start growing along the Au(788) step edges, referred here as the first-row position (blue arrow). Fig. 1a shows a representative STM image of 9-AGNRs with PD = 1 Å, with short GNRs with an average length of 14 nm, growing solely at this position. As PD increases to 2 and 3 Å, GNRs continue to grow exclusively at the step edges with average GNR length reaching 19 nm and 35 nm for PDs of 2 Å and 3 Å, respectively (Figs. 1b-c). The growth of GNRs at the first-row position only, along the step edges, can be attributed to the higher catalytic activity and altered surface chemistry caused by the greater negative charge density at the lower step edge[40,41], which facilitates the nucleation and growth process. For samples with low PD

between 1 and 3 Å, the inter-ribbon distance remains constant and is determined by the width of the terraces, approximately 3.8 nm[42].

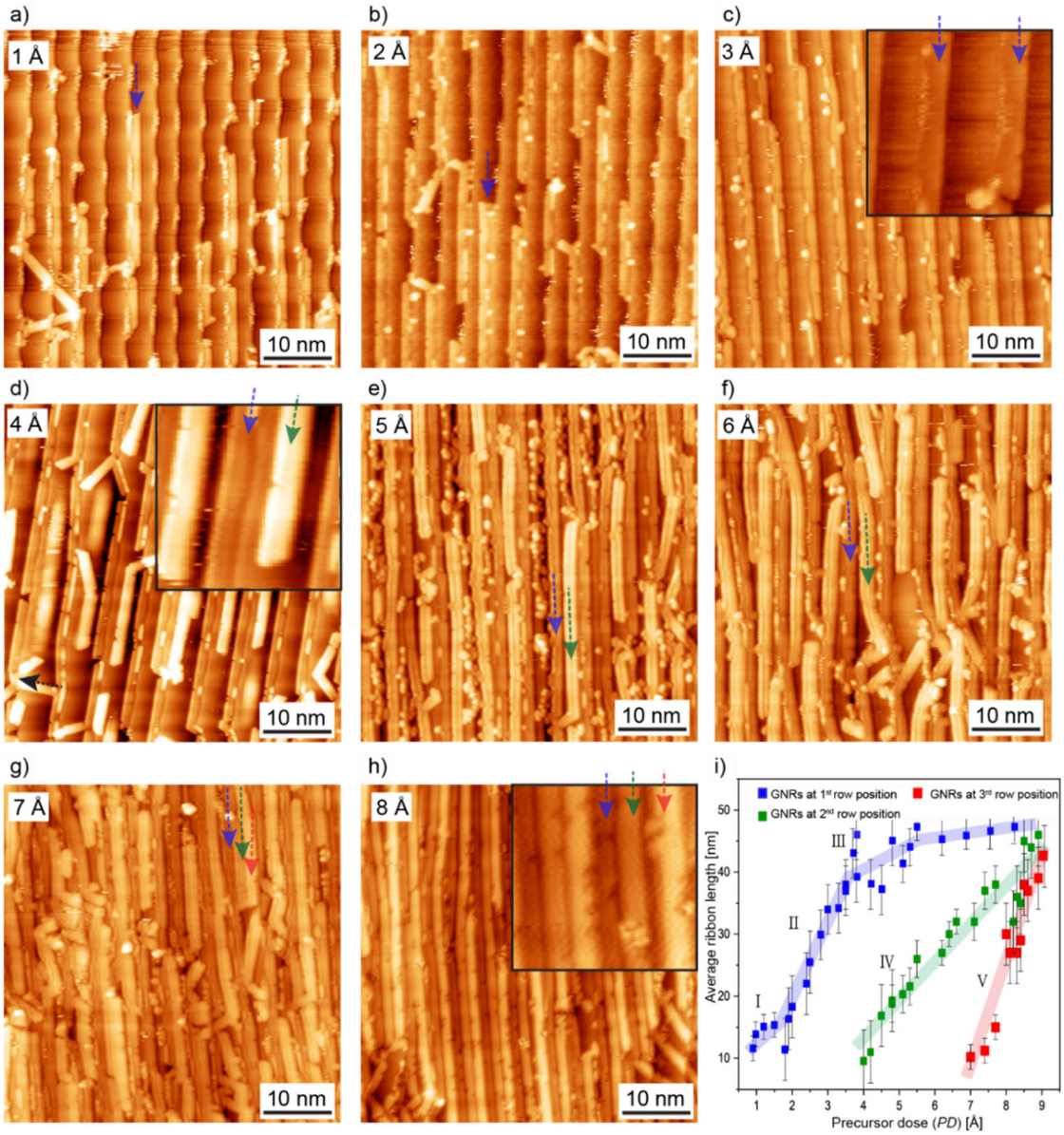

Figure 1: Evolution of 9-AGNR growth on Au(788) with increasing precursor dose (PD). (a-c) STM images show the length evolution of GNRs at the first-row position (blue arrows) along the lower step edges as PD increases from 1 Å to 3 Å. d) STM image shows GNRs at the second-row position (green arrow) growing parallel to first-row GNRs (blue) at PD = 4 Å. (e-f) STM images revealing the length evolution of GNRs at the second-row position (green arrows) at PD = 5 Å and PD = 6 Å, respectively. g) STM image at PD = 7 Å, revealing the formation of a GNR at the third-row position (red arrow), growing parallel to the GNRs grown previously at the first and second-row positions. h) STM image of a monolayer of 9-AGNRs with GNRs grown in three parallel rows (blue, green, and red arrows) along each terrace at PD = 8 Å. i) Histogram illustrating GNR length evolution for 30 samples across all PDs, with error bars representing standard deviation. Tunneling parameters for STM images: V_b = -1.5 V, I_t = 30 pA.

For samples prepared with PD of 4 Å, the lower step edges are fully decorated with 9-AGNRs, and additional GNRs start to grow in the middle of the Au(788) terraces, referred here as the

second-row position (green arrow). Initially, GNRs at this position are also short with an average length of 14 nm, due to the low amount of precursors available on the terraces. In some instances, such short GNRs also grow misaligned to the step edge (Fig. 1d, black arrow).

As PD further increases to 5 Å, 6 Å, and 7 Å, the average length of GNRs at the second-row position steadily increases to 22 nm, 30 nm, and 36 nm, respectively (Figs. 1e-g). Notably, at PD = 7 Å, we also observe short GNRs (red arrow, Fig. 1g) growing at the third-row position close to the descending step edge of the terrace, with an average length of 13 nm. At PD = 8-9 Å, a complete monolayer is formed, with three rows of ribbons per terrace (Fig. 1h). In the monolayer samples, GNRs at the first-row exhibit an average length of ~46 nm, the second-row GNRs of ~42 nm, and the third-row GNRs of ~ 36 nm.

Figure. 1i shows an overview of the length evolution of GNRs, displaying the average length distribution based on measurements of a total of 30 samples for PD ranging from 1 to 9Å. To obtain these data, we scanned large-scale STM images (100 x 100 nm), allowing for the examination of more than 800 GNRs per sample. As a complement, we summarize the average GNR lengths for selected PDs in Table S1. The length evolution data displayed in Fig. 1i evidence significantly different growth rates for GNRs growing in first, second, and third-row positions, as well as a non-linear growth behavior for 1st-row GNRs, which, however, can be approximated by a sequence of three linear regimes. We performed linear curve fitting to the data in Fig. 1i for each of the 5 regimes I to V of GNR length evolution, as discussed in the following.

Regime I corresponds to GNRs growing with PDs ranging from 0 to 2 Å. At these very low precursor coverages, GNR growth is dominated by nucleation at the step edges, more specifically at defect sites. This leads to a low growth rate of 5 nm Å^{-1}, and the average length of the nucleating GNRs thus only increases by 5 nm as PD increases from 1 to 2 Å. Upon increasing PD beyond 2 Å (regime II), we observe a much faster growth (16 nm Å^{-1}), with the average GNR length increasing to 35 nm at PD = 3 Å. This corresponds to the situation where further GNR nucleation at the step edge is low, and most incoming precursors contribute to increasing the length of GNRs growing along the step edges. In regime III, starting at PD = 4 Å, all step edges become saturated, with only an incremental increase (4 nm Å^{-1}) in the average length of GNRs, up to the final average first-row GNR length of 43 nm. Already somewhat before the step edges are fully passivated, GNRs also start to grow at the second-row position (on the Au (788) terraces), which is regime IV (PD = 4 to 9 Å). Here we observe a strictly linear length evolution leading to a steady increase in GNR length by 8 nm Å^{-1}. We attribute this relatively slow growth rate to a combination of significant nucleation density and the fact that, in this regime of 2nd-row GNR growth, incoming precursors also contribute to complete 1st-row GNRs and nucleation/lengthening of 3rd-row GNRs. Finally, when the second-row GNR growth approaches saturation, GNRs start to grow a the third-row position, close to the upper step edge of each terrace. This is regime V, with a high growth rate of 23 nm Å^{-1}, leading to a third-row GNR length increase from 13 to 36 nm as PD increases from 7 to 9 Å. We attribute this rapid increase in GNR length to the presence of fewer nucleation sites, therefore the incoming precursors mostly contribute to the elongation of GNRs at this position.

We note that GNR growth at first-, second, and third-row positions is not a strictly sequential process, but Fig. 1i clearly shows that growth in the next row position starts before the previous row has been fully completed, as evidenced by the overlap of regimes III and IV as well as IV and V. This simply reflects the balance between nucleation and diffusion at play, which may be somewhat influenced by the growth temperature. We have not explored this aspect, which thus remains for future work. Overall, the details findings discussed above provide important insight into the growth of GNRs on vicinal surfaces and highlight the influence of growth position on the substrate and PD on GNR length evolution.

9-AGNR quality and alignment as a function of PD on Au(788) and after substrate transfer

After transferring GNRs onto an insulating substrate, their characterization using STM becomes infeasible due to the requirement for a conductive sample surface. Raman spectroscopy provides a non-destructive and rapid alternative for assessing GNR quality and orientation regardless of the substrate's nature,[30,34,43] and we have thus performed detailed Raman analysis for the samples presented above.

The main Raman active mode for GNRs is the G mode, located in the high-frequency spectral range at approximately ~1600 cm^{-1} [44–46,35]. This model is present in all sp^2 carbon-based materials and originates from in-plane vibrations[47]. Additionally, several phonon modes are detected in the high-frequency spectral range of 1100-1500 cm^{-1}, which are associated with the edge structure of GNRs and collectively referred to as CH-D modes[35,44–46]. Specifically, the CH-bending mode at ~1200 cm^{-1} corresponds to the bending vibrations of the hydrogen atoms at the GNR edges, while the D mode at ~1300 cm^{-1} indicates disarrangement of the periodic graphene honeycomb lattice. It is important to note that unlike in graphene, the D peak in GNRs is an intrinsic mode resulting from the precise atomic edges, rather than defects[48]. Another intrinsic peak in GNRs is the radial breathing-like mode (RBLM), which is located in the low-frequency range and provides information about GNR width[35,49,50]. This mode is similar to the radial breathing mode (RBM) in carbon nanotubes (CNTs), whose frequency is directly related to the diameter and chirality of the CNTs[51]. After the transfer of the substrate (in Figure 2), we have successfully identified several additional modes, which we attribute to overtones, including the RBLM3 at 845 cm^{-1} [43].

Here, Raman measurements are conducted in a home-built vacuum chamber (~10^{-2} mbar) using 785 nm excitation wavelength (1.58 eV). In addition, an optimized mapping approach (maps of 10 µm x 10 µm, 10 x 10 pixels) is used to further limit damage to the GNRs[34]. Figure. 2a shows representative Raman spectra acquired directly on the growth substrate Au (788) for 9-AGNRs with PDs from 1 to 9 Å. All spectra show the presence of the RBLM, CH, D, and G modes, with the intensity of the Raman peaks increasing proportionally with PD. In samples with high PD, we observe an additional peak in the CH-D area at ~ 1302 cm^{-1} on Au(788) and ~ 1285 cm^{-1} after substrate transfer. This additional peak could be related to the interaction between GNRs, likely due to the high coverage and shorter inter-GNR distances (Figs. 2a and 2b).

To investigate the electronic properties of GNRs in device architecture, a substrate transfer process is required. Here, we transfer the aligned 9-AGNRs from Au(788) onto a Raman-optimized substrate (ROS)[34] using electrochemical delamination transfer[30,34]. Figure 2b shows Raman spectra of 9-AGNRs with PD from 1-9 Å after substrate transfer onto a ROS. The presence of all 9-AGNR intrinsic Raman peaks (RBLM, CH, D, and G) after the substrate transfer process suggests the preservation of the GNRs' structural integrity during transfer. To evaluate GNR quality before and after substrate transfer we extract the full-width at half maximum (FWHM) and peak positions of the RBLM, CH, D, and G modes for all samples, and summarize the results in Table S2 and Table S3.

Upon substrate transfer, samples with medium and high PDs (4-9 Å) exhibit negligible changes in the FWHM for RBLM, D, CH, and G Raman modes, with all values falling within the experimental accuracy of the Raman measurements (3 cm^{-1}). However, for low-PD samples (1-3 Å), we observe a significant standard deviation in the FWHM between the samples in this range, particularly for the CH mode. The CH mode is an edge mode, and the increase in FWHM could be attributed to the presence of defects at the edges induced by the transfer process. This effect is particularly prominent in low PD samples where GNRs are strongly attached to the step edges, leading to lower GNR quality upon transfer[37]. By evaluating the peak positions of the Raman active modes for all samples, we observe negligible shifts in the G, D, and RBLM modes. However, the CH vibrational modes exhibit a notable shift of approximately 10-12 cm^{-1} for high, medium, and low PD samples, which may be explained by the different interaction of the edge modes with the ROS substrate compared to Au.

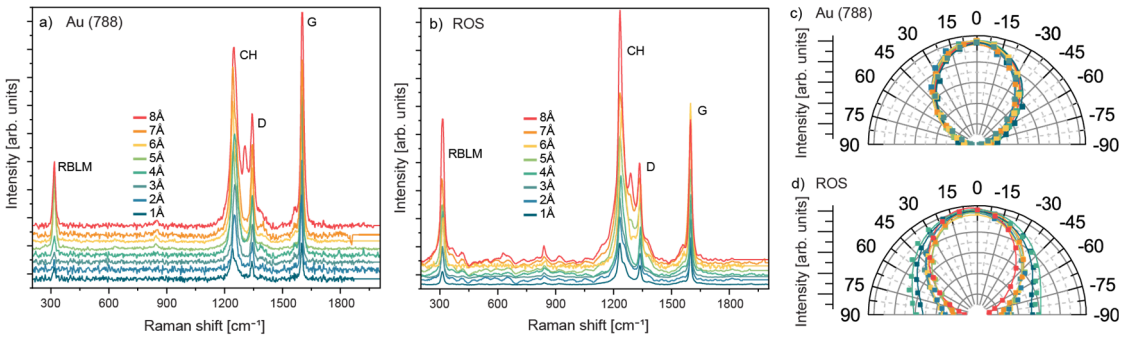

Figure 2: Raman characterization of 9-AGNRs at PDs from 1-8 Å on Au(788).a) and after substrate transfer onto ROS (b). Panels. (c) and (d) show polar plots of the polarization dependence of the G-mode for each PD on Au(788) and the ROS, respectively. The intensities in the polar plots are normalized to the 8 Å precursor dose. The polar diagrams follow the $cos^2(\theta)$ function expected for the parallel-polarized (PP) configuration and are fitted with a modified angular model based on Ref [37](lines). The Raman measurements are obtained under vacuum conditions with a 785 nm excitation wavelength and the (NA) configuration, where the incident laser's angle (θ_{in}) is altered relative to GNRs' alignment direction (θ = 0°). This is achieved without employing a polarizer in the detection path.

To achieve optimal performance in GNR-based FET devices and improve device yield[16,35], it is crucial to determine the alignment direction of GNRs such as to transfer them well aligned with the the source to drain direction. Here we use polarized Raman spectroscopy to investigate the orientation of GNRs on the growth substrate and after substrate transfer[30,37,43]. The laser excitation source (785nm) is polarized from -90° to 90° at 10° increments, and the scattered

light is detected without using an analyzing polarizer (the spectrograph collects scattering data for all polarizations).

By measuring the polarization-dependent intensity of scattered light, we observe that the Raman intensity of the G mode follows a $\cos^2(\theta_{in})$ polarization-dependent behavior, with maximum intensity at 0° and minimum at 90°, as shown in the polar plots in Figs. 2c and 2d. To quantitatively characterize the alignment of GNRs, we use two methods. The first is the Raman polarization anisotropy (P)[30,37,43], defined by Eq. (1):

$$P = (I_{\parallel} - I_{\perp}) / (I_{\parallel} + I_{\perp}) \tag{1}$$

where $I_{\parallel}$ and $I_{\perp}$ represent the Raman intensities with polarization along and perpendicular to the GNR axis, respectively. A perfect uniaxial alignment of GNRs corresponds to $P=1$, while $P=0$ indicates random orientation. The second approach is an extended Gaussian distribution, initially detailed in our earlier work[37]. Here we have modified our model, to take into account that no analyzing polarizer was used during the measurements Eq. (2).

$$I_{exp}(\vartheta) = A \cdot \int_{0°}^{360°} cos^2(\varphi) \cdot \frac{1}{\sigma\sqrt{2\pi}} e^{-\frac{(\vartheta-\varphi-\vartheta_0)^2}{2\sigma^2}} d\varphi + B \cdot \frac{1}{2} \tag{2}$$

ϑ_0 is the azimuthal angle along which GNRs are preferentially aligned; A is the fraction of surface area that exhibits aligned GNRs; σ is the width of the Gaussian distribution characterizing the angular distribution around ϑ_0 (quality of alignment); and B is the fraction of the surface area contributing to the isotropic, polarization-independent Raman signal. From A and B we also define the overall disorder present on the surface: $OD=B/(B+A)\cdot 100\%$.

We apply both methods to investigate the alignment of GNRs for all PDs. To guarantee representative results we investigated 40 samples with PD between 1-9 Å on the Au (788) growth surface and 27 samples of them after substrate transfer onto ROS. We extract P, σ, and OD for all Raman modes (RBLM, CH, D, and G), and summarize the results in Fig. 3 and Table 1 (for the G mode) and Fig. S1 (for the RBLM, CH, and D modes).

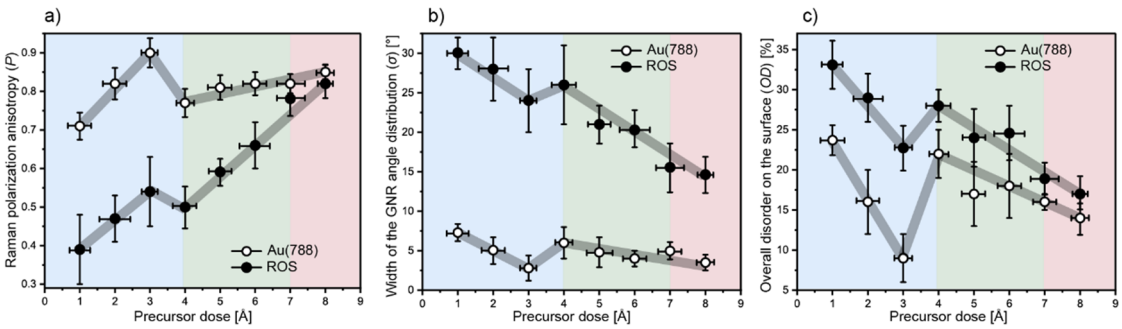

Figure 3: Impact of PD on the alignment of GNRs on Au(788) and after substrate transfer onto ROS. Panels (a), (b), and (c) show the average P, σ, and OD extracted for the G mode, respectively, as a function of PD on both the Au(788) (open circles) and on ROS (closed circles) with error bars representing the standard deviation. The colored background represents the regimes in which GNRs grow preferentially at the first-row position (blue), at the second-row position (green), and at the third-row position (red).

Parameters	Raman polarization anisotropy (*P*)		Quality of alignment (*σ*) [°]		Overall disorder (*OD*) [%]	
Substrate	Au(788)	ROS	Au(788)	ROS	Au(788)	ROS
1 Å	0.71± 0.04	0.39± 0.09	7± 1	30± 2	24± 2	33± 3
2 Å	0.82± 0.04	0.47± 0.06	5± 2	28± 4	16± 4	29± 3
3 Å	0.90 ± 0.04	0.55± 0.09	3± 1	24± 4	9± 4	23± 3
4 Å	0.77± 0.02	0.50± 0.02	6± 2	26± 5	22± 3	28± 2
5 Å	0.81± 0.03	0.65± 0.04	5± 2	21± 1	17± 4	24± 4
6 Å	0.82± 0.03	0.70± 0.06	4± 1	20± 2	18± 4	25± 3
7 Å	0.82± 0.03	0.78± 0.02	5± 1	16± 4	16± 1	19± 2
8-9 Å	0.85± 0.02	0.82± 0.05	4± 1	15± 4	14± 3	17± 3

Table 3: Average *P*, *σ*, and *OD* of the G mode as a function of PD, on Au(788) and after substrate transfer to ROS.

We start by discussing the low-PD regime, where GNRs grow solely on the step edges (highlighted in blue). In this regime, we observe a clear trend that $P_{Au(788)}$ increases and $\sigma_{Au(788)}$ becomes narrower as the length of GNRs increases, indicating a higher quality of alignment for longer GNRs on both Au(788) and ROS. GNRs grown at the first-row position with average lengths of 14, 19, and 39 nm (for PD = 1, 2, and 3 Å, respectively) show $P_{Au(788)}$ = 0.71, 0.82, and 0.90, and $\sigma_{Au(788)}$ = 7°, 5°, and 3°, respectively (Figs. 3a, 3b and Table 1). These results are consistent with our STM studies (Fig. 1) and reflect that longer GNRs tend to better align with the step edge, while shorter GNRs can also grow across the gold terraces. At PD = 4 Å, where GNR growth at the second-row position has started, we observe a kink in all curves of Figure 3. The overall degree of GNR alignment decreases, with $P_{Au(788)}$ = 0.77 and $\sigma_{Au(788)}$ = 6° (Figs. 3a and 3b). For this PD, the step edges are fully saturated, and GNRs grow at the second-row position, located in the center of the terraces (highlighted in green), with an average length of 14 nm (Fig. 1d). As the second-row GNRs grow longer, the quality of alignment improves again, reaching $P_{Au(788)}$ = 0.81 and 0.82 with $\sigma_{Au(788)}$ = 5 and 4° for precursor doses of 5 Å (average GNR length = 22 nm) and 6 Å (average GNR length = 30 nm), respectively. Finally, in the high-PD regime (highlighted in red), the substrate is fully covered with GNRs, and the quality of alignment reflects the behavior of GNRs grown at all three positions, as a full monolayer: with $P_{Au(788)}$ = 0.82 and 0.85, and $\sigma_{Au(788)}$ = 5° and 4° for PD = 7 Å and 9 Å, respectively (Figs. 3a and 3b). The appearance of GNRs at the third-row position with an average length of 12 nm for PD = 7 Å does not negatively influence the quality of alignment, unlike the case of short GNRs grown with PD =1 Å and 4 Å. At this particular PD, GNRs at the third-row position grow well aligned because they are strictly confined between the second-row GNRs and the upper step edge of the adjacent substrate terrace.

The evolution of *P*, *σ*, with PD for GNRs transferred onto the ROS follows the same trend, with overall increasing quality of alignment with increasing coverage, except for the same kink at PD = 4 Å. However, compared to GNRs on Au(788), substrate-transferred GNRs exhibit a significantly decreased *P* and an increased *σ*. In the low-PD regime (highlighted in blue), we extract P_{ROS} = 0.39, 0.47, and 0.55, and σ_{ROS} = of 30°, 28°, and 24°, for PD= 1, 2, and 3 Å respectively. We attribute the striking reduction in alignment after substrate transfer to the strong interaction of GNRs with the Au(788) step edges, which hinders their transfer, along with increased GNR mobility due to the low coverage preparation (Figs. 3a and 3b and polar plots in Fig. 2c and 2d). Longer GNRs at higher coverages, however, preserve their alignment better upon substrate transfer (Table 1). For samples with PD = 4 Å, the degree of alignment decreases

slightly, with P_{ROS} = 0.5 and σ_{ROS} = 26°, which we attribute to the presence of short GNRs growing at the second-row position. These short second-row GNRs exhibit a high mobility upon transfer, which negatively impacts their degree of alignment.

As PD increases, we observe a steady increase in the preservation of alignment with P_{ROS} = 0.65, 0.7, 0.78, 0.82, and σ_{ROS} = 21°, 20°,16°, and 15° for PD= 5 Å, 6 Å, 7 Å, and 9 Å, respectively. As the amount of GNRs on the surface increases (along with their length), their mobility during substrate transfer decreases, leading to a better preservation of alignment. Similar behavior was observed for full monolayer samples by Senkovskiy et al.[30], Overbeck et al. [43], Zhao et al. [2], and by us in our previous work[37], where P = 0.72- 0.82 was observed for different transferred AGNRs. Overbeck et al.[43] also reported the influence of GNR length on polarization dependence for short 5-AGNRs with an average length of 3.8 nm, where the low polarization anisotropy ($P_{Au(788)}$ = 0.3 before and P_{ROS} =0.4 after substrate transfer) was attributed to the GNRs' reduced shape anisotropy and the high mobility of short ribbons.

Next, we briefly discuss the overall disorder present on the surface (*OD*) for all samples before and after transfer. The average values of *OD* for the Raman modes RBLM, CH, D, and G are presented in Fig. 3c and Table 1 (for the G mode), as well as in Fig. S1 (for the RBLM, CH, and D modes). For samples on Au(788), the origin of $OD_{Au(788)}$ is attributed to very short GNRs, irregularly fused precursor monomers, and the presence of impurities from the precursor[37]. Here, we observe a systematic decrease of $OD_{Au(788)}$ as the GNRs grow longer: $OD_{Au(788)}$ = 24%, 16%, and 9%, for samples with PD = 1, 2, and 3 Å, respectively (Fig. 3c, highlighted in blue). As GNRs start to grow at the second-row position (PD = 4 Å), $OD_{Au(788)}$ increases to 22%, which reflects the presence of very short GNRs (that do not exhibit polarization dependence) growing on the terraces. As PD continues to increase (and therefore GNR length), $OD_{Au(788)}$ linearly decreases, reaching 14% for the full monolayer. Upon substrate transfer, OD_{ROS} increases for all samples. However, the most significant increase is observed for low-PD samples, with OD_{ROS} = 33%, 29%, and 23% (for PD = 1, 2, and 3 Å, respectively), compared to the full monolayer OD_{ROS} =17% (PD = 9 Å). This arises from an inefficient transfer in the case of low-PD samples, which may result in partially broken GNRs due to their strong physical interaction with the Au(788) step edges. Additionally, at these low precursor doses, the Au substrate is more exposed to PMMA and other contaminants, which may react with the Au surface and transfer along the GNRs, contributing to an increase in OD_{ROS}. In general, as shown in Figs. 3, we observed slight changes in P and *OD* values for high PD samples of Au(788) and ROS, except for σ. Previous studies elucidate this discrepancy[37], explaining that P is a reliable indicator for larger σ values, reflecting the combined impact of σ and *OD*, but is relatively insensitive to σ < 15°.

Finally, we comment on the success rate of transferring GNR samples grown from different PDs. Initially, we fabricated and studied 40 samples of 9-AGNR on the Au(788) substrate, and out of those, 27 samples were successfully transferred to the ROS. We note that the transfer success rate was larger for samples with higher PD, 77% for PD=7-9 Å, compared to those with medium PD= 4-6 Å (60%) and low PD = 1-3 Å (53%), endorsing our results that GNRs at higher coverages transfer more efficiently.

Conclusions

We investigated the growth and alignment of 9-AGNRs on Au(788) with varying PD, both on the growth substrate and upon substrate transfer. By STM we characterized 40 samples with different PDs ranging from 0 to 9 Å and observed that GNRs grow sequentially at three positions on Au(788) depending on PD: only at the lower step edges at low precursor doses (and thus low coverages), in the middle of the terraces at medium doses, and at the upper step edges at coverages approaching a complete monolayer. In terms of alignment, longer GNRs show better unidirectional alignment on Au(788), achieving near-perfect alignment for PD=3 Å, when a single row of GNRs saturates the Au(788) step edges. As PD increases and GNRs start to grow in the center of the terraces the overall degree of alignment decreases due to the presence of short GNRs. A high degree of alignment is again observed once a high PD is used to grow full monolayer samples. Upon substrate transfer, we observe a significant decrease in the degree of alignment for low-PD samples, while alignment is largely preserved for high-PD ones.

We also quantified the overall disorder on the surface and observed that the presence of short GNRs increases the overall disorder on the growth surface, while a combination of short GNRs and impurities increases the overall disorder after substrate transfer. Finally, we also find a PD-dependent substrate transfer success rate, with samples grown from higher PD being more successfully transferred (77%) than lower PD samples (53%).

Our work unravels the role of precursor dose on the growth of 9-AGNRs, their length evolution, quality of alignment, and overall surface disorder,– which are crucial parameters for the growth and transfer of high-quality GNR samples for device integration.

Methods

On-surface synthesis and STM characterization of 9-AGNRs

The Au(788) single crystal growth substrate (MaTecK GmbH, Germany) was cleaned in ultra-high vacuum (UHV) with two cycles of sputtering at 1 kV Ar+ (for 10 minutes) and annealing at 420 °C (for 10 minutes). Subsequently, the 9-AGNR precursor monomer, 3′,6′-di-iodine-1,1′:2′,1′′-terphenyl (DITP)[38], was sublimated onto the pristine Au surface from a quartz crucible heated to 70 °C, while the substrate remained at room temperature. To control the deposition rate, a quartz microbalance was employed to maintain a constant deposition rate of 1 Å/min. This deposition rate is not calibrated to accurately correspond to the true surface coverage. Instead, it is calibrated relative to a standard measurement obtained through STM, by counting the number of GNRs. 8-9 Å corresponds to the amount of precursor molecules resulting in GNR monolayer saturation coverage. Following deposition, with deposition times varying to afford from 1 to 9 Å deposits, the substrate was heated to 200 °C (0.5 K/s) for 10 minutes to initiate DITP polymerization, followed by annealing at 400 °C (0.5 K/s) for 10 minutes to induce cyclodehydrogenation. After the sample cooled down to room temperature (RT), STM images

were acquired at RT in constant current mode, typically with a -1.5 V sample bias and a 0.03 nA setpoint current using a Scienta Omicron VT-STM.

Transfer of GNRs to ROS

To transfer the 9-AGNRs from the Au(788) growth substrate to ROS, electrochemical delamination was used. First, a support layer of poly(methyl methacrylate) (PMMA) was spin-coated (4 PMMA layers, 2500 rpm for 90 s) on the 9-AGNR/Au(788) surface, followed by a 10-minute curing process at 80 °C. To accelerate PMMA delamination, samples were treated for 80 minutes in a UV-ozone oven, followed by a 3-minute development in water/isopropanol to remove PMMA from the edges of the Au(788) crystal. 1 M NaOH aqueous solution was used as an electrolyte, and delamination occurred by applying a DC voltage of 5 V (current ≈0.2 A) between the PMMA/9-AGNR/Au(788) cathode and a glassy carbon electrode as the anode. The delaminated PMMA/GNR layer was transferred to the ROS followed by a two-step annealing: 80 °C for 10 minutes + 110 °C for 20 minutes to improve adhesion between the ROS and the PMMA/GNR layer. Finally, PMMA was dissolved in acetone for 15 minutes, and the resulting GNR/ROS was rinsed with ethanol and ultra-pure water.

Raman spectroscopy

Raman spectroscopy measurements were performed using a WITec confocal Raman microscope (WITec Alpha 300R) with a 785 nm (1.5 eV) laser line and a power of 40 mW. A 50x microscope objective was used to focus the laser beam on the sample and collect the scattered light. The Raman spectra were calibrated using the Si peak at 520.5 cm^{-1}. The laser wavelength, power, and integration time were optimized for each substrate to maximize the signal while minimizing sample damage. To prevent sample damage, a Raman mapping approach with a size of 10×10 pixels (10×10 µm) was employed, and the measurements were conducted in a home-built vacuum suitcase at a pressure of approximately 10^{-2} mbar. Polarized Raman measurements were conducted without the analyzing polarizer to collect all the scattered light. A motorized half-wave plate was used to change the polarization direction of the incident laser beam from -90° to +90° in steps of 10°. The scattered signal, with an excitation wavelength of 785 nm, was detected with a 300 mm lens-based spectrometer equipped with a grating of 300 g mm^{-1} (grooves/mm) and a cooled deep-depletion CCD.

Using the WITec software, a cosmic ray filter was applied to all raw maps to remove signatures of photoluminescence. Afterward, the Raman maps were averaged and polynomial background subtraction was applied, followed by batched fitting with a Lorentzian function for all polarization angles between -90° to 90° for each Raman mode. The fitting using the equations mentioned in the results and discussion was done in IGOR Pro software (Wavemetrics Inc.), and the fitting parameters were obtained through the lowest stable Chi-square values.

References

1. Ruffieux, P. *et al.* Electronic Structure of Atomically Precise Graphene Nanoribbons. *ACS Nano* **6**, 6930–6935 (2012).
2. Zhao, S. *et al.* Optical Imaging and Spectroscopy of Atomically Precise Armchair Graphene Nanoribbons. *Nano Lett.* **20**, 1124–1130 (2020).
3. Denk, R. *et al.* Exciton-dominated optical response of ultra-narrow graphene nanoribbons. *Nat. Commun.* **5**, 4253 (2014).
4. Talirz, L. *et al.* On-Surface Synthesis and Characterization of 9-Atom Wide Armchair Graphene Nanoribbons. *ACS Nano* **11**, 1380–1388 (2017).
5. Kimouche, A. *et al.* Ultra-narrow metallic armchair graphene nanoribbons. *Nat. Commun.* **6**, 10177 (2015).
6. Talirz, L., Ruffieux, P. & Fasel, R. On-Surface Synthesis of Atomically Precise Graphene Nanoribbons. *Adv Mater* **28**, 6222–6231 (2016).
7. Cai, J. *et al.* Atomically precise bottom-up fabrication of graphene nanoribbons. *Nature* **466**, 470–473 (2010).
8. Yang, L., Park, C.-H., Son, Y.-W., Cohen, M. L. & Louie, S. G. Quasiparticle Energies and Band Gaps in Graphene Nanoribbons. *Phys. Rev. Lett.* **99**, (2007).
9. Rizzo, D. J. *et al.* Topological band engineering of graphene nanoribbons. *Nature* **560**, 204–208 (2018).
10. Cao, T., Zhao, F. & Louie, S. G. Topological Phases in Graphene Nanoribbons: Junction States, Spin Centers, and Quantum Spin Chains. *Phys. Rev. Lett.* **119**, 076401 (2017).
11. Ruffieux, P. *et al.* On-surface synthesis of graphene nanoribbons with zigzag edge topology. *Nature* **531**, 489–492 (2016).
12. Sun, Q. *et al.* Massive Dirac Fermion Behavior in a Low Bandgap Graphene Nanoribbon Near a Topological Phase Boundary. *Adv. Mater.* **32**, 1906054 (2020).
13. Gröning, O. *et al.* Engineering of robust topological quantum phases in graphene nanoribbons. *Nature* **560**, 209–213 (2018).
14. Llinas, J. P. *et al.* Short-channel field-effect transistors with 9-atom and 13-atom wide graphene nanoribbons. *Nat. Commun.* **8:633**, 1–6 (2017).
15. El Abbassi, M. *et al.* Controlled Quantum Dot Formation in Atomically Engineered Graphene Nanoribbon Field-Effect Transistors. *ACS Nano* **14**, 5754–5762 (2020).
16. Braun, O. *et al.* Optimized graphene electrodes for contacting graphene nanoribbons. *Carbon* **184**, 331–339 (2021).
17. Bennett, P. B. *et al.* Bottom-up graphene nanoribbon field-effect transistors. *Appl. Phys. Lett.* **103**, 253114 (2013).
18. Wang, H. *et al.* Graphene nanoribbons for quantum electronics. *Nat. Rev. Phys.* **3**, 791–802 (2021).
19. Mutlu, Z. *et al.* Short-Channel Double-Gate FETs with Atomically Precise Graphene Nanoribbons. in *2021 IEEE International Electron Devices Meeting (IEDM)* 37.4.1-37.4.4 (2021). doi:10.1109/IEDM19574.2021.9720620.

20. Zhang, J. *et al.* Ultimately-scaled electrodes for contacting individual atomically-precise graphene nanoribbons. Preprint at https://doi.org/10.48550/arXiv.2209.04353 (2022).

21. Zhang, J. *et al.* Tunable Quantum Dots from Atomically Precise Graphene Nanoribbons Using a Multi-Gate Architecture. *Adv. Electron. Mater.* **9**, 2201204 (2023).

22. Borin Barin, G. *et al.* Growth Optimization and Device Integration of Narrow-Bandgap Graphene Nanoribbons. *Small* 2202301 (2022) doi:10.1002/smll.202202301.

23. Chen, Z., Narita, A. & Müllen, K. Graphene Nanoribbons: On-Surface Synthesis and Integration into Electronic Devices. *Adv. Mater.* **32**, 2001893 (2020).

24. Passi, V. *et al.* Field-Effect Transistors Based on Networks of Highly Aligned, Chemically Synthesized *N* = 7 Armchair Graphene Nanoribbons. *ACS Appl. Mater. Interfaces* **10**, 9900–9903 (2018).

25. Martini, L. *et al.* Structure-dependent electrical properties of graphene nanoribbon devices with graphene electrodes. *Carbon* **146**, 36–43 (2019).

26. Slota, M. *et al.* Magnetic edge states and coherent manipulation of graphene nanoribbons. *Nature* **557**, 691–695 (2018).

27. Blackwell, R. E. *et al.* Spin splitting of dopant edge state in magnetic zigzag graphene nanoribbons. *Nature* **600**, 647–652 (2021).

28. Kan, E., Li, Z., Yang, J. & Hou, J. G. Half-Metallicity in Edge-Modified Zigzag Graphene Nanoribbons. *J. Am. Chem. Soc.* **130**, 4224–4225 (2008).

29. Zhao, S. *et al.* Optical Investigation of On-Surface Synthesized Armchair Graphene Nanoribbons. *Phys. Status Solidi B* **254**, 1700223 (2017).

30. Senkovskiy, B. V. *et al.* Making Graphene Nanoribbons Photoluminescent. *Nano Lett.* **17**, 4029–4037 (2017).

31. Son, Y.-W., Cohen, M. L. & Louie, S. G. Energy Gaps in Graphene Nanoribbons. *Phys. Rev. Lett.* **97**, 216803 (2006).

32. Yang, L., Park, C.-H., Son, Y.-W., Cohen, M. L. & Louie, S. G. Quasiparticle Energies and Band Gaps in Graphene Nanoribbons. *Phys. Rev. Lett.* **99**, 186801 (2007).

33. Wang, X.-Y. *et al.* Bottom-Up Synthesis of Heteroatom-Doped Chiral Graphene Nanoribbons. *J. Am. Chem. Soc.* **140**, 9104–9107 (2018).

34. Overbeck, J. *et al.* Optimized Substrates and Measurement Approaches for Raman Spectroscopy of Graphene Nanoribbons. *Phys. Status Solidi B* **256**, 1900343 (2019).

35. Borin Barin, G. *et al.* Surface-Synthesized Graphene Nanoribbons for Room Temperature Switching Devices: Substrate Transfer and ex Situ Characterization. *ACS Appl. Nano Mater.* **2**, 2184–2192 (2019).

36. Wang, Y. *et al.* Electrochemical Delamination of CVD-Grown Graphene Film: Toward the Recyclable Use of Copper Catalyst. *ACS Nano* **5**, 9927–9933 (2011).

37. Darawish, R. *et al.* Quantifying Alignment and Quality of Graphene Nanoribbons: A Polarized Raman Spectroscopy Approach. Preprint at https://doi.org/10.48550/arXiv.2307.09490 (2023).

38. Di Giovannantonio, M. *et al.* On-Surface Growth Dynamics of Graphene Nanoribbons: The Role of Halogen Functionalization. *ACS Nano* **12**, 74–81 (2018).

39. Fairbrother, A. *et al.* High vacuum synthesis and ambient stability of bottom-up graphene nanoribbons. *Nanoscale* **9**, 2785–2792 (2017).

40. Classen, T. *et al.* Templated Growth of Metal-Organic Coordination Chains at Surfaces. *Angew. Chem. Int. Ed.* **44**, 6142–6145 (2005).

41. Cañas-Ventura, M. E. *et al.* Self-Assembly of Periodic Bicomponent Wires and Ribbons. *Angew. Chem. Int. Ed.* **46**, 1814–1818 (2007).

42. Rousset, S., Repain, V., Baudot, G., Garreau, Y. & Lecoeur, J. Self-ordering of Au(111) vicinal surfaces and application to nanostructure organized growth. *J. Phys. Condens. Matter* **15**, S3363–S3392 (2003).

43. Overbeck, J. *et al.* A Universal Length-Dependent Vibrational Mode in Graphene Nanoribbons. *ACS Nano* **13**, 13083–13091 (2019).

44. Gillen, R., Mohr, M., Thomsen, C. & Maultzsch, J. Vibrational properties of graphene nanoribbons by first-principles calculations. *Phys. Rev. B* **80**, 155418 (2009).

45. Gillen, R., Mohr, M. & Maultzsch, J. Symmetry properties of vibrational modes in graphene nanoribbons. *Phys. Rev. B* **81**, 205426 (2010).

46. Verzhbitskiy, I. A. *et al.* Raman Fingerprints of Atomically Precise Graphene Nanoribbons. *Nano Lett.* **16**, 3442–3447 (2016).

47. Maghsoumi, A., Brambilla, L., Castiglioni, C., Müllen, K. & Tommasini, M. Overtone and combination features of G and D peaks in resonance Raman spectroscopy of the C78H26 polycyclic aromatic hydrocarbon. *J. Raman Spectrosc.* **46**, 757–764 (2015).

48. Eckmann, A., Felten, A., Verzhbitskiy, I., Davey, R. & Casiraghi, C. Raman study on defective graphene: Effect of the excitation energy, type, and amount of defects. *Phys. Rev. B* **88**, 035426 (2013).

49. Liu, D., Daniels, C., Meunier, V., Every, A. G. & Tománek, D. In-plane breathing and shear modes in low-dimensional nanostructures. *Carbon* **157**, 364–370 (2020).

50. Zhou, J. & Dong, J. Vibrational property and Raman spectrum of carbon nanoribbon. *Appl. Phys. Lett.* **91**, 173108 (2007).

51. Levshov, D. I. *et al.* Accurate determination of the chiral indices of individual carbon nanotubes by combining electron diffraction and Resonant Raman spectroscopy. *Carbon* **114**, 141–159 (2017).

Supporting information

Length evolution of 9-AGNRs on Au(788)

Precursor dose	1Å	2Å	3Å	4Å	5Å	6Å	7Å	8-9Å
GNR length at 1st-row position	14± 2	19± 5	35± 4	39± 4	43± 3	44± 2	45± 2	46± 2
GNR length at 2nd-row position				14± 5	22± 3	30± 2	36± 3	42± 5
GNR length at 3rd-row position							13± 2	36±5

Table S1: Length evolution of 9-AGNRs on Au(788). Average length (in nm) of GNRs at the first, second, and third-row positions for 30 samples of 9-AGNRs with different PDs ranging from 1-9 Å, along with their respective standard deviation.

9-AGNR quality and alignment as a function of PD on Au(788) and after substrate transfer

Raman mode	RBLM		CH		D		G	
Substrate	Au(788)	ROS	Au(788)	ROS	Au(788)	ROS	Au(788)	ROS
1 Å	14±1	15±2	30±5	35±4	13±2	14±1	11±2	13±1
2 Å	13±1	16±2	30±6	38±6	14±2	15±1	12±2	12±1
3 Å	15±2	17±5	29±5	33±9	13±2	19±8	13±2	12±1
4 Å	13±1	15±3	32±6	37±4	14±2	17±5	13±2	14±2
5 Å	14±1	16±1	32±5	33±4	13±1	16±4	12±2	14±1
6 Å	14±1	16±1	32±5	33±4	15±1	16±4	13±1	14±1
7 Å	16±1	15±1	33±5	32±4	17±2	18±4	14±2	15±2
8-9 Å	16±1	15±2	32±4	32±4	17±2	18±4	14±2	15±2

Table S2: The average full-width at half maximum (FWHM, in cm-1) of the RBLM, CH, D, and G modes measured for PDs from 1-9 Å in samples on Au(788) (40 samples) and after substrate transfer onto ROS (27 samples). These data are obtained from Raman maps acquired in vacuum using a 785 nm excitation wavelength.

Raman mode	RBLM		CH		D		G	
Substrate	Au(788)	ROS	Au(788)	ROS	Au(788)	ROS	Au(788)	ROS
1 Å	311±1	313±1	1242±3	1231±1	1334±1	1337±1	1596±1	1593±1
2 Å	311±1	312±1	1245±3	1235±2	1335±2	1337±1	1596±1	1593±2
3 Å	312±1	313±1	1245±2	1235±1	1336±1	1338±1	1597±1	1593±2
4 Å	312±2	313±1	1242±4	1235±1	1334±3	1337±1	1597±1	1594±2
5 Å	311±1	314±1	1246±2	1234±2	1334±1	1337±1	1596±1	1594±1
6 Å	311±1	313±1	1247±2	1236±2	1336±2	1338±1	1596±1	1594±2
7 Å	311±1	312±1	1247±3	1235±2	1338±2	1339±1	1597±1	1595±2
8-9 Å	312±1	313±1	1245±2	1232±2	1339±2	1339±1	1597±1	1594±1

Table S3: The average peak position (in cm-1) of the RBLM, CH, D, and G modes measured for PDs from 1-9 Å in samples on Au(788) (40 samples) and after substrate transfer onto ROS (27 samples). These data are obtained from Raman maps acquired in a vacuum using a 785 nm excitation wavelength.

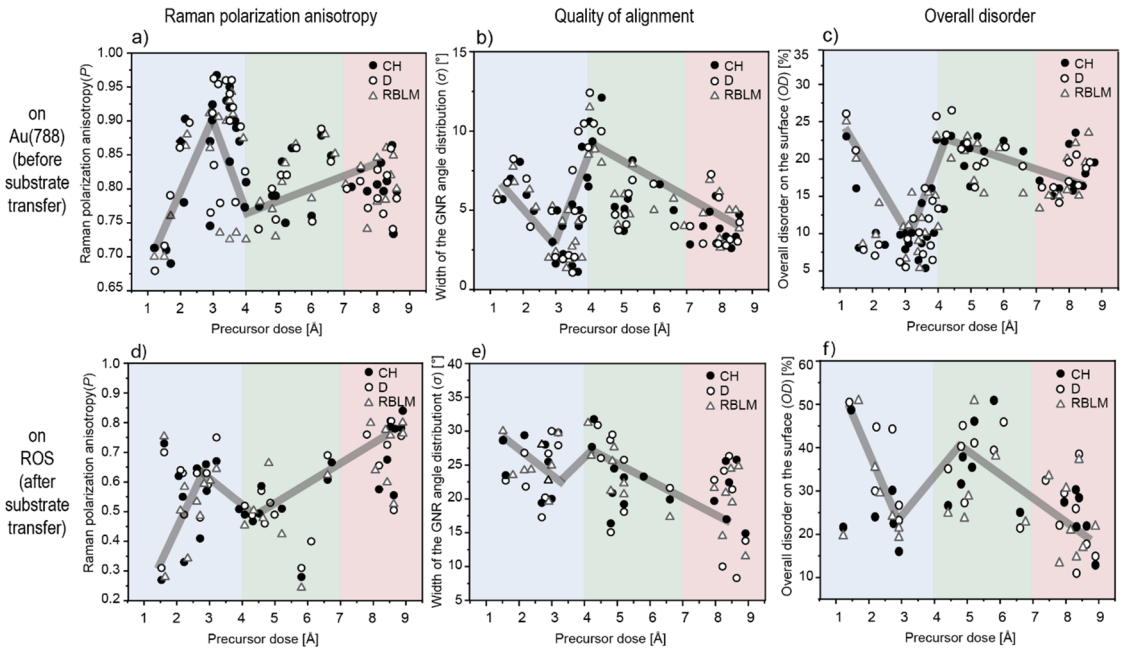

Figure S1: Impact of PD on the alignment of 9-AGNRs on Au(788) and after substrate transfer onto ROS. The alignment was evaluated using Eq (2) from polarized Raman data for different Raman-active modes (RBLM, CH, and D). Panels (a), (b), and (c) show the average *P, σ,* and *OD* of RBLM, CH, and D modes, respectively, as a function of PD from 1-9 Å on Au(788), and panels (d), (e) and (f) after substrate transfer onto ROS. The colored background areas represent the growth regimes in which GNRs predominantly grow at the first-row position (blue), at the second-row position (green), and at the third-row position (red). The data were acquired in a vacuum using 785 nm excitation.

The impact of inefficient substrate transfer on GNR integrity and alignment

Here, we investigate the effect of inefficient substrate transfer on the integrity and alignment of GNRs in low-PD samples (3 Å) using Raman characterization. Figure S2 shows the Raman spectra and polar plot for a sample with PD=3 Å on the growth surface Au(788) and after inefficient substrate transfer onto ROS. Table S4 presents the FWHM and peak position for the RBLM, CH, D, and G modes acquired with the 9-AGNRs on Au(788) and after their transfer onto ROS. Our observations indicate that inefficient substrate transfer resulted in an increase in FWHM and peak shifts for all active Raman modes. Specifically, we observe a large shift of 10 cm^{-1} for the RBLM and a significant shift of 44 cm^{-1} for the CH mode. The FWHM of RBLM, CH, D, and G modes broaden from 11, 31, 12, and 13 cm^{-1} on Au(788) to 25, 100, 85, and 44 cm^{-1}on ROS, respectively, confirming the inefficiency of the substrate transfer for this sample. Changes in the CH-D region can be attributed to damage in the GNR edge structure[1–3], while changes in the G and RBLM modes suggest the presence of defects and/or doping[4–6].

To investigate the influence of inefficient substrate transfer on the alignment and overall disorder on the surface (*OD*), we extract *P*, *σ*, and *OD* on both substrates for the G mode (Table S5). We observe a significant decrease in *P* along with broadening of *σ*: $P_{Au(788)}$ = 0.92 ($\sigma_{Au(788)}$= 1°) to P_{ROS}= 0.40 (σ_{ROS}= 40°). Additionally, *OD* increases from 14% on Au (788) to 35% on ROS.

These findings confirm that GNRs are susceptible to defects and can vary in quality upon electrochemical delamination transfer.

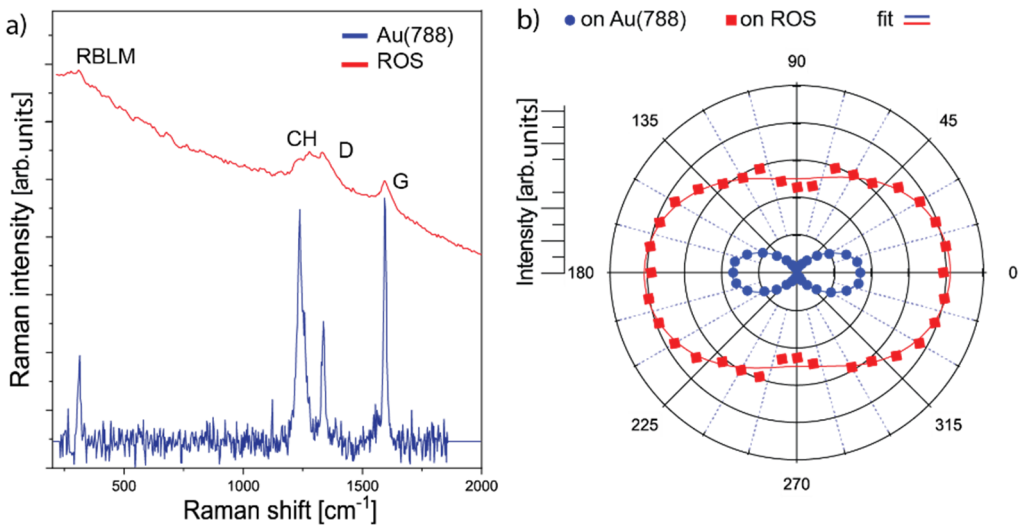

Figure S2: Raman spectra and G-mode polar plots for a 9-AGNR sample grown with PD =3 Å on Au(788) and after inefficient substrate transfer onto the ROS. (a) Raman spectra on Au(788) in blue and on the ROS in red. (b) Polar plot of the Raman intensity of the G-mode on Au(788) in blue and on the ROS in red. Spectra were acquired using an excitation wavelength of 785 nm under vacuum conditions and changing the incident laser's angle (θ_{in}) with respect to GNRs' alignment direction (θ = 0°), without utilizing a polarizer in the detection path.

Substrate	Raman mode	RBLM	CH	D	G
Au(788)	Peak position [cm^{-1}]	312	1240	1339	1593
	FWHM [cm^{-1}]	11	31	12	13
ROS	Peak position [cm^{-1}]	302	1284	1337	1591
	FWHM [cm^{-1}]	25	100	85	44

Table S4: Peak position and FWHM of the RBLM, CH, D, and G modes for the sample in Fig. S2 on Au(788), and after transfer onto ROS.

Substrate	Au(788)	ROS
Raman polarization anisotropy (*P*)	0.92	0.4
Quality of alignment (σ) [°]	1±0.05	40±0.8
Overall disorder on the surface (*OD*) [%]	14	35

Table S5: *P*, σ, and *OD* of the G mode for the sample in Fig. S2 on Au(788), and after transfer onto ROS.

References

1. Senkovskiy, B. V. *et al.* Making Graphene Nanoribbons Photoluminescent. *Nano Lett.* **17**, 4029–4037 (2017).
2. Barin, G. B. *et al.* Surface-synthesized graphene nanoribbons for room-temperature switching devices: substrate transfer and ex-situ characterization. *ACS Appl. Nano Mater.* (2019) doi:10.1021/acsanm.9b00151.
3. Overbeck, J. *et al.* Optimized Substrates and Measurement Approaches for Raman Spectroscopy of Graphene Nanoribbons. *Phys. Status Solidi B* **256**, 1900343 (2019).
4. Senkovskiy, B. V. *et al.* Boron-Doped Graphene Nanoribbons: Electronic Structure and Raman Fingerprint. *ACS Nano* **12**, 7571–7582 (2018).
5. Ma, C. *et al.* Oxidization stability of atomically precise graphene nanoribbons. *Phys. Rev. Mater.* **2**, (2018).
6. Senkovskiy, B. V. *et al.* Semiconductor-to-Metal Transition and Quasiparticle Renormalization in Doped Graphene Nanoribbons. *Adv. Electron. Mater.* **3**, 1600490 (2017).

Chapter 5

Quantification of graphene nanoribbon transfer efficiency: A polarized Raman spectroscopy analysis

Introduction

Graphene nanoribbons (GNRs) exhibit distinctive physicochemical properties such as tunable bandgaps[1] arising from quantum confinement and due to their nanometer-scale widths[2–5] and atomically precise edge topologies[1,6–11]. Such tunability achieved at the atomic scale opens an immense potential for applications in electronics[12–23], spintronics[24–26], and photonic[27–31] devices.

To achieve atomic-level precision in the synthesis of GNRs, on-surface synthesis is the method of choice[5]. This technique involves sublimating specifically designed precursor molecules on a metallic catalyst substrate in an ultra-high vacuum (UHV), followed by their surface-assisted covalent coupling and subsequent cyclization. Remarkable progress has been achieved since the groundbreaking research by Cai et al. in 2010[5], resulting in the synthesis of armchair-edge GNRs (AGNRs) with various widths (including 5-[3], 7-[30], 9-[2], and 13[32]-AGNRs) and edge topologies (armchair[33], zigzag[10], cove[34], etc.), as well as exotic topological quantum phases[6,7].

To integrate GNRs into field-effect transistor (FET) devices, a key aspect is the precise control of GNR growth orientation. Uniaxially aligned GNRs significantly enhance device performance and yield if the GNRs are oriented along the source-to-drain direction[19,22]. To achieve this, GNRs need to be grown on a vicinal surface such as Au(788), where they grow uniaxially aligned along the template step edges of the vicinal surface[15]. Successful device integration requires transferring GNRs from the growth surface to the device while preserving their alignment and structural integrity. The transfer of GNRs from vicinal crystals is achieved by an electrochemical delamination method, initially developed for CVD-grown graphene[35,36] and later adapted for GNRs[37,29]. This method involves the generation of hydrogen bubbles via water electrolysis between the GNRs and the metal substrate, which results in the delamination of GNRs normally supported by a polymer layer such as PMMA[37,29].

In Chapter 4, we discuss the transfer success rate of 27 transferred samples out of 40 samples on the Au(788) with varying surface coverages, transferred by the electrochemical delamination method. We observed a significant decrease in the transfer success rate as the surface coverage decreased -77% vs. 53% (from a full monolayer to 1 GNR per step edge, respectively). In a recent study, Lin *et al* also observed a striking difference in device yield by varying the initial surface coverage of non-aligned 9-AGNRs. In their work, the yield is defined as the percentage of devices with a drain current at least 10 times larger than the gate leakage current. While

experimental yields for high, medium, and low coverage samples are in the order of 100%, 80%, and 40% respectively, simulated yields are found to be 60%, 65%, and 40%. Variances between experimental and simulated yields are attributed to inter-ribbon conductance, which becomes pronounced in densely packed samples and is not considered in the simulations[38].

These results indicate the significant impact of surface coverage on the transfer success rate and yield of devices. Therefore, accurately quantifying the number of transferred GNRs becomes crucial to better understanding the behavior of GNR-based devices.

In this chapter, we address the challenge of quantifying GNR transfer efficiency, denoted as "η", through an experimental approach combining Raman spectroscopy and scanning tunneling microscopy (STM). We develop a systematic sample preparation and characterization process and derive a mathematical equation to determine the transfer efficiency of aligned 9-AGNRs with varying surface coverages. First, we use STM to characterize 9-AGNR samples on Au(788) in terms of surface coverage, GNR quality, and alignment. Polarized Raman spectroscopy is then used to characterize GNR quality and alignment both on the growth substrate and after substrate transfer. Finally, we quantify the amount of transferred GNRs based on the polarized Raman data collected before and after transfer, and unveil the influence of surface coverage on GNRs transfer efficiency.

Results and discussion:

Raman and STM characterization

To quantify the amount of GNRs being transferred we conduct a systematic procedure for sample preparation, transfer, and characterization. The procedure consists of the following steps: (1) growth of GNR samples and characterization by STM to confirm their initial surface coverage, (2) transfer of GNRs onto a Raman-optimized substrate (ROS)[37], and (3) assessment of their integrity and alignment using Raman spectroscopy and polarized Raman spectroscopy on both the growth surface and after substrate transfer, Fig. 1. For this procedure, we prepare two types of samples: aligned 9-AGNRs samples with different surface coverages to be quantified after substrate transfer, and non-aligned 9-AGNRs samples as a reference.

To prepare aligned 9-AGNRs, we initially deposit the precursor molecule 3',6'-diiodine-1,1':2',1''-terphenyl (DITP) [33] on a catalytic surface of Au(788) followed by two annealing steps to activate the polymerization and cyclodehydrogenation reactions[5,4]. By controlling the deposition rate and time, we achieve surface coverages of 1 monolayer (1 ML), 0.8 ML, and 0.4 ML of 9-AGNRs. Representative STM images of each sample are presented in Fig. 1e.

In addition to the aligned 9-AGNR samples, we synthesize two samples with 1 ML of non-aligned 9-AGNRs on Au(111)/mica, using the same monomer and preparation steps as for the aligned GNR samples. We use this sample (1 ML 9-AGNR grown on Au(111) /mica) as the reference sample for 100% successful transfer efficiency, as previous studies have demonstrated that GNRs transferred from Au(111) films via the polymer-free transfer are transferred in fully and

homogeneously across the target substrate.[40] The STM images of the 1 ML 9-AGNRs on Au(111)/mica samples used as a reference in this work are shown in Fig. 1a and Fig. S1.

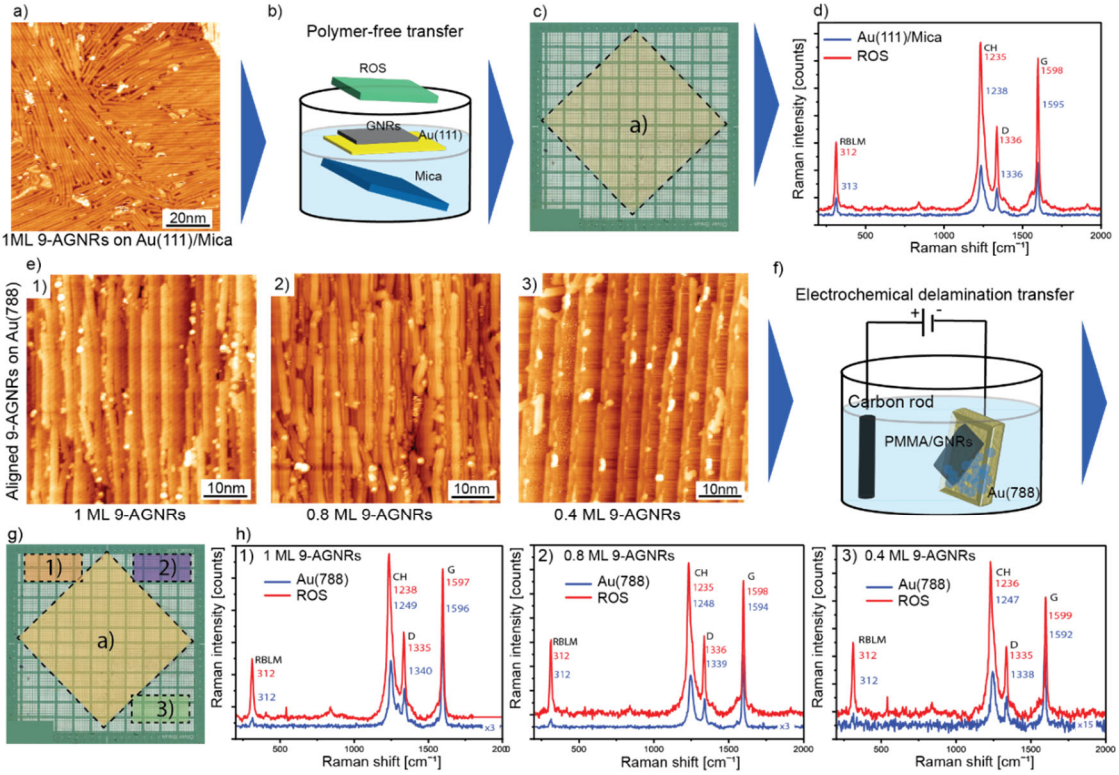

Figure 1: Fabrication, substrate transfer, and characterization of 9-AGNRs. (a) STM image of 1 ML of non-aligned 9-AGNRs on Au(111)/mica (reference sample). b) Schematic representation of the polymer-free transfer method used to transfer the reference samples from Au(111)/mica to the ROS. c) Illustration highlighting the transferred sample's position on the ROS. d) Raman spectra of the reference sample on the growth surface (blue) and after substrate transfer onto the ROS (red). e) STM images of aligned 9-AGNRs with surface coverages of 1 ML, 0.8 ML, and 0.4 ML on Au(788). The images highlight the parallel growth of GNRs along the Au(788) step edges. f) Schematic representation of the electrochemical delamination transfer process employed to transfer 1 ML, 0.8 ML, and 0.4 ML from Au(788) to the ROS. g) Illustration highlighting the transferred samples' position on the ROS. (h) Raman spectra of the 1 ML, 0.8-0.9 ML, and 0.4 ML samples on the growth surface (blue) and after substrate transfer onto the ROS (red).

Following the preparation and characterization of the samples by STM, we transfer them from the growth surface to a Raman-optimized substrate (ROS)[37] for Raman characterization. Here, we employ two different transfer methods depending on the growth substrate. For the reference sample consisting of non-aligned 9-AGNRs grown on an Au(111)/mica, we employ a polymer-free transfer method. This method involves delaminating the Au/GNR film from the mica, picking up the GNR/Au layer with the target substrate, and finally etching away the Au layer[40], Fig. 1b. For the aligned 9-AGNR samples grown on Au(788) the electrochemical delamination transfer is used, Fig. 1f [37,29]. To eliminate any substrate-related differences that might influence the Raman signals, we transfer all the samples onto the same ROS following a specific substrate transfer sequence: First, we transfer one of the reference samples from Au(111)/mica to the ROS. Then, we sequentially transfer the aligned samples with 1 ML, 0.8 ML, and 0.4 ML surface coverage from the Au(788) substrate to the same ROS. Finally, we transfer a second reference sample from Au(111)/mica onto the same ROS (see Fig. S1). It is important to note that we collect Raman spectra immediately after each substrate transfer, to avoid any potential GNR

damage due to the different annealing and chemical treatment processes that occur during each transfer (more details in the supplementary information Fig. S2).

Raman spectroscopy is our method of choice to characterize GNRs after substrate transfer. Raman spectroscopy is a non-destructive technique that provides valuable information on carbon-based materials[41,42], including graphene[43], carbon nanotubes (CNTs)[41], and GNRs[44]. It allows for the probing of large areas (50 µm or even 100x100 µm), enabling accurate measurements for overall homogeneity. Additionally, Raman spectroscopy can efficiently characterize GNRs' structural integrity, alignment, and edge structure both on the growth surface and after substrate transfer[29,37,40]. In our analysis, we focus on characterizing GNR fingerprint modes, with a specific emphasis on the G mode which is located at ~1600 cm^{-1} [45,46]. This mode arises from in-plane vibrations and is present in all sp^2 carbon-based materials[47,43]. Furthermore, we also examine the high-frequency CH-D modes between 1100-1500 cm^{-1}, as they provide insights into the edge structure of GNRs[45,46,48,49]. Specifically, the CH-bending mode at ~1200 cm^{-1} corresponds to the vibrations of the edge hydrogen atoms, while the D peak at ~1300 cm^{-1} indicates the breaking of the periodicity of a perfect honeycomb lattice. It is important to note that in GNRs, unlike graphene, the D peak is an intrinsic mode resulting from the presence of atomic precision edges rather than defects[50,51]. Additionally, we measure the radial breathing-like mode (RBLM), which is found at low Raman frequencies[52,22,2], and is directly related to the GNR width.

Raman spectra of aligned 9-AGNR samples with a surface coverage of 1 ML, 0.8 ML, and 0.4 ML, as well as the non-aligned 9-AGNR reference samples on Au(111)/mica, are taken under vacuum (~10^{-2} mbar) using a home-built vacuum chamber, with a 785 nm laser wavelength, 40 mW power, and a 50x objective, Figs. 1d and 1h, in blue. After substrate transfer onto the ROS, we obtain Raman spectra in ambient conditions using a 785 nm laser wavelength, 1.5 mW power, and a 100x objective lens, Figs. 1d and 1h, in red. The ROS samples are measured in air due to the large size of the substrate, which did not fit in our home-built vacuum chamber.

After substrate transfer, all intrinsic Raman peaks of 9-AGNRs (RBLM, CH, D, and G) are present in the 1 ML, 0.8 ML, and 0.4 ML samples, as well as the reference samples, confirming the overall preservation of GNRs' structural integrity during both transfer processes.

Quantification of GNR transfer efficiency

The accurate determination of the transfer efficiency by Raman spectroscopy is not a straightforward task due to the various factors influencing the Raman intensity, especially after substrate transfer. In the previous chapters 3 and 4, we highlight the coverage-dependent nature of the transfer quality of aligned GNRs. The overall decrease in the signal-to-noise ratio for samples with low surface coverages as well as the low transfer successful rate, indicate that these samples transfer less efficiently[39]. To address this difference in the quantity of GNR being transferred, we introduce a transfer efficiency factor denoted by "η" in Eq. (1). Here, I_{ROS} represents the Raman intensity measured on the ROS, while $I_{Au(788)}$ represents the Raman intensity obtained on the Au(788) growth surface.

$$I_{ROS} = I_{Au(788)} \cdot \eta \quad (1)$$

For a more accurate quantification, we consider the following factors that can influence the Raman intensity: (i) the substrate factor (M_{sub}) which takes into account the influence of the substrate surface on the Raman signal, considering the transition from a metallic surface (GNR growth surface) to an oxide-based one (ROS), (ii) the measurement condition factor (M_{cond}) accounts for differences in Raman measurement conditions, such as environment (vacuum versus air) and hardware (lens and laser power differences), and (iii) the alignment and isotropic contribution factor, which is introduced to address the influence of GNR angle distribution (alignment) and the polarized-independent Raman intensity (isotropic contribution) on the overall Raman signal. ($A_{Au(788)}^{Align}$) and (A_{ROS}^{Align}) denote the angle distribution of the total surface area of aligned GNRs on the growth surface and ROS, respectively. As observed in the previous chapters 3 and 4, these factors are highly dependent on surface coverage. In subsequent sections, each parameter's contribution to the final transfer efficiency quantification is discussed in detail.

By including all three factors we derive equations (2) and (3). These equations calculate η by considering the ratio of (A_{ROS}^{Align}) to that on the growth surface ($A_{Au(788)}^{Align}$) while accounting for the various factors that can influence the Raman intensity (M_{sub} and M_{cond}):

$$A_{ROS}^{Align} = M_{sub} \cdot M_{cond} \cdot A_{Au(788)}^{Align} \cdot \eta \quad (2)$$

$$\eta = \frac{A_{ROS}^{Align}}{M_{sub} \cdot M_{cond} \cdot A_{Au(788)}^{Align}} \quad (3)$$

Our study is centered on the G mode intensities. The G peak in GNRs' Raman spectra encompasses two in-plane optical modes: the longitudinal-optical (LO) mode, or G1 peak, and the transverse-optical (TO) mode, or G2 peak[2,40]. Our measurements employ a 785 nm laser, resolving only the LO (G1) mode. For clarity, we refer to this mode as the G mode throughout our study.

The substrate factor (M_{sub})

To accurately quantify η of GNRs based on their Raman signal on different substrates, it is crucial to consider the influence of the substrate surface. In our experiment, we expect that the Raman signal of GNRs on a gold surface will be quenched. In contrast, our ROS enhances the Raman signal due to the constructive interference that happens on the 40 Al_2O_3/80nm Au surface. Therefore, we introduce a M_{sub} factor to calibrate the enhancement effect of the ROS compared to the quenching effect of metallic substrates.

To determine this factor, we require a sample that has been fully transferred from the growth surface to the ROS with a 100% transfer efficiency. This ensures that any variations in the Raman signal can be attributed only to the substrate and not to the change in the quantity of transferred GNRs or measurement conditions. Following the methodology described in Fig. 1,

we prepared two reference samples (non-aligned 1 ML9-AGNRs) and transferred them using the polymer-free transfer method onto the ROS (Fig. 1 and Fig. S1). We acquire the Raman spectra of these samples on the Au(111)/mica substrate and after substrate transfer onto ROS under identical measurement and environmental conditions. By employing a Lorentzian curve fitting for the G mode, we extract the area of the G mode on both the ROS (A_{ROS}) and the Au(111)/mica substrate ($A_{Au(111)/mica}$). Specifically, M_{sub} is obtained as the ratio A_{ROS} to $A_{Au(111)/mica}$, as described in Eq. (4).

$$M_{sub} = \frac{A_{ROS}}{A_{Au(111)/mica}} \tag{4}$$

Considering that the ROS enhances the Raman signal, the calculated value of the M_{sub} is expected to be greater than 1. To obtain a reliable estimation of M_{sub}, we average the values obtained from the two reference samples, resulting in a value of 42±5. These findings are consistent with previous studies by Overbeck, J. et al.,[37] which reported a Raman signal enhancement factor of 43 for 9-AGNRs on ROS compared to the GNRs on Au surface.

Measurements conditions factor (M_{cond})

Raman measurements before and after transfer are taken under different conditions, in a vacuum using a 50x objective lens and 40 mW laser power for samples on the Au (788) growth substrate and in ambient conditions for samples on the ROS with a 100x objective lens and 1.3 mW laser power. Therefore, it is important to evaluate the differences that might arise in the Raman intensity. To account for these differences, we characterized a 1 ML 9-AGNR sample on Au(111)/mica in both vacuum and ambient environments and normalized the Raman intensity concerning the objective and laser power. The factor M_{cond} is determined from the G mode acquired from the Raman maps of a 1 ML 9-AGNR layer on the Au(111)/mica surface, obtained at several locations in the two different conditions we explained above. These different conditions are in vacuum (50x objective lens and 40 mW laser power) and in ambient conditions (100x objective lens and 1.3 mW laser power). A Lorentzian curve fit of the G mode peak allowed us to determine the area of the G mode under both ambient conditions ($A_{ambient}$) and vacuum conditions (A_{vacuum}). M_{cond} is then calculated as the ratio of $A_{ambient}$ to A_{vacuum}, as described in Eq. (5). We determined M_{cond} = 2.3±0.4, indicating that the G mode's area for the same sample is doubled in ambient conditions relative to those in a vacuum, taking into consideration both the laser power and objective. This observation implies that the thickness of the window in our custom-built vacuum chamber plays a part in decreasing the Raman intensity.

$$M_{cond} = \frac{A_{ambient}}{A_{vacuum}} \tag{5}$$

The alignment and isotropic contribution factor ($A^{Align}_{Au(788)/ROS}$)

As discussed in the previous chapters, we find significant differences in GNR alignment on Au(788) and ROS based on the initial surface coverage. Alongside the change in alignment, there is also a change in the isotropic Raman contribution arising from small polycyclic aromatic

hydrocarbons (PAHs), short GNRs, and polymer residues after substrate substrate transfer. These components result in a non-zero Raman intensity for directions orthogonal to the GNR axis. We incorporated this factor into our equation to correct for GNR alignment and account for isotropic contribution variations, both on the growth surface and post-transfer, due to the change in coverage. To address this, we extract ($A_{Au(788)}^{Align}$) and (A_{ROS}^{Align})so it takes the fitted values that take into account the coverage dependence using Eq. (6), which is explained in chapters 3 and 4.

$$I_{exp}(\vartheta) = A_x^{Align} \cdot \int_{0°}^{360°} cos^2(\varphi) \cdot \frac{1}{\sigma\sqrt{2\pi}} e^{-\frac{(\vartheta-\varphi-\vartheta_0)^2}{2\sigma^2}} d\varphi + B \cdot \frac{1}{2} \quad (6)$$

Through this equation, we extract the fraction A_x^{Align}, which represents the surface area of GNRs aligned on either the ROS or Au(788), as indicated by 'x'. Additionally, we define σ as the width of the Gaussian distribution, which is used as a metric for the quality of alignment. Fraction B corresponds to the surface area contributing to the isotropic Raman signal. In this context, the fraction A is associated with a specific σ and isotropic contribution, which are coverage-dependent.

The transfer efficiency (η)

After extracting (A_{ROS}^{Align}), ($A_{Au(788)}^{Align}$), M_{sub} and M_{cond}, we calculate the transfer efficiency using Eq.3 to be η = 52%, 70%, and 35% for the samples with surface coverage = 1 ML, 0.8 ML, and 0.4 ML, respectively. The samples with higher surface coverage, such as the 1 ML and 0.8 ML samples, consistently have higher values of η. This can be mostly attributed to GNRs behaving like a film at such higher coverages, increasing the likelihood of being fully transferred. However, variations among high-coverage samples indicate potential limitations in the reproducibility of the transfer process. This observation is in line with our findings in Chapter 4, where high-surface coverage samples show a transfer success rate of 77% while medium- and low-surface coverages yielded success rates of 60% and 54%, respectively. In contrast, the low η (35%) for 0.4 ML can be explained by the strong interaction of GNRs with the Au(788) step edges and the lack of film-like behavior.

To further explore the relationship between surface coverage and η, we analyzed 29 samples transferred to ROS. These samples were synthesized by depositing the DITP precursor molecule onto Au(788) at a consistent deposition rate of 1 Å/min, with deposition times ranging from 1 to 8-9 minutes and following the same preparation steps of the aligned samples in Fig. 1. By maintaining a deposition rate of 1 Å/min and increasing the deposition time in 1-minute intervals, we achieved coverages ranging from 1 to 9 Å on the surface. After 9-AGNR synthesis, these samples were individually transferred using electrochemical delamination onto different ROS. Fig. 2 displays η values determined for these 29 samples. We find a clear trend in η based on sample surface coverage. Low-coverage samples (1 Å, 2 Å, 3 Å) exhibit an average η of approximately 26% ± 21%(standard deviation), while medium-coverage samples (4 Å, 5 Å, 6 Å) show an average η of around 44% ± 26%. Notably, high-coverage samples ranging from 7-9 Å display the highest η, averaging approximately 65% ± 13%. Even though we observe a strong

variation, our results indicate a general trend of better transfer efficiency with increasing surface coverage.

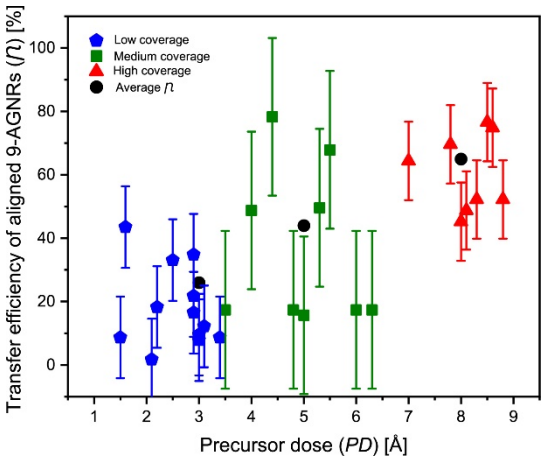

Figure 2: Impact of surface coverage on substrate transfer efficiency η of 9-AGNRs for 29 different samples. Low-coverage samples (1 Å, 2 Å, 3 Å) are shown in blue, medium-coverage samples (4 Å, 5 Å, 6 Å) in green, and high-coverage samples (7-9 Å) in red. These samples exhibit average η values of approximately 26%, 44%, and 65%, for low-, medium-, and high-coverage samples respectively. The black circle represents the averages η, and the error bars indicate the standard deviation of η at each surface coverage. The variation among these samples highlights reproducibility challenges in the electrochemical delamination method.

Long-term stability of GNR structural integrity and alignment in correlation to their surface coverage

Assessing the long-term stability of GNRs under ambient conditions is crucial for their room-temperature (RT) FET applications. To evaluate the long-term stability of aligned 9-AGNRs, the transferred samples (1 ML, 0.8 ML, and 0.4 ML) depicted in Fig. 1 were stored at RT under ambient conditions for 30 months. Raman spectra were then obtained in ambient conditions with a 100x objective lens and 1.3 mW laser power as used to characterize the sample after direct substrate transfer, as shown in Fig. 3. Comparing the profiles immediately after substrate transfer (0 months, blue) to those after 30 months of storage (red), it is observed that all Raman active modes are still present, but with a pronounced decrease in intensity, especially for low coverage samples.

Changes in peak characteristics are monitored by examining the FWHM and peak position for all the samples immediately after substrate transfer and after 30 months of storage. The FWHM of the G and D modes show no change for the 1 ML and 0.8 ML samples after 30 months of storage. However, the 0.4 ML sample exhibits increased FWHM values for the G (from 13 cm^{-1} to 17 cm^{-1}) and D modes (from 17 cm^{-1} to 39 cm^{-1}). Notably, the FWHM of the CH peak for the 0.4 ML sample significantly increases from 39 cm^{-1} to 61 cm^{-1} after 30 months of storage. In contrast, the 1 ML and 0.8 ML samples show a CH mode broadening in the order of 9 cm^{-1} and 2 cm^{-1}, respectively. Regarding peak shifts, the RBLM, D, and G modes for all samples remain within the Raman experimental accuracy (3 cm^{-1}). After 30 months of storage, all samples exhibit a consistent blue shift of approximately 6-9 cm^{-1} in the edge CH mode compared to measurements taken immediately after substrate transfer. Notably, these shifts become more

pronounced with decreasing surface coverage. This phenomenon aligns with findings from a previous study that also identified a correlation between GNR coverage and peak shifts[54]. Such differences can be attributed to the adsorption and intercalation of airborne molecules onto the Au surface. The long-term stability also seems to be influenced by the surface coverage, where a full monolayer GNR coverage serves as a protective barrier, slowing down the intercalation/degradation process.

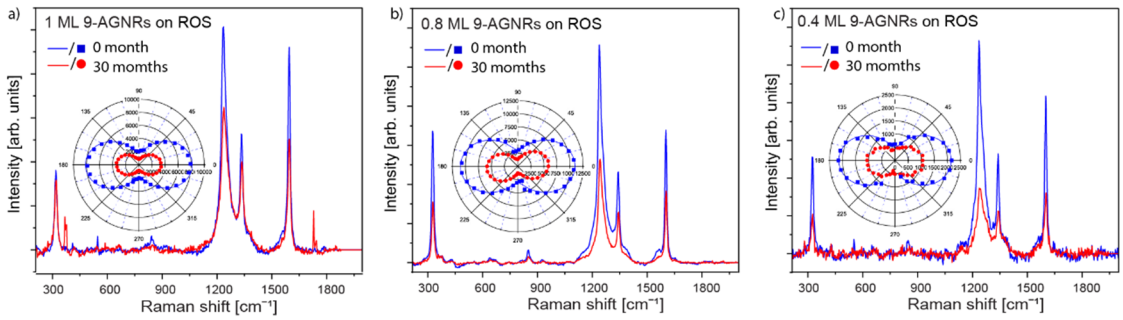

Figure 3: Long-term storage effects on Raman spectra of 9-AGNRs. The Raman spectra of 9-AGNRs with coverages of 1 ML, 0.8 ML, and 0.4 ML are recorded immediately after their transfer onto ROS (0 months, depicted in blue) and after 30 months of storage under ambient conditions (shown in red). The inset features a Polar plot that illustrates the intensity of the G mode as a function of polarization angle ϑ. The blue and red solid lines represent the fits to the measured data using an extended Gaussian distribution model[39].

We also evaluated the quality of alignment of the transferred samples over time by polarized Raman spectroscopy. To evaluate GNR alignment, we used the two approaches described in chapters 3 and 4: Raman polarization anisotropy (*P*) and an extended Gaussian distribution model (Eq.6).

We extracted *P*, σ, and *OD* immediately after substrate transfer (0 months) and again after 30 months, Table S1. The corresponding polar plots for the samples are depicted in the inset of Fig. 3. The 1 ML and 0.8 ML samples show negligible alignment decrease after 30 months, with *P* and σ values changing from $P_{0\ month}$= 0.58 to $P_{30\ month}$= 0.58 (from $\sigma_{0\ month}$ = 15° to $\sigma_{30\ month}$ = 16°) for 1ML and $P_{0\ month}$= 0.62 to $P_{30\ month}$= 0.63 for 0.8-9 ML (from $\sigma_{0\ month}$ = 16° to $\sigma_{30\ month}$ = 15°). However, the 0.4ML sample exhibits a significant decrease in GNR alignment after 30 months, with *P* values decreasing from $P_{0\ month}$ = 0.58 to $P_{30\ month}$ = 0.45) and a broadening of σ (from $\sigma_{0\ month}$ = 19° to $\sigma_{30\ month}$ = 32°). This decrease in alignment can reflect the lack of support between sparsely distributed GNRs.

Comparing the *OD* values after 30 months with the initial measurements (0 months) for all samples, we observe that surface saturation with polarized independent impurities reaches its maximum after substrate transfer, showing no significant increase over time.

Overall, these results highlight the importance of GNR coverage in preserving long-term GNR structural integrity and alignment. Our findings demonstrate that low-coverage samples exhibit the least stability in terms of both structural integrity and degree of alignment, while high-coverage samples demonstrate better structural integrity and alignment stability. These findings emphasize the critical role of GNR coverage in achieving long-term structural integrity and alignment stability, which are important aspects of GNR-based device applications.

Conclusion

In summary, we have presented an accurate quantification of the transfer efficiency (η) of graphene nanoribbons (GNRs) based on Raman and polarized Raman spectroscopy. Factors such as the substrate, measurement conditions, and alignment of the GNRs can affect the Raman intensity and are taken into account in the quantitative equation for η. Our findings show that η is coverage-dependent: 26% for low-, 44% for medium-, and 65% for high-coverage samples. The variation within each group highlights the challenges in achieving consistent reproducibility. Additionally, we performed a stability analysis of GNRs over 30 months. We found that the GNR stability was also coverage-dependent, with the lower-coverage GNRs degrading more rapidly and getting more misaligned compared to the high-coverage samples. Overall, our study provides valuable insights into the transfer efficiency and stability of GNRs at different coverages. These findings underscore the importance of consistent methods and can contribute to the optimization of GNR-based device performance. Furthermore, our approach can be extended to different GNR structures and substrates, enhancing the understanding of substrate transfer efficiency and device performance in FET applications.

Methods

On-Surface Synthesis and STM Characterization of 9-AGNRs

The Au(788) single crystal growth substrate (MaTecK GmbH, Germany) was cleaned in ultra-high vacuum (UHV) with two cycles of sputtering at 1 kV Ar+ for 10 minutes and annealing at 420 °C for 10 minutes. The 9-AGNR precursor monomer 3′,6′-di-iodine-1,1′:2′,1′′-terphenyl (DITP) was then sublimated onto the clean Au surface from a quartz crucible heated to 70 °C while the substrate remained at room temperature[33]. A quartz microbalance was used to control the deposition rate of the precursor molecules at 1 Å /min. The deposition rate is not calibrated to accurately correspond to the true surface coverage. Instead, it is calibrated relative to a standard measurement obtained through STM. High- and low-coverage samples were obtained by DITP deposition for 8 and 3 minutes, respectively. Following deposition, the substrate was heated to 200 °C (0.5 K/s) for 10 minutes to initiate DITIP polymerization, followed by annealing at 400 °C (0.5 K/s) for 10 minutes to form the GNRs by cyclodehydrogenation [5,2,4,33].

Scanning tunneling microscopy images of 9-AGNRs grown on Au(788) were acquired at room temperature using a Scienta Omicron VT-STM. Topographic images were acquired in constant current mode using a sample bias of -1.5 V and a setpoint current of 0.03 nA.

Substrate transfer of GNRs

AGNRs were transferred from their Au/mica or Au(788) growth substrate to silicon-based substrates by two different transfer methods. The polymer-free transfer was used to transfer Au/mica samples, whereas the Electrochemical delamination transfer method (bubbling transfer)was used to transfer Au(788) samples. For polymer-free transfer, GNR/Au/mica was

floated in 38% HCl in water[40], which delaminated the mica and left the Au film floating. While the sample is floating, the acid is diluted by adding water to reduce the HCL concentration. The RO substrate was used to pick up the floating gold film, with the GNRs facing the dielectric surface. A drop of ethanol was applied to the top of the Au film to enhance adhesion between the Au film and the target substrate. The sample was then annealed at 100 °C for 10 minutes. Following that, KI/L2 was used to etch the gold. Finally, the sample was cleaned by immersing it in ultrapure water for 5 minutes and then rinsing it with acetone/ethanol.

Transfer of 9-AGNRs from their Au(788) growth substrate to the Raman-optimized substrates (ROS) was done by electrochemical delamination transfer[37,29]. First, a support layer of poly(methyl methacrylate) (PMMA) was spin-coated (4 PMMA layers, 2500 rpm for 90 s) on the 9-AGNR/Au(788) samples, followed by a 10-minute curing process at 80 °C. To shorten the time required for PMMA delamination, PMMA was removed from the Au(788) crystal's edges using an 80-minute UV exposure, followed by a 3-minute development in water/isopropanol. Electrochemical delamination was performed in an aqueous solution of NaOH (1 M) as the electrolyte. A DC voltage of 5V (current ≈0.2 A) was applied between the PMMA/9-AGNR/Au(788) cathode and a glassy carbon electrode used as the anode. At the interface between PMMA/GNRs and Au, hydrogen bubbles form, resulting in the delamination of the PMMA/GNR layer from the Au(788) surface. The delaminated PMMA/GNR layer was left in ultra-pure water for 5 minutes before being transferred to the target substrate. To increase the adhesion between the target substrate and the PMMA/GNR layer, the sample was annealed for 10 minutes at 80°C and then 20 minutes at 110°C. Finally, the PMMA was dissolved in acetone for 15 minutes, and the resulting GNR/ROS was washed with ethanol and ultrapure water.

Raman Spectroscopy

Raman spectroscopy and polarized Raman measurements were obtained using a WITec confocal Raman microscope (WITec Alpha 300R) with a laser line of 785 nm (1.5 eV). The measurements were conducted in vacuum conditions on the sample before substrate transfer, utilizing a power of 40 mW and a 50× microscope objective (with a numerical aperture of 0.55), and a working distance of 9.1 mm, resulting in a laser spot size of 600 nm. This objective was used to focus the laser beam onto the sample and collect the scattered light. After substrate transfer, the measurements were performed under ambient conditions with a power of 1.3 mW and a 100× microscope objective (with an NA of 0.9). The Raman spectrum was calibrated using the Si peak at 520.5 cm^{-1}. To maximize signal while avoiding sample damage, laser wavelength, power, and integration time were optimized for each substrate[37]. For polarized Raman measurements of aligned GNRs, the linear polarization of the exciting lasers was adjusted parallel to the GNRs. A motorized half-wave plate was used to change the polarization direction of the incident laser beam from -90° to +90° in steps of 10°. The backscattered light was detected without an analyzing polarizer and coupled with a 300 mm lens-based spectrometer with a grating of 300 g mm^{-1} (grooves/mm) and equipped with a cooled deep-depletion CCD

Raman data processing

Using the WITec software, a cosmic ray filter was applied to all raw maps to remove signatures of photoluminescence. Afterward, the Raman maps were averaged and polynomial background subtraction was applied, followed by batched fitting with a Lorentzian function for all polarization angles between -90° to 90° for each Raman mode. The fitting using Eq. (6) was done in IGOR Pro software (Wavemetrics Inc.), and the fitting parameters were obtained through the lowest stable Chi-square values.

References

1. Yang, L., Park, C.-H., Son, Y.-W., Cohen, M. L. & Louie, S. G. Quasiparticle Energies and Band Gaps in Graphene Nanoribbons. *Phys. Rev. Lett.* **99**, (2007).
2. Talirz, L. *et al.* On-Surface Synthesis and Characterization of 9-Atom Wide Armchair Graphene Nanoribbons. *ACS Nano* **11**, 1380–1388 (2017).
3. Kimouche, A. *et al.* Ultra-narrow metallic armchair graphene nanoribbons. *Nat. Commun.* **6**, 10177 (2015).
4. Talirz, L., Ruffieux, P. & Fasel, R. On-Surface Synthesis of Atomically Precise Graphene Nanoribbons. *Adv Mater* **28**, 6222–6231 (2016).
5. Cai, J. *et al.* Atomically precise bottom-up fabrication of graphene nanoribbons. *Nature* **466**, 470–473 (2010).
6. Gröning, O. *et al.* Engineering of robust topological quantum phases in graphene nanoribbons. *Nature* **560**, 209–213 (2018).
7. Rizzo, D. J. *et al.* Topological band engineering of graphene nanoribbons. *Nature* **560**, 204–208 (2018).
8. Qiang, S., Groening, O., Overbeck, J., Braun, O. & et. al. Massive Dirac Fermion Behavior in a Low Bandgap Graphene Nanoribbon Near a Topological Phase Boundary. *Adv. Mater.* 1906054 (2020).
9. Cao, T., Zhao, F. & Louie, S. G. Topological Phases in Graphene Nanoribbons: Junction States, Spin Centers, and Quantum Spin Chains. *Phys. Rev. Lett.* **119**, 076401 (2017).
10. Ruffieux, P. *et al.* On-surface synthesis of graphene nanoribbons with zigzag edge topology. *Nature* **531**, 489–492 (2016).
11. Sun, Q. *et al.* Massive Dirac Fermion Behavior in a Low Bandgap Graphene Nanoribbon Near a Topological Phase Boundary. *Adv. Mater.* **32**, 1906054 (2020).
12. Llinas, J. P. *et al.* Short-channel field-effect transistors with 9-atom and 13-atom wide graphene nanoribbons. *Nat. Commun.* **8:633**, 1–6 (2017).
13. Chen, Z., Narita, A. & Müllen, K. Graphene Nanoribbons: On-Surface Synthesis and Integration into Electronic Devices. *Adv. Mater.* **32**, 2001893 (2020).
14. Bennett, P. B. *et al.* Bottom-up graphene nanoribbon field-effect transistors. *Appl. Phys. Lett.* **103**, 253114 (2013).
15. Passi, V. *et al.* Field-Effect Transistors Based on Networks of Highly Aligned, Chemically Synthesized *N* = 7 Armchair Graphene Nanoribbons. *ACS Appl. Mater. Interfaces* **10**, 9900–9903 (2018).

16. Wang, H. *et al.* Graphene nanoribbons for quantum electronics. *Nat. Rev. Phys.* **3**, 791–802 (2021).

17. Mutlu, Z. *et al.* Short-Channel Double-Gate FETs with Atomically Precise Graphene Nanoribbons. in *2021 IEEE International Electron Devices Meeting (IEDM)* 37.4.1-37.4.4 (2021). doi:10.1109/IEDM19574.2021.9720620.

18. El Abbassi, M. *et al.* Controlled Quantum Dot Formation in Atomically Engineered Graphene Nanoribbon Field-Effect Transistors. *ACS Nano* **14**, 5754–5762 (2020).

19. Braun, O. *et al.* Optimized graphene electrodes for contacting graphene nanoribbons. *Carbon* **184**, 331–339 (2021).

20. Zhang, J. *et al.* Ultimately-scaled electrodes for contacting individual atomically-precise graphene nanoribbons. Preprint at https://doi.org/10.48550/arXiv.2209.04353 (2022).

21. Zhang, J. *et al.* Tunable Quantum Dots from Atomically Precise Graphene Nanoribbons Using a Multi-Gate Architecture. *Adv. Electron. Mater.* **9**, 2201204 (2023).

22. Borin Barin, G. *et al.* Growth Optimization and Device Integration of Narrow-Bandgap Graphene Nanoribbons. *Small* 2202301 (2022) doi:10.1002/smll.202202301.

23. Martini, L. *et al.* Structure-dependent electrical properties of graphene nanoribbon devices with graphene electrodes. *Carbon* **146**, 36–43 (2019).

24. Blackwell, R. E. *et al.* Spin splitting of dopant edge state in magnetic zigzag graphene nanoribbons. *Nature* **600**, 647–652 (2021).

25. Slota, M. *et al.* Magnetic edge states and coherent manipulation of graphene nanoribbons. *Nature* **557**, 691–695 (2018).

26. Kan, E., Li, Z., Yang, J. & Hou, J. G. Half-Metallicity in Edge-Modified Zigzag Graphene Nanoribbons. *J. Am. Chem. Soc.* **130**, 4224–4225 (2008).

27. Zhao, S. *et al.* Optical Imaging and Spectroscopy of Atomically Precise Armchair Graphene Nanoribbons. *Nano Lett.* **20**, 1124–1130 (2020).

28. Zhao, S. *et al.* Optical Investigation of On-Surface Synthesized Armchair Graphene Nanoribbons. *Phys. Status Solidi B* **254**, 1700223 (2017).

29. Senkovskiy, B. V. *et al.* Making Graphene Nanoribbons Photoluminescent. *Nano Lett.* **17**, 4029–4037 (2017).

30. Denk, R. *et al.* Exciton-dominated optical response of ultra-narrow graphene nanoribbons. *Nat. Commun.* **5**, 4253 (2014).

31. Cocchi, C. *et al.* Optical Excitations and Field Enhancement in Short Graphene Nanoribbons. *J. Phys. Chem. Lett.* **3**, 924–929 (2012).

32. Chen, Y.-C. *et al.* Tuning the Band Gap of Graphene Nanoribbons Synthesized from Molecular Precursors. *ACS Nano* **7**, 6123–6128 (2013).

33. Di Giovannantonio, M. *et al.* On-Surface Growth Dynamics of Graphene Nanoribbons: The Role of Halogen Functionalization. *ACS Nano* **12**, 74–81 (2018).

34. Shinde, P. P. Graphene nanoribbons with mixed cove-cape-zigzag edge structure. 10 (2021).

35. Wang, Y. *et al.* Electrochemical Delamination of CVD-Grown Graphene Film: Toward the Recyclable Use of Copper Catalyst. *ACS Nano* **5**, 9927–9933 (2011).

36. Gao, L. *et al.* Repeated growth and bubbling transfer of graphene with millimetre-size single-crystal grains using platinum. *Nat. Commun.* **3**, 699 (2012).

37. Overbeck, J. *et al.* Optimized Substrates and Measurement Approaches for Raman Spectroscopy of Graphene Nanoribbons. *Phys. Status Solidi B* **256**, 1900343 (2019).

38. Lin, Y. *et al.* Scaling and Statistics of Bottom-Up Synthesized Armchair Graphene Nanoribbon Transistors. 27.

39. Darawish, R. *et al.* Quantitative Characterization of Graphene Nanoribbons Orientation and Quality by Polarized Raman Spectroscopy. *submitted* (2023).

40. Borin Barin, G. *et al.* Surface-Synthesized Graphene Nanoribbons for Room Temperature Switching Devices: Substrate Transfer and ex Situ Characterization. *ACS Appl. Nano Mater.* **2**, 2184–2192 (2019).

41. Dresselhaus, M. S., Jorio, A., Hofmann, M., Dresselhaus, G. & Saito, R. Perspectives on Carbon Nanotubes and Graphene Raman Spectroscopy. *Nano Lett.* **10**, 751–758 (2010).

42. Maghsoumi, A., Brambilla, L., Castiglioni, C., Müllen, K. & Tommasini, M. Overtone and combination features of G and D peaks in resonance Raman spectroscopy of the C78H26 polycyclic aromatic hydrocarbon. *J. Raman Spectrosc.* **46**, 757–764 (2015).

43. Tommasini, M., Castiglioni, C. & Zerbi, G. Raman scattering of molecular graphenes. *Phys. Chem. Chem. Phys.* **11**, 10185 (2009).

44. Overbeck, J. *et al.* A Universal Length-Dependent Vibrational Mode in Graphene Nanoribbons. *ACS Nano* **13**, 13083–13091 (2019).

45. Gillen, R., Mohr, M., Thomsen, C. & Maultzsch, J. Vibrational properties of graphene nanoribbons by first-principles calculations. *Phys. Rev. B* **80**, 155418 (2009).

46. Verzhbitskiy, I. A. *et al.* Raman Fingerprints of Atomically Precise Graphene Nanoribbons. *Nano Lett.* **16**, 3442–3447 (2016).

47. Malard, L. M., Pimenta, M. A., Dresselhaus, G. & Dresselhaus, M. S. Raman spectroscopy in graphene. *Phys. Rep.* **473**, 51–87 (2009).

48. Vandescuren, M., Hermet, P., Meunier, V., Henrard, L. & Lambin, Ph. Theoretical study of the vibrational edge modes in graphene nanoribbons. *Phys. Rev. B* **78**, 195401 (2008).

49. Cançado, L. G., Pimenta, M. A., Neves, B. R. A., Dantas, M. S. S. & Jorio, A. Influence of the Atomic Structure on the Raman Spectra of Graphite Edges. *Phys. Rev. Lett.* **93**, 247401 (2004).

50. Eckmann, A., Felten, A., Verzhbitskiy, I., Davey, R. & Casiraghi, C. Raman study on defective graphene: Effect of the excitation energy, type, and amount of defects. *Phys. Rev. B* **88**, 035426 (2013).

51. Thomsen, C. & Reich, S. Double Resonant Raman Scattering in Graphite. *Phys. Rev. Lett.* **85**, 5214–5217 (2000).

52. Liu, D., Daniels, C., Meunier, V., Every, A. G. & Tománek, D. In-plane breathing and shear modes in low-dimensional nanostructures. *Carbon* **157**, 364–370 (2020).

53. Pelletier, M. J. Quantitative Analysis Using Raman Spectrometry. *Appl. Spectrosc.* **57**, 20A-42A (2003).

54. Fairbrother, A. *et al.* High vacuum synthesis and ambient stability of bottom-up graphene nanoribbons. *Nanoscale* **9**, 2785–2792 (2017).

Supporting information

Raman and STM characterization of GNR

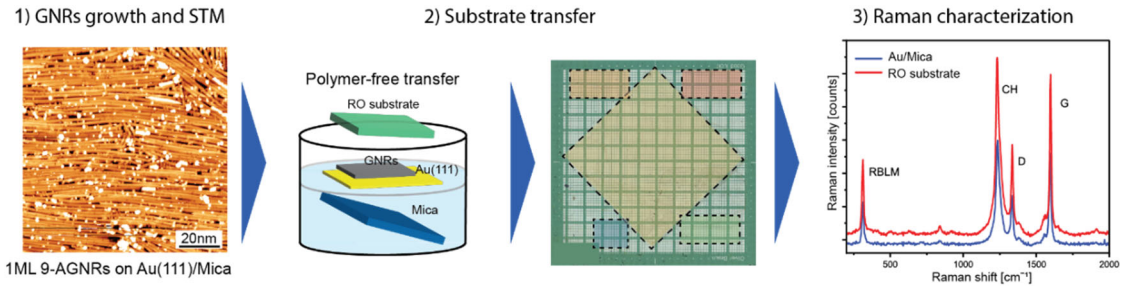

Figure S1: Fabrication, substrate transfer, and characterization of the reference sample of 9-AGNRs. (1) STM image of 1ML non-aligned 9-AGNRs on Au(111)/mica. (2) Schematic representation of the polymer-free substrate transfer method, followed by an image of the ROS where this transferred sample is located in the blue-shaded area. (3) Raman spectra comparing the monolayer of non-aligned 9-AGNRs on Au(111)/mica and after substrate transfer onto ROS.

Impact of chemical treatment and annealing on GNR integrity during substrate transfer

The structural integrity of GNRs can be influenced by various processes involved in their transfer onto the ROS including annealing, chemical treatment, and etching. In our study, the reference sample (Fig. 1) undergoes multiple annealing and acetone immersion steps each time we transfer one of the aligned samples (ML, 0.8-0.9 ML, and 0.3-0.4 ML) onto the same ROS using the electrochemical delamination transfer method (Fig. 1). Additionally, it experiences the Au etching step during the transfer of the other reference sample using polymer-free transfer, shown as polymer-free transfer in Fig. S1.

To investigate the impact of these chemical treatments and annealing on the GNR integrity, we conduct a series of experiments that mimic the electrochemical delamination transfer method and polymer-free transfer. We prepare a monolayer of non-aligned 9-AGNRs on Au(111)/Mica transfer it onto ROS using polymer-free transfer and characterize it using Raman spectroscopy. Subsequently, we subject the transferred sample to annealing at 80°C for 10 minutes followed by 110°C for 20 minutes. Then it is immersed in acetone for 15 minutes and rinsed with ethanol and ultrapure water. This process mimics the steps involved in the electrochemical delamination transfer method, similar to what the GNRs in our first transferred reference sample experience after transferring the first aligned sample (ML). This mimicking step is represented as the "First mimicking of the electrochemical delamination transfer method" in Fig. S2. We repeat this mimicking step two more times to mimic the other two samples (0.8-0.9 ML, and 0.3-0.4 ML) transferred with the electrochemical delamination transfer method, with Raman characterization performed after each mimicking step. These steps are represented as the "Second mimicking" and "Third mimicking" of the electrochemical delamination transfer method, as shown in Fig. S2. Finally, to mimic the etching of the gold film during the last transfer of the reference sample

using the polymer-free transfer (Fig. S1), we apply a gold etchant to the sample, and this step is represented as "Au etching" in Fig. S2. While all spectra in Fig. S2 exhibited the presence of all Raman active modes (RBLM, CH, D, and G), the "Third mimicking" step and "Au etching" showed a significant decrease in peak intensity compared to the other spectra. This indicates the influence of chemical treatment and annealing on the integrity of GNRs specifically during the "Third mimicking" step and "Au etching" process. The FWHM of the CH mode broadens from 34 cm^{-1} on Au(111)/mica to 36 cm^{-1} after the "Third mimicking" step and further to 38 cm^{-1} following "Au etching". To mitigate the impact of these processes on the integrity of GNRs, we conduct Raman measurements in Fig. 1 and Fig. S1 immediately after each substrate transfer, following a specific transfer methodology sequence that minimizes the exposure of GNRs to chemical treatment and annealing.

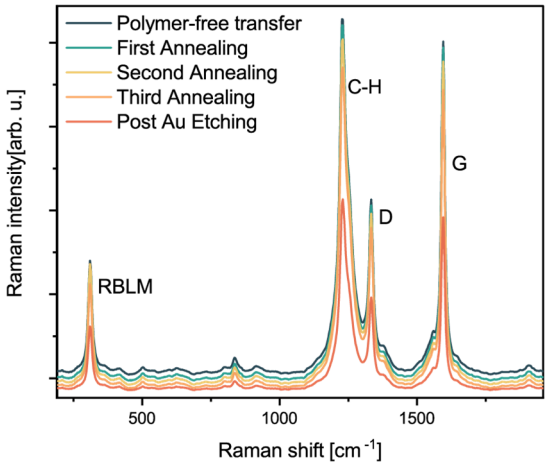

Figure S2: Raman spectroscopy of 9-AGNRs to show the effect of multiple annealing, chemical treatments, and Au etching on the structural quality of 9-AGNRs.

Optimizing characterization of GNR samples: Selecting homogeneous areas

Accurate characterization of GNR samples requires the selection of a homogeneous area that can represent the overall GNR distribution and provides reliable Raman intensity measurements. Raman intensity maps over large areas offer insights into sample homogeneity, but they are subject to two limitations. Firstly, non-homogeneous areas may contain regions where GNRs were not successfully transferred, leading to reduced Raman signal intensity. Secondly, the surface of the sample is not exactly flat and may deviate in and out of the focal plane of the microscope objective.

Figure. S3a presents a large area map (100 x 100 µm) of the G-peak intensity, highlighting the homogeneous regions where all GNRs have been successfully transferred to the ROS. In contrast, Fig. S3b shows non-homogeneous regions (100 x 100 µm) characterized by patches over which GNRs were transferred (appearing bright yellow and orange on the map) and regions in between where no GNRs were transferred (appearing dark). Figure. S3c provides the average

Raman intensity for both homogeneous and non-homogeneous areas, with the latter being significantly lower in intensity.

To mitigate the impact of non-homogeneous areas, we perform a fast Raman characterization on a large mapping area to assess homogeneity. Subsequently, we select a smaller homogeneous area (10 x 10 µm) with high-quality GNRs to ensure accurate and reliable Raman measurements.

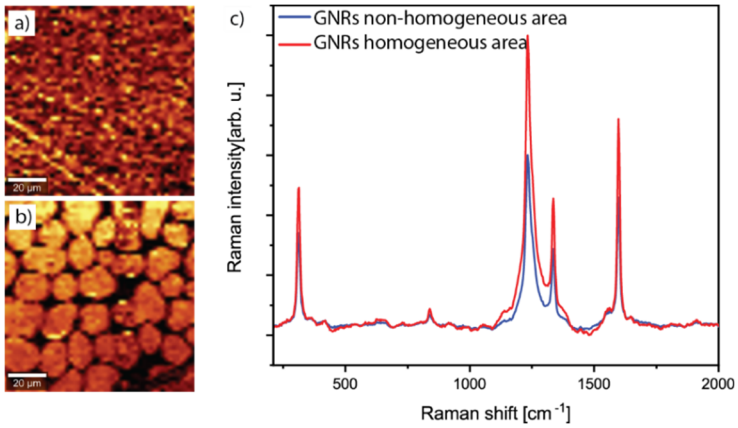

Figure S3: Raman characterization of homogeneous and non-homogeneous areas of 9-AGNRs after substrate transfer onto the ROS. Panel (a) displays the G-peak intensity map specifically highlighting the homogeneous areas (100 x 100 µm), while panel (b) shows the G-peak intensity map for the non-homogeneous areas (100 x 100 µm). Panel (c) presents the average Raman spectra for the homogeneous (in red) and non-homogeneous (in blue) areas, corresponding to the intensity maps.

Impact of gold surface thickness on Raman signal of 9-AGNRs: Comparative analysis between Au(111)/Mica and Au(111) crystal

Since we were comparing the Raman signal for non-aligned 9-AGNRs on the Au(111)/mica surface to aligned 9-AGNRs on a bulk crystal of Au(788), it is important to consider the influence of gold surface thickness on the Raman signal. To investigate this, we prepared two samples: a monolayer of non-aligned 9-AGNRs on the Au(111)/mica surface and the Au(111) crystal. Raman characterization is conducted using a 785 nm laser wavelength and a small mapping area (10x10 µm) in a home-built vacuum chamber.

In Figs S5.a and b, we show the scanning tunneling microscopy (STM) images of the non-aligned 9-AGNRs on the Au/mica and on the Au(111) crystal, respectively. Figure 5c displays the Raman profiles of the two samples. To assess the impact of the gold thickness factor, we used the G peak and compared the area of the Lorentzian fitting of the G mode intensity on the Au(111) crystal to that on Au(111)/mica. The calculated gold thickness factor was found to be 1.1, indicating a minor influence of the Au surface thickness on the transfer efficiency. As a result, the thickness of the Au surface was excluded from Eq. (3).

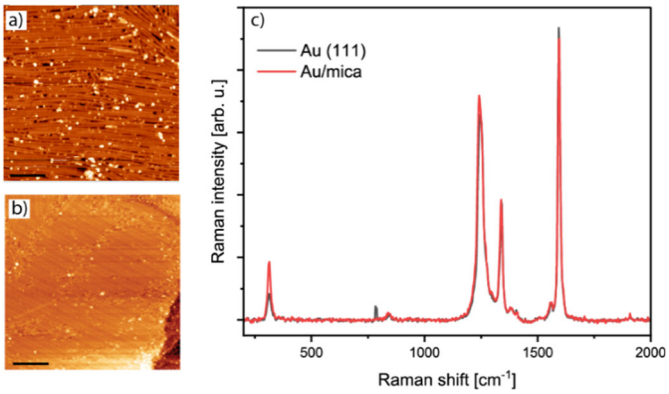

Figure S4: STM and Raman characterization of Non-Aligned 9-AGNRs. a) on Au(111) crystal and b) Au(111) film/Mica surfaces. Parameters: -1.5V and 0.3 nA. c) Raman spectra of1ML 9-AGNRs on Au(111) crystal (black) and Au(111)/mica (red).

The alignment stability of GNRs after substrate transfer

Coverage	ML			0.8-0.9ML			0.3-0.4 ML		
Substrate	Au(788)	ROS		Au(788)	ROS		Au(788)	ROS	
Time (Months)	-	0	30	-	0	30	-	0	30
P	0.8	0.58	0.58	0.8	0.62	0.63	0.85	0.58	0.45
(σ) [°]	2	15	16	2	16	15	1	19	32
(*OD*) [%]	18	30	32	19	30	36	25	45	43

Table S1: The G mode Raman polarization anisotropy (*P*), quality of alignment (σ), and the overall disorder on the surface (*OD*), for the ML, 0.8-0.9 ML and 0.3-0.4 ML samples. These measurements are taken on the growth surface of Au(788), immediately after substrate transfer onto the ROS (0 months), and after 30 months of storage under ambient conditions.

Chapter 6

Optimization of substrate transfer: High-quality graphene nanoribbons for STM and Raman characterization

Introduction

The first report on bottom-up fabrication of graphene nanoribbons (GNRs) in 2010 paved the way for the development of GNRs with atomically precise widths and edge structures. The electronic bandgap of GNRs can be tuned by adjusting their width[2–5] and edge topology[1,6–10]. This makes GNRs an attractive platform for diverse device applications, ranging from transistors[11–15], spintronics[16–18], and photonics[19–22].

However, a significant limitation of this fabrication method lies in the requirement for gold to catalyze the on-surface reaction. To investigate GNR transport properties in a device, GNRs need to be transferred from their metallic growth substrates to technologically relevant ones, such as silicon with various oxides[11–13]. While several techniques exist for transferring graphene and other 2D materials, adapting these for GNRs remains challenging. The most used wet transfer method, using KI/I_2 to etch the Au, efficiently transfers GNRs from thin Au(111) films on mica or glass[23]. While wet transfer methods have successfully preserved GNR structure quality and quantity, they are limited to thin films that can be etched, cannot be used in devices with gold (Au) electrodes, and do not enable the growth of aligned GNRs.

From a device perspective, achieving a uniaxial alignment of ribbons is crucial to improving device yields. This alignment enables the bridging of GNRs along the source and drain of EFT, which can enhance device yield to up to 85%[14]. For transferring these aligned samples, the electrochemical delamination method, originally developed for CVD graphene transfers from metals[28,29] like Cu or Pt, has been adapted for GNRs and is the method of choice used throughout this thesis [21,30]. This method relies on the formation of hydrogen bubbles through the reduction of water in an electrolytic cell to delaminate GNRs from metal crystals. During this process, the poly(methyl methacrylate) (PMMA)polymer support layer, provides temporary rigid support to the GNRs, ensuring they maintain their shape and integrity. The choice of PMMA is due to its low viscosity, excellent mechanical properties, flexibility after curing, and solubility in various organic solvents[34]. After the transfer, it's crucial to remove the PMMA layer to ensure a clean surface.

These polymer removal approaches have not all been investigated for transferred GNRs to date. Although PMMA removal processes have been extensively studied in the context of graphene, many challenges persist. The strong interaction between PMMA and graphene often results in

PMMA residues on the surface, even after several rounds of cleaning with Acetone[35–37]. Such residues can induce a p-doping effect and act as scattering centers for charge carriers, compromising the carrier mobility and electrical properties of the graphene layer[39,40]. Consequently, a variety of methods have been developed to clean polymer residues from transferred graphene, aiming to optimize the electrical and optoelectronic properties of graphene devices [35–37].

The standard technique for eliminating PMMA residues has traditionally been acetone treatment. Efforts to improve this approach have included employing a secondary PMMA layer to mechanically relax the first PMMA layer in direct contact with the graphene, prolonging the acetone immersion time, and using vapor acetone treatments[41–43]. Besides conventional acetone treatments, other wet-based methods, such as acetic acid[44] and chloroform[45], have been proposed. However, methods using strong solvents can detrimentally affect graphene's electrical characteristics[35,36]. Other methods, including UV-assisted[46,47] and thermal annealing in vacuum[39,45], were observed to remove PMMA more efficiently, leading to improved graphene properties.

In this study, we explore nine different methods to remove PMMA residues from the surface of transferred 9-AGNRs. We show an optimal cleaning method, that allows us to successfully characterize transferred 9-AGNRs onto a semiconducting (Graphene/SiC) using scanning tunneling microscopy (STM). Finally, the quality and alignment of such samples are also studied by Raman spectroscopy.

Results and discussion

To synthesize aligned 9-AGNRs, we deposit the precursor monomer 3′,6′-di-iodine-1,1′:2′,1′′-terphenyl (DITP)[48] onto the clean vicinal surface of Au(788). After deposition, the samples undergo two annealing steps: the first at 200°C for 10 minutes to initiate polymerization, and the second at 400°C for 10 minutes to induce cyclodehydrogenation, resulting in the formation of GNRs[5,2,4,49]. In this study, we prepare three distinct sample sets. The first is a full monolayer sample to investigate the effect of electrochemical delamination duration on the GNR quality. The second consists of two full monolayer samples for assessing various PMMA removal treatment protocols. The third set includes one full monolayer and one sub-monolayer sample for STM characterization after transfer.

After the growth of GNRs, all samples are transferred via the electrochemical delamination method to the Raman-optimized substrate (ROS), using PMMA-950k (4% in ethyl-lactate)) as the support layer.

Exploring the impact of electrochemical delamination duration without PMMA supporting layer on GNR quality

We center our focus on exploring the effects of electrochemical delamination duration (or bubbling time) without PMMA supporting layer on the quality of GNRs. For this, we prepare a

full monolayer of 9-AGNRs on the Au(788) surface. Here, we immerse the sample (GNR/Au(788)), without the PMMA supporting layer, into 1 M NaOH electrolyte. We proceed by applying a voltage of 5 V (current ~0.2 A) to form the hydrogen bubbles on the interface of the GNR/Au(788) sample for a total time of 60 seconds in steps of 10 seconds. We measure the Raman spectrum of the sample after each 10-second step, Fig. 1.

All Raman measurements for this study are done in a home-built vacuum chamber (~10^{-2} mbar) with a 785 nm wavelength, minimizing potential photochemical reactions[21,30]. We also use a map approach (10 µm x 10 µm) to extract the average spectrum, ensuring a high signal-to-noise ratio[30].

Figure 1, shows the Raman spectrum of the 9-AGNR sample on Au(788) before any bubbling time, and after 10, 20, 30, 40, 50, and 60 seconds of bubbling time - without the presence of a PMMA layer. 9-AGNRs on Au(788) before any bubbling time will serve as a reference and will be termed the "control sample". The Raman spectra in Fig. 1 show the intrinsic Raman fingerprint characteristic of 9-AGNRs, highlighting modes such as the G mode ~1600 cm^{-1} associated with carbon-carbon bond stretching in the sp^2 lattice[55,56,30,23]and the D mode at ~1335−1340 cm^{-1} (intrinsic from the GNRs edges)[23,57,58,55]. Other modes include the CH mode ~1235cm^{-1} associated with hydrogen-carbon bending at GNR edges[23,58,55] and the radial breathing-like mode (RBLM) which is directly related to the the ribbon width[57,58,56].

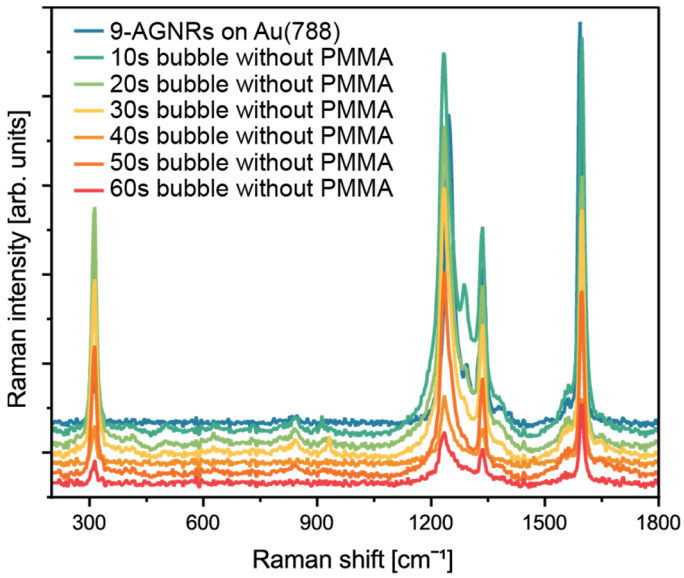

Figure 1: Raman spectra of 9-AGNRs sample after bubbling process without PMMA layer. The spectra are acquired with an excitation wavelength of 785 nm under vacuum conditions.

Figure 1 indicates a decrease in 9-AGNRs Raman intensity as bubbling time increases. To assess the GNRs' structural quality, we extract the full width at half-maximum (FWHM) and peak position of the RBLM, D, CH, and G modes[23,30] from the Raman profile in Fig. 1. Results of this analysis are present in Fig.2 and Table 1. Figure 2 displays the FWHM and peak positions of CH and D modes after each bubbling time step compared to the control sample. After 60 seconds of bubbling time without PMMA, we observe a broadening in the CH (~44 cm^{-1}) and D modes

(~21 cm^{-1}) relative to the control sample, where CH and D modes are ~26 cm^{-1} and ~16 cm^{-1}, respectively. This broadening indicates that ribbons without the PMMA supporting layer turn more defective as the bubbling time increases. However, changes in the RBLM and G peaks are negligible.

In addition, we observe a blue shift of 4-5 cm^{-1} for the G mode and a red shift of 10 cm^{-1} for the CH mode compared to the control sample. The shifts in CH and G modes could result from the bubbling process and hydrogen intercalation between the Au and the GNRs. For D and RBLM modes, shifts remain within the range of experimental accuracy.

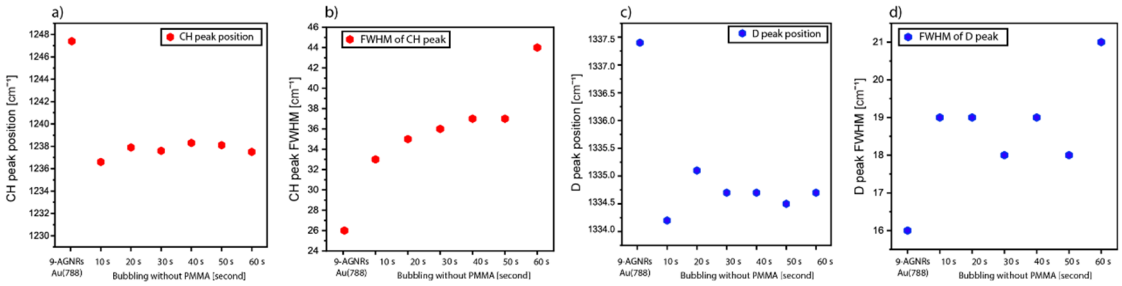

Figure 2: The impact of different durations of bubbling without a PMMA supporting layer on FWHM and peak position of the CH-D region in comparison to the control sample on Au(788): a) and b) CH mode FWHM and peak position. c) and d) D mode FWHM and peak position.

9-AGNRs	RBLM		CH		D		G	
	FWHM	Position	FWHM	Position	FWHM	Position	FWHM	Position
Au (788)	14	312	26	1247	16	1337	12	1593
10s bubble	14	312	33	1237	19	1334	15	1598
20s bubble	14	312	35	1238	19	1335	13	1598
30s bubble	14	312	36	1238	18	1335	13	1597
40s bubble	13	312	37	1238	19	1335	14	1598
50s bubble	14	312	37	1238	18	1335	13	1597
60s bubble	13	312	44	1238	21	1335	14	1597

Table 1: Raman active modes FWHM and peak position for high coverage aligned 9AGNRs sample on Au(788) and after several bubbling times without the presence of the PMMA layer.

Impact and efficacy of different PMMA removal techniques on 9-AGNRs quality

To identify the most effective PMMA removal method, we prepared one sample of full monolayer-aligned 9-AGNRs on Au(788). Using electrochemical delamination, we delaminated the PMMA/GNRs from the growth surface. To ensure the minimization of any impact from the transfer process on our measurements, we target the preparation of full monolayer-aligned 9-AGNR which has normally high transfer efficiency compared to the coverages. Afterward, the transferred sample is divided into nine pieces. Each piece was then transferred onto a clean target substrate of ROS. Following the transfer to ROS, the PMMA drying process was done in three steps: 1. Dry with nitrogen to improve PMMA/GNRs/ROS contact and reduce water 2. Baking at 80°C for 5 minutes. 3. bake at 110°C for 20 minutes.

Subsequently, we investigated nine different methodologies for PMMA residue removal:

1. Acetone Treatment (AC): This method employed a two-stage process: 7 minutes at 50°C followed by another 7 minutes at room temperature (RT). This process will be referred to later as AC treatment[28–30].

2. PMMA-AC: An additional PMMA layer with a lower molecular weight (PMMA-50K, 6% in anisole) is introduced over the PMMA/GNRs/ROS. Subsequently, the AC treatment is applied. The additional PMMA layer relaxes the first layer mechanically so fewer cracks are formed in the GNR film upon removal.[41,42].

3. PMMA-AC-1h: After introducing an additional PMMA layer, the sample has AC treatment and is subsequently immersed in acetone for an hour[41,43].

4. AC-H: This involves a combination of a 3-hour acetone bath at 80°C, followed by 7 minutes immersion in acetone at room temperature[37,43].

5. AC-V: A 3-hour vacuum annealing at 300°C and 1 bar is applied, succeeded by AC treatment[43,60].

6. Acetic Acid Immersion (AA): The PMMA/GNRs/ROS sample is submerged in acetic acid for 3 hours[60].

7. PMMA-AA: Before a 3-hour acetic acid immersion, a second PMMA layer is added to the sample[60].

8. UV/Ozone-5 minutes: This process entails UV/ozone irradiation for 5 minutes (using a 185 nm wavelength) at ambient conditions, concluding with an AC treatment to dissolve the degraded PMMA[47].

9. UV/Ozone-30 minutes: Similar to the previous method, the UV/ozone irradiation is extended to 30 minutes[47].

To evaluate the GNRs' quality post-treatment, we employ Raman spectroscopy on the transferred high-coverage 9-AGNRs samples. Figure 3a displays the normalized Raman spectra from the various PMMA removal techniques, highlighting the presence of 9-AGNRs Raman fingerprints, RBLM, CH, D, and G modes. However, we observe a significant difference depending on the removal process. The least affected (or degraded) sample is "PMMA-AC-1h ", represented by the highest intensity, whereas the most affected sample is "AA", as indicated by its lowest intensity. To better understand the impact of the removal process on GNR quality, we analyze the FWHM and peak position of the RBLM, D, CH, and G modes (Table 2).

The method with the least change in FWHM and peak shift indicates a minimal impact on GNR quality and will be considered optimal. Figs. 3b and c show the FWHM and peak position of CH and D modes after each treatment. Our results suggest that PMMA-AC-1h has the least impact on GNR quality. On the other hand, the AA method had the most negative impact, resulting in significant GNR degradation.

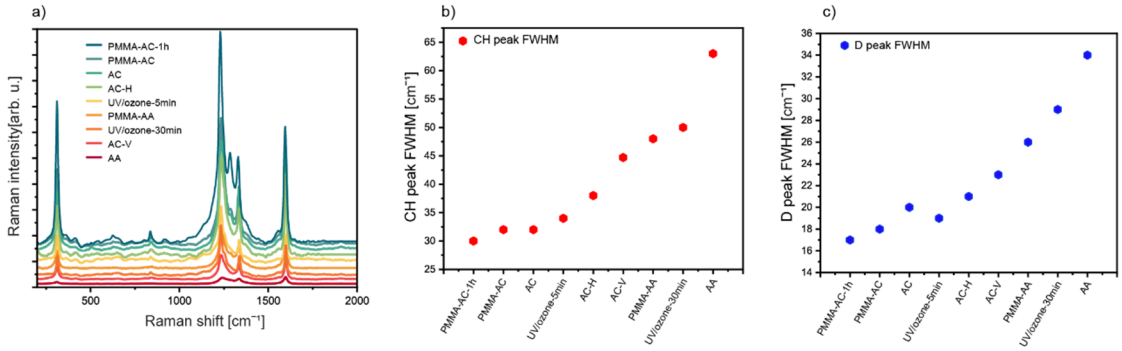

Figure 3: Raman characterization of the nine distinct PMMA removal approaches on high coverage 9-AGNRs. a) Raman spectra of 9-AGNRs at high-coverage samples treated with nine distinct PMMA removal approaches after substrate transfer onto ROS. b, c) The FWHM of CH and D peaks respectively for the high-coverage samples in Fig. 1a, which went through the nine different PMMA removal methods upon substrate transfer onto ROS.

Acetone is widely used to remove PMMA due to its excellent solubility with organic compounds and its low toxicity. Typically, hot acetone and extended immersion are employed to improve its dissolving capability and ensure PMMA's decomposition into smaller fragments. Previous studies found that introducing a second PMMA layer mechanically relaxes and re-dissolves the polymer chains, reducing tension, and increasing the solubility of residuals in solvent [41,42]. Indeed, the approach PMMA-AC-1h sample is the method showing the least FWHM changes. However, we also observe that an extended three-hour immersion in acetone vapor (AC-H) decreases the GNR quality, as reflected by increased FWHM values of 38 cm^{-1} (CH) and 21 cm^{-1} (D). The sample treated with acetone, followed by a three-hour vacuum (1 bar) anneal at 300°C (AC-V), showed FWHM values of 45 cm^{-1} (CH) and 23 cm^{-1} (D). These shifts imply that annealing might introduce structural defects, possibly due to GNR oxidation and interactions with the oxidized silicon substrate. It's also important to mention that these samples did not show a significant peak shift within the experimental accuracy of the Raman measurements (3 cm^{-1}).

Using acetic acid (AA) for PMMA removal caused the most significant changes in the Raman spectra with an increase in FWHM values: 63 cm^{-1} (CH) and 34 cm^{-1} (D), and significant shifts in the RBLM, CH, and D peaks, Table 2.

	RBLM peak		CH peak		D peak		G peak	
	FWHM	Position	FWHM	Position	FWHM	Position	FWHM	Position
Au788	15	312	32	1243	20	1337	16	1597
PMMA-AC-1h	14	311	30	1236	17	1330	17	1597
PMMA-AC	15	313	32	1238	18	1335	13	1598
AC	15	313	32	1238	20	1335	14	1598
UV/ozone-5min	14	314	34	1233	19	1336	12	1599
AC-H	16	312	38	1240	21	1333	13	1598
AC-V	17	312	45	1239	23	1334	15	1599
PMMA-AA	19	311	48	1241	26	1334	23	1598
UV/ozone-30min	15	314	50	1232	29	1334	13	1596
AA	27	309	63	1248	34	1330	25	1596

Table 2: 9-AGNRs Raman active modes peak FWHM and position for high coverage aligned 9AGNRs sample on ROS after various treatments to remove PMMA layer.

STM and Raman characterization of GNRs after substrate transfer onto SiC

We prepare two distinct GNR samples for this study: 0.4 of a monolayer and a full monolayer of 9-AGNRs on Au(788), here called low- and high-coverage samples, respectively (Fig. 4). A representative STM image of the high-coverage sample shows three ribbons per terrace growing uniaxially along the step edges (Fig. 4a). For the low-coverage sample, STM reveals longer GNRs growing along the step edge with shorter GNRs growing across the terraces (Fig. 4b).

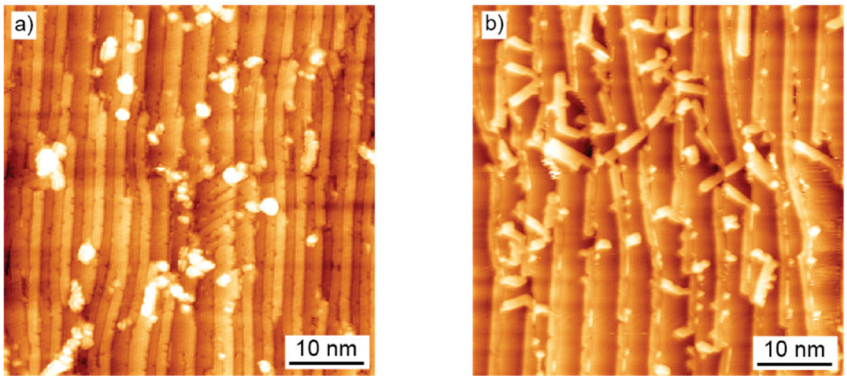

Figure 4: STM characterization of aligned 9-AGNRs on Au (788). a) and b) show the STM topology image of high- and low-coverage samples on Au (788), respectively. Taken at V_b = -1.5 V, I_t = 0.3nA.

Next, we clean the target substrate, graphene/SiC[64], before GNR transfer, with an annealing step at 500°C for 30 minutes in UHV. Representative STM images (Fig. 5a) reveal a uniform graphene/SiC surface at RT. We further characterize the clean graphene/SiC using Raman spectroscopy. Using wavelengths of 488, 532, and 785 nm, we detect the primary peak of graphene, the G mode at ~ 1596 cm^{-1}, Fig. 5b. We also identify the two-phonon 2D band ~ 2715 cm^{-1}. We also note a weak defect-induced (D) peak at ~ 1400 cm^{-1} indicating that the graphene also has the presence of a few defects.

Next, we use electrochemical delamination to transfer both high- and low-coverage samples (Figs. 4a and b) onto the clean graphene/SiC substrate. Each sample is divided into 2 pieces, with one segment transferred to graphene/SiC for STM characterization and the other to ROS for Raman assessment. To eliminate PMMA residues from the GNR surface post-transfer, we utilize the PMMA-AC-1h method.

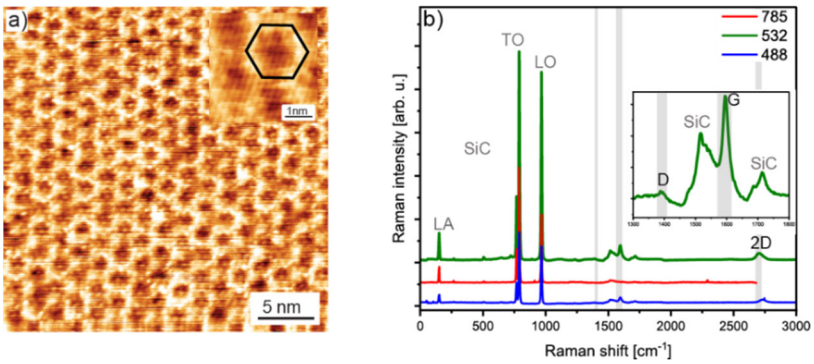

Figure 5: STM and Raman characterization of graphene/SiC. a) STM topology image of graphene/SiC, taken at V_b = -1.5 V, I_t = 0.3nA. b) Raman spectroscopy of graphene/SiC using 532 nm.

Raman and polarized Raman characterization

We investigate the structural quality and alignment of GNRs of both high- and low-coverage samples from the growth surface to after substrate transfer onto ROS and graphene/SiC using Raman and polarized Raman spectroscopy (Fig. 6). The Raman profiles in Fig. 6 display all 9-AGNRs fingerprints Raman signatures (RBLM, CH, D, and G modes) for both coverages on the metal substrate and after transferring to graphene/SiC and ROS. We observed a change in intensity post-transfer between the two samples. To assess the GNRs' structural quality, we extract the FWHM of the RBLM, D, CH, and G peaks. The high-coverage sample's average Raman profile exhibits negligible changes in FWHMs pre- and post-substrate transfer, indicating GNRs preserved structural quality. On the other hand, the low-coverage sample shows substantial FWHM broadening for the CH peak (from ~$26_{Au(788)}$ to 35_{RO} and 34_{SiC} cm^{-1}) and the D peak (from ~$13_{Au(788)}$ to 17_{RO} and 18_{SiC} cm^{-1}). This broadening suggests that not all GNRs retain their quality and quantity post-transfer.

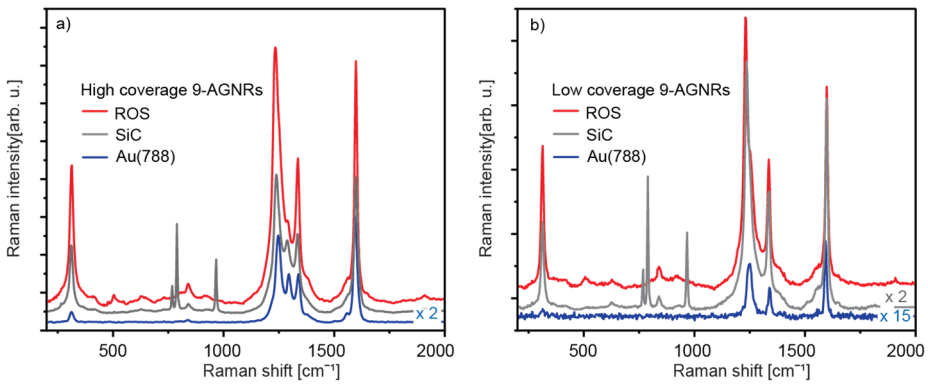

Figure 6: Raman spectra of high and low coverage 9-AGNRs samples on Au(788) and upon substrate transfer onto ROS and graphene/SiC substrate. a) and b) Raman spectra of high and low coverage 9-AGNRs, respectively on Au(788) in blue, after substrate transfer onto ROS (in red) and graphene/SiC (in gray). The spectra are acquired with an excitation wavelength of 785 nm under vacuum conditions.

We utilized polarized Raman spectroscopy to study the orientation of GNRs on the growth substrate and after substrate transfer. Using a 785nm laser excitation source, the incident laser beam was polarized from -90° to +90° in steps of 10°. The backscattered light was detected without an analyzing polarizer. This revealed a $cos^2(\theta_{in})$ polarization-dependent behavior for the Raman intensity of the G mode, as illustrated in the polar plots in Fig. 7. We employed two methods to quantitatively assess GNR alignment: the Raman polarization anisotropy (*P*) and an extended angle distribution model detailed in our previous chapters 3 and 4 (Table 3). Our data shows a decrease in alignment from $P_{Au(788)}$= 0.8 and $\sigma_{Au(788)}$= 8° to P_{ROS}= 0.7 and σ_{ROS}= 14° for ROS, and P_{SiC}= 0.7 and σ_{SiC}= 15° for graphene/SiC for the high coverage sample. For low coverage sample exhibited a decrease in alignment from$P_{Au(788)}$= 0.8 and $\sigma_{Au(788)}$= 5° to P_{ROS}= 0.6 and σ_{ROS}= 2° for ROS and P_{SiC}= 0.6 and σ_{SiC}= 17° for graphene/SiC. The more pronounced decrease in alignment disruption in low-coverage samples post-transfer, relative to high-coverage samples, is consistent with our previous observations in chapters 3 and 4.

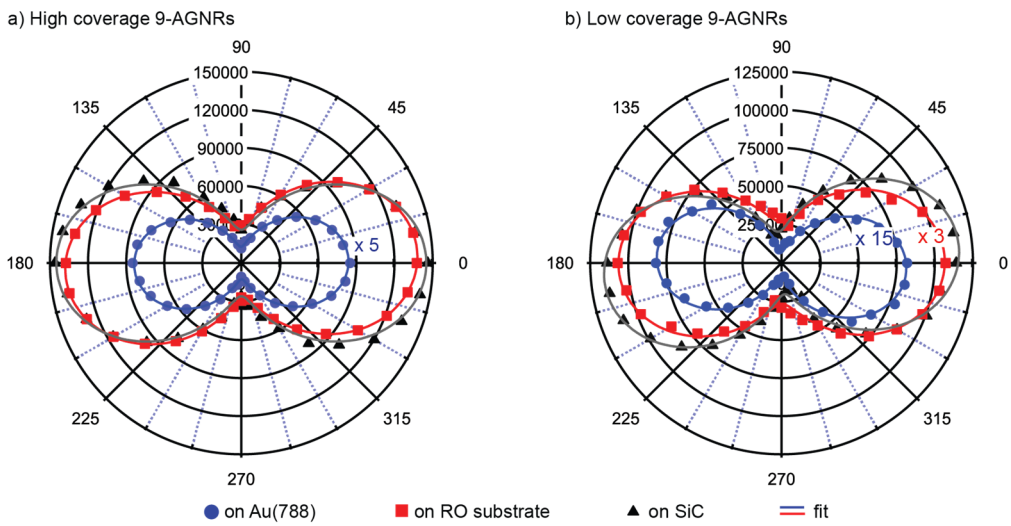

Figure 7: Polarized Raman of high and low coverage 9-AGNRs samples on Au(788) and upon substrate transfer onto ROS and graphene/SiC substrate. a) and b)The represented Polar diagrams of G mode intensities of high and low coverage in Fig. 6, respectively, as a function of the polarization angle on Au(788) (blue circles) and after transfer to ROS (red squares) and onto graphene/SiC (black triangle). The blue red and black solid lines represent the fits to the measured data using fit. The spectra are acquired with an excitation wavelength of 785 nm under vacuum conditions

Substrate	High coverage		Low coverage	
	P	*σ*	*P*	*σ* [°]
Au(788)	0.8	8	0.8	5
ROS	0.7	14	0.6	26
graphene/SiC	0.7	15	0.6	30

Table 3: Average *P*, and σ of the G mode for high and low/ coverage samples, on Au(788) and after substrate transfer to ROS and graphene/SiC.

STM characterization

After completing the substrate transfer and cleaning processes, we attempt to directly characterize our samples using STM. However, this proved challenging for both high- and low-coverage samples on graphene/SiC. Initial attempts with annealing at 200°C in UHV do not give the full information (characterization with STM was hard). Consequently, we anneal the samples in UHV at 450°C for 30 minutes. Fig. 8 shows the representative STM images for both high- and low-coverage samples after annealing at 450°C for 30 minutes, indicating that both samples are successfully transferred to the graphene/SiC substrate.

The length and orientation analysis (see Fig. 9) of high-coverage samples on the graphene/SiC are uniformly distributed and uniaxially aligned GNRs. We observe a slight reduction in average GNR length, from 37± 14 nm on Au(788) to 35± 19 nm on graphene/SiC. The preservation in length and alignment is attributed to the high-coverage film behavior. Based on the analysis of numerous STM images covering an area of 100x100 nm, we approximate a transfer efficiency of 90%. Notably, in a previous study (Chapter 5), the transfer efficiency for higher coverage samples is determined to be 70% using Raman analysis. This observed difference can likely be attributed to the distinct measurement scales – nanometers for STM compared to micrometers for Raman. The average angle distribution also broadened from 0.1± 9° (Au(788)) to -0.2±8° after substrate transfer, as detailed in Fig. 9.

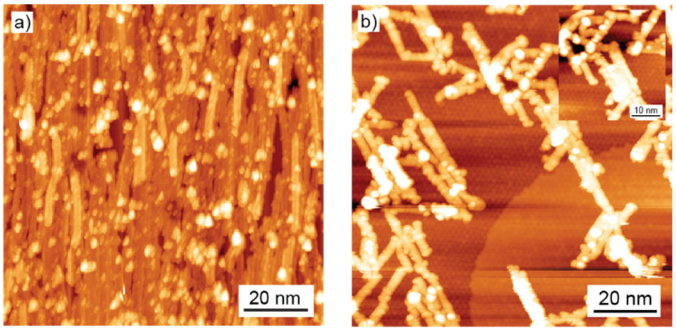

Figure 8: STM characterization of aligned 9-AGNRs at high and low-coverage levels after they are transferred onto graphene/SiC. a),b, high-and low-coverage on graphene/SiC, respectively taken at V_b = -1.5 V, I_t = 0.3nA.

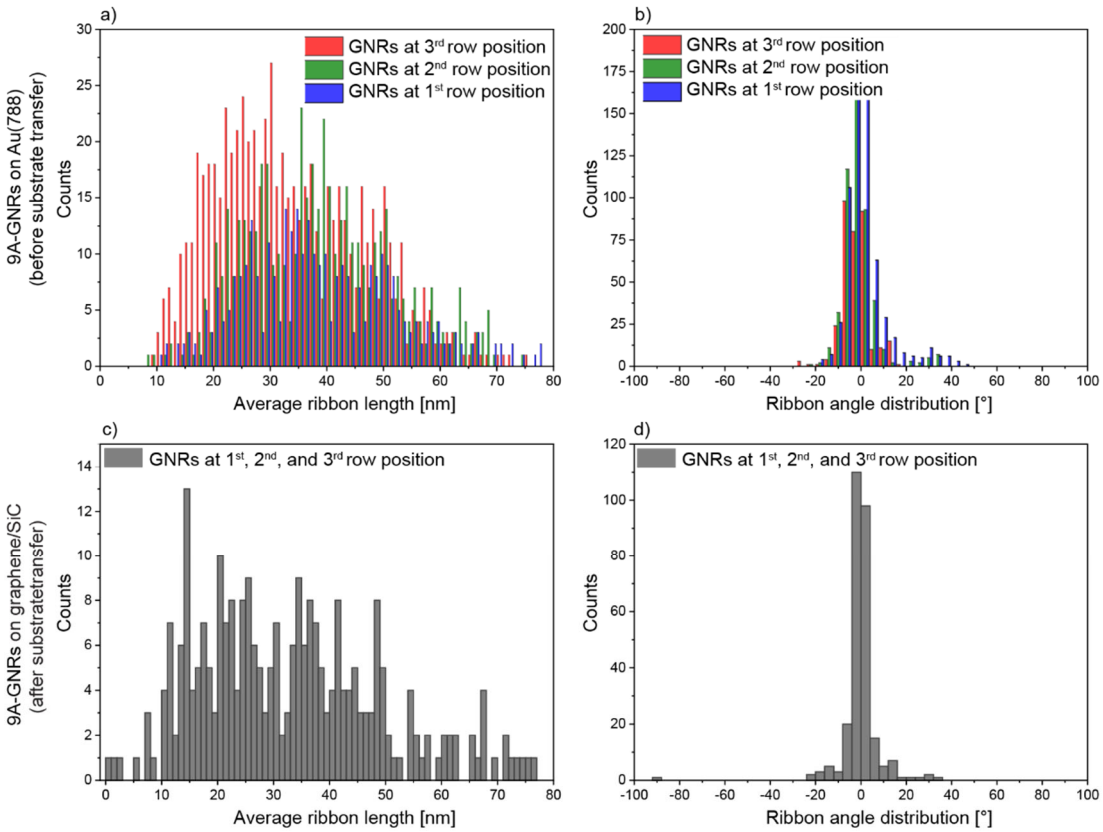

Figure 9: Histogram of the length and angle distribution of 9-AGNRs high-coverage samples. a) on Au(788). b) after substrate transfer onto graphene/SiC.

The length and orientation analysis (see Fig. 10) for low-coverage samples on the graphene/SiC show less uniform and more misaligned GNRs compared to the high-coverage samples. STM characterization reveals a decrease in both the average length and alignment of the GNRs. On Au(788), GNRs growing along the step edge measure 41± 17 nm, while those growing across the terraces are at 3± 1 nm. Post transfer, we observe GNR average length at 17± 7 nm. The average angle distribution also broadened from 6± 3° (first-row GNRs on Au(788)) and 86± 33° (second-row GNRs on Au(788)) to -14± 53° after substrate transfer, as detailed in Fig. 10. We attribute this reduction in length and alignment to the absence of film behavior and stronger GNR-substrate interactions. From various 100x100 nm STM images, we determine a 55% ribbon transfer efficiency.

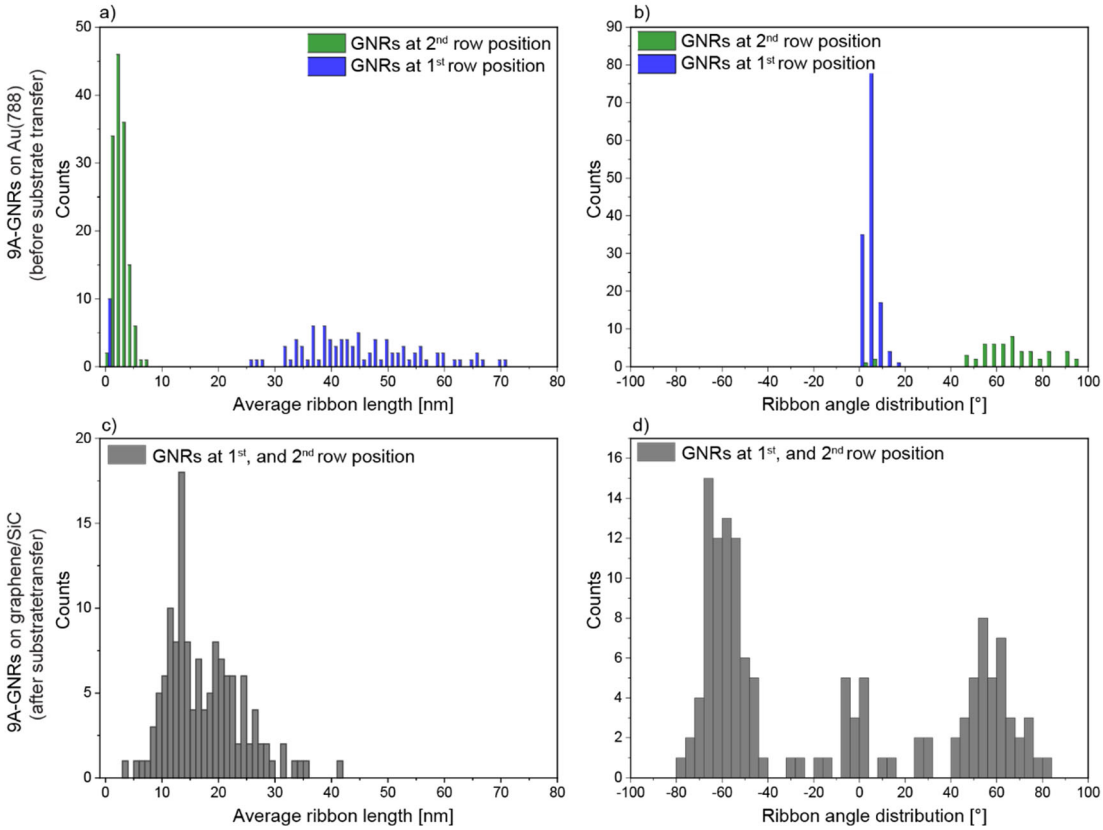

Figure 10: Histogram of the length and angle distribution of 9-AGNRs low-coverage samples. a) on Au(788). b) after substrate transfer onto graphene/SiC.

Impact of Various Annealing Processes on the Quality of Transferred GNRs

Characterizing both high- and low-coverage samples on graphene/SiC without annealing is challenging. However, we succeeded in studying the GNRs after a 30-minute annealing at 450°C. We delve into exploring the effects of various UHV annealing processes on the quality of GNRs transferred to graphene/SiC, examining both high and low-coverage samples. We employ STM for these investigations (Figs. 11 and 12).

For the high-coverage sample, we sequentially anneal the sample in UHV at 450°C (30min), 500°C (10min), 600°C (20min), and 750°C (30min). The representative STM image in Fig. 11 shows that GNRs remain on the surface after multiple annealing treatments. Interestingly, we observe a slight increase in the gap between these GNRs with the appearance of bright dots (and etched edges at 750ºC). This indicates that higher temperatures might decrease the film's behavior, and maybe GNRs are desorbing and moving. However, further investigation is required at lower temperatures with higher resolution to understand the influence of the sequenced annealing on GNRs after substrate transfer onto graphene/SiC and the cases of defects.

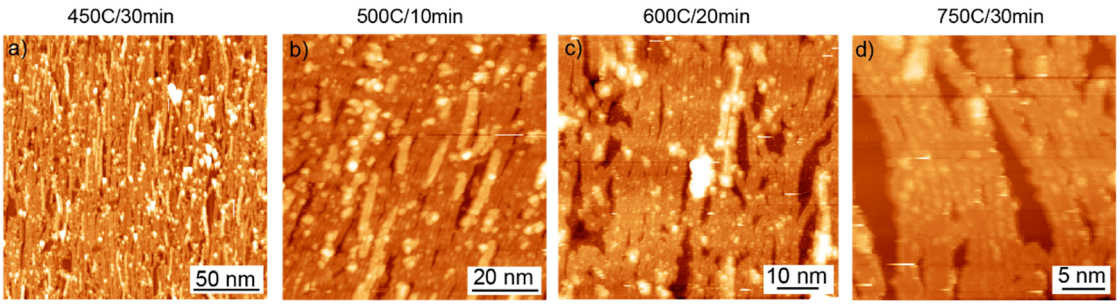

Figure 11: STM characterization annealing process of 9-AGNRs high coverage after substrate transfer onto graphene/SiC. Taken at V_b = -1.5 V, It = 0.3nA**.**

Conversely, the STM results for low-coverage samples present a different scenario (Fig. 12). After storing in UHV for two weeks, we observe significant surface contamination and some adsorbates at the GNR surface. Furthermore, after sequential annealing at 450°C (30min), 500°C (10min), 600°C (20min), and 750°C (30min), the GNRs seem to degrade/desorb from the graphene/SiC substrate.

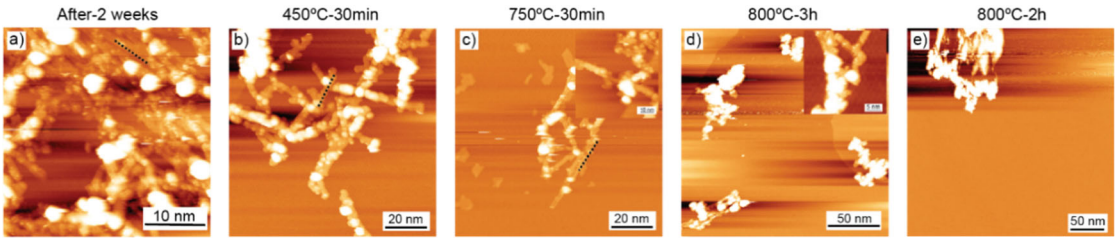

Figure 12: STM characterization annealing process of 9-AGNRs low coverage after substrate transfer onto graphene/SiC. a)STM after annealing to 450-20 min and sorted in a vacuum for two weeks. b) STM after annealing to 450-20 min. c) STM after annealing to 750-30 min. d) STM after annealing to 800-3 hours. e) STM after annealing to 800-2 hours, taken at V_b = -1.5 V, I_t = 0.3nA.

Conclusion:

In conclusion, this study aimed to optimize the electrochemical delamination transfer to improve GNR quality. The effectiveness of different PMMA removal approaches was evaluated using Raman spectroscopy, and it was found that PMMA-AC-1h was the least impact approach on GNR quality. On the other hand, acetic acid was found to be the most impacting approach on GNR quality resulting in significant degradation of GNRs.

Using this optimal PMMA removal approach after substrate transfer of 9-AGNRs at high and low-coverage samples onto graphene/SiC, we were able to characterize them using STM. The results showed that the high-coverage GNRs exhibited a uniform distribution with uniaxial alignment preserved, while the low-coverage samples showed a decrease in both the average length and overall alignment of GNRs after transfer. Our study also revealed that the transfer process was coverage-dependent, with approximately 90% of the high-coverage 9-AGNRs being transferred to the graphene/SiC substrate, while around 55% of the low-coverage samples were transferred.

Methods

On-surface synthesis and STM characterization of 9-AGNRs

The Au(788) single crystal growth substrate, sourced from MaTecK GmbH in Germany, underwent cleaning in an ultra-high vacuum (UHV). This involved two cycles: sputtering with 1 kV Ar+ for 10 minutes and annealing at 420°C for an equivalent duration. Subsequently, the 9-AGNR precursor monomer, 3′,6′-di-iodine-1,1′:2′,1′′-terphenyl (DITP), was sublimated onto the pristine Au surface from a quartz crucible at 70°C, with the substrate at ambient temperature. The deposition rate of the precursor molecules, monitored using a quartz microbalance, was set at 1 Å/min. This rate isn't calibrated for precise surface coverage but is relative to a standard STM measurement. Samples with high and low coverage were achieved by depositing DITP for 8-9 minutes. Post-deposition, the substrate faced heating to 200°C (0.5 K/s) for 10 minutes for DITIP polymerization. This was followed by annealing at 400°C (0.5 K/s) for 10 minutes for the GNR formation through cyclodehydrogenation.

Scanning tunneling microscopy (STM) images of the 9-AGNRs on Au(788) were captured at room temperature using a Scienta Omicron VT-STM. Topographic images were taken in constant current mode, employing a sample bias of -1.5 V and a setpoint current of 0.03 nA.

Substrate transfer of GNRs

The transfer of 9-AGNRs from the Au(788) growth substrate to Raman-optimized substrates (ROS) was executed via electrochemical delamination transfer. Initially, a support layer of poly(methyl methacrylate) (PMMA) was spin-coated onto the 9-AGNR/Au(788) samples, first layer of PMMA-50K, 6% in anisole (spin at 2500 rpm for 40 seconds) then 4 layers of PMMA-950k (4% in ethyl-lactate) (spin at 2500 rpm for 40 seconds) with waiting time of 30 second after each spin, followed by a 10-minute curing at 80°C. To expedite PMMA delamination, the edges of the Au(788) crystal were exposed to UV for 80 minutes, and then developed in a water/isopropanol mix for 3 minutes. The electrochemical delamination took place in a 1 M NaOH aqueous solution, with a DC voltage of 5V (current approx. 0.2 A) applied between the PMMA/9-AGNR/Au(788) cathode and a glassy carbon electrode anode. Hydrogen bubbles formed at the PMMA/GNRs and Au interface, causing the PMMA/GNR layer to delaminate from the Au(788) surface. This layer was then soaked in ultra-pure water for 5 minutes before being transferred to the target substrate and then divided into a few pieces to have a manz sample for the study. To enhance adhesion between the substrate and the PMMA/GNR layer, the sample was annealed first at 80°C for 10 minutes and then at 110°C for 20 minutes. The PMMA was finally treated with a different PMMA removal process and the resultant GNR/ROS was rinsed with ethanol and ultra-pure water.

Raman spectroscopy

Raman spectroscopy data were acquired using a WITec confocal Raman microscope (WITec Alpha 300R) with a 785 nm laser line (1.5 eV) at 40 mW power. A 50× microscope objective (0.55 numerical aperture) with a 9.1 mm working distance was employed. Calibration was based on the Si peak at 520.5 cm-1. Laser parameters were optimized for each substrate to maximize signal and minimize potential damage. Raman mapping was conducted with a 10×10 pixel grid (10×10 µm) in a custom vacuum chamber with a pressure of approximately 10^{-2} mbar. The chamber was mounted on a piezo stage for scanning.

For polarized Raman measurements, with the polarizing of the incident lights no polarizer analyzer is used for the scattered light. A motorized half-wave plate adjusted the incident laser beam's polarization direction in 10° increments from -90° to +90°. For 785 nm wavelength measurements, the scattered signal was detected using a 300 mm lens-based spectrometer with a 300 g mm-1 grating, and a cooled deep-depletion CCD.

All raw maps have a cosmic ray filter application using WITec software to eliminate photoluminescence signatures. Post-filtering, Raman maps were averaged, subjected to polynomial background subtraction, and batch-fitted with a Lorentzian function for all polarization angles between -90° and 90° for each Raman mode. Fitting, based on Eq. (9), was conducted in IGOR Pro software (Wavemetrics Inc.), with parameters derived from the most stable Chi-square values.

References:

1. Yang, L., Park, C.-H., Son, Y.-W., Cohen, M. L. & Louie, S. G. Quasiparticle Energies and Band Gaps in Graphene Nanoribbons. *Phys. Rev. Lett.* **99**, (2007).
2. Talirz, L. *et al.* On-Surface Synthesis and Characterization of 9-Atom Wide Armchair Graphene Nanoribbons. *ACS Nano* **11**, 1380–1388 (2017).
3. Kimouche, A. *et al.* Ultra-narrow metallic armchair graphene nanoribbons. *Nat. Commun.* **6**, 10177 (2015).
4. Talirz, L., Ruffieux, P. & Fasel, R. On-Surface Synthesis of Atomically Precise Graphene Nanoribbons. *Adv Mater* **28**, 6222–6231 (2016).
5. Cai, J. *et al.* Atomically precise bottom-up fabrication of graphene nanoribbons. *Nature* **466**, 470–473 (2010).
6. Gröning, O., Wang, S. & et al. Engineering of robust topological quantum phases in graphene nanoribbons. *Rev. 2018* (2018).
7. Rizzo, D. J. *et al.* Topological band engineering of graphene nanoribbons. *Nature* **560**, 204–208 (2018).
8. Qiang, S., Groening, O., Overbeck, J., Braun, O. & et. al. Massive Dirac Fermion Behavior in a Low Bandgap Graphene Nanoribbon Near a Topological Phase Boundary. *Adv. Mater.* 1906054 (2020).

9. Cao, T., Zhao, F. & Louie, S. G. Topological Phases in Graphene Nanoribbons: Junction States, Spin Centers, and Quantum Spin Chains. *Phys. Rev. Lett.* **119**, 076401 (2017).

10. Ruffieux, P. *et al.* On-surface synthesis of graphene nanoribbons with zigzag edge topology. *Nature* **531**, 489–492 (2016).

11. Llinas, J. P. *et al.* Short-channel field-effect transistors with 9-atom and 13-atom wide graphene nanoribbons. *Nat. Commun.* **8:633**, 1–6 (2017).

12. Abbassi, M. E. *et al.* Controlled quantum dot formation in atomically engineered graphene nanoribbons field-effect transistors. *ArXiv191210712 Cond-Mat* (2019).

13. Braun, O. *et al.* Optimized graphene electrodes for contacting graphene nanoribbons. *Carbon* **184**, 331–339 (2021).

14. Borin Barin, G. *et al.* Growth Optimization and Device Integration of Narrow-Bandgap Graphene Nanoribbons. *Small* 2202301 (2022) doi:10.1002/smll.202202301.

15. Zhang, J. *et al.* Tunable Quantum Dots from Atomically Precise Graphene Nanoribbons Using a Multi-Gate Architecture. *Adv. Electron. Mater.* **9**, 2201204 (2023).

16. Slota, M. *et al.* Magnetic edge states and coherent manipulation of graphene nanoribbons. *Nature* **557**, 691–695 (2018).

17. Blackwell, R. E. *et al.* Spin splitting of dopant edge state in magnetic zigzag graphene nanoribbons. *Nature* **600**, 647–652 (2021).

18. Kan, E., Li, Z., Yang, J. & Hou, J. G. Half-Metallicity in Edge-Modified Zigzag Graphene Nanoribbons. *J. Am. Chem. Soc.* **130**, 4224–4225 (2008).

19. Zhao, S. *et al.* Optical Imaging and Spectroscopy of Atomically Precise Armchair Graphene Nanoribbons. *Nano Lett.* **20**, 1124–1130 (2020).

20. Zhao, S. *et al.* Optical Investigation of On-Surface Synthesized Armchair Graphene Nanoribbons. *Phys. Status Solidi B* **254**, 1700223 (2017).

21. Senkovskiy, B. V. *et al.* Making Graphene Nanoribbons Photoluminescent. *Nano Lett.* **17**, 4029–4037 (2017).

22. Denk, R. *et al.* Exciton-dominated optical response of ultra-narrow graphene nanoribbons. *Nat. Commun.* **5**, 4253 (2014).

23. Borin Barin, G. *et al.* Surface-Synthesized Graphene Nanoribbons for Room Temperature Switching Devices: Substrate Transfer and ex Situ Characterization. *ACS Appl. Nano Mater.* **2**, 2184–2192 (2019).

24. Cai, J. *et al.* Graphene nanoribbon heterojunctions. *Nat. Nanotechnol.* **9**, 896–900 (2014).

25. Fairbrother, A. *et al.* High vacuum synthesis and ambient stability of bottom-up graphene nanoribbons. *Nanoscale* **9**, 2785–2792 (2017).

26. Bouwmeester, D. *et al.* MoRe Electrodes with 10 nm Nanogaps for Electrical Contact to Atomically Precise Graphene Nanoribbons. *ACS Appl. Nano Mater.* **6**, 13935–13944 (2023).

27. Martini, L. *et al.* Structure-dependent electrical properties of graphene nanoribbon devices with graphene electrodes. *Carbon* **146**, 36–43 (2019).

28. Wang, Y. *et al.* Electrochemical Delamination of CVD-Grown Graphene Film: Toward the Recyclable Use of Copper Catalyst. *ACS Nano* **5**, 9927–9933 (2011).

29. Gao, L. *et al.* Repeated growth and bubbling transfer of graphene with millimetre-size single-crystal grains using platinum. *Nat. Commun.* **3**, 699 (2012).

30. Overbeck, J. *et al.* Optimized Substrates and Measurement Approaches for Raman Spectroscopy of Graphene Nanoribbons. *Phys. Status Solidi B* **256**, 1900343 (2019).

31. Passi, V. *et al.* Field-Effect Transistors Based on Networks of Highly Aligned, Chemically Synthesized *N* = 7 Armchair Graphene Nanoribbons. *ACS Appl. Mater. Interfaces* **10**, 9900–9903 (2018).

32. Barin, G. B. *et al.* Growth optimization and device integration of narrow-bandgap graphene nanoribbons. 33.

33. Overbeck, J. *et al.* Optimized Substrates and Measurement Approaches for Raman Spectroscopy of Graphene Nanoribbons. *Phys. Status Solidi B* **0**,.

34. Jiao, L. *et al.* Creation of Nanostructures with Poly(methyl methacrylate)-Mediated Nanotransfer Printing. *J. Am. Chem. Soc.* **130**, 12612–12613 (2008).

35. Yang, X. & Yan, M. Removing contaminants from transferred CVD graphene. *Nano Res.* **13**, 599–610 (2020).

36. Zhuang, B., Li, S., Li, S. & Yin, J. Ways to eliminate PMMA residues on graphene —— superclean graphene. *Carbon* **173**, 609–636 (2021).

37. Chen, Y., Gong, X. & Gai, J. Progress and Challenges in Transfer of Large-Area Graphene Films. *Adv. Sci.* **3**, 1500343 (2016).

38. Lin, Y.-C. *et al.* Graphene Annealing: How Clean Can It Be? *Nano Lett.* **12**, 414–419 (2012).

39. Pirkle, A. *et al.* The effect of chemical residues on the physical and electrical properties of chemical vapor deposited graphene transferred to SiO_2. *Appl. Phys. Lett.* **99**, 122108 (2011).

40. Kang, J., Shin, D., Bae, S. & Hong, B. H. Graphene transfer: key for applications. *Nanoscale* **4**, 5527 (2012).

41. Borin Barin, G. *et al.* Optimized graphene transfer: Influence of polymethylmethacrylate (PMMA) layer concentration and baking time on graphene final performance. *Carbon* **84**, 82–90 (2015).

42. Suk, J. W. *et al.* Transfer of CVD-Grown Monolayer Graphene onto Arbitrary Substrates. *ACS Nano* **5**, 6916–6924 (2011).

43. Park, H., Brown, P. R., Bulović, V. & Kong, J. Graphene As Transparent Conducting Electrodes in Organic Photovoltaics: Studies in Graphene Morphology, Hole Transporting Layers, and Counter Electrodes. *Nano Lett.* **12**, 133–140 (2012).

44. Her, M., Beams, R. & Novotny, L. Graphene transfer with reduced residue. *Phys. Lett. A* **377**, 1455–1458 (2013).

45. Cheng, Z. *et al.* Toward Intrinsic Graphene Surfaces: A Systematic Study on Thermal Annealing and Wet-Chemical Treatment of SiO_2 -Supported Graphene Devices. *Nano Lett.* **11**, 767–771 (2011).

46. Jeong, H. J. *et al.* Improved transfer of chemical-vapor-deposited graphene through modification of intermolecular interactions and solubility of poly(methylmethacrylate) layers. *Carbon* **66**, 612–618 (2014).

47. Sun, H. *et al.* High quality graphene films with a clean surface prepared by an UV/ozone assisted transfer process. *J. Mater. Chem. C* **5**, 1880–1884 (2017).

48. Di Giovannantonio, M. *et al.* On-Surface Growth Dynamics of Graphene Nanoribbons: The Role of Halogen Functionalization. *ACS Nano* **12**, 74–81 (2018).

49. Darawish, R. *et al.* Quantitative Characterization of Graphene Nanoribbons Orientation and Quality by Polarized Raman Spectroscopy. *submitted* (2023).

50. Hallam, T., Berner, N. C., Yim, C. & Duesberg, G. S. Strain, Bubbles, Dirt, and Folds: A Study of Graphene Polymer-Assisted Transfer. *Adv. Mater. Interfaces* **1**, n/a-n/a (2014).

51. Raman spectroscopy in graphene related systems. (Wiley-VCH, 2011).

52. Tuinstra, F. Raman Spectrum of Graphite. *J. Chem. Phys.* **53**, 1126 (1970).

53. Dresselhaus, M. S., Jorio, A., Hofmann, M., Dresselhaus, G. & Saito, R. Perspectives on Carbon Nanotubes and Graphene Raman Spectroscopy. *Nano Lett.* **10**, 751–758 (2010).

54. Maghsoumi, A., Brambilla, L., Castiglioni, C., Müllen, K. & Tommasini, M. Overtone and combination features of G and D peaks in resonance Raman spectroscopy of the C78H26 polycyclic aromatic hydrocarbon. *J. Raman Spectrosc.* **46**, 757–764 (2015).

55. Gillen, R., Mohr, M., Thomsen, C. & Maultzsch, J. Vibrational properties of graphene nanoribbons by first-principles calculations. *Phys. Rev. B* **80**, (2009).

56. Gillen, R., Mohr, M. & Maultzsch, J. Symmetry properties of vibrational modes in graphene nanoribbons. *Phys. Rev. B* **81**, (2010).

57. Vandescuren, M., Hermet, P., Meunier, V., Henrard, L. & Lambin, Ph. Theoretical study of the vibrational edge modes in graphene nanoribbons. *Phys. Rev. B* **78**, 195401 (2008).

58. Verzhbitskiy, I. A. *et al.* Raman Fingerprints of Atomically Precise Graphene Nanoribbons. *Nano Lett.* **16**, 3442–3447 (2016).

59. Kim, S. *et al.* Robust graphene wet transfer process through low molecular weight polymethylmethacrylate. *Carbon* **98**, 352–357 (2016).

60. Park, H. *et al.* Optimized poly(methyl methacrylate)-mediated graphene-transfer process for fabrication of high-quality graphene layer. *Nanotechnology* **29**, 415303 (2018).

61. Langston, X. & Whitener, K. E. Graphene Transfer: A Physical Perspective. *Nanomaterials* **11**, 2837 (2021).

62. Classen, T. *et al.* Templated Growth of Metal-Organic Coordination Chains at Surfaces. *Angew. Chem. Int. Ed.* **44**, 6142–6145 (2005).

63. Cañas-Ventura, M. E. *et al.* Self-Assembly of Periodic Bicomponent Wires and Ribbons. *Angew. Chem. Int. Ed.* **46**, 1814–1818 (2007).

64. de Heer, W. A. *et al.* Epitaxial graphene. *Solid State Commun.* **143**, 92–100 (2007).

Chapter 7

Exploratory studies on substrate passivation and self-assembled mono-layer intercalation

7.1 Passivation of Au(788) step edges with Poly(p-phenylene) (PPP)

The results presented in this section are a part of the master project of Lüthi, D. et al [1]

As already shown in previous chapters, substrate transfer of GNRs from their metallic growth surfaces to semiconducting or insulating substrates like SiO_2/Si is a key challenge. In this thesis, we used two main methods to transfer GNRs, (i) a polymer-free transfer [2], and (ii) the electrochemical delamination method [3]. Although the electrochemical delamination transfer is the method of choice to transfer aligned GNRs [4], it is now evident that this method has limitations, especially regarding the transfer efficiency of samples with low surface coverages.

As detailed in Chapter 5, 9-AGNR samples with high surface coverage show transfer efficiency up to 52-70%, with a sharp decrease down to 35% for 9-AGNR samples with low surface coverage. We attributed this behavior to the strong interaction between GNRs and the Au(788) step edge, leading to a significant decrease in transfer quality, as is indicated by the decrease in alignment and increased ribbon damage after the transfer.

In this sub-chapter, we explore the idea of passivating the Au(788) step edges with poly(p-phenylene) (PPP), to decrease the interaction between GNR-Au, and consequently improve GNR quality and transfer efficiency. Figure 1 summarizes the main advantages and disadvantages of transferring aligned 9-AGNRs with high (a) and low (b) coverage and the proposed strategy we explored.

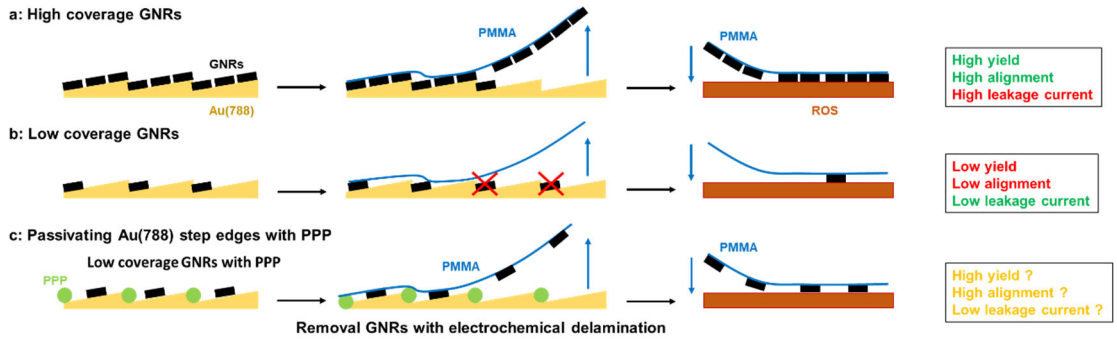

Figure 1: Challenges in substrate transfer of GNRs with different surface coverage. (a) High coverage increases device yield due to the large amount of GNRs being transferred, but it also introduces leakage current problems. (b) Low coverage leads to unreliable transfer and decreased ribbon alignment. (c) Proposed solution: Passivating Au(788) step edges with PPP to improve growth and transfer of low-coverage aligned 9-AGNRs. The scheme is reproduced from Ref 1.

Poly(para-phenylene) (PPP) wires can be considered the narrowest form of GNRs, with only 3 atoms on its width (3-AGNRs) [5–10]. To avoid confusion with 9-AGNRs, we, however, refrain from referring to the PPP as a GNR and instead refer to a PPP wire. With a band gap of 3.2eV [5], PPP is an optimal choice for passivating the Au(788) edge, as PPP wires grow similarly to 9-AGNRs, and the wide bandgap would not influence the performance of 9-AGNR-based FET devices. Furthermore, PPP could act as a supportive template during substrate transfer, leading to well-aligned low-coverage 9-AGNRs. Figure 2 summarizes the mechanism of PPP growth from the 4,4"-dibromo-p-terphenyl (DBTP) precursor and the possibility of lateral fusion to form wider GNRs upon annealing at higher temperatures

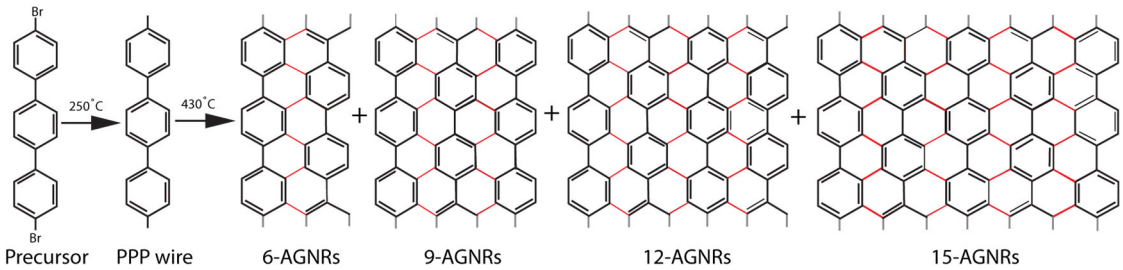

Figure 2: Schematic representation of the bottom-up synthesis of PPP. It starts from the precursor DBTP and the lateral fusion of PPP into 6-, 9-, 12-, and 15-AGNRs.

Here, we investigate the growth of PPP and PPP+ 9-AGNR on Au(788) with STM and Raman spectroscopy. For this study we prepared three different types of samples: (i) PPP on Au(788), (ii) low coverage 9-AGNRs on Au(788), and (iii) PPP and 9-AGNRs on Au(788). Samples with only PPP (i) or only 9-AGNRs (ii) are used as references. Moreover, we also explore the growth and lateral fusion, upon high-temperature annealing, of PPP wires on Au(788) and determine the effects of PPP passivation on the growth of 9-AGNRs on Au(788). Finally, we use Raman spectroscopy and polarized Raman spectroscopy to investigate 9-AGNR + PPP samples in terms of structural integrity and GNR alignment after substrate transfer.

Exploring growth and fusion of PPP wires on Au(788)

PPP wires are synthesized by sublimating the DBTP precursor from a quartz crucible at 120°C onto Au(788) under UHV conditions. We synthesize PPP samples with two different surface coverages: high-coverage PPP samples (deposition time: 10 min) and low-coverage PPP samples (deposition time: 2 min 35 sec). The synthesis involves one-step annealing at approximately 250°C, leading to ordered and extended PPP wires through Ullmann-like coupling between debrominated precursor units, as shown in Fig. 2. Heating PPP at approximately 400°C triggers dehydrogenative reactions, transforming the PPP wires into wider AGNRs [5,7,10] (Fig. 2). Figure 3 shows a representative STM image of a low-coverage PPP sample after annealing at 250°C, revealing one PPP wire per terrace growing along step-edges. This observation provides clear evidence of the preferential diffusion of precursors towards the step edges, promoting polymerization at those specific locations. Further annealing this sample to 400°C results in the lateral fusion of small segments of PPP, observed across the terraces, Fig. 3b. Despite that, most PPP wires do not fuse and remain at the step-edge. In contrast, annealing high-coverage PPP samples at 400°C leads to significant fusion between PPP wires, as illustrated in the STM image shown in Fig, 3c. Given that 9-AGNRs' cyclodehydrogenation occurs around 400°C, we anticipate that high coverage PPP's lateral fusion will trigger the formation of other AGNR types, and therefore we have produced all samples of PPP+9-AGNRs with a low surface coverage of PPP.

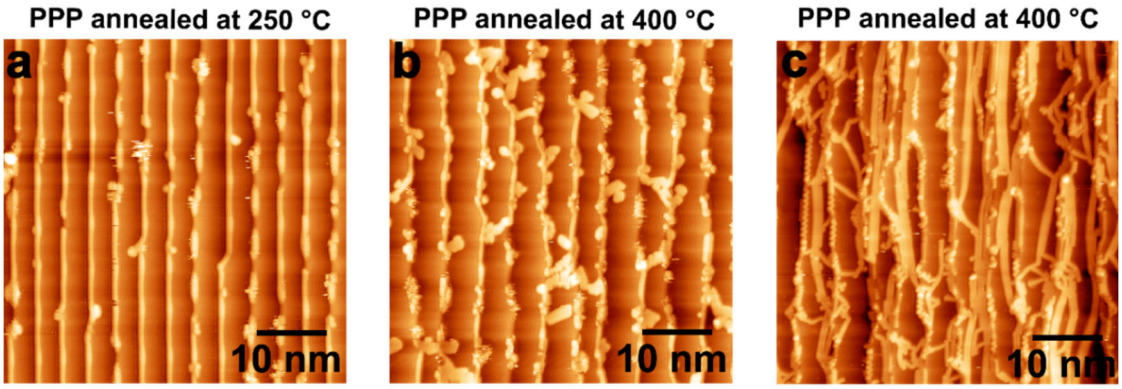

Figure 3: STM images of high- and low-coverage PPP samples, probing the impact of temperature on varying PPP coverage. a) Low-coverage PPP sample annealed at 250°C (V_b =0.2 V, I_t =30 pA). b) Low-coverage PPP annealed to 400°C (V_b =-1.5 V, I_t =30 pA). c) High-coverage PPP sample annealed to 400°C (V_b =-1V, I_t =30 pA).

We further characterize PPP samples synthesized with low- and high-coverage that underwent different annealing temperatures using multiwavelength Raman spectroscopy (488 nm, 532 nm, and 785 nm), Fig. 4. As the PPP can be classified as the narrowest GNR with width N = 3, it is expected that similar peaks arise compared to Raman spectroscopy of wider GNRs due to the same symmetry. Indeed, at wavelengths of 488 nm and 532 nm, all samples exhibit pronounced G, CH, and D modes similar to wider GNRs.

Raman spectra of low-coverage samples (annealed at 400°C) and high-coverage samples (annealed at 250°C) do not show any features when measured with 785 nm. It is expected that PPP is completely out of resonance with this laser energy (1.5 eV) due to its large bandgap (3.2 eV). This also suggests that no significant PPP fusion is happening at these coverages and

temperatures. However, the situation is completely different when a high coverage sample of PPP is annealed at 400°C (black spectrum, right panel). This Raman spectrum resembles one of wider GNRs, showing the RBLM of the 6-AGNR at 463 cm^{-1} and the RBLM of the 9-AGNR at 314 cm^{-1}, corroborating our STM results that show PPP wires fused into wider GNRs when prepared with a high surface coverage and annealed at higher temperatures, Fig. 3c.

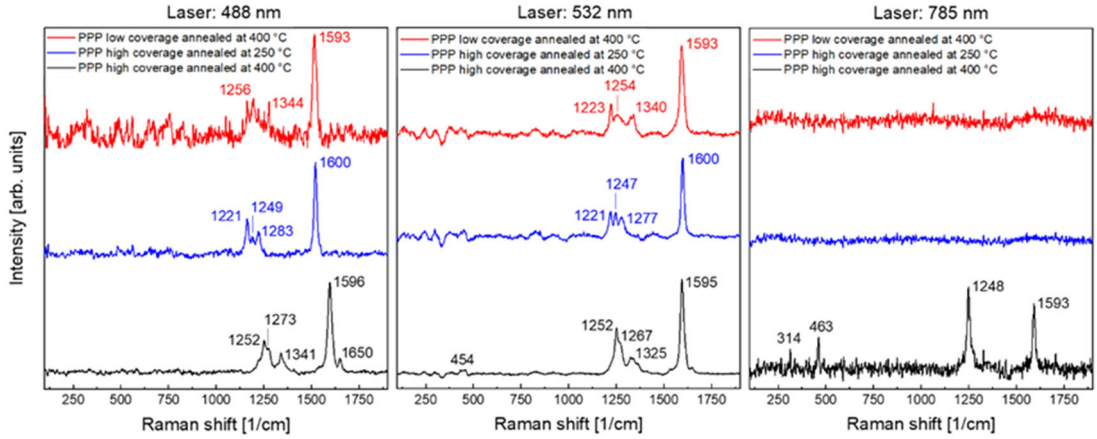

Figure 4: Comparison of Raman spectra for a high-coverage PPP at different temperatures. a) High-coverage PPP sample annealed at 250°C (in blue), High-coverage PPP sample annealed at 400°C (in black), and a low-coverage PPP sample annealed at 400°C (in red). Lasers with wavelengths of 488 nm, 532 nm, and 785 nm were used.

9-AGNRs on Au(788) edge-passivated with PPP (9-AGNR + PPP)

We start by synthesizing one PPP wire per step on Au(788) (deposition of DBTP at 102 °C for 2 min 35 sec, followed by a single annealing step at 250°C), followed by the deposition of low coverage 9-AGNR (deposition of DITP on the same surface at 67 °C for 3 min and subsequently annealed at 200 °C and then 400 °C for a 10 min holding time on each step), Fig. 5b-c.

Our STM investigation reveals that when 9-AGNRs grow on Au(788) with PPP-passivated edges, the PPP wires appear to stay intact and their diffusion away from the step edges is strongly reduced. In Fig. 5a we observe 9-AGNRs growing distinctly together with PPP: GNR 1, growing near the step-edge, distinguished by its dark contrast. GNR 2, situated on the terrace adjacent to a PPP wire, exhibits no apparent fusion, with discernible bite defects within the 9-AGNR. GNR 3 growing next to another GNR (not fused, characterized by a noticeable gap between them). The ribbon 3 grows towards the center of the terrace since the step-edge is already occupied by another ribbon.

STM images such as those discussed above suggest that PPP may act as a passivator, as even when grown with 9-AGNRs, PPP remains close to the step-edge, and no fusion occurs during 9-AGNR cyclodehydrogenation. This results in the growth of 9-AGNRs toward the center of the terrace, potentially positively influencing substrate transfer by avoiding the strong adhesion of 9-AGNRs to step edges due to the PPP-passivated edges.

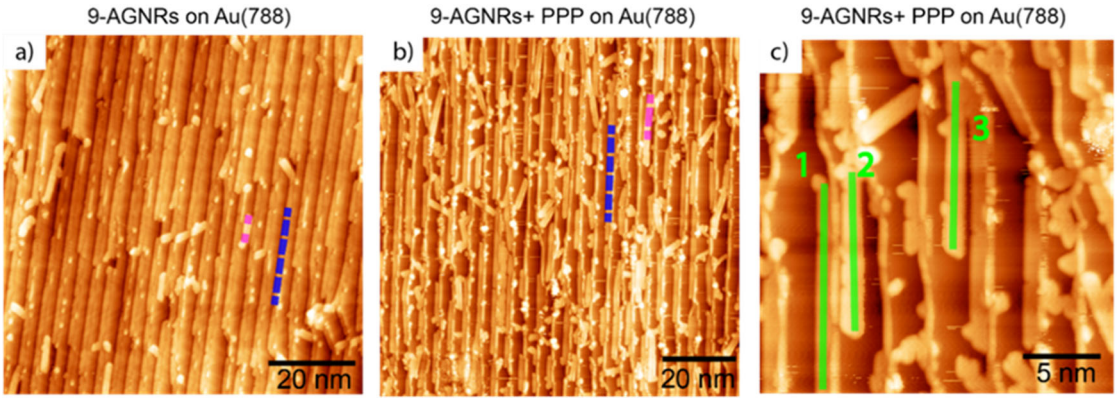

Figure 5: STM characterization of 9-AGNRs and PPP+9-AGNRs samples. a) STM image of low-coverage 9-AGNRs growing along the step-edge (highlighted in blue) and on the terrace (highlighted in pink) of Au(788), for reference (V_b =-1.5 V, I_t =0.3 nA). b) STM image of one PPP grown per step, followed by the growth of one 9-AGNR per step, on Au(788). Ribbons growing along the step edge are highlighted in blue, and ribbons growing on top of the terrace are highlighted in pink. c) Close-up STM image depicting the growth of one PPP per step on Au(788), followed by the growth of 9-AGNR slightly below the coverage of one 9-AGNR per step (V_b =-2.1V, I_t =30 pA).

We further characterized several low-coverage 9-AGNR+PPP samples using multiwavelength Raman spectroscopy on Au (788) (in red) and after substrate transfer to the Raman optimized substrate (ROS)[3] (in blue), Fig. 6. For comparison, we also plot the Raman spectrum of transferred low-coverage 9-AGNRs (in black). The 9-AGNR+PPP on Au(788) shows the typical 9-AGNR G, CH, and D modes for both 532 and 488 nm laser lines. For the 785 nm laser, as reflected by the low signal-to-noise ratio for the low coverage 9-AGNR + PPP sample, we did not manage to obtain a high-quality spectrum due to issues with the laser settings during the measurements.

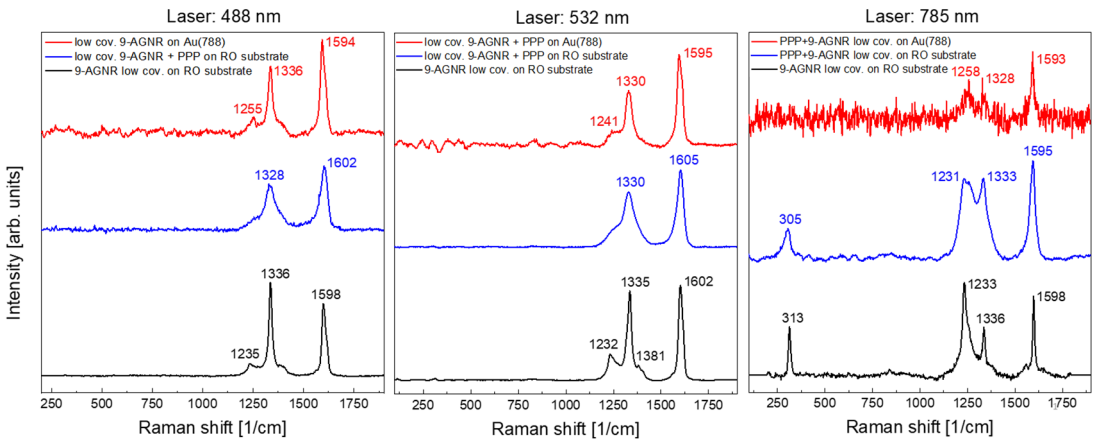

Figure 6: Raman spectra of low-coverage 9-AGNR + PPP sample before and after substrate transfer with different laser wavelengths. On Au(788) (before transfer, red curves) and on the ROS (after transfer, blue curves) measured with the 488 nm, 532 nm, and 785 nm lasers. The Raman spectra of low-coverage 9-AGNR on the ROS (black curves) are used as a reference

After substrate transfer, we observe a broadening of the G and D modes for all laser wavelengths, indicating that the investigated low-coverage 9-AGNR sample with a single PPP per step-edge has not transferred reliably. While the CH-D and G modes show a blueshift due to the interaction of the 9-AGNRs and the PPP with the surface of the ROS compared to the

situation on Au(788) for all lasers, we observe a distinct redshift of the RBLM to 305 cm^{-1} in the 785 nm laser spectrum. As the 785 nm laser has been shown to only be resonant with the 9-AGNRs, a signal contribution of PPP can be excluded. The presence of PPP could however lead to a change in the interaction of the 9-AGNRs with the substrate after transfer, causing a shift. The observed RBLM is also broadened significantly. Consequently, this broadening could go in hand with defects, leading to an alteration of the width-related vibrations. To draw stronger conclusions, however, it would be necessary to grow and transfer a larger number of samples. The single sample investigated in this preliminary study may not be representative.

Nevertheless, we also investigated the effect of PPP edge passivation on the preservation of the degree of alignment during substrate transfer. We transferred both the low-coverage 9-AGNRs+PPP and the low-coverage 9-AGNRs samples onto the ROS and characterized both samples with polarized Raman spectroscopy. The polarization direction was varied from -90 to 90 degrees relative to the direction of the terraces. The polar plot shown in Figure 7 shows the G mode intensity extracted by a Lorentzian fit of the G peak for each angle. The G peak intensity follows a $\cos^4(\theta)$ dependence, which θ denotes the angle between light polarization and the GNR alignment axis [3,4]. Using the Raman polarization anisotropy (P) defined as $P = (I_{//} - I_{\perp}) / (I_{//} + I_{\perp})$, where $I_{//}$ and $I_{\perp}$ represent the Raman intensities measured with polarization along and perpendicular to the GNR axis, we quantitatively characterize the degree of GNR alignment [3,4,11]. A perfect uniaxial alignment of GNRs corresponds to P=1, while P=0 indicates random orientation. We observe P=0.25 for 9-AGNRs and P=0.47 for 9-AGNRs+PPP. The higher P value for 9-AGNR + PPP reflects significantly better preservation of GNR alignment compared to the sample containing only 9-AGNRs. It is important to highlight that we have observed P values up to 0.6 for other transfers of low-coverage 9-AGNRs, highlighting the significant variability of sample quality upon transfer.

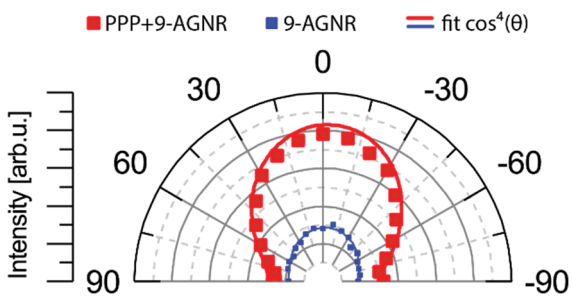

Figure 7: Polar diagrams of G mode intensities for 9-AGNRs and PPP/9-AGNRs samples. Representative polar diagrams illustrating the G mode intensities of 9-AGNRs samples (blue squares) and PPP/9-AGNRs (red squares) after substrate transfer onto ROS. Blue and red solid lines represent the $cos^4(\theta)$ that fits the measured data.

Conclusions

In this preliminary study, we have investigated the passivation of Au(788) step edges with PPP wires and their interaction with 9-AGNRs using STM and Raman spectroscopy. We observe that controlled DBTP precursor deposition led to PPP wires growing along 9-AGNRs on the Au(788) surface. STM characterization revealed that the passivation of the step edges by PPP leads to 9-

AGNRs growing predominantly on the terraces. We characterize the Raman fingerprints of PPP upon different growth conditions and confirm that high-quality 9-AGNRs can be grown in the presence of PPP at the Au(788) step edges. Finally, we note that the transfer of a low-coverage 9-AGNR+PPP sample to a ROS did not yield a high-quality sample, as indicated by peak broadening and shifts in Raman spectra. However, polarization anisotropy values reveal significantly better preservation of GNR alignment upon transfer than for 9-AGNRs samples without PPP.

7.2. Intercalation of GNRs with self-assembled monolayrs (SAMs)

In the field of surface science, self-assembled monolayers (SAMs) have been widely studied[12–16], because they represent a systematic approach to surface modification/functionalization at the molecular level. These monolayers are typically constituted by the spontaneous organization of molecules on a substrate surface via chemical interactions, resulting in a structurally uniform, oriented assembly. The nature and properties of SAMs are predominantly governed by the choice of molecule, substrate, and surrounding environment, given tunable physicochemical characteristics such as hydrophobicity, and chemical reactivity [17].

Thiol-based SAMs, commonly applied to noble metal surfaces like gold and silver, stand as an archetype due to their robustness and well-defined structure. The formation of such SAMs from solution involves a rapid initial physisorption onto the gold substrate followed by slow chemisorption[12]. Thiol molecules are strongly bound to the Au(111) surface through their sulfur headgroup, and their alkyl chains are typically directed away from the metal surface[12–16], Fig. 8a. Figs. 8b and c show an example of an octanethiol-based SAM (solution with Dimethylformamide (DMF)) on Au(111), revealing the formation of an ordered SAM with a (√3×√3)R30° superlattice structure [12].

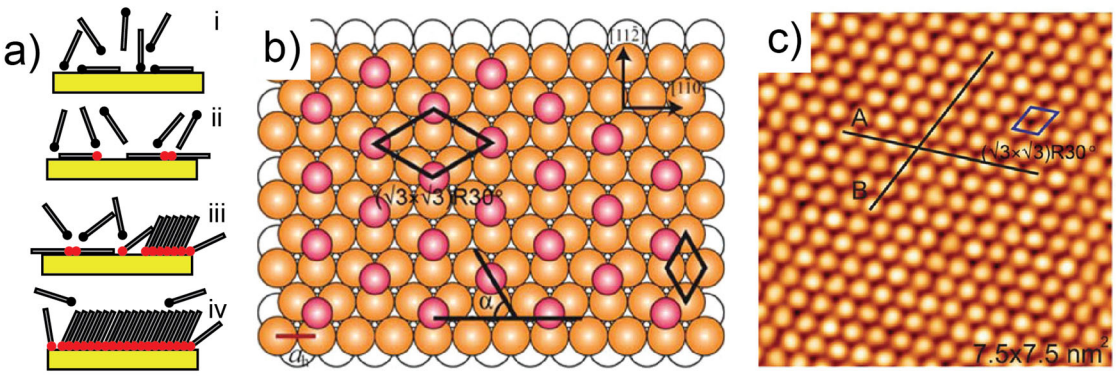

Figure 8: Schematic mechanistic diagram depicting the self-assembly of alkanethiols on Au(111). a) (i) Initial adsorption, (ii) Lying-down phase formation, (iii) Two-dimensional phase transition from a lying-down to a standing-up configuration, and (iv) Formation of a complete SAM. b) Schematic illustrations of octanethiol-SAM on Au(111), including the structural model of the (√3 × √3)R30° superlattice. c) STM topographical images of octanothiol (in DMF) SAM on Au(111). Schemes b and c are Reprinted with permission from [Mamun, A. H. A. et al. J. Phys. Chem. C 116, 22441–22448 (2012)][18], Copyright © 2012, American Chemical Society.

Here we explore the strong thiol-based SAM-Au bond as a strategy to decrease the interaction between GNRs and the Au surface, to thus improve GNR quality and transfer efficiency. This approach is also relevant in view of transferring graphene nanostructures that are sensitive to air, such as graphene nanoribbons with zigzag edges and spin chains, which are ill-suited for existing wet-transfer techniques. To develop a dry-transfer method, ideally in UHV, a crucial step involves minimizing the interaction between GNR and the underlying growth substrate, e.g. via intercalation of a SAM.

We use 1,8,13-trimercaptomethyl-triptycene (T1) SAMs, which possess a tripod-shaped tri-thiol structure composed of a rigid adamantane core and three CH_2SH legs [18,19], Fig. 9a. Due to the presence of multiple anchoring sites, T1 tends to adopt nested 2D hexagonal structures with high structural uniformity and orientational order as shown in the STM image in Figs. b and c [18].

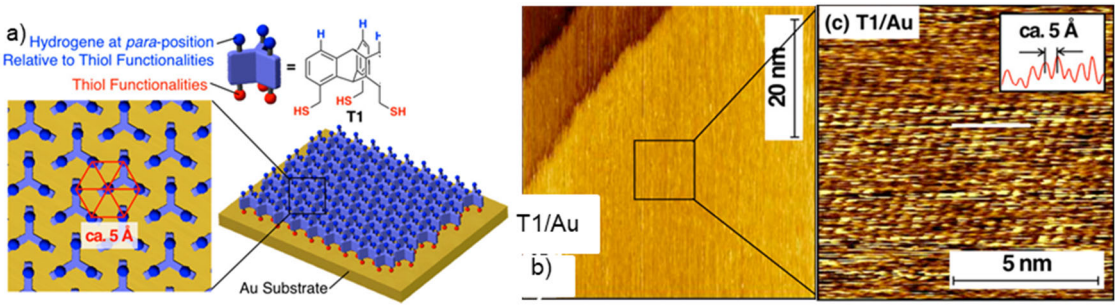

Figure 9: Schematic structure and illustration of molecular arrangement of T1 on Au(111) as observed in STM features for T1 on Au(111). The scheme is reproduced from Ref. The scheme is Reprinted with permission from [Ishiwariet al. F.et al., J. Am. Chem. Soc. 141 (2019) 5995–6005] [18], used under Creative Commons CC license.

We investigate the intercalation of 9-armchair graphene nanoribbons (9-AGNRs) at medium coverage on Au(111)/mica with T1 from both the gas phase (sublimated in UHV) and from liquid (solution) environments. We explore the influence of concentration, time, temperature, and storage conditions of T1 to determine the optimal parameters for intercalating 9-AGNRs.

Preparation of T1-SAMs on Au(111)

The Au(111)/mica samples undergo standard cleaning procedures, involving two cycles of sputtering and annealing under UHV conditions, which will be referred to later as clean Au(111)/mica samples. Subsequently, the T1/Au is prepared by immersing the cleaned Au(111)/mica substrates in a degassed Tetrahydrofuran (THF) solution of T1 at 25°C. The samples are then washed with THF, air-dried, and annealed for one hour at 120°C and 1 bar pressure.

T1/THF solution concentration and immersion times

To optimize T1 concentration and immersion time for GNR intercalation, we investigate different T1/THF solution concentrations (1 µM, 2 µM, 5 µM) and immersion times (1 and 24 hours). After immersing the clean Au(111)/mica samples in the solutions for the given times, the cleaned and dried samples are introduced into a UHV system and characterized by STM topography images

(Fig. 10). For an immersion time of 24 hours, STM reveals that, regardless of the concentration, T1 seems to cover the entire Au surface, thus forming a full monolayer, with 5 µM concentration showing the most densely packed and uniform SAM. The dark circles observed in all the STM images with different concentrations correspond to gold vacancy islands known as etch pits. These etch pits form when the thiol's sulfur covalently binds to gold, leading to the lifting off of individual gold atoms, with the created Au vacancies then assembling into vacancy islands [20].

In a previous study by Ishiwari et al. [18], it was noted that at 2 µM concentrations of the T1/THF solution, T1 on the Au(111) surface formed a 2D nested hexagonal structure with 5-6 Å separation between the bright spots, which were attributed to the phenyl rings of the triptycene units. Our observations fall within the same range (5 Å).

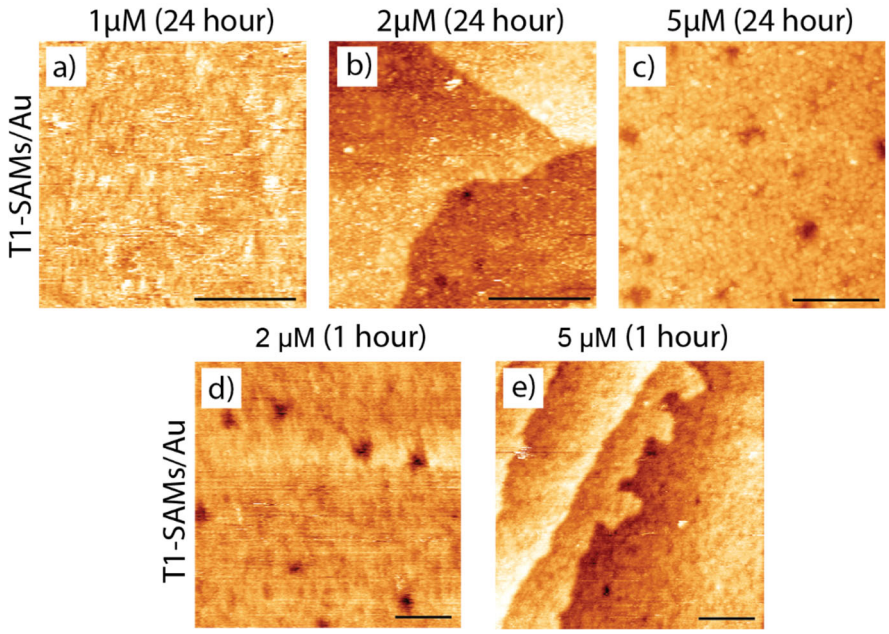

Figure 10: STM topographical images of the Au(111)/mica surface after immersing in SAM of T1. Au(111)/mica surface after immersing in SAM of T1 with concentrations of 2 µM, and 5 µM for 24 hours and 1 hour of immersing time, with a scale bar of 10 nm (V_b =0.5 V, I_t =0.3 nA).

To investigate the influence of immersion times in particular 24 hours versus 1 hour for different concentrations, we also prepared two samples immersed for only 1 hour in T1/THF solutions with 2 µM and 5 µM concentrations. Representative STM images are shown in Figs. 10 d and f. We do not observe a significant difference for both samples with 1-hour immersion time compared to the samples with the same concentration but 24-hour immersion. Apart from the fact that the sample immersed in the T1/THF of 2 µM was significantly more challenging to scan due to the presence of mobile molecules at room temperature. This could suggest a less densely packed monolayer on the surface.

Thermal stability of T1-SAM on Au(111)

The thermal stability of T1 on Au(111)/mica has been investigated by annealing a sample immersed in a 5 µM T1/THF solution for 24 hours at temperatures of 120 °C for 1 hour, 130 °C

for 20 minutes, 230 °C for 20 minutes, and 420 °C for 20 minutes in UHV, Figs. 11 a and d, respectively. T1 seems to remain intact only up to 130 °C. Beyond this temperature, we start to observe changes related to the dimerization of sulfur head groups followed by the monomer's desorption and increasing surface disorder.

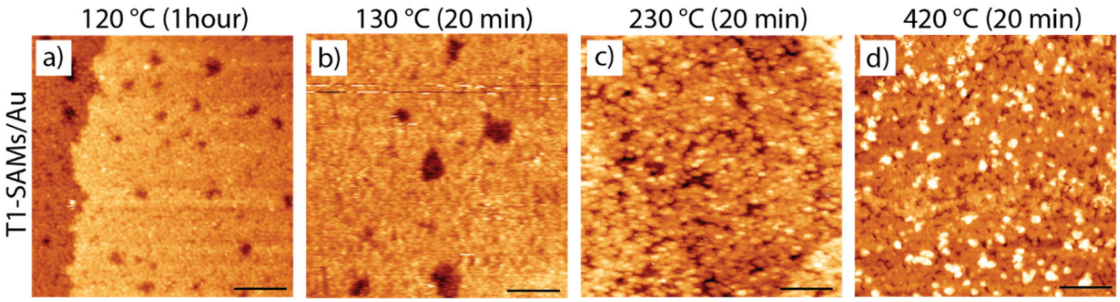

Figure 11: STM topographical images of T1-SAMs (5 µM /24 hours) on Au(111)/mica surface after different annealing procedures. Scale bar:20 nm. Scanning parameters: V_b =0.5 V, I_t =0.3 nA.

Intercalation of 9-AGNRs with T1-SAM

To investigate whether T1-SAMs can intercalate between 9-AGNRs and the Au(111) surface, we initially grow a medium coverage of 9-AGNRs on Au(111)/mica (Fig. 12a). Subsequently, the resulting samples are removed from the UHV system and immersed in a 5 µM T1/THF solution for 24 hours. They are then air-dried, annealed for one hour in a vacuum oven (1 bar) at 120°C, and finally re-inserted into the UHV system for STM characterization. For typical samples resulting from such a procedure, STM reveals a few GNRs intercalated with T1/SAM (Fig. 12b, black arrows). However, comparing Figs. 12a and b reveal that the post-intercalation 9-AGNR coverage appears notably reduced. There are two possible explanations for the "missing" 9-AGNRs: Either GNRs are washed away to the T1/THF solution, or the GNRs are rendered "invisible" to the STM because they are covered by the T1-SAM.

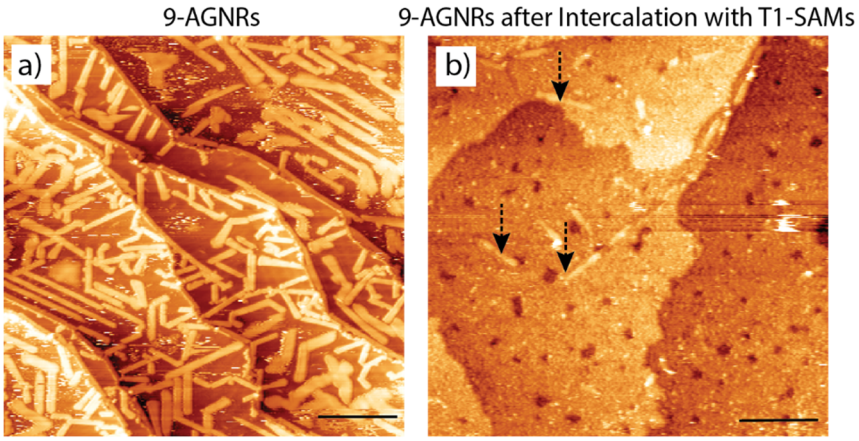

Figure 12: STM images illustrating the intercalation of 9-AGNRs by the T1-SAM. a) Medium coverage of 9-AGNRs on Au(111)/mica before the intercalation step. b) 9-AGNRs on Au(111)/mica after the intercalation process, with a scale bar of 20 nm (V_b =0.5 V, I_t =0.3 nA).

To shed light on the apparent reduction in 9-AGNR coverage during intercalation, we immersed a clean ROS [21] overnight in the same T1/THF solution that was used for the intercalation attempt described above. Afterward, this ROS is characterized with Raman spectroscopy. The Raman spectra reveal the fingerprints modes RBLM, CH, D, and G of 9-AGNRs (Fig. 13), which proves that the T1/THF solution indeed contains 9-AGNRs that have been re-deposited on the ROS surface upon immersion of the clean ROS. We cannot presently quantify the washing away of 9-AGNRs upon immersion in the T1/THF solution, but it is plausible that the washing away is the dominant effect underlying the observed reduction of 9-AGNR coverage.

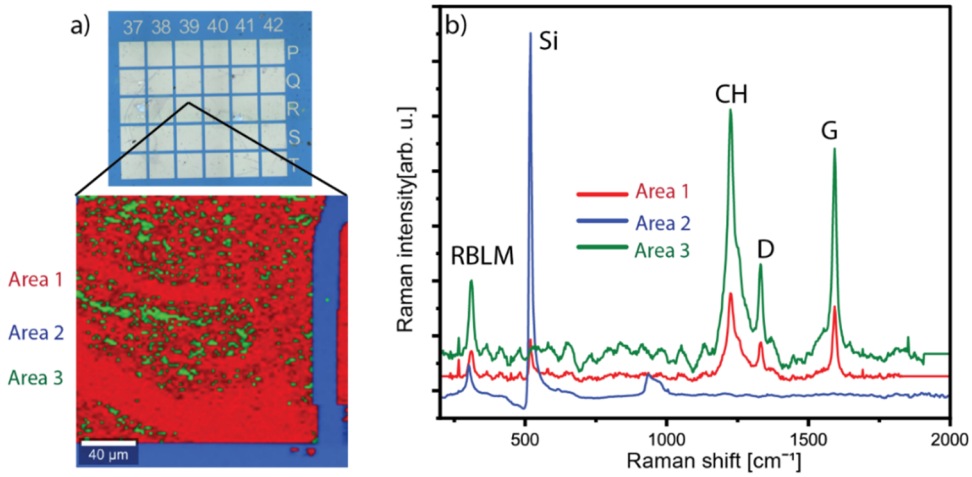

Figure 13: Raman characterization of ROS after immersing in the intercalation solution of T1-SAM. a) Image of ROS device after immersing in a solution that was previously used for 9-AGNR intercalation. Optical zoom-in with Raman G-intensity map. b) The corresponding Raman spectra of the optical zoom area, showing the main peaks of 9-AGNRs RBLM, CH-D, and G modes in areas 1, 2, and 3 while area 3 is the SiO_2.

Intercalation of 9-AGNRs with 1-Octanethiol-SAMs

Finally, we also made a very preliminary investigation of the possible intercalation of 9-AGNRs with octanethiol-based SAMs (1-Octanethiol- ($C_8H_{18}S$)). To start with, we analyzed the structure of the octanethiol SAM alone on Au(111). The procedure involves preparing a clean Au(111)/mica substrate (sputtered and annealed) in UHV, immersing it in 1M octanethiol/ethanol solution for 24 hours, followed by annealing in vacuum at 120° (1 bar) for 1 hour[22], and subsequent UHV STM characterization. The resulting STM image (Fig. 14) indicates full coverage of the Au(111) surface with octanethiol SAMs.

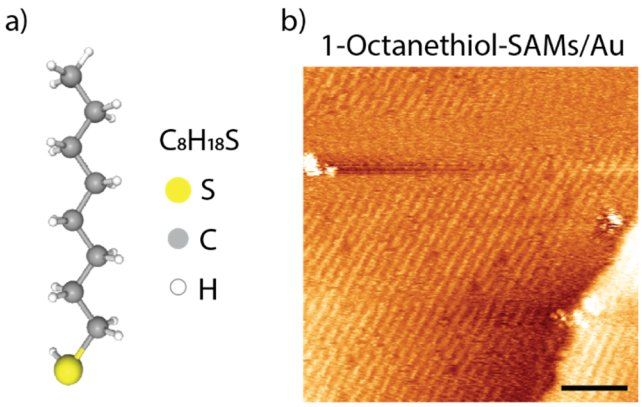

Figure 14: 1-Octanethiol-SAMs ($C_8H_{18}S$) covering the Au(111)/mica surface. This sample was after immersion in 1M octanethiol/ethanol solution for 24 hours, with a scale bar of 20 nm (V_b =0.5 V, I_t =0.3 nA).

After applying this procedure to Au/Mica samples with pre-grown 9-AGNRs (Figs. 15a), STM images (Figs. 15b and c) indicate a reduced GNR coverage after intercalation compared to the initial coverage on Au(111) (Figure 15a), with few GNR segments being intercalated, very similar to the situation described above with T1.

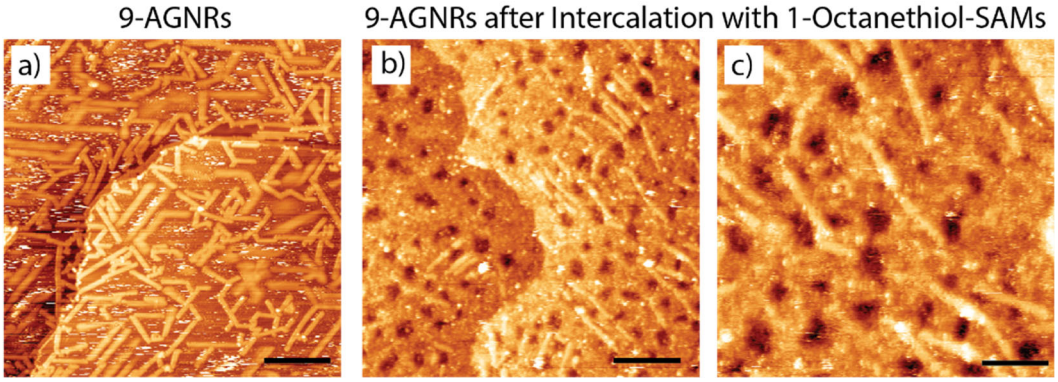

Figure 15: STM topographical images illustrating the intercalation of 9-AGNRs using the 1-octanethiol-SAMs. a) Medium coverage of 9-AGNRs on Au(111)/mica before the intercalation step. b) and c) Intercalated 9-AGNRs on top of octanethiol SAMs after the intercalation process, with a scale bar of 20 nm for a and b and 10 for c (V_b =0.5 V, I_t =0.3 nA).

Conclusions

We have investigated the intercalation process of 9-AGNRs using two different self-assembled monolayers formed by immersing 9-AGNR/Au/mica samples in SAM precursor/THF solutions. We observe that both SAMs form a full monolayer on Au(111), which successfully intercalates a few GNR segments. However, we also observe a significant reduction in the number of GNRs after SAM formation/intercalation. Raman experiments suggest that GNRs are lost during the intercalation to the solution. We performed preliminary investigations of UHV-based sublimation deposition of SAM precursors for intercalating GNRs but it did not show any intercalation. Therefore more investigations are necessary for this part.

References

1. Lüthi, D. Edge passivation of vicinal surfaces for controlled growth and substrate transfer of graphene nanoribbons. *MASTER THESIS* UNIVERSITY OF BASEL (2021).

2. Barin, G. B. *et al.* Surface-synthesized graphene nanoribbons for room-temperature switching devices: substrate transfer and ex-situ characterization. *ACS Appl. Nano Mater.* (2019) doi:10.1021/acsanm.9b00151.

3. Overbeck, J. *et al.* Optimized Substrates and Measurement Approaches for Raman Spectroscopy of Graphene Nanoribbons. *Phys. Status Solidi B* **256**, 1900343 (2019).

4. Senkovskiy, B. V. *et al.* Making Graphene Nanoribbons Photoluminescent. *Nano Lett.* **17**, 4029–4037 (2017).

5. Merino-Díez, N. *et al.* Width-Dependent Band Gap in Armchair Graphene Nanoribbons Reveals Fermi Level Pinning on Au(111). *ACS Nano* **11**, 11661–11668 (2017).

6. Song, S., Kojima, T., Nakae, T. & Sakaguchi, H. Wide graphene nanoribbons produced by interchain fusion of poly(p-phenylene) via two-zone chemical vapor deposition. *Chem. Commun.* **53**, 7034–7036 (2017).

7. De Boni, F. *et al.* Templating Effect of Different Low-Miller-Index Gold Surfaces on the Bottom-Up Growth of Graphene Nanoribbons. *ACS Appl. Nano Mater.* **3**, 11497–11509 (2020).

8. Sun, K. *et al.* On-Surface Synthesis of 8- and 10-Armchair Graphene Nanoribbons. *Small* **15**, 1804526 (2019).

9. Basagni, A. *et al.* Tunable Band Alignment with Unperturbed Carrier Mobility of On-Surface Synthesized Organic Semiconducting Wires. *ACS Nano* **10**, 2644–2651 (2016).

10. Basagni, A. *et al.* Molecules–Oligomers–Nanowires–Graphene Nanoribbons: A Bottom-Up Stepwise On-Surface Covalent Synthesis Preserving Long-Range Order. *J. Am. Chem. Soc.* **137**, 1802–1808 (2015).

11. Darawish, R. *et al.* Quantitative Characterization of Graphene Nanoribbons Orientation and Quality by Polarized Raman Spectroscopy. *submitted* (2023).

12. Mamun, A. H. A. & Hahn, J. R. Effects of Solvent on the Formation of Octanethiol Self-Assembled Monolayers on Au(111) at High Temperatures in a Closed Vessel: A Scanning Tunneling Microscopy and X-ray Photoelectron Spectroscopy Study. *J. Phys. Chem. C* **116**, 22441–22448 (2012).

13. Love, J. C., Estroff, L. A., Kriebel, J. K., Nuzzo, R. G. & Whitesides, G. M. Self-Assembled Monolayers of Thiolates on Metals as a Form of Nanotechnology. *Chem. Rev.* **105**, 1103–1170 (2005).

14. Guo, Q. & Li, F. Self-assembled alkanethiol monolayers on gold surfaces: resolving the complex structure at the interface by STM. *Phys. Chem. Chem. Phys.* **16**, 19074 (2014).

15. Vericat, C. *et al.* Self-assembled monolayers of thiolates on metals: a review article on sulfur-metal chemistry and surface structures. *RSC Adv* **4**, 27730–27754 (2014).

16. Vericat, C., Vela, M. E., Benitez, G., Carro, P. & Salvarezza, R. C. Self-assembled monolayers of thiols and dithiols on gold: new challenges for a well-known system. *Chem. Soc. Rev.* **39**, 1805 (2010).

17. Ulman, A. Formation and Structure of Self-Assembled Monolayers. *Chem. Rev.* **96**, 1533–1554 (1996).

18. Ishiwari, F. *et al.* Triptycene Tripods for the Formation of Highly Uniform and Densely Packed Self-Assembled Monolayers with Controlled Molecular Orientation. *J. Am. Chem. Soc.* **141**, 5995–6005 (2019).

19. Kitagawa, T., Matsubara, H., Okazaki, T. & Komatsu, K. Electrochemistry of the Self-Assembled Monolayers of Dyads Consisting of Tripod-Shaped Trithiol and Bithiophene on Gold. *Molecules* **19**, 15298–15313 (2014).

20. Deering, A. L., Van Lue, S. M. & Kandel, S. A. Ambient-Pressure Vapor Deposition of Octanethiol Self-Assembled Monolayers. *Langmuir* **21**, 10260–10263 (2005).

21. Overbeck, J. *et al.* Optimized Substrates and Measurement Approaches for Raman Spectroscopy of Graphene Nanoribbons. *Phys. Status Solidi B* **0**,.

22. Ohtomo, M., Sekine, Y., Hibino, H. & Yamamoto, H. Graphene nanoribbon field-effect transistors fabricated by etchant-free transfer from Au(788). *Appl. Phys. Lett.* **112**, 021602 (2018).

Chapter 8

Summary and outlook

The central inquiry of this research was the efficient transfer of atomically precise GNRs to device substrates — a question that is increasingly vital in the quest to address limitations in contemporary semiconductor technology[1]. According to the International Roadmap for Devices and Systems for 2022[2], a crucial challenge is to extend current semiconductor technologies to alternative channel materials that should have "controlled properties" and can allow for the operation of devices at a "high-density at the nanometer scale". GNRs could satisfy both of these conditions. Their electronic properties, for example, their bandgap, depend sensitively on the exact width and edge structure, which can be tailored with the necessary structural quality using the atomic precision afforded by on-surface synthesis[3]. However, any technological application of GNRs faces three major challenges. The first challenge is the synthesis of GNRs that meet stringent quality conditions essential for device integration. The second challenge involves transferring these high-quality GNRs from their metallic growth substrates to device substrates. The third challenge is the actual integration of these transferred GNRs into device architectures.

In the context of these overarching challenges, this thesis addressed the second obstacle in detail. How do we transfer the synthesized GNRs from the growth substrates to the device substrates? How can we do this with close to 100 % efficiency? In answering these questions, the work presented here has advanced our understanding of the transfer process for GNRs. It developed key insights into the growth of aligned GNRs. Crucially, it identified key strategies to improve the transfer and device yields and their quality.

The starting point for this thesis was the pivotal insight resulting from previous studies that highlighted the importance of aligned GNRs in device integration. By aligning device contacts along the growth directions, the device yield could be substantially increased from 10 % to 85 %[4]. In this thesis, it was unraveled how the surface of a vicinal crystal enforces the globally aligned growth of the GNRs by performing STM measurements on an extensive series of samples with varying GNR coverage. It could be shown that it is far more stable for the GNRs to grow parallel to the step edges than growing across them. Additionally, the step edges serve as a template for the 1D growth of the GNRs, leading to a sequential growth based on the precursor dose on the surface.

This thesis also presented a model to relate Raman measurements quantitatively with the GNR coverage on various substrates. It could thus obtain the GNR coverage on the growth substrate with Raman, removing the necessity of obtaining STM measurements for every sample. Additionally, it now allows the calculation of the GNR coverage after transfer based on Raman measurements only. This allowed us to quantify the fraction of GNRs that were transferred and to correlate transfer efficiency with the as-grown GNR coverage. This led to the unexpected

observation that GNRs grown with a low coverage on a vicinal single crystal surface had lower transfer efficiency (~35 %) compared to the transfer efficiency of 52-70 % seen for high-coverage samples. Moreover, the development of the quantitative model not only supersedes the need for STM measurements for each sample but also introduces a scalable metric for optimizing GNR transfer efficiency.

In addition to quantifying the GNR coverage, the research reported in this thesis also delved into the subtleties of GNR alignment. It presented a model to obtain the degree of alignment of the GNRs using Polarized Raman measurements. Applying this model to data from a wide range of samples, it was shown that GNRs could be grown well-aligned even at low coverages. However, they suffered a loss of alignment upon substrate transfer. The loss of alignment could be quantified and correlated with decreasing GNR coverage on the growth substrates.

The observations reported in this thesis led to an intuitive model for GNR behavior during the growth and transfer processes. Initially, at low coverages, GNRs preferentially adsorb next to step edges on a vicinal crystal. This adsorption is stable enough to resist detachment during transfer. GNR growth on the terrace away from a step edge occurs only after these edges are fully passivated by GNRs. These terrace-based GNRs are more amenable to transfer. However, GNRs tend to lose their alignment on the growth substrate unless the surface is nearly fully covered with GNRs. In such cases, adjacent GNRs serve as a scaffold, resisting lateral diffusion and maintaining alignment. This scaffolding effect is effective only when GNRs are constrained to move in a plane. Moreover, our results show that the adhesion to the substrates used during the transfer process is therefore sufficiently strong to prevent any out-of-plane diffusion of GNRs.

Armed with this intuitive understanding, two targeted strategies to mitigate these identified challenges were explored. Initially, it was tried to preserve GNR alignment and increase substrate transfer yield by passivating the step-edges of the vicinal crystal. For this, long, aligned 9-AGNRs were successfully grown next to a wide bandgap 1D polymer, poly-*para*-phenylene[5], passivating the edges. Given the larger bandgap of the polymer compared to 9-AGNRs, it serves as an effective passivating agent without altering the electronic properties of subsequent devices.

A second strategy focused on minimizing GNR adhesion to the step-edges (as well as to the gold surface in general) by forming self-assembled monolayers of 1,8,13-trimercaptomethyl-triptycene (T1) SAMs and n-octane thiol on the gold substrates on which the GNRs were grown[6]. The concept is straightforward: since GNRs are only physisorbed, introducing a molecule that chemically binds to the substrate may enable its intercalation beneath the GNRs. The experiments reported in this thesis confirmed partial, yet ineffective intercalation in solution.

Finally, while Raman spectroscopy proved invaluable for assessing GNR quality, it falls short in detecting surface residues post-transfer. In the bubble-transfer method extensively examined in this research, the predominant residue is polymethyl methacrylate (PMMA), used to support GNRs during transfer. PMMA removal is challenging and any residual PMMA can severely compromise device performance. Considering that the width of GNRs is comparable to that of a single PMMA molecule, even a trace amount of PMMA can obstruct electrical connectivity

between contacts and GNRs. Within the present thesis, techniques to effectively remove PMMA residues were thus developed, enabling for the first time to capture STM images of substrate-transferred GNRs. These images conclusively demonstrate that the GNRs maintain their atomically precise structure throughout the transfer process.

Overall, this thesis has systematically addressed the multifaceted challenges in GNR synthesis, transfer, and characterization while also offering innovative solutions. At the same time, remarkable progress in device fabrication is accelerating the transition of GNRs from theoretical curiosity to technological reality. For instance, it is now possible to establish electrical contacts with individual GNRs using carbon nanotubes[7], which allows for devices exhibiting single-electron transport via Coulomb blockade. This technological leap opens avenues for incorporating atomically precise GNRs into multigate quantum-dot devices, setting the stage for the next era of electronics.

Recent seminal work by Mishra et al.[8–10] has shown the possibility of creating atomically precise magnetic carbon nanostructures through on-surface synthesis, structures that exhibit extraordinary quantum phenomena. However, these materials are highly sensitive to oxygen exposure[11,12], which nullifies their magnetic properties. Current substrate transfer techniques optimized for chemically stable GNRs are incompatible with such reactive species. Therefore, future work must focus on either stabilizing these sensitive molecular systems without affecting their unique properties or on developing transfer techniques that can operate in an oxygen-free environment.

Given these limitations with current techniques, the strategy to reduce GNR-substrate interactions using self-assembled monolayers (SAMs) for intercalation could potentially be adapted for vacuum-based transfer methods. Over the last decade, there has been a surge in dry-transfer techniques for reactive 2D materials, some of which are now automated and conducted entirely in vacuum chambers[13]. Pairing these developments with advances in 2D heterostructure assembly and exotic on-surface synthesized materials could usher in a new age of quantum technologies.

References

1. Wang, H. et al. Graphene nanoribbons for quantum electronics. Nat Rev Phys 3, 791–802 (2021).
2. International Roadmap for Devices and Systems (IRDSTM) 2022 Edition. https://irds.ieee.org/images/files/pdf/2022/2022IRDS_BC.pdf (2022).
3. Houtsma, R. S. K., Rie, J. de la & Stöhr, M. Atomically precise graphene nanoribbons: interplay of structural and electronic properties. Chem. Soc. Rev. 50, 6541–6568 (2021).
4. Borin Barin, G. et al. Growth Optimization and Device Integration of Narrow-Bandgap Graphene Nanoribbons. Small 2202301 (2022) doi:10.1002/smll.202202301.
5. Yuan, B. et al. Resolving Quinoid Structure in Poly(para-phenylene) Chains. J. Am. Chem. Soc. 142, 10034–10041 (2020).
6. Ohtomo, M., Sekine, Y., Hibino, H. & Yamamoto, H. Graphene nanoribbon field-effect transistors fabricated by etchant-free transfer from Au(788). Appl. Phys. Lett. 112, 021602 (2018).
7. Zhang, J. et al. Contacting individual graphene nanoribbons using carbon nanotube electrodes. Nat Electron 6, 572–581 (2023).
8. Mishra, S. et al. Topological frustration induces unconventional magnetism in a nanographene. Nature nanotechnology 15, 22–28 (2020).
9. Mishra, S. et al. Observation of fractional edge excitations in nanographene spin chains. Nature 598, 287–292 (2021).
10. Mishra, S. et al. Large magnetic exchange coupling in rhombus-shaped nanographenes with zigzag periphery. Nat. Chem. 13, 581–586 (2021).
11. Lawrence, J. et al. Circumventing the stability problems of graphene nanoribbon zigzag edges. Nat. Chem. 14, 1451–1458 (2022).
12. Lawrence, J. et al. Probing the Magnetism of Topological End States in 5-Armchair Graphene Nanoribbons. ACS Nano acsnano.9b10191 (2020) doi:10.1021/acsnano.9b10191.
13. Mannix, A. J. et al. Robotic four-dimensional pixel assembly of van der Waals solids. Nat. Nanotechnol. 17, 361–366 (2022).

List of publications

CHAPTER 3

Quantifying alignment and quality of graphene nanoribbons: A polarized Raman spectroscopy Approach.

Rimah Darawish, Jan Overbeck, Klaus Müllen, Michel Calame, Pascal Ruffieux, Roman Fasel, and Gabriela Borin Barin (submitted for publication) https://doi.org/10.48550/arXiv.2307.09490 (2023).

CHAPTER 4

Unraveling the role of precursor coverage in the synthesis and substrate transfer of graphene nanoribbons

Rimah Darawish, Oliver Braun, Klaus Müllen, Michel Calame, Pascal Ruffieux, Roman Fasel, and Gabriela Borin Barin (in preparation).

CHAPTER 5

Quantification of graphene nanoribbon transfer efficiency: A polarized Raman spectroscopy analysis

Rimah Darawish, Oliver Braun, Klaus Müllen, Michel Calame, Pascal Ruffieux, Roman Fasel, and Gabriela Borin Barin (in preparation).

CHAPTER 6

Optimization of substrate transfer: High-quality graphene nanoribbons for STM and Raman characterization

Rimah Darawish, Oliver Braun, Klaus Müllen, Michel Calame, Pascal Ruffieux, Roman Fasel, and Gabriela Borin Barin (in preparation).

1. Zhang, J., Braun, O., Barin, G.B., Sangtarash, S., Overbeck, J., **Darawish, R.**, Stiefel, M., Furrer, R., Olziersky, A., Müllen, K., Shorubalko, I., Daaoub, A.H.S., Ruffieux, P., Fasel, R., Sadeghi, H., Perrin, M.L., Calame, M., 2023. Tunable Quantum Dots from Atomically Precise Graphene Nanoribbons Using a Multi-Gate Architecture.

   Adv. Electron. Mater. **9**, 2201204 (2023). https://doi.org/10.1002/aelm.202201204

2. Braun, O., Overbeck, J., El Abbassi, M., Käser, S., Furrer, R., Olziersky, A., Flasby, A., Borin Barin, G., Sun, Q., **Darawish, R**., Müllen, K., Ruffieux, P., Fasel, R., Shorubalko, I., Perrin, M.L., Calame, M. Optimized graphene electrodes for contacting graphene nanoribbons.

   Carbon **184**, 331–339 (2021). https://doi.org/10.1016/j.carbon.2021.08.001

3. Mutlu, Z., Lin, Y., Borin Barin, G., Zhang, Z., Pitner, G., Wang, S., **Darawish, R**., Di Giovannantonio, M., Wang, H., Cai, J. and Passlack, M., 2021, December. Short-Channel Double-Gate FETs with Atomically Precise Graphene Nanoribbons.

   In *2021 IEEE International Electron Devices Meeting (IEDM)* 37.4.1-37.4.4 (2021). doi:10.1109/IEDM19574.2021.9720620.

4. Zhao, S., Barin, G.B., Cao, T., Overbeck, J., **Darawish, R**., Lyu, T., Drapcho, S., Wang, S., Dumslaff, T., Narita, A., Calame, M., Müllen, K., Louie, S.G., Ruffieux, P., Fasel, R., Wang, F.,. Optical Imaging and Spectroscopy of Atomically Precise Armchair Graphene Nanoribbons.

   Nano Lett. **20**, 1124–1130 (2020). https://doi.org/10.1021/acs.nanolett.9b04497

5. Overbeck, J., Barin, G.B., Daniels, C., Perrin, M.L., Braun, O., Sun, Q., **Darawish, R**., De Luca, M., Wang, X.-Y., Dumslaff, T., Narita, A., Müllen, K., Ruffieux, P., Meunier, V., Fasel, R., Calame, M., A Universal Length-Dependent Vibrational Mode in Graphene Nanoribbons.

   ACS Nano **13**, 13083–13091 (2019). https://doi.org/10.1021/acsnano.9b05817.

6. Overbeck, J., Borin Barin, G., Daniels, C., Perrin, M.L., Liang, L., Braun, O., **Darawish, R**., Burkhardt, B., Dumslaff, T., Wang, X.-Y., Narita, A., Müllen, K., Meunier, V., Fasel, R., Calame, M., Ruffieux, P., Optimized Substrates and Measurement Approaches for Raman Spectroscopy of Graphene Nanoribbons.

   Phys. Status Solidi B **256**, 1900343 (2019). https://doi.org/10.1002/pssb.201900343.

7. Castellano, M., Alloisio, M., **Darawish, R**., Dodero, A., Vicini, S., Electrospun composite mats of alginate with embedded silver nanoparticles: Synthesis and characterization.

   J. Therm. Anal. Calorim. (2019). https://doi.org/10.1007/s10973-018-7979-z.

Acknowledgments

This work was supported by the Swiss National Science Foundation under grant no. 200020_182015, the European Union Horizon 2020 research and innovation program under grant agreement no. 881603 (GrapheneFlagship Core 3), and the Office of Naval Research BRC Program under the grant N00014-18-1-2708. I greatly appreciate the financial support from the Werner Siemens Foundation (CarboQuant). I also acknowledge the funding from the University of Bern

The journey of completing this thesis has been both challenging and rewarding. It would not have been possible without the support, guidance, and encouragement of many individuals.

Firstly, I express my heartfelt gratitude to Prof. Dr. Roman Fasel. His guidance was a beacon throughout this journey. His patience, expertise, and belief in my capabilities were pivotal in shaping my research.

Dr. Gabriela Borin Barin, or Gabi as I fondly call her, has been a constant source of encouragement. As her first Ph.D. student, our journey was filled with mutual learning and growth. She was there every step of the way, guiding, supporting, and cheering me on. Her hands-on approach during intricate phases of my research was invaluable.

Special thanks to Dr. Pascal Ruffieux for his invaluable mentorship, consistent guidance, and insights. His dedication to my academic growth and his vast expertise enriched my PhD experience.

Christine Tran ensured all administrative tasks were handled smoothly, allowing me to focus on my research. Her efforts in organizing team events contributed greatly to the camaraderie and spirit of the nanotech@surfaces laboratory. I appreciate her dedication to fostering a cohesive team environment. Lukas Rotach was instrumental in ensuring our laboratory operations run seamlessly. His technical expertise and approachable nature facilitated my research and enriched our team dynamics.

Dr. Amogh Kinikar, a colleague and dear friend, was a cornerstone of my PhD journey. His insights and camaraderie were invaluable, and our discussions, both scientific and casual, were highlights of my time at Empa. Heartfelt thanks to Lucia Palomino Ruiz for her genuine warmth and steadfast emotional support at Empa.

The nanotech@surfaces laboratory team was pivotal in shaping my journey at Empa. The collaborative spirit, insightful discussions, and shared dedication were enriching. I'm particularly grateful to Oliver Gröning and Roland Widmer for their leadership and guidance. Additionally, I would like to acknowledge Max Bommert, Nils Krane, Chenxiao Zhao, Feifei Xiang, Debopriya Dutta, Lucia Palomino Ruiz, Elia Turco, Wangwei Xu, Nicolo Bassi, Dominik Lüthi, Shivani Singh, Jeong Ha Hwang, Bruno Schuler, Jonas Allerbeck, Eve Ammerman, Lysander Huberich, Laric

Bobzien, Daniele Passerone, Carlo Pignedoli, Aliaksandr Yakutovich, Andres Ortega Guerrero, Anooja Jayaraj, Goncalo Santos Catarina, and Raymond Amador. Your collective efforts fostered an environment of innovation, growth, and camaraderie.

I would like to express my deep gratitude to our former colleagues who have left an indelible mark on our team. Dr. Marco Di Giovannantonio, Dr. José Ignacio Urgel, Dr. Shantanu Mishra, Dr. Néstor Merino Díez, Dr. Samuel Stolz, and Dr. Qiang Sun have each brought their unique expertise and perspectives, contributing significantly to the foundation and progress of our endeavors.

I would like to extend my heartfelt appreciation to the members of the 405-Transport at Nanoscale Interfaces group at Empa. Prof. Dr. Michel Calame, Dr. Jan Overbeck, Dr. Oliver Braun, Dr. Jian Zhang, Prof. Dr. Mickael Lucien Perrin, Rico Muff, Dr. Ivan Shorubalko, and Dr. Mirjana Dimitrievska. Their combined expertise and dedication have been instrumental in driving our successful high-quality publications.

Outside the lab, Dani Schnider and Andrea Kennel were not only my guides to the Swiss way of life but also took care of me as if I were their own, making my stay in Switzerland both memorable and comforting. My husband, Dr. Mohamed Sadiq Ikbal, has been my rock, offering unwavering support during the most challenging times. Lastly, my family and friends have been my foundation. Their constant encouragement, love, and support have been sources of strength, reminding me of the bigger picture and the importance of perseverance.

In conclusion, this thesis reflects not only my work but also the collective efforts, guidance, and support of all these wonderful individuals. I am deeply grateful and consider myself fortunate to have been part of such a supportive community.

Declaration of consent

on the basis of Article 18 of the PromR Phil.-nat. 19

Name/First Name: Rimah, Darawish

Registration Number: 17-127-465

Study program: PhD in Chemistry and Molecular Sciences

Bachelor ☐ Master ☐ Dissertation ☑

Title of the thesis: Graphene nanoribbon growth and substrate transfer for device applications.

Supervisor: Roman Fasel

I declare herewith that this thesis is my own work and that I have not used any sources other than those stated. I have indicated the adoption of quotations as well as thoughts taken from other authors as such in the thesis. I am aware that the Senate pursuant to Article 36 paragraph 1 litera r of the University Act of September 5th, 1996 and Article 69 of the University Statute of June 7th, 2011 is authorized to revoke the doctoral degree awarded on the basis of this thesis.
For the purposes of evaluation and verification of compliance with the declaration of originality and the regulations governing plagiarism, I hereby grant the University of Bern the right to process my personal data and to perform the acts of use this requires, in particular, to reproduce the written thesis and to store it permanently in a database, and to use said database, or to make said database available, to enable comparison with theses submitted by others.

Dübendorf/ 26.06.2023

Place/Date

Signature Rimah